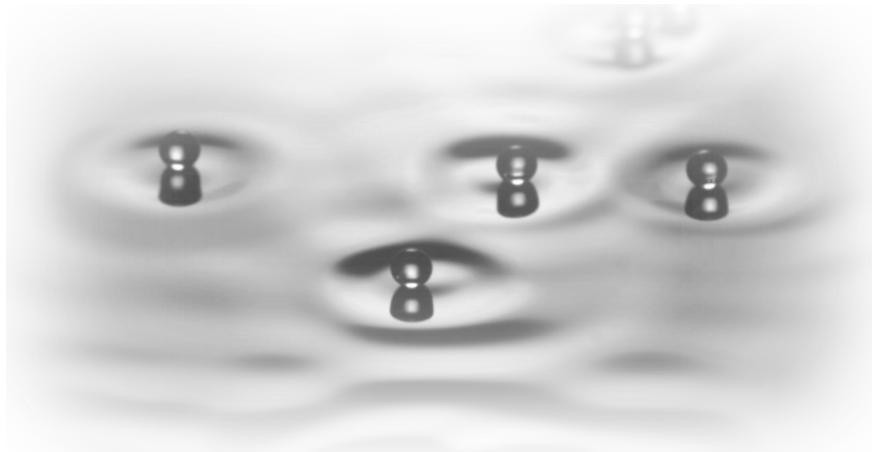




MONASH University

# Superwalking Droplets and Generalised Pilot-Wave Dynamics



**Rahil Valani**

*Academic Advisors:*

Dr. Anja Slim

Assoc. Prof. Tapio Simula

Prof. Kristian Helmerson

A thesis submitted for the degree of

**Doctor of Philosophy**

at Monash University

School of Physics & Astronomy

November 2020



# Abstract

On vertically vibrating a bath of liquid, a droplet of the same liquid can be made to bounce and walk on the liquid surface. This walking droplet, also known as a walker, locally generates slowly decaying waves on each bounce. It then interacts with these waves on subsequent bounces to propel itself giving rise to a self-propelled droplet-wave entity. Such walkers have been shown to mimic several peculiar behaviours that were previously thought to be exclusive to the quantum realm. In this thesis, I present the discovery of a new class of walking droplets, coined *superwalkers*, that emerge when the bath of liquid is simultaneously driven at two frequencies. We investigate the characteristics of solitary superwalkers in experiments and show that superwalkers can be more than double the size and can walk at more than triple the speeds of typical single-frequency driven walkers. We also present results of interactions of multiple superwalkers and show that their interactions give rise to novel multi-droplet behaviours. We then formulate a theoretical model for superwalkers by deriving a new form of the wave field generated by a superwalker and couple it to the existing theoretical models for walkers. By performing numerical simulations using this model, we can explain the experimentally observed characteristics of small- to moderate-size superwalkers. We also numerically explore a novel behaviour of superwalkers, stop-and-go motion (SGM), that emerges when the two driving frequencies are slightly detuned.

We then move on to explore the dynamics of two identical walking droplets using a theoretical stroboscopic model in a generalised pilot-wave framework. We capture the experimentally observed two-droplet states as well as uncover a rich array of more exotic dynamics. We explore these rich behaviours and the bifurcations between different two-droplet states through analytic and numerical linear stability analyses and through fully nonlinear numerical simulation. We also numerically study two-droplet pair correlations that arise when two identical droplets are launched toward each other at an angle. Finally, using the stroboscopic model with different forms of the wave field, we explore the chaotic nature and the statistical behaviour of the unsteady dynamics of a single droplet that arises for small inertia and large wave forcing.



## Declaration

This thesis is an original work of my research and contains no material which has been accepted for the award of any other degree or diploma at any university or equivalent institution and that, to the best of my knowledge and belief, this thesis contains no material previously published or written by another person, except where due reference is made in the text of the thesis.

Signature:

Name: Rahil Valani

Date: Sunday 29<sup>th</sup> November, 2020



## Acknowledgements

First and foremost, I would like to thank my supervisors, Anja and Tapio, for their selfless support, enthusiasm and being fantastic mentors. Specifically, I would like to thank Anja for always being there to answer any questions I had and encouraging me to step outside my comfort zone, and I would like to thank Tapio for his helpful advice on various things and having wonderful discussions.

I would like to thank Prof. John Bush for inviting me to visit his lab at the start of my PhD. I would like to thank Prof. Kristian Helmersen for his support and allowing me to use various equipment from his lab for my experiments. I would like to thank Steve Morton for allowing me to borrow various imaging equipment for my experiments and also teaching me how to use them. I would also like to thank Daniel Duke for letting me borrow his high speed video camera. I would like to thank Shaun Johnstone for always being there to assist with any problems I had with my experiments. We miss you Shaun. I would like to thank Prof. David Paganin for having wonderful research related discussions and for his infectious enthusiasm for Physics. I would like to thank Joel Miller, Theodore Vo and Andy Hammerlindl for having wonderful discussion related to my research. I would also like to thank my collaborator, Jack Dring, for helping me out with simulations.

I would like to thank my Mum and Dad for always supporting me throughout my PhD. I would like to thank my brother, Kelvin, for always being there to discuss random things at random times. I would like to thank all the students from the science workshops I conduct at the local community centre. You have kept me motivated to spread the joy of science and helped me in ways you may not even know. I would like to thank all my friends with whom I have interacted with during the past three and a half years. You have all been a healthy distraction from my research work. Special thanks to Simran, Naail, Ali and Samita for keeping me entertained during the writing of this thesis in lockdown.

This research was supported by an Australian Government Research Training Program (RTP) Scholarship.



# Table of contents

<b>1</b>	<b>Introduction</b>	<b>1</b>
1.1	Bouncing and walking droplets . . . . .	1
1.2	Interactions of multiple droplets . . . . .	3
1.3	Hydrodynamic quantum analogues . . . . .	4
1.4	Thesis overview . . . . .	7
1.5	List of publications . . . . .	9
<b>2</b>	<b>Theoretical Framework</b>	<b>11</b>
2.1	Setup of the system . . . . .	11
2.2	Vertical dynamics . . . . .	12
2.2.1	Notation for vertical bouncing modes . . . . .	14
2.3	Droplet deformations . . . . .	15
2.4	Wave field of a walker . . . . .	17
2.4.1	Faraday waves . . . . .	17
2.4.2	Damped Faraday waves generated by a walker . . . . .	18
2.5	Horizontal dynamics . . . . .	21
2.6	Stroboscopic models . . . . .	21
<b>I</b>	<b>Superwalking Droplets</b>	<b>25</b>
<b>3</b>	<b>From walkers to superwalkers</b>	<b>27</b>
3.1	Introduction . . . . .	27
3.2	Details of the experiment . . . . .	29
3.3	Bouncing modes notation for superwalkers . . . . .	31
3.4	Dynamics of solitary superwalkers . . . . .	33
3.4.1	Effect of varying the droplet radius . . . . .	33
3.4.2	Effect of varying the phase difference . . . . .	35

3.4.3	Effect of varying the acceleration amplitudes . . . . .	36
3.5	Contact with the underlying wave field . . . . .	38
3.6	Interactions of multiple superwalkers . . . . .	40
3.7	Bubble-droplets . . . . .	44
3.8	Conclusion . . . . .	45
<b>4</b>	<b>Emergence of superwalking droplets: a numerical approach</b>	<b>47</b>
4.1	Introduction . . . . .	47
4.2	Theoretical setup . . . . .	48
4.3	Waves excited under two-frequency driving . . . . .	49
4.3.1	Decay rate of damped Faraday waves . . . . .	55
4.3.2	Faraday instability thresholds . . . . .	56
4.3.3	Amplitude and phase shift of damped Faraday waves . . . . .	57
4.3.4	Wave field of a superwalker . . . . .	59
4.3.5	Comparison of a superwalker and a walker wave field . . . . .	61
4.4	Numerical method and parameter values . . . . .	63
4.5	Emergence of superwalking . . . . .	65
4.5.1	Importance of the phase difference . . . . .	66
4.5.2	Speed-size characteristics of superwalking droplets . . . . .	68
4.5.3	Dynamics in the acceleration amplitudes parameter space . . . . .	70
4.5.4	Comparison of different droplet models . . . . .	70
4.6	Discussion and conclusion . . . . .	74
<b>5</b>	<b>Stop-and-go motion (SGM) of superwalkers</b>	<b>77</b>
5.1	Introduction . . . . .	77
5.2	SGM: experimental observation . . . . .	78
5.3	Theoretical model . . . . .	79
5.4	Emergence of SGM . . . . .	80
5.4.1	Parameter space exploration of the SGM . . . . .	82
5.4.2	Back-and-forth SGM . . . . .	83
5.5	Discussion and conclusion . . . . .	85
<b>II</b>	<b>Generalised Pilot-Wave Dynamics</b>	<b>87</b>
<b>6</b>	<b>Pilot-wave dynamics of two droplets</b>	<b>89</b>
6.1	Introduction . . . . .	89
6.2	Theoretical formulation . . . . .	91

6.3	Parameter space description . . . . .	92
6.4	Stationary states . . . . .	94
6.4.1	Linear stability analysis . . . . .	94
6.5	Inline oscillations . . . . .	99
6.6	Parallel walking . . . . .	100
6.6.1	Linear stability analysis . . . . .	100
6.7	Oscillating walkers . . . . .	104
6.7.1	Lopsided walkers . . . . .	104
6.7.2	Switching walkers . . . . .	106
6.8	Wandering walkers . . . . .	107
6.8.1	Back-and-forth walkers . . . . .	107
6.8.2	Discrete-turning walkers . . . . .	108
6.8.3	Continuously turning walkers . . . . .	110
6.8.4	Closed trajectories and nearly closed trajectories . . . . .	110
6.9	Chasers . . . . .	112
6.9.1	Linear stability analysis . . . . .	114
6.10	Conclusion . . . . .	117
<b>7</b>	<b>Two-droplet correlations</b>	<b>119</b>
7.1	Introduction . . . . .	119
7.2	Theoretical model . . . . .	121
7.2.1	System parameters . . . . .	123
7.2.2	Numerical experiments . . . . .	123
7.3	Two-droplet correlations . . . . .	125
7.4	Conclusion . . . . .	129
<b>8</b>	<b>Unsteady dynamics of a walking droplet</b>	<b>131</b>
8.1	Introduction . . . . .	131
8.2	Linear stability of a walking droplet in 2D . . . . .	132
8.3	Generalised 1D stroboscopic model with an arbitrary wave form . . . . .	134
8.3.1	Steady walking solution . . . . .	135
8.3.2	Linear stability analysis . . . . .	135
8.4	Droplet dynamics with a Bessel wave field . . . . .	136
8.4.1	Steady solution and linear stability analysis . . . . .	136
8.4.2	Simulations in the parameter space . . . . .	138
8.5	Droplet dynamics with a Gaussian wave field . . . . .	140
8.6	Droplet dynamics with a sinusoidal wave field . . . . .	140

---

8.6.1	Steady walking solution and linear stability analysis . . . . .	140
8.6.2	Reducing the integro-differential equation to a finite system of ODEs . . . . .	141
8.6.3	Simulations in the parameter space . . . . .	142
8.7	Chaotic aspects of the unsteady dynamics . . . . .	144
8.7.1	Lorenz system and the droplet's dynamics . . . . .	144
8.7.2	1D map of the velocity time series . . . . .	149
8.8	Statistical aspects of the unsteady dynamics . . . . .	150
8.8.1	Statistical properties of the flip-flop process . . . . .	150
8.8.2	Analysis of the diffusion-like dynamics . . . . .	155
8.9	Conclusion . . . . .	155
<b>9</b>	<b>Conclusions and outlook</b>	<b>157</b>
	<b>References</b>	<b>163</b>
	<b>Appendix A Effects of horizontal vibrations and air currents in experi- ments</b>	<b>173</b>
	<b>Appendix B Determination of parameters in simulations with super- walkers</b>	<b>175</b>
	<b>Appendix C Numerical Method for simulating droplets in the strobo- scopic model</b>	<b>177</b>

# Chapter 1

## Introduction

We find many examples in nature where animate entities consume energy from the environment and convert it into directed motion. These include many living organisms, including humans, who consume energy from food and self-propel by exhibiting various modes of locomotion from walking to flying. Self-propulsion is also ubiquitous in the microscopic world of bacteria, cells, algae and other micro-organisms. A novel inanimate system that also exhibits self-propulsion is walking droplets discovered by Yves Couder and colleagues in 2005. In this system, a droplet-wave entity self-propels on the free surface of a vertically vibrating bath of liquid. Intriguingly, such a macroscopic self-propelled droplet-wave entity has been shown to mimic several peculiar features that were previously thought to be exclusive to the quantum realm.

### 1.1 Bouncing and walking droplets

In 1831, Michael Faraday observed that a liquid container subjected to vertical vibrations gives rise to beautiful patterns of standing waves on the free surface of the liquid [1]. These standing waves, now known as Faraday waves, either oscillate at the same frequency as the driving (harmonic Faraday waves) or at half the driving frequency (subharmonic Faraday waves) [2]. Moreover, these standing waves are a result of an instability, now known as the Faraday instability, that occurs above a certain threshold of the amplitude of vertical vibrations. More than 100 years later, Jearl Walker demonstrated that in such a system, droplets of the same liquid can be made to bounce and float on the liquid surface for several minutes when these standing waves are present [3]. More recently in 2005, Yves Couder and colleagues showed that even for low amplitudes of vibrations below the Faraday instability threshold, where the surface of the liquid bath is flat, a droplet of the same liquid can be made to bounce

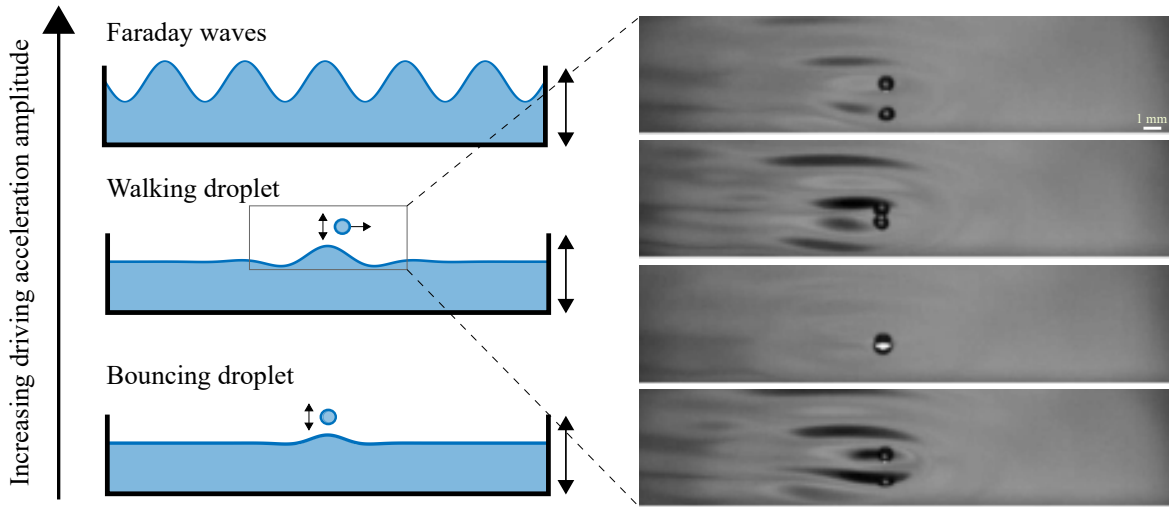


Figure 1.1 : System of walking droplets. Vertically vibrating a bath of liquid at high driving acceleration amplitudes gives rise to Faraday waves (top left panel). At low driving accelerations below the Faraday instability, a droplet can bounce indefinitely on the liquid surface (bottom left panel). At intermediate driving accelerations below the Faraday instability, the steady bouncing state becomes unstable to a walking state giving rise to a self-propelled droplet-wave entity called *walker* (middle left panel and right panels).

indefinitely on the liquid surface [4]. This happens because as the air film separating the droplet and the liquid bath gets squeezed upon the droplet's impact, there is not enough time for this air film to drain completely before the droplet lifts off, resulting in a steady bouncing state [4].

For certain size droplets, this steady bouncing state becomes unstable to a walking state as the amplitude of the vibration increases [5]. This walking droplet, also known as a *walker*, locally excites damped subharmonic Faraday waves on each bounce. The walker then interacts with these waves on subsequent bounces such that each impact of the walker is on a sloped liquid interface (see figure 1.1). This results in the wave imparting horizontal momentum to the droplet and giving rise to a self-propelled droplet-wave entity on the liquid surface. The decay time of the Faraday waves excited by the walker is inversely proportional to the proximity to the Faraday threshold. Hence, below but close to the Faraday instability threshold, the waves generated by the walker on each impact decay very slowly in time. This gives rise to path memory in the system where the walker's dynamics is influenced not only by the wave it generated on its most recent bounce, but also by waves it generated in the distant past resulting in non-Markovian dynamics.

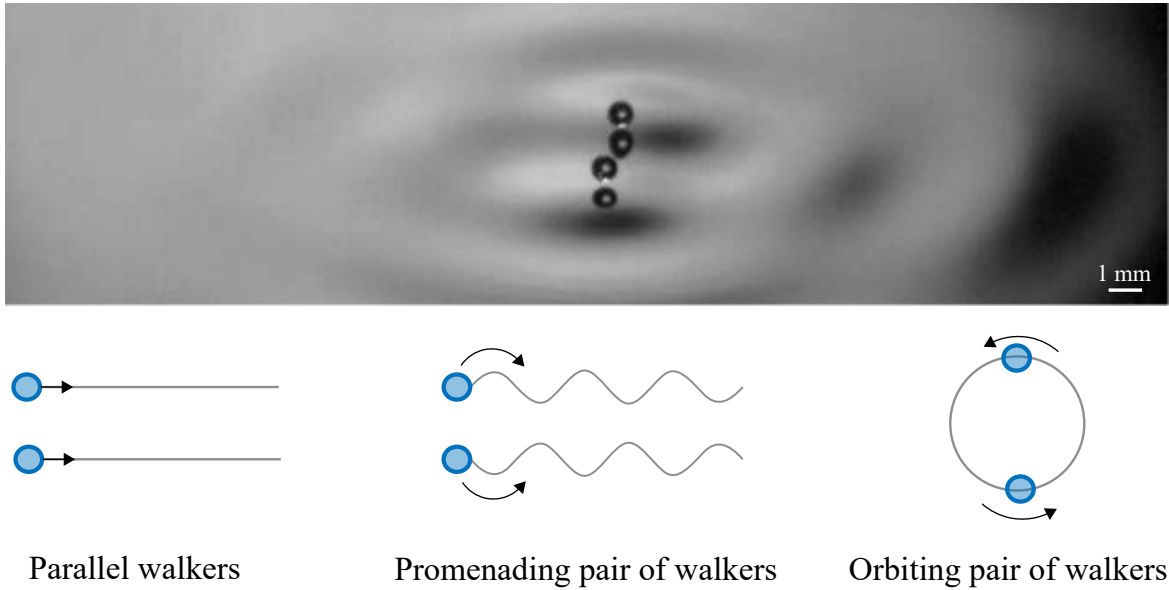


Figure 1.2 : Interactions of multiple walkers. *Top panel:* Two (or more) walkers interact with each other primarily through their underlying wave fields. *Bottom panel:* Schematic showing typical dynamic bound states of two walkers: parallel walkers, promenading pair of walkers and orbiting pair of walkers.

## 1.2 Interactions of multiple droplets

Multiple bouncing and walking droplets can interact in two different ways: (i) via direct droplet-droplet contact interactions or (ii) via interactions mediated by the underlying wave field. Most interactions of droplets are mediated by the underlying wave field and result in rich static and dynamical behaviours. Two bouncing droplets can remain bound at discrete distances apart with no horizontal motion. The discrete separations between them are proportional to the Faraday wavelength, the wavelength of the waves generated by the droplet [6]. When three such droplets bind to each other, they can either form a linear or a triangular configuration. Adding more droplets results in them self-organising into more intricate crystal-like structures [7] including Archimedean lattices [8].

Two walking droplets can also form various dynamical states where the walkers perform intricate dances while remaining bound to each other (see figure 1.2). Since for typical walkers, the bouncing frequency is half the driving frequency, two walkers can either have in-phase or out-of-phase interactions. For in-phase interactions, the two droplets impact the bath simultaneously, while in out-of-phase interactions, one droplet is at the peak bouncing height when the other droplet impacts the bath [6]. A common bound state observed for walkers is a parallel walking pair where two identical

droplets walk side by side on parallel trajectories [6]. In this state the separation can take a discrete set of values. Promenading pairs are also ubiquitous where the droplets oscillate towards and away from each other while parallel walking [6, 9, 10]. Another common bound state is an orbiting pair of walkers where two droplets orbit each other at various discrete distances apart [6, 10]. When two droplets are identical, they orbit symmetrically around their common centre of rotation, while the orbits of two mismatched droplets typically results into the larger droplet orbiting around a centre of rotation closer to the smaller droplet. Such mismatched orbiting droplets also display a variety of exotic orbits including oscillating and epicycloidal orbits [11]. Two mismatched droplets can also form a ratcheting pair where one droplet walks behind another at a constant low velocity compared to a typical isolated walker. Here the walking direction of the ratcheting pair can be reversed by varying the amplitude of the driving acceleration [12, 13]. In a confined annular cavity, multiple identical walkers have also been reported to form droplet trains where droplets walk one behind another such that the walking speed of the train is larger than a single walker [14]. Aggregates of many mismatched droplets exhibit slow spontaneous translation and rotation of the whole cluster [12].

### 1.3 Hydrodynamic quantum analogues

Very close to but below the Faraday instability threshold, the droplet is strongly influenced by the long-lived Faraday waves it lays down along its trajectory. In this high memory regime, the walker has been shown to mimic several peculiar quantum-like behaviours. We briefly review these hydrodynamic quantum analogues in this section.

On confining a walker in a circular cavity whose diameter is a few times the Faraday wavelength, the walker exhibits circular trajectories inside the cavity at low driving amplitudes below the Faraday threshold i.e., low memory. As the memory is increased, the droplet transitions to epicycloidal trajectories. In the high memory regime which is just below the Faraday threshold, the droplet's trajectory inside the cavity becomes chaotic. In this regime, a coherent wave-like structure emerges in the probability distribution of the droplet's position [15–20]. This is analogous to quantum corrals experiments, where an electron confined in a corral of iron atoms has a wave-like pattern in the probability density with the characteristic wavelength as the de Broglie wavelength of the trapped electron [21]. The walker exhibits a similar wave-like structure with the Faraday wavelength playing the role of the de Broglie wavelength. Similarly, confining a walker in an elliptical corral and introducing

localised inhomogeneities in the form of submerged wells can lead to resonant projection effects in the walker's statistics similar to a quantum mirage [22]. Wave-like statistics emerge in these closed systems when (i) the decay time of the waves generated by the droplet is longer than the time required for the droplet to cross its domain so that the droplet can continually navigate its self-excited wave field, and (ii) the droplet's dynamics is chaotic and it switches intermittently between different unstable periodic orbits [15, 22]. Recently, such wave-like statistics have also been reported in an open system where the walker has been shown to exhibit a hydrodynamic analogue of Friedel oscillations [23]. Friedel oscillations are the statistical signature of an impurity on a metal surface, spatially decaying wave-like modulations in the probability density function of the surrounding electron sea [24, 25]. In the hydrodynamic analogue, a walker interacting with a submerged well displays a statistical signature in the vicinity of the well that is strikingly similar to Friedel oscillations.

Walkers confined in potentials with a central force have been shown to give rise to quantised orbits [26–28, 20, 29–33]. Encapsulating ferrofluids within the walker and applying a magnetic field that varies radially, the walker can be confined in a two-dimensional harmonic potential. A discrete set of orbits are observed such as circles, ovals, lemniscates and trefoils [26]. Perrard et al. [26] showed that the dynamic constraint imposed on the walker by its guiding wave field results in a double quantisation in the mean energy and angular momentum of the orbiting states. This results in quantum-like eigenstates emerging from memory-mediated interactions in the walker system.

A walker on the surface of a bath that is rotating about a vertical axis exhibits circular trajectories in the low memory regime. Here the orbital radius decreases monotonically with increase in rotation speed. Intriguingly, at high memory, certain orbital radii become unstable resulting in a quantisation in the radius of the inertial orbits of walkers similar to Landau levels of electrons [34]. Moreover, it has been shown that as the memory is increased progressively, the orbital states become unstable, giving way to wobbling orbital motions and then more complex periodic or aperiodic trajectories. In the high memory limit, irregular chaotic trajectories emerge as the walker drifts between unstable orbits resulting in multimodal statistics in the radius of curvature of the droplet's trajectory [35–37]. In the limit where the rotation rate of the bath tends to zero, these orbiting states of a walker, known as spin states, are unstable in experiments but they can be stabilised in simulations where parameters are not restricted to the experimental values [38–40]. By investigating a pair of walkers on this rotating experimental setup, it was found that the orbital radii of a pair of orbiting

droplets increases or decreases based on whether the pair is rotating in the same or opposite sense to the bath rotation, hinting at an analogy with Zeeman splitting of atomic energy levels [41].

A walker interacting with a submerged barrier typically gets reflected from the barrier [42, 43]. Eddi et al. [44] showed that occasionally, the interactions of the droplet-wave entity with the barrier can lead to droplet tunnelling across the barrier. The tunnelling probability decreases exponentially with the barrier width and increases as the Faraday threshold is approached [44–46]. Thus, the complex interaction of the walker with its underlying wave field results in unpredictable tunnelling of the droplet.

Walkers passing through slit geometries can give rise to diffraction patterns. Couder and Fort [47] directed walkers one at a time through their single and double slit geometries. In their single-slit study, by directing 125 walkers, one at a time towards the slit and quantifying the diffraction angle in the far field, they found a diffraction pattern similar to single photon diffraction experiments. Moreover, they also examined a hydrodynamic analogue of the double-slit experiment with photons or electrons. They observed a wave-like pattern in the histogram of the deflection angle of walkers that is similar to the interference pattern one would get if a monochromatic wave of Faraday wavelength diffracted through the double slit. They proposed that while the walker passes through one slit or the other, its guiding wave passes through both and the walker effectively feels the second slit by virtue of its underlying wave. These results were later contested by Andersen et al. [48] who observed no clear diffraction or interference patterns in such experiments. Pucci et al. [49] revisited these experiments with a more refined experimental setup and reported that the system behaviour is strongly dependent on the vibration forcing. They observed three dominant central peaks in the histogram of the deflection angle but were unable to recover the Fraunhofer-like dependence of the number of peaks on the slit width as reported by Couder and Fort [47]. Although they concluded that quantum-like diffraction is not possible with slits of the form considered in their setup because the system behaviour is dominated by walker–wall interactions, they noted walkers may exhibit diffraction in the absence of boundaries, like in the Kapitza-Dirac effect. Moreover, they noted that in the quantum double-slit experiments, there is a significant disparity in scales between the slit width and the de Broglie wavelength. They pointed out that achieving the same scaling is not currently feasible in experiments with walkers and suggested that such geometries can be explored in simulations of walker which may yield interesting results. Walker diffraction through single and double slit has also been recently revisited by Ellegaard [50], who undertook a comprehensive exploration of parameter space and reported

observation consistent with Pucci et al. [49]. Moreover, they also found rich diffraction patterns in the double-slit arrangement.

Thus, the walkers have been shown to mimic several quantum-like behaviours such as diffraction through slit geometries, tunnelling across submerged barriers, level splitting and quantisation in rotating frames and harmonic potential, and wave-like statistics in confined and open geometries. We refer the reader to Bush [51] and Bush and Oza [52] for a detailed review of hydrodynamic quantum analogues. It is remarkable that a macroscopic wave-particle entity in the form of a walker is able to exhibit several peculiar features that were once thought to be exclusive to the quantum realm.

## 1.4 Thesis overview

This thesis is organised into two parts. Part I, comprising of Chapters 3, 4 and 5, presents an experimental and numerical study of a new class of walking droplets, coined *superwalkers*, that emerge when a liquid bath is driven at two frequencies. Part II, comprising of Chapters 6, 7 and 8, focuses on the analytical and numerical study of the rich dynamics of a single droplet and a pair of identical droplets in a generalised pilot-wave framework.

In Chapter 2, we provide the necessary theoretical framework that underpins numerical results of this thesis. We provide details of existing theoretical models for the vertical dynamics, the horizontal dynamics and the underlying wave field of the walking droplets. We highlight the intermediate complexity models of walkers that will be adapted in Chapter 4 to model superwalkers. We also provide details of the coarse grained stroboscopic models that provide the theoretical framework for the results presented in Part II of the thesis.

### Part I - Superwalking droplets (Chapters 3 to 5)

In Chapter 3, we present experimental results of a new class of walking droplets, superwalkers, that emerge when a liquid bath is driven simultaneously at a frequency and half that frequency. We show that superwalkers can be more than double the size and can walk at more than triple the speeds of typical single-frequency driven walkers. We also present results of interactions of multiple superwalkers and show that their interactions give rise to novel multi-droplet behaviours.

In Chapter 4, we adapt the previously established theoretical models of single-frequency driven walkers (presented in Chapter 2) to two-frequency driven superwalkers.

We derive a new form of the wave field for a superwalker and couple it to the existing vertical and horizontal dynamics models of walkers. Using the new theoretical model of superwalkers, we can explain the emergence of superwalkers and rationalise the experimentally observed characteristics of small- to moderate-size superwalkers.

In Chapter 5, we explore a novel behaviour of superwalking droplets, coined *stop-and-go motion*, that emerges when the two driving frequencies are slightly detuned. We explore this motion using the theoretical model of superwalkers developed in Chapter 4 and uncover various types of stop-and-go dynamics.

## Part II - Generalised pilot-wave dynamics (Chapters 6 to 8)

In Chapter 6, we explore the dynamics of two identical walking droplets using a stroboscopic model for walkers. We encounter a remarkably rich range of behaviours as a function of the two system parameters, the ratio of inertia to drag and the ratio of wave forcing to drag. We capture the two-droplet bound states that have been observed in experiments such as parallel walkers, promenading pairs and orbiting pairs. Moreover, we also uncover a rich array of more exotic dynamics such as regularly and chaotically switching walkers, wandering walkers and intriguing closed-loop trajectories. We explore these rich behaviours and the bifurcations between them through analytic and numerical linear stability analyses and through fully nonlinear numerical simulation.

In Chapter 7, we present a numerical study of two-droplet pair correlations for identical walking droplets. Two walking droplets are launched towards each other at an angle with different initial path differences. We quantify the likelihood of such droplets pairing up in a two-droplet bound state by measuring the probability of finding the droplets in a bound state at late times. We find anomalous correlations where the droplets may become correlated for certain initial path differences and remain uncorrelated for others, while in other cases, the droplets may never produce bound states.

In Chapter 8, we explore the unsteady dynamics of a single walking droplet that arises in the parameter space regime of small inertia and large wave forcing. The steady walking motion of a droplet becomes unstable and a variety of unsteady motions are realised such as random walk-like motion, oscillating walker and self-trapped oscillations of the droplet. We explore the chaotic nature of these unsteady motions as well as their statistical behaviour.

Finally, we provide conclusions in Chapter 9 and discuss potential future directions of the work presented in this thesis.

## 1.5 List of publications

Many of the results presented in this thesis have been published in journals. These are listed below:

- Chapter 3 - Ref. [53]: R. N. Valani, A. C. Slim and T. Simula, *Superwalking Droplets*, Physical Review Letters **123** 024503 (2019).
- Chapter 4 - Ref. [54]: R. N. Valani, J. Dring, T. Simula and A. C. Slim, *Emergence of superwalking droplets*, Journal of Fluid Mechanics **906**, A3 (2021).
- Chapter 6 - Ref. [55]: R. N. Valani and A. C. Slim, *Pilot-wave dynamics of two identical, in-phase bouncing droplets*, Chaos **28**, 096114 (2018).
- Chapter 7 - Ref. [56]: R. N. Valani, A. C. Slim and T. Simula, *Hong–Ou–Mandel-like two-droplet correlations*, Chaos **28**, 096104 (2018).



# Chapter 2

## Theoretical Framework

In this chapter, we will review various theoretical models to describe bouncing and walking droplets. These range from phenomenological stroboscopic models that only capture the horizontal dynamics to sophisticated models that resolve the vertical and horizontal dynamics and the detailed evolution of the surface waves created by the walker. Intermediate complexity models that resolve the vertical and horizontal dynamics but assume a predetermined form for the standing wave created by the droplet have been widely used. The intermediate complexity models and the stroboscopic models will be described in detail as we adapt these models for many of the results presented in the later chapters of the thesis.

### 2.1 Setup of the system

Consider a droplet of mass  $m$  and radius  $R$  bouncing on a bath of liquid of density  $\rho$ , kinematic viscosity  $\nu$  and surface tension  $\sigma$ . The bath is vibrating vertically with acceleration  $\gamma(t) = \Gamma_f g \sin(\Omega t)$ . Here  $\Omega = 2\pi f$  is the angular frequency,  $\Gamma_f$  is the acceleration amplitude of the driving relative to gravity  $g$ . This configuration is shown schematically in figure 2.1. The system is described in the oscillating frame of the bath by horizontal coordinates  $\mathbf{x} = (x, y)$  and vertical coordinate  $z$ , with  $z = 0$  chosen to coincide with the undeformed surface of the bath. In this frame, the centre of mass of the droplet is located at a horizontal position  $\mathbf{x}_d$  and the south pole of the droplet at a vertical position  $z_d$  such that  $z_d = 0$  would represent initiation of contact with the undeformed surface of the bath. The free surface elevation of the liquid filling the bath is at  $z = h(\mathbf{x}, t)$ .

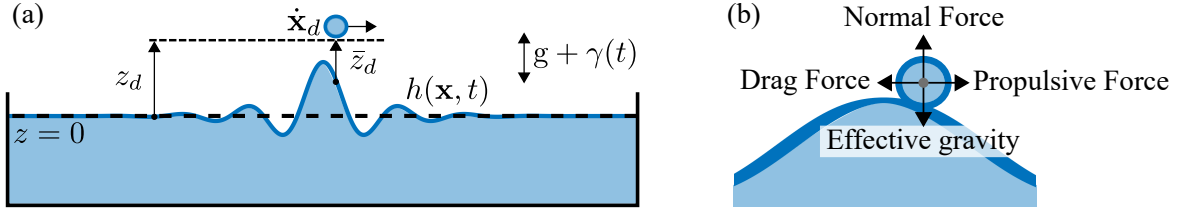


Figure 2.1 : (a) Schematic of the system consisting of a bath of liquid vibrated vertically with acceleration  $\gamma(t)$ , and a droplet of the same liquid walking horizontally at velocity  $\dot{\mathbf{x}}_d$  and located at vertical position  $z_d$  relative to the free surface of the liquid at rest. Panel (b) shows the vertical and horizontal forces acting on the droplet in the oscillating frame of the bath. In the vertical direction, the droplet experiences an effective gravity,  $-m[g + \gamma(t)]$ , and a normal force,  $F_N(t)$ , during contact. In the horizontal direction, the droplet experiences a propulsive force,  $-F_N(t)\nabla h(\mathbf{x}_d, t)$ , during contact due to the slope of the wave field and a lumped drag force composed of momentum loss during contact,  $-D_{mom}\dot{\mathbf{x}}_d$ , and air drag,  $-D_{air}\dot{\mathbf{x}}_d$ .

## 2.2 Vertical dynamics

When the driving acceleration amplitude  $\Gamma_f$  of the bath exceeds the bouncing threshold, a droplet can bounce indefinitely on the free surface of the bath [6]. A variety of models have been developed for the vertical bouncing motion of the droplet. Moláček and Bush [57] modelled the vertical bouncing dynamics of the droplet using various spring models, inspired by the investigations of Gilet and Bush [58], Okumura et al. [59] and Moláček and Bush [60]. In this model, the vertical equation of motion of the droplet in the comoving frame of the bath is given by

$$m\ddot{z}_d = -m[g + \gamma(t)] + F_N(t), \quad (2.1)$$

where the first term on the right hand side is the effective gravitational force on the droplet in the bath's frame of reference. The second term on the right hand side is the normal force imparted to the droplet during contact with the liquid surface (see figure 2.1(b)). To model the contact interaction, Moláček and Bush [57] developed three different models: (i) a simple linear spring model, (ii) an improved linear spring model and (iii) a logarithmic spring model. In the simple linear spring model, this normal force is calculated by modelling the interaction with the bath as a linear spring and damper according to,

$$F_N(t) = H(-\bar{z}_d) \left( -k_s \bar{z}_d - b \dot{\bar{z}}_d \right). \quad (2.2)$$

Here  $H(\cdot)$  is the Heaviside step function and,  $\bar{z}_d = z_d - h(\mathbf{x}_d, t)$ , is the height of the droplet's south pole above the free surface of the liquid. The constants  $k_s$  and  $b$  are the spring constant and damping force coefficient, respectively. The values of these parameters are not derived from the model and they were obtained by fitting to experimental data on the coefficient of restitution and the contact time of the droplet with the bath [57]. By examining the reaction force more closely in the above model, Moláček and Bush [57] noted that towards the end of contact the reaction force acting on the droplet pulls it towards the bath, an unphysical effect if the dynamics of the intervening air is neglected. Hence, they developed the following improved linear spring model that ensures that the reaction force is always non-negative:

$$F_N(t) = H(-\bar{z}_d) \max\left(-k_s \bar{z}_d - b \dot{\bar{z}}_d, 0\right). \quad (2.3)$$

They also developed a nonlinear logarithmic spring model that fit their experimental data better. This logarithmic spring model gives the following equation for the vertical dynamics:

$$\left(1 + \frac{C_3}{\ln^2 \left| \frac{C_1 R}{\bar{z}_d} \right|}\right) m \ddot{\bar{z}}_d + \frac{4 \pi \nu \rho R C_2}{3 \ln^2 \left| \frac{C_1 R}{\bar{z}_d} \right|} \dot{\bar{z}}_d + \frac{2 \pi \sigma}{\ln \left| \frac{C_1 R}{\bar{z}_d} \right|} \bar{z}_d = -m[g + \gamma(t)], \quad (2.4)$$

when the droplet is in contact with the bath. While in air, the vertical dynamics of the droplet is governed by  $m \ddot{\bar{z}}_d = -m[g + \gamma(t)]$ . The typical values of the parameters  $C_1$ ,  $C_2$  and  $C_3$  for walkers are  $C_1 = 2$ ,  $C_2 = 12.5$  (for 20 cSt viscosity silicone oil) and  $C_3 = 1.4$ . It is not completely clear whether this model is more accurate than the linear spring models and hence the linear spring models are often used for simplicity [61].

Other models solve for the free-surface evolution of the waves created by the droplet and include the droplet's impact through a pressure field on the interface [62, 43, 63]. Blanchette [64] modelled the bouncing dynamics of a droplet using a linear spring model similar to Moláček and Bush [57] and derived an expression for the contact force between the droplet and the underlying wave field. A more complete model for the vertical dynamics was developed by Galeano-Rios et al. [65] where they model the impact of a droplet on the surface of a fluid bath by coupling the free-surface Navier-Stokes equations to the motion of a hydrophobic sphere through dynamic adjustment of the contact area and matching velocities. Their approach allows them to eliminate fitting parameters from their model for the vertical dynamics.

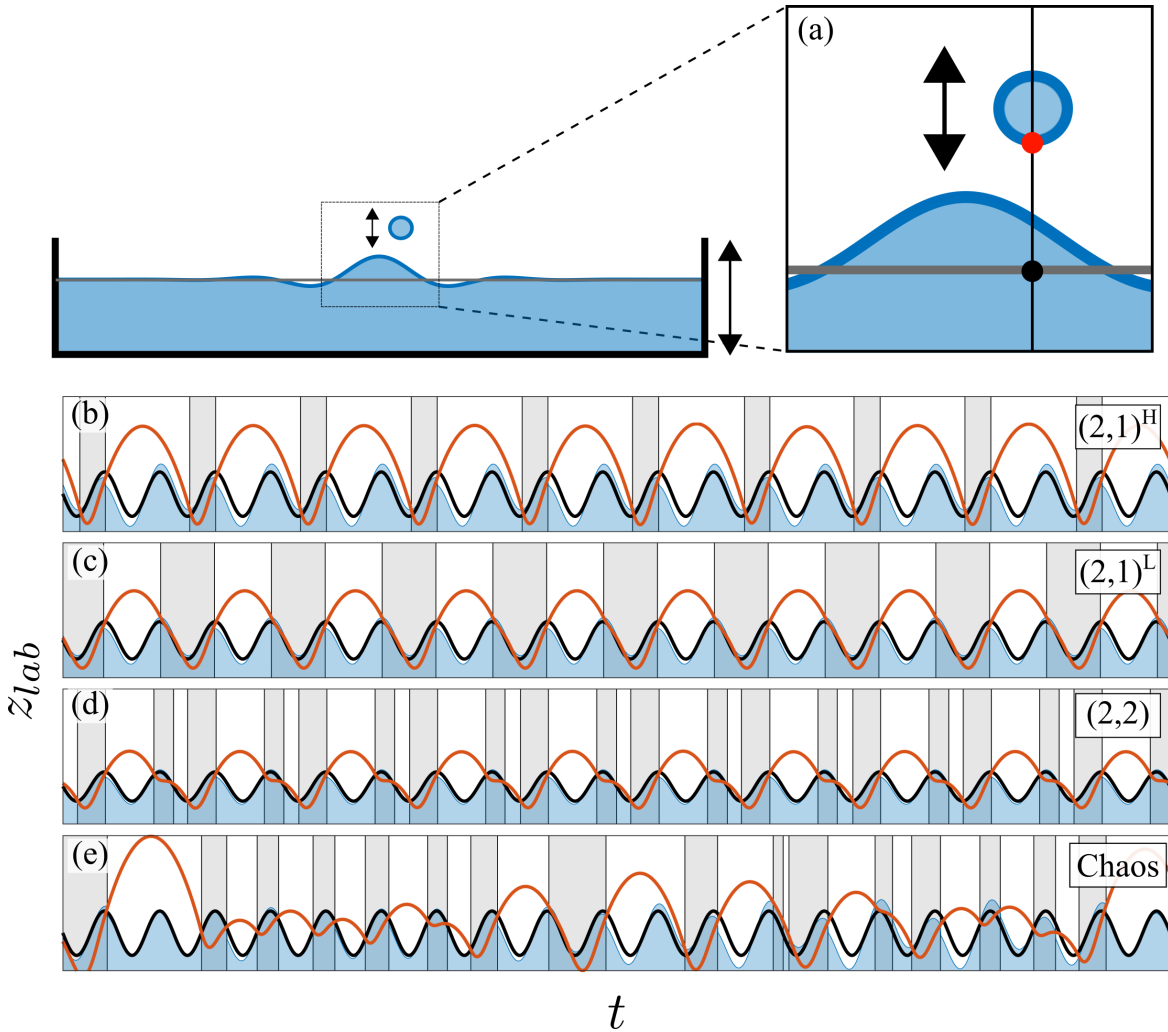


Figure 2.2 : Bouncing modes plot. (a) The vertical dynamics of the droplet as a function of time can be described by plotting the evolution of the vertical position of the south pole of the droplet (red dot), the vertical position of the bath (black dot) and the height of the wave directly beneath the centre of the droplet, all in the lab frame. Different periodic bouncing mode plots obtained using this method are shown in panels (b)-(d) while an aperiodic bouncing mode plot is shown in panel (e). In these panels, the grey region represents times at which there is contact between the droplet and the underlying wave field.

### 2.2.1 Notation for vertical bouncing modes

The vertical motion of the bouncing droplet is known to be complex and to show various periodic and chaotic behaviours. Similar behaviour is also observed when a ball bounces on an oscillating solid surface [66, 67]. To describe the periodic vertical

dynamics concisely, the notation  $(m, n)$  has been widely used [58, 57], where the droplet impacts the surface  $n$  times during  $m$  oscillations of the bath.

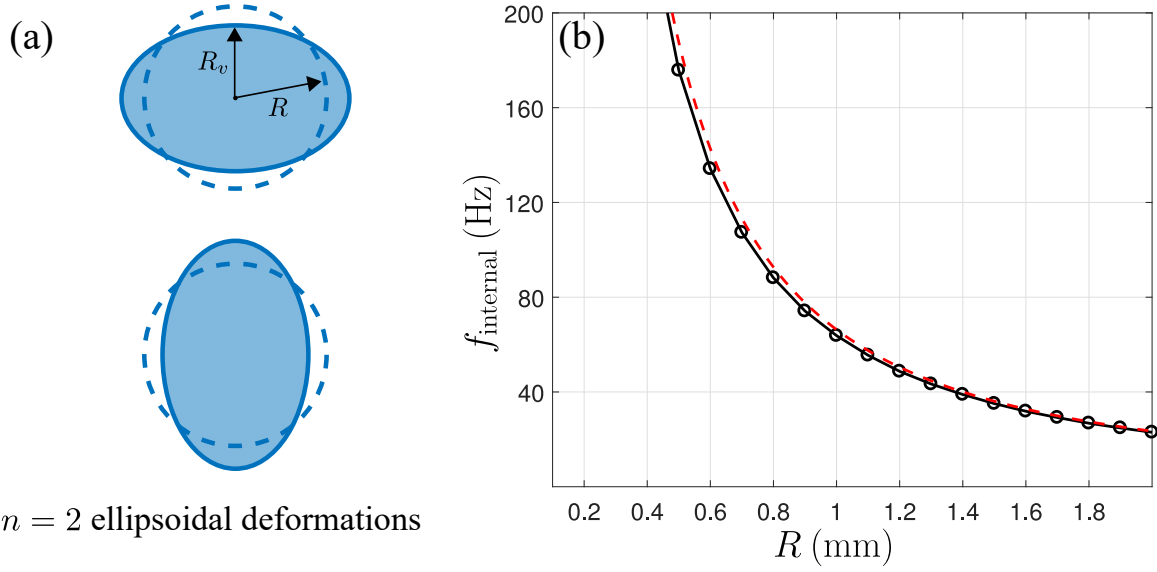
Figure 2.2 describes the method of obtaining bouncing modes plots that will be used in this thesis along with a schematic of some common bouncing modes shown in panels (b)-(e) of that figure. For walking droplets, one of the most commonly observed bouncing modes is  $(2, 1)$ , with the droplets leaping over every second peak in the bath's motion. After Moláček and Bush [57], we distinguish two different styles of  $(2, 1)$  walking with a high-bouncing, short-contact mode denoted by  $(2, 1)^H$  and a low-bouncing, long-contact mode denoted by  $(2, 1)^L$ . Another commonly observed mode is  $(2, 2)$ , in which the droplets no longer are able to leap over intermediate peaks, and contact the bath twice, typically a high bounce and a low bounce, every two up-and-down cycles of the bath. Note that experimentally it is difficult to distinguish between a  $(2, 1)^L$  and a  $(2, 2)$  mode (see figures 2.2(c) and (d), and also figures 7 and 8 of Galeano-Rios et al. [68]). Other less commonly observed modes include  $(4, 2)$ ,  $(4, 3)$  and  $(4, 4)$  [69]. Finally, bouncing modes with no discernible periodicity or those with periodic contact but aperiodic modulation of the peak bouncing heights are common. We refer to these as chaotic modes.

## 2.3 Droplet deformations

Droplet deformations are typically insignificant for smaller walking droplets [57] but may play a significant role for larger walking droplets and even larger superwalking droplets that will be considered in this thesis. The decay rate and the frequency of small oscillations of a droplet's deformations can be adequately described by linear theory and have been considered in several classic papers [70–74]. The natural frequency of infinitesimal oscillations of an inviscid droplet is given by

$$\omega = \sqrt{\frac{N_\omega \sigma}{\rho R^3}}, \quad (2.5)$$

where,  $N_\omega = n(n-1)(n+2)$ , with the integer  $n$  indicating the mode of deformation [70, 71]. The  $n = 2$  mode corresponding to ellipsoidal deformations (see figure 2.3(a)) is found to decay the slowest with decay rate  $3.8\nu/R^2$  [73, 57]. The dashed curve in figure 2.3(b) shows the frequency of the dominant  $n = 2$  ellipsoidal oscillations of droplets using equation (2.5) as a function of their radii for typical silicone oil used in experiments with walking droplets. The solid curve in figure 2.3(b) shows the corresponding result corrected for viscosity (after figure 1 of [74]).



$n = 2$  ellipsoidal deformations

Figure 2.3 : (a) A schematic showing the droplet deformations in the  $n = 2$  ellipsoidal mode. Here  $R$  is the radius of the undeformed droplet while  $R_v$  is the radius of the droplet along a vertical line passing through the droplet's centre. (b) Frequency of infinitesimal ellipsoidal oscillations of droplets,  $f_{\text{internal}} = \omega/2\pi$ , as a function of their undeformed radius  $R$  for inviscid droplets (dashed curve) and  $\nu = 20$  cSt viscosity droplets (solid curve with circles). The density,  $\rho = 950 \text{ kg/m}^3$ , and surface tension,  $\sigma = 20.6 \text{ mN/m}$ , are chosen as the typical values for silicone oil used in experiments with walking droplets.

Deformation of droplets has been modelled using several linear spring models [75–77, 64]. We here consider the droplet deformation models of Blanchette [75] and Gilet et al. [76]. In the model of Blanchette [75], the vertical radius (see figure 2.3(a)) of the droplet  $R_v$  is modelled as a linear spring whose evolution is governed by

$$m\ddot{R}_v + c_d\dot{R}_v + m\omega^2(R_v - R) = -F_N(t), \quad (2.6)$$

where  $c_d = 3.8m\nu/R^2$  is the effective damping coefficient of the droplet deformations. For the dominant ellipsoidal mode  $n = 2$ , we get  $N_\omega = 8$  if the droplet deformation amplitude is assumed to be small, but  $N_\omega = 5.84$  is more appropriate for intermediate amplitudes [78] and will be used in this thesis. The model of Gilet et al. [76] also reduces to an identical equation for droplet deformations after some algebra and is given by

$$c_3m\ddot{R}_v + \frac{c_5m\nu}{R^2}\dot{R}_v + c_4\sigma(R_v - R) = -c_6F_N(t), \quad (2.7)$$

where the parameters  $c_3 = 0.1$ ,  $c_4 = 10$ ,  $c_5 = 3.3$  and  $c_6 = 1$ . To implement both of these droplet deformation models, we can couple them with the vertical dynamics



Figure 2.4 : Faraday waves. Vibrating a bath of liquid vertically results in the (a) initially flat surface of the liquid becoming unstable to (b) standing Faraday waves when the driving acceleration amplitude exceeds the Faraday threshold  $\Gamma_F$ . Panels (b) and (c) show the side view and the top view of a typical Faraday wave pattern.

equation of a bouncing droplet. Once the above droplet deformation models are coupled with the vertical dynamics equation in (2.1), the criteria for contact changes from  $\bar{z}_d \leq 0$  to  $\bar{z}_d + R - R_v \leq 0$ .

## 2.4 Wave field of a walker

### 2.4.1 Faraday waves

When a bath of liquid is vibrated vertically, the free surface of the liquid becomes unstable to standing Faraday waves when the driving acceleration amplitude exceeds the Faraday threshold  $\Gamma_F$  (see figure 2.4). This was first demonstrated by Michael Faraday [1] in 1831 where he also noted that the frequency of these standing waves is subharmonic and they oscillate at half the driving frequency. Matthiessen [79] performed further experiments and reported Faraday waves that oscillate at the same frequency as that of the driving. This discrepancy led Lord Rayleigh [80, 81] to conduct further experiments and he confirmed Faraday's observations. The discrepancy between Faraday and Rayleigh's observations, and Matthiessen's observations was explained mathematically by Benjamin et al. [2]. Benjamin et al. [2] theoretically investigated the problem using a linearised inviscid potential flow model with surface tension. They showed that the response of the planar free surface of the fluid under vertical vibrations is governed by the Mathieu equation, which can give rise to either harmonic or subharmonic oscillations. Hence, they concluded that depending on the parameters, the Faraday waves may be of harmonic or subharmonic nature. Kumar and Tuckerman [82] reconsidered the linear stability problem theoretically by including the effects of viscosity and found good agreement in the harmonic and subharmonic instability tongues between their theoretical predictions and experiments.

Faraday waves have also been observed when the bath is driven at two frequencies simultaneously. Two frequency forcing results in novel Faraday wave patterns such as quasi-periodic waves patterns, in addition to the regular crystalline patterns such as lines, squares and hexagons that are also observed for single frequency driving. Moreover, it was shown that two frequency driving with frequencies  $f$  and  $f/2$  typically results in either subharmonic ( $f/4$ ) or harmonic ( $f/2$ ) Faraday waves depending on the relative amplitudes of the two frequencies and the phase difference between them [83].

## 2.4.2 Damped Faraday waves generated by a walker

Each bounce of a walking droplet generates a fast outwardly propagating wave and leaves behind a localised, slowly decaying Faraday standing wave [84]. As the walker propels horizontally, it keeps laying down these localised Faraday waves on each bounce and the total wave field results from the linear superposition of the individual waves generated along the trajectory. Thus the free surface  $z = h(\mathbf{x}, t)$  can be approximated as the linear superposition of all the individual waves generated by the droplet on its previous bounces [84, 85]

$$h(\mathbf{x}, t) = \sum_n h_n(\mathbf{x}, t),$$

where  $h_n(\mathbf{x}, t)$  is the wave field generated by the  $n$ th bounce at location  $\mathbf{x}_n$  and time  $t_n$ . Various different models of the wave form have been developed to describe a single impact of a walker [84, 85, 62, 86]. Eddi et al. [84] proposed the following form for the wave field generated by a walker on each impact

$$h_n^{(E)}(\mathbf{x}, t) = \frac{A^{(E)}}{\sqrt{|\mathbf{x} - \mathbf{x}_n|}} \cos(k_F |\mathbf{x} - \mathbf{x}_n| + \psi) \exp\left[-\frac{t - t_n}{\tau_d}\right] \exp\left[-\frac{|\mathbf{x} - \mathbf{x}_n|}{\delta}\right].$$

This equation describes a wave that has a sinusoidal spatial dependence to account for spatial oscillations at Faraday wavenumber  $k_F = 2\pi/\lambda_F$ , with  $\lambda_F$  being the Faraday wavelength, and a free phase parameter  $\psi$ . The localised nature of the wave field is captured through an exponential spatial decay with length scale  $\delta$ . The wave also decays exponentially in time with decay constant  $\tau_d \propto (1 - \Gamma_f/\Gamma_F)^{-1}$  inversely proportional to the proximity to the Faraday threshold. The values of  $\delta$  and  $\tau_d$  are obtained from experiments. The wave amplitude  $A^{(E)}$  is effectively a free parameter since this wave model does not account for the forcing from the droplet. This wave form is singular at the point of impact and thus although the model captures the qualitative structure of the walker's wave field, it cannot be used to rationalise the bouncing-to-walking transition.

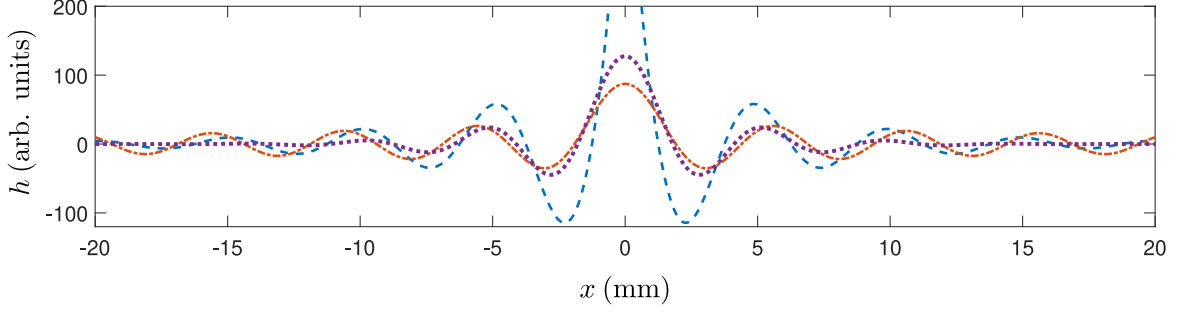


Figure 2.5 : Comparison of the wave field generated by a single instantaneous impact of a walker at  $\Gamma_{80} = 3.8$  with  $\Gamma_F = 4.15$  using three different models: (i) Eddi et al. [84] model (blue dashed curve) with parameters  $\tau = 10 T_F$  and  $\delta = 1.6 \lambda_F$ , (ii) Moláček and Bush [85] model (red dashed dotted curve) and (iii) Tadrist et al. [86] model (purple dotted curve).

An improved form of the wave field and one of the most commonly used is that of Moláček and Bush [85], given by

$$h_n^{(M)}(\mathbf{x}, t) = \frac{A^{(M)}}{\sqrt{t - t_n}} \cos\left(\frac{\Omega t}{2}\right) J_0(k_F |\mathbf{x} - \mathbf{x}_n|) \exp\left[-\frac{t - t_n}{T_F \text{Me}}\right], \quad (2.8)$$

where  $\text{Me} = T_d/T_F(1 - \Gamma_f/\Gamma_F)$  is the memory parameter that determines the proximity to the Faraday threshold with  $\Gamma_F$  being the dimensionless acceleration amplitude at the Faraday threshold. In this expression,  $T_d = 1/\nu_e k_F^2$  is the time constant for wave decay and  $\nu_e$  is the effective kinematic viscosity. This model describes a wave with the shape of a Bessel function of the first kind,  $J_0$ , that oscillates at the subharmonic frequency  $f/2$  and decays exponentially in time with a decay constant inversely proportional to the memory parameter. In their model, Moláček and Bush [85] allow for a finite contact time with the wave field. Hence, the location  $\mathbf{x}_n$  and the time  $t_n$  of the droplet's impact are approximated respectively by

$$\mathbf{x}_n = \int_{t_n^i}^{t_n^c} \mathbf{x}_d(t') F_N(t') dt' / \int_{t_n^i}^{t_n^c} F_N(t') dt', \quad t_n = \int_{t_n^i}^{t_n^c} t' F_N(t') dt' / \int_{t_n^i}^{t_n^c} F_N(t') dt', \quad (2.9)$$

where  $t_n^i$  and  $t_n^c$  are the time of initiation and completion of the  $n$ th impact. The equation for the wave amplitude coefficient  $A^{(M)}$  is

$$A^{(M)} = \sqrt{\frac{2\nu_e}{\pi} \frac{k_F^3}{3\sigma k_F^2 + \rho g}} \int_{t_n^i}^{t_n^c} \sin\left(\frac{\Omega t'}{2}\right) F_N(t') dt'.$$

A detailed theoretical study of the waves generated by a single bounce of a walker was undertaken by Tadrict et al. [86]. They derived the following improved wave form for the wave generated by an instantaneous impact of a walker of force strength  $F_0$  at location  $\mathbf{x}_n$  and time  $t_n$ ,

$$h_n^{(T)}(\mathbf{x}, t) = \frac{A_0^{(T)}}{\sqrt{t - t_n}} \cos\left(\frac{\Omega t}{2} + \theta_F^+\right) J_0(k_F |\mathbf{x} - \mathbf{x}_n|) \exp\left[-\frac{(t - t_n)}{T_F \text{Me}^{(T)}} - \frac{T_F |\mathbf{x} - \mathbf{x}_n|^2}{8\pi D(t - t_n)}\right]. \quad (2.10)$$

In this expression, the memory parameter is given by  $\text{Me}^{(T)} = -1/2\pi\delta_F^+$  with  $\delta_F^+$  the decay rate of the longest-lived Faraday wave. This improved form of the wave field has two new additions: (i) the phase shift  $\theta_F^+$  of the Faraday waves relative to the driving signal and (ii) an exponential spatial decay with diffusive spreading (with a diffusion coefficient  $D$ ). Note that similar additions can also be obtained following the derivation of Moláček and Bush [85] by including higher-order terms in their decay rate expansions. The amplitude coefficient  $A_0^{(T)}$  takes the form,

$$A_0^{(T)} = \sqrt{\frac{2\pi}{\Omega^5 D}} \frac{2k_F^2}{\pi\rho} B_F^+(t_n) F_0,$$

where  $B_F^+(t_n)$  is a function that prescribes the amplitude based on the instant of impact  $t_n$  and is given by

$$B_F^+(t_n) = \frac{-2 \cos(\Omega t_n/2 + \theta_F^-)}{(\delta_F^+ - \delta_F^-) [\cos(\Omega t_n + \theta_F^+ + \theta_F^-) + \cos(\theta_F^+ - \theta_F^-)] - 2 \sin(\theta_F^+ - \theta_F^-)},$$

where  $\theta_F^-$  and  $\delta_F^-$  are the phase shift and decay rate respectively of a companion short-lived Faraday wave. The reader is referred to Tadrict et al. [86] for further details on these parameters. A comparison of the three different forms of the wave fields presented is shown in figure 2.5.

Milewski et al. [62] introduced a more complete description of the waves generated by a walker by introducing a quasi-potential, weakly viscous wave model. This model is able to capture many more subtle features of the walker system, such as the travelling wave fronts reported by Eddi et al. [84], but neglected in the earlier standing wave models, and it captures the Doppler effect in the wave field reported by Eddi et al. [84].

## 2.5 Horizontal dynamics

When the driving acceleration amplitude  $\Gamma_f$  exceeds the walking threshold, the pure vertical bouncing state becomes unstable and a walking droplet emerges. The most widely used model to describe the horizontal dynamics of the walking droplet is that of Moláček and Bush [85] where the horizontal equation of motion takes on the following form:

$$m\ddot{\mathbf{x}}_d = - [D_{mom}(t) + D_{air}] \dot{\mathbf{x}}_d - F_N(t)\nabla h(\mathbf{x}_d, t). \quad (2.11)$$

The term in parentheses on the right hand side is the total instantaneous drag force, composed of momentum loss during contact,  $D_{mom}(t) = C\sqrt{\rho R/\sigma}F_N(t)$ , and an air drag of the form  $D_{air} = 6\pi R\mu_a$ . Here  $\mu_a$  is the dynamic viscosity of air and  $C$  is the contact drag coefficient. The parameter  $C$  is not determined theoretically and is obtained by doing a best fit of the experimental results of walkers. The final term on the right hand side is the horizontal component of the contact force arising from the slope of the underlying wave field during contact. The slope of the interface is assumed to be small  $|\nabla h| \ll 1$  and hence the horizontal contact force can be approximated as  $-F_N(t)\nabla h(\mathbf{x}_d, t)$ . We note that such an approximation loses accuracy when the contact time of the drop becomes comparable to the Faraday period because the slope of the interface will change significantly during contact. Coupling this equation of horizontal dynamics in (2.11) with the vertical dynamics through the normal force  $F_N(t)$  and the underlying wave field  $h(\mathbf{x}, t)$  as described in previous sections, we obtain a complete model that describes the bouncing and walking dynamics of the droplet.

A more sophisticated model for horizontal dynamics that provides a more accurate modelling of the walking droplet was developed by Galeano-Rios et al. [68]. They coupled the vertical dynamics model of Galeano-Rios et al. [65] with the free surface wave evolution model of Milewski et al. [62] to obtain a walking droplet model free of any impact parametrisation. Using their model they were able to accurately reproduce experimental observations of bouncing modes, impact phases and time-dependent wave field topography for bouncing and walking droplets.

## 2.6 Stroboscopic models

The models described in previous sections give an accurate description of the system at the time scale of a single bounce and capture both the horizontal and vertical dynamics of a walker. However, in application of walking droplets to hydrodynamic quantum analogues, mainly the horizontal motion of walkers over a long time is of primary

interest. Hence, further reduced stroboscopic models have been developed that average over the periodic vertical motion and only describe the horizontal dynamics.

The first stroboscopic model of the horizontal motion of a walker was developed by Protière et al. [6] where they described the horizontal motion in one dimension of a single walker using the following equation:

$$m\ddot{x}_d = F^b \sin\left(\frac{2\pi\dot{x}_d}{V_F^\phi}\right) - f_v\dot{x}_d. \quad (2.12)$$

The left hand side represents the inertia of the droplet and on the right hand side are all the forces acting on the droplet during contact. The first term on the right hand side is the force during contact with the inclined surface of the wave with coefficient  $F^b \sim mg\Gamma_f(A_w/\lambda_F)(\tau/T_F)$ . Here  $A_w$  is the wave amplitude,  $\tau$  is the contact time between the drop and the bath and  $V_F^\phi$  is the phase velocity of waves. The second term represents the dissipation that was assumed to arise from the shear drag generated by the thin air layer created during impact. This scales as  $f^V \sim (\mu_a s/h_F)(\tau/T_F)$  where  $\mu_a$  is the viscosity of air,  $s$  is the contact area and  $h_F$  is the thickness of the air layer between the droplet and the bath. Using this model they were able to capture a key feature of the system which is the bouncing-to-walking transition. By seeking a steady walking solution of equation (2.12), they showed a supercritical pitchfork bifurcation in the walking velocity  $V_W$  which transitions from  $V_W = 0$  to

$$V_W/V_F^\phi = \pm(\sqrt{6}/2\pi)\sqrt{(F^b - F_c^b)/F^b},$$

when  $F^b$  becomes larger than a threshold value  $F_c^b = f^V(V_F^\phi/2\pi)$ . However, this model does not take into account the waves generated from all the previous bounces of the droplet and hence it is unable to capture the intricate dynamics that is dependent on the memory of the walkers that is critical for many hydrodynamic quantum analogues. A similar approach was taken by Shirokoff [87] for description of walkers in confined geometries.

An improved version of this trajectory equation was developed by Oza et al. [88] by averaging over the vertical dynamics in the model of Moláček and Bush [85] and assuming a periodic  $(2, 1)^H$  bouncing mode with a constant impact phase for the walker. This was rationalised on the grounds that the time scale of horizontal motion is much greater than the time scale of the vertical motion and thus the walker can be viewed as a continuous moving source of standing waves. By averaging equation (2.11) over

the bouncing period  $T_F$  for a droplet in a  $(2, 1)^H$  mode, they obtained

$$m\ddot{\mathbf{x}}_d = -D\dot{\mathbf{x}}_d - mg\nabla h(\mathbf{x}_d, t), \quad (2.13)$$

with

$$h(\mathbf{x}, t) = \frac{A}{T_F} \int_{-\infty}^t J_0(k_F |\mathbf{x} - \mathbf{x}_d(s)|) e^{-(t-s)/T_F \text{Me}} ds. \quad (2.14)$$

Here the averaged drag coefficient is  $D = Cmg\sqrt{\rho R/\sigma} + 6\pi\mu_a R(1 + T_F\rho_a gR/24\mu_a)$ , where  $\mu_a$  and  $\rho_a$  are the dynamic viscosity and density of air, and  $C$  is the non-dimensional drag coefficient. The amplitude coefficient is given by

$$A = \sqrt{\frac{\nu_e}{2\pi T_F}} \frac{k_F R}{3k_F^2 R^2 + Bo} \frac{k_F^2 R}{\sigma} mg T_F \sin(\Phi),$$

where  $Bo = \rho g R^2 / \sigma$  is the Bond number,  $\sin(\Phi)$  is the impact phase and  $\nu_e$  is the effective kinematic viscosity. We refer the reader to Oza et al. [88] for explicit equations for these parameters. Substituting equation (2.14) into equation (2.13) we obtain the following trajectory equation:

$$m\ddot{\mathbf{x}}_d + D\dot{\mathbf{x}}_d = \frac{F}{T_F} \int_{-\infty}^t J_1(k_F |\mathbf{x}_d(t) - \mathbf{x}_d(s)|) \frac{\mathbf{x}_d(t) - \mathbf{x}_d(s)}{|\mathbf{x}_d(t) - \mathbf{x}_d(s)|} e^{-(t-s)/T_F \text{Me}} ds,$$

where  $F = mgAk_F$ . We non-dimensionalise this equation by choosing  $1/k_F$  and  $T_F \text{Me}$  as the length and time scales respectively, giving us non-dimensional variables  $\mathbf{x}' = k_F \mathbf{x}$  and  $t' = t/T_F \text{Me}$ . Substituting this in the above equation and dropping primes we get

$$\kappa \ddot{\mathbf{x}}_d + \dot{\mathbf{x}}_d = \beta \int_{-\infty}^t J_1(|\mathbf{x}_d(t) - \mathbf{x}_d(s)|) \frac{\mathbf{x}_d(t) - \mathbf{x}_d(s)}{|\mathbf{x}_d(t) - \mathbf{x}_d(s)|} e^{-(t-s)} ds, \quad (2.15)$$

where  $\kappa = m/DT_F \text{Me}$  and  $\beta = Fk_F T_F \text{Me}^2/D$  are the non-dimensional mass and the non-dimensional memory coefficient respectively. This model can accurately predict the bouncing-to-walking transition and the dependence of the free walking speed on memory. It also provides a theoretical rationale for several single walker behaviours that were reported in experiments such as the stability of circular orbits in a rotating frame or a simple harmonic potential [28, 20, 31, 35–37].

This model was further improved by adding spatial damping to the wave field as it may play a crucial role in the dynamics of multiple interacting walkers and interactions of a walker with boundaries [89]. Moreover, although the assumption of a constant impact phase has proven to be sufficient for describing the motion of a single droplet, it

has limitations when describing the interactions of multiple drops where modulations of the vertical dynamics are known to arise. To account for these variations in the impact phase, Oza et al. [89] and Arbelaiz et al. [10] improved the above stroboscopic model by determining the dependence of the impact phase parameter on the forcing acceleration through an empirical fit to the experimental results. Recently, Couchman et al. [61] developed a more complete variable phase stroboscopic model to obtain a robust horizontal trajectory equation for a walking droplet that accounts for modulations in the drop's vertical dynamics that may arise when it interacts with boundaries or other droplets.

All the above stroboscopic models approximate the complex wave field generated by a droplet on each bounce by a standing wave. This was improved by Durey and Milewski [63] who developed a discrete-time model where the droplet's motion is still averaged over the vertical dynamics and the droplet impacts are assumed to be instantaneous, but they couple the droplet's dynamics to the more complete wave model of Milewski et al. [62] to accurately capture the droplet's wave field. Using their model they were able to reproduce the dynamics of single and multiple droplets observed in experiments as well as various hydrodynamic quantum analogues [63, 32, 17]. We also refer the reader to the work of Turton et al. [90] which provides a review of the theoretical modelling of walking droplets.

# Part I

## Superwalking Droplets



# Chapter 3

## From walkers to superwalkers

In this chapter, we present experimental results of a new class of walking droplets, coined *superwalkers*, that emerge when a bath of silicone oil is driven at two driving frequencies. Superwalkers may be more than double the size of the largest walkers, may travel at more than triple the speed of the fastest ones, and enable a plethora of novel multi-droplet behaviours.

This chapter is based on the following published paper:

R. N. Valani, A. C. Slim and T. Simula, [Superwalking Droplets](#), Physical Review Letters **123** 024503 (2019).

### 3.1 Introduction

Walkers emerge when a bath of silicone oil is driven by a single frequency sinusoidal wave with acceleration  $\Gamma_f g \sin(\Omega t)$ , where  $\Gamma_f$  is the dimensionless amplitude of the driving acceleration and  $\Omega = 2\pi f$  is the angular frequency with  $f$  being the driving frequency. For a commonly studied system of silicone oil with 20 cSt viscosity and  $f = 80$  Hz, droplet radii of 0.3 mm to 0.5 mm and walking speeds of up to 15 mm/s have been observed [85, 69]. We have discovered a new class of walking droplets, which we coin *superwalkers*, that emerge when the fluid bath is driven simultaneously at a frequency  $f$  and the subharmonic frequency  $f/2$  with a phase difference  $\Delta\phi$  according to the acceleration

$$\gamma(t) = \Gamma_f g \sin(\Omega t) + \Gamma_{f/2} g \sin(\Omega t/2 + \Delta\phi). \quad (3.1)$$

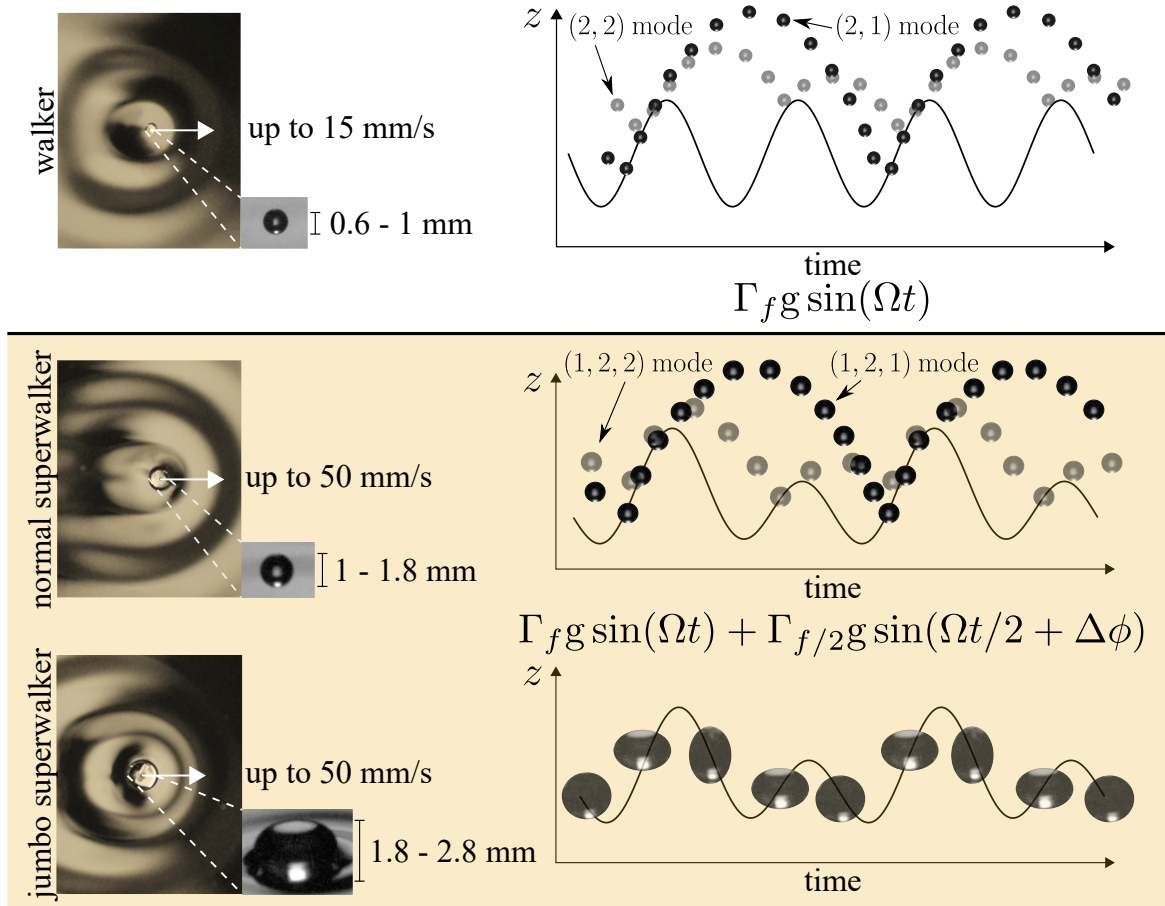


Figure 3.1 : Comparison of a walker (top), a normal superwalker (middle) and a jumbo superwalker (bottom). Superwalkers emerge when the bath is driven at two frequencies  $f$  and  $f/2$  with a phase difference  $\Delta\phi$ . They may be significantly larger than walkers and may move significantly faster. Left panels show top views of typical droplets and their wave fields, and side views of the same droplets. Right panels show the bath motion (solid curve) and the typical bouncing motion of the droplets.

In the commonly studied system noted above, superwalkers can be significantly larger than walkers with radii up to  $1.4 \text{ mm}$  and they can walk at up to  $50 \text{ mm/s}$ . The largest superwalkers undergo significant internal deformation and barely lift off from the surface of the bath. We call these *jumbo superwalkers*. The key differences between a walker and the two kinds of superwalkers are summarised in the schematic of figure 3.1. Fundamental differences between walkers and superwalkers are also evident in their inter-droplet interactions. Due to their large inertia, superwalkers may easily overcome the wave barrier that typically prevents contact interactions between walking droplets, enabling superwalkers to form a variety of novel stationary and dynamic bound states.

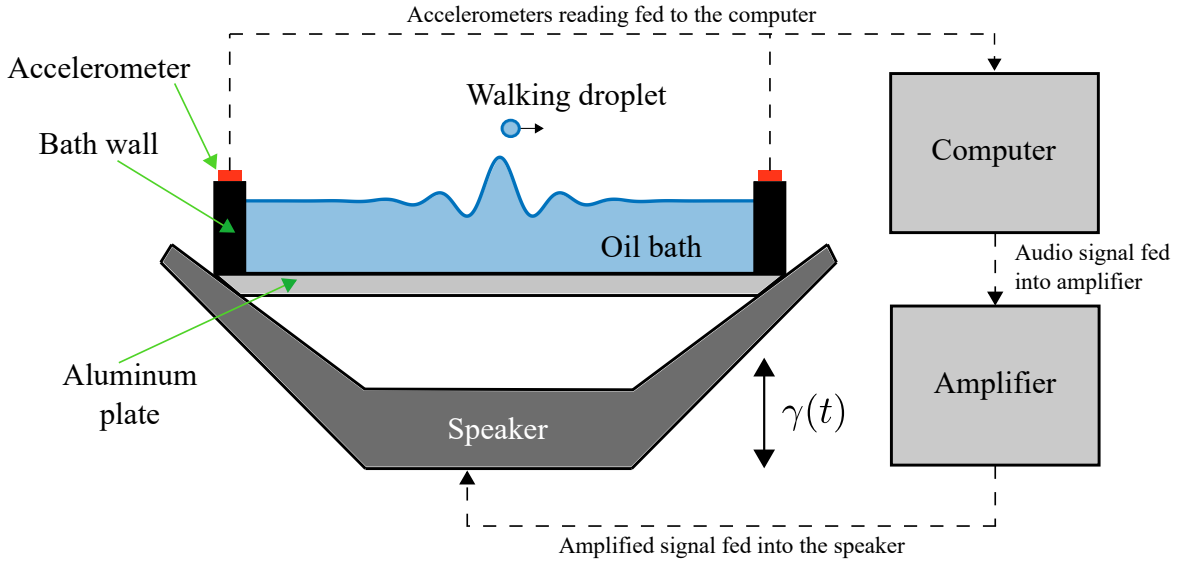


Figure 3.2 : Schematic of the experimental setup. A bath of silicone oil is mounted on a subwoofer speaker cone. The bath is driven vertically with acceleration prescribed in equation (3.1). Millimetre size droplets of the same oil can be created using a needle or a syringe.

## 3.2 Details of the experiment

The experiments were performed using a circular bath of diameter 18 cm filled to a height of approximately 8 mm of nominal viscosity 20 cSt and density  $950 \text{ kg/m}^3$  at  $25^\circ\text{C}$ . A schematic of the experimental setup is shown in figure 3.2. The bath had a circular aluminium base of diameter 218 mm and thickness 6 mm with a 3D-printed annular ring adhesively bonded to it to form the vertical wall. The bath was mounted on a subwoofer speaker cone (UM12-22 12" Ultimax DVC Subwoofer 2 ohms Per Coil) that was placed on an optical breadboard. The quality of uniaxial vibrations and levelling of the bath were investigated using accelerometers and by observing uniform generation of Faraday waves [91]. We verified that the subwoofer acceleration axis was vertical with horizontal vibrations about 5% of the vertical vibrations. That the remaining, unavoidable horizontal vibrations do not affect our conclusions is described in Appendix A.

The speaker cone was driven simultaneously at frequencies  $f$  and  $f/2$  via two independent voice coils at a prescribed phase shift. Superwalkers were observed for driving frequencies in the range  $50 \text{ Hz} \lesssim f \lesssim 100 \text{ Hz}$ . For our detailed investigation, we used  $f = 80 \text{ Hz}$ . The two voice coils were driven by connecting them to an amplifier (Crown XLS1002 Drivecore, 1100 W), which in turn was connected to a computer running the audio editing software Audacity to generate the driving signals. The

acceleration of the bath was measured using two horizontally mounted, diametrically opposed accelerometers (MPU6050 Module 3 Axis Gyroscope + accelerometer) on the annular ring. These accelerometers were connected to the same computer using an Arduino UNO microcontroller. For each accelerometer, the dimensionless acceleration amplitudes  $\Gamma_{40}$  and  $\Gamma_{80}$  and the phase shift  $\Delta\phi$  were extracted using nonlinear least square fitting of the measured accelerometer signal to equation (3.1). A Fourier transform of the signals was also used to verify that there was no significant power at spurious frequencies. The measured peak acceleration amplitude decayed over time, presumably due to the Ohmic heating of the copper in the voice coils. For collecting several data sets at the same acceleration, a feedback loop was used to adjust the amplitude of the input signal based on the measured amplitude using the past 2 seconds of accelerometer readings. Adjustments to the input signal were made approximately every 10 seconds, much quicker than the time scale of decay of approximately 1 – 2 minutes. This was sufficient to maintain the accelerations within  $\pm 0.05$  g. The measured phase difference  $\Delta\phi$  from the accelerometer differed from the input phase difference by a constant value, presumably due to damping inherent to this periodically driven oscillator. The uncertainty in the measured phase difference of approximately  $\pm 3^\circ$  was calculated as the difference between the phase readings of the two diametrically opposed accelerometers. We found that the speaker heated up over time, raising the temperature of the silicone oil. This altered its viscosity and decreased the Faraday threshold. Therefore, the temperature of the oil was measured using a thermocouple and it was kept in the range 21-23°C by limiting the time of each experimental run to approximately 20 minutes. This limited the variability in the Faraday threshold to within approximately 0.1 g, which is comparable to the uncertainty permitted in the feedback loop.

Small droplets with radius less than 0.8 mm were created by swiftly extracting a needle from the oil bath while larger droplets with radius greater than 0.8 mm were created using a syringe with needles of different diameters. The droplet's horizontal motion was recorded from above using a Nikon D90 DSLR camera in burst mode at 4 frames per second. Typically 4-8 images were taken of a droplet walking in a straight line, which were then used to determine the size and the speed of the droplet. High speed videos of the droplets were taken using Chronos 1.4 high-speed camera in order to determine the bouncing mode of a single droplet and visualise many droplet dynamics at a typical frame rate of 4000 frames per second. A Phantom VEO 640 high-speed camera was used to visualise the large internal deformations of a jumbo superwalker. An LED panel placed above the camera provided sufficient illumination

for the overhead images while another LED source illuminated the droplets from the side for the videos taken using the high-speed camera. The size of a droplet was measured from the overhead images using a Hough circle transform implemented in MATLAB and was taken as the average value from the overhead burst sequence. The speed was calculated as the total distance that the centre of the droplet travelled divided by the duration of the burst sequence.

The superwalkers were not affected significantly by the ambient air currents, presumably due to their large inertia. Nevertheless, the experiments were performed under a shroud to protect the smaller droplets from spurious drifting due to air currents. To verify that this was sufficient, we performed controlled experiments with an enclosed system as described in Appendix A. Performing the remaining experiments without the enclosure permitted easier droplet manipulation.

We measured the Faraday threshold for single-frequency forcing at 80 Hz as  $\Gamma_{F80} \approx 4.2$  and for single-frequency forcing at 40 Hz as  $\Gamma_{F40} \approx 1.3$ . We observed that for a fixed moderate value of  $\Gamma_{40}$ , as  $\Gamma_{80}$  is increased progressively, circular concentric waves start forming at the edges of the bath with their radial extent increasing as Faraday threshold  $\Gamma_{F80}$  is approached from below. This results in the superwalkers becoming frequently confined to walking along the edges of the bath. Such waves did not form with single-frequency forcing either for 40 Hz or 80 Hz.

### 3.3 Bouncing modes notation for superwalkers

To describe the vertical dynamics of superwalkers, we extend the notation described for walkers in Section 2.2.1 to two-frequency driving. We denote the bouncing behaviour of droplets driven by two frequencies using the generic notation  $(l, m, n)$  indicating that the droplet impacts the surface  $n$  times during  $m$  oscillation periods of the bath at frequency  $f$ , which equals  $l$  oscillation periods of the bath at frequency  $f/2$ .

For small- to moderate-size superwalkers, the most common bouncing mode we observe is the  $(1, 2, 1)^H$  mode, with the droplets leaping over every second peak in the bath's motion. As described in Section 2.2.1 we distinguish two different styles of  $(1, 2, 1)$  bouncing with a high-bouncing, short-contact mode denoted by  $(1, 2, 1)^H$  and a low-bouncing, long-contact mode denoted by  $(1, 2, 1)^L$ . For large superwalkers we observe the  $(1, 2, 2)$  mode, in which the droplets are no longer able to leap over intermediate peaks, and contact the bath twice, typically a high bounce and a low bounce, every two up-and-down cycles of the bath. We note that very large superwalkers hardly lift off from the liquid surface and hence it is experimentally difficult to distinguish between

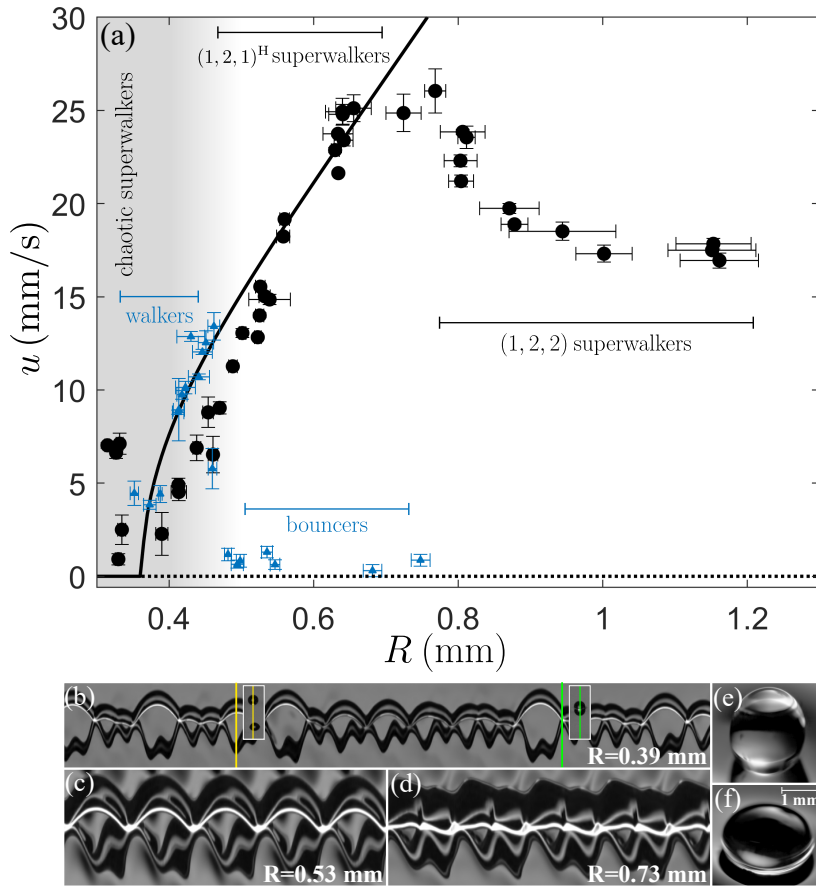


Figure 3.3 : Speed-size characteristics of solitary superwalkers. (a) Walking speed  $u$  as a function of droplet radius  $R$  for fixed values  $\Gamma_{80} = 3.8$  and  $\Delta\phi = 130^\circ$ , and two different values of  $\Gamma_{40}$ , specifically  $\Gamma_{40} = 0$  (blue markers) and  $\Gamma_{40} = 0.6$  (black markers). The size and speed error bars for each data point represent the standard deviation of the values for a single droplet calculated from the given droplet's burst sequence of images. For larger superwalkers, the error in the size is greater because internal deformation of the droplet causes appreciable variations in its radius. The spread of data provides an indication of the uncertainty in the acceleration amplitudes of the bath. The theoretical prediction from the stroboscopic model of Oza et al. [88] is shown as solid black curve. Three different bouncing behaviours are indicated for superwalkers: chaotic,  $(1, 2, 1)^H$  and  $(1, 2, 2)$ . Vertical slice-time plots of droplets are shown for (b) chaotic, (c)  $(1, 2, 1)^H$  and (d)  $(1, 2, 2)$  bouncing modes corresponding to the black markers at the radii indicated. These spatiotemporal images are generated by juxtaposing vertical sections one pixel wide passing through the droplet's centre. Panels (e) and (f) show the two extremes of the shape deformations of a jumbo superwalker.

the  $(1, 2, 1)^L$  and  $(1, 2, 2)$  bouncing mode. Even for walkers, it has been difficult to experimentally distinguish between a  $(2, 1)^L$  and a  $(2, 2)$  mode (see figures 7 and 8 of Galeano-Rios et al. [68]). Bouncing modes with no discernible periodicity or those with

periodic contact but aperiodic modulation of the peak bouncing heights are common for smaller droplets. We refer to these as chaotic modes.

## 3.4 Dynamics of solitary superwalkers

This section provides experimental results on the horizontal and vertical dynamics of solitary superwalkers. We investigate the effect of varying the peak driving accelerations  $\Gamma_f$  and  $\Gamma_{f/2}$ , phase difference  $\Delta\phi$  and droplet radius  $R$  on the droplet's dynamics.

### 3.4.1 Effect of varying the droplet radius

The relationship between speed and size of solitary superwalkers is shown in figure 3.3. Figure 3.3(a) shows the speed of a droplet  $u$  as a function of its radius  $R$  for fixed values of  $\Gamma_{80}$  and  $\Delta\phi$  and two different values of  $\Gamma_{40} = 0$  and 0.6, illustrating the significant size and speed increase possible for two-frequency driven superwalkers. Three prominent types of walking are observed for two-frequency driving and are identified in figure 3.3(a).

The smallest droplets, which are walkers for single-frequency driving, become chaotic superwalkers upon adding the subharmonic driving signal. These droplets bounce aperiodically, see figure 3.3(b), and walk unsteadily with significant fluctuations in their walking speed. Similar irregular walking dynamics for two-frequency forcing at 80 Hz and 64 Hz has been observed previously [92].

Much larger droplets that would not be able to walk at single-frequency driving can now walk with two-frequency driving. Like walkers, they move at a constant speed  $u$  in straight line trajectories with typically greater speeds than the fastest walkers. Two different bouncing modes are observed for such superwalkers. Small- to moderate-sized superwalkers that lie on the ascending branch of the speed-size curve in figure 3.3(a) bounce in a  $(1,2,1)^H$  mode where they impact the bath once every two up-and-down motions of the bath (see figure 3.3(c)) and their speed increases almost linearly with increasing size of the droplet.

Large superwalkers that lie on the descending branch bounce in a  $(1,2,2)$  mode (see figure 3.3(d)). In contrast to the  $(1,2,1)^H$  superwalkers, the speed of  $(1,2,2)$  superwalkers decreases with increasing droplet size. We attribute this behaviour to the increased drag due to the prolonged contact time between the droplet and the bath. Superwalkers with radius  $R \gtrsim 0.9$  mm undergo significant internal deformation and do not seem to lift off from the surface. We refer to these as *jumbo superwalkers* (see

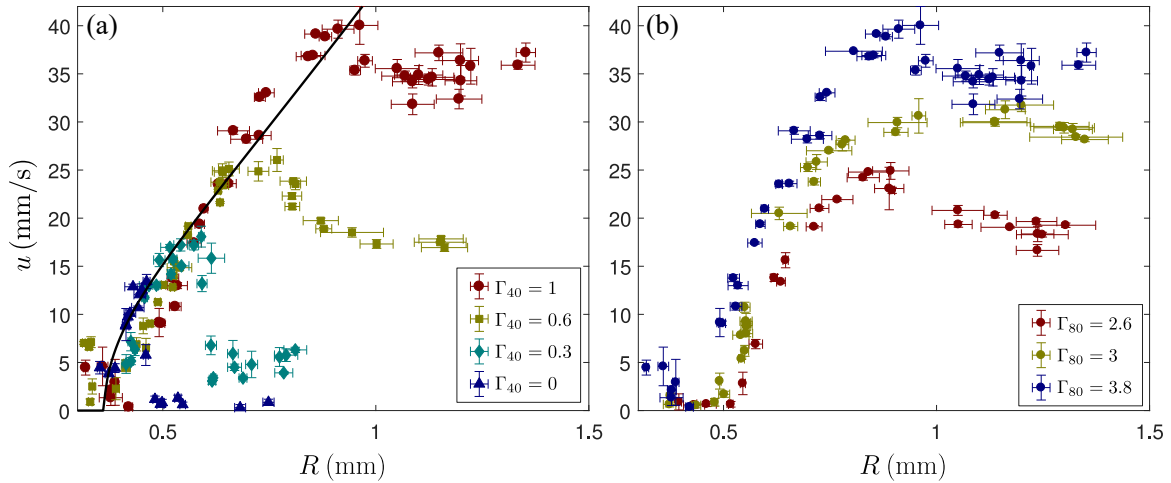


Figure 3.4 : Speed-Size characteristics of solitary superwalkers at a fixed phase difference  $\Delta\phi = 130^\circ$  and different acceleration amplitudes  $\Gamma_{80}$  and  $\Gamma_{40}$ . (a) Speed as a function of radius for fixed  $\Gamma_{80} = 3.8$  and four different value of  $\Gamma_{40} = 0, 0.3, 0.6,$  and  $1$ . The black curve is the prediction from the stroboscopic model for single-frequency walkers. (b) Speed as a function of radius for fixed  $\Gamma_{40} = 1$  and  $\Gamma_{80} = 2.6, 3,$  and  $3.8$ . The size and speed error bars for each data point represent the standard deviation of the values for a single droplet calculated from the given droplet's burst sequence of images. For larger superwalkers, the error in the size is greater because internal deformation of the droplet causes appreciable variations in its radius. The spread of data provides an indication of the uncertainty in the acceleration amplitudes of the bath.

figures 3.3(e) and (f), and also Supplemental Video S1 of [53]). The frequency of the elliptical shape vibrations (see figure 2.3) of the jumbo superwalkers is close to their bouncing frequency [71, 74]. Intriguingly, we find that jumbo superwalkers cannot simply bounce without walking.

The solid curve in figure 3.3(a) is the predicted speed-size relationship for a  $(2,1)^H$  walker with single-frequency driving using the stroboscopic model (see equation (2.15)). For this model, we set the adjustable parameters of the impact phase parameter and the non-dimensional drag coefficient as  $\sin(\Phi) = 0.2$  and  $C = 0.17$  respectively. For the accelerations, we use only the  $\Gamma_{80}$  value and the  $\Gamma_{F80}$  Faraday threshold value. All other parameters are specified from the experimental conditions. Surprisingly, this curve accurately captures the speed of  $(1,2,1)^H$  superwalkers, despite not having explicit dependence on the value of  $\Gamma_{40}$  (we refer the reader to Chapter 4 where an explanation is provided). Since the stroboscopic model is only valid for walkers bouncing in a  $(2,1)^H$  mode, we do not expect it to be applicable for modelling the  $(1,2,2)$  superwalkers.

Figure 3.4(a) provides an extension of the results presented in figure 3.3(a) at additional different values of  $\Gamma_{40}$ . For  $(1,2,1)^H$  superwalkers on the ascending branch

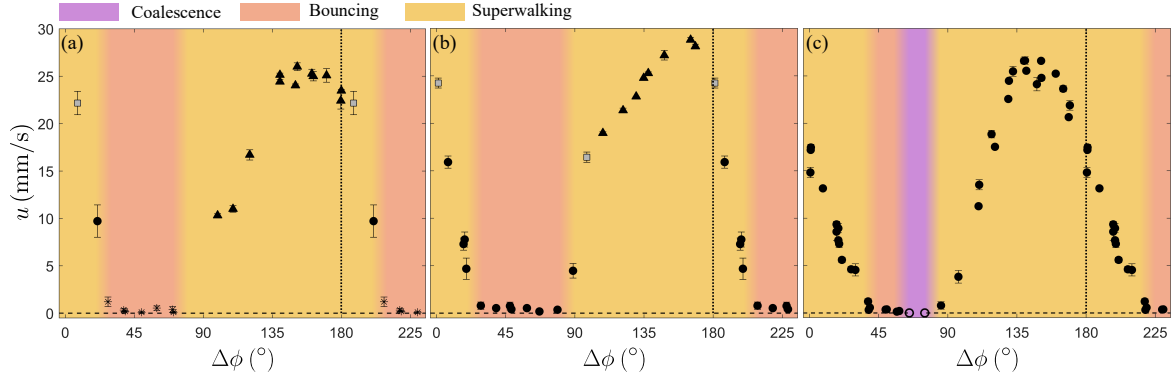


Figure 3.5 : Walking speed  $u$  as a function of the phase difference  $\Delta\phi$  is shown at fixed driving acceleration amplitudes  $\Gamma_{80} = 3.8$  and  $\Gamma_{40} = 0.6$  for droplets of radii (a)  $R = 0.54 \pm 0.03$  mm, (b)  $R = 0.60 \pm 0.02$  mm and (c)  $R = 0.83 \pm 0.03$  mm. A  $(1,2,2)$  bouncing mode is shown as black filled circles, a  $(1,2,1)^H$  bouncing mode is shown as black filled triangles, transition between  $(1,2,1)^H$  and  $(1,2,2)$  is shown as grey squares and chaotic bouncing is shown as black asterisks. The data to the right of the vertical dashed line is repeated.

we find that despite the presence of  $\Gamma_{40}$  being essential to the existence of these superwalkers, its magnitude only marginally affects their speed. This is consistent with the observations for  $(2,1)$  walkers, for which the walking speed is only weakly dependent on the driving amplitude at higher accelerations above the walking threshold [85]. Moreover, we find that as  $\Gamma_{40}$  increases, larger droplets that coalesce at either single frequency driving ( $\Gamma_{40} = 0$ ) or at low  $\Gamma_{40}$  are now able to superwalk at high  $\Gamma_{40}$ . To complement figure 3.4(a), figure 3.4(b) shows the speed of solitary superwalkers as a function of its radius for fixed  $\Gamma_{40}$  and  $\Delta\phi$  and three different values of  $\Gamma_{80}$ . We find that increasing  $\Gamma_{80}$  results in an increased speed for steadily walking superwalkers.

### 3.4.2 Effect of varying the phase difference

The value of the phase difference  $\Delta\phi$  between the two driving signals crucially affects the behaviour of droplets. Figure 3.5 shows data for the speed of a droplet  $u$  as a function of the phase difference  $\Delta\phi$  for fixed  $\Gamma_{80}$  and  $\Gamma_{40}$  and three different radii of  $R = 0.54$  mm,  $R = 0.60$  mm and  $R = 0.83$  mm. We find that superwalkers only exist for a limited range of phase difference and outside this range they either coalesce (open markers) or bounce without walking. In the bouncing region, the smaller  $R = 0.54$  mm droplet bounces chaotically while the larger  $R = 0.60$  mm and  $R = 0.83$  mm droplets bounce in a  $(1,2,2)$  mode. Inside the superwalking region, the droplet may bounce in a  $(1,2,1)^H$  or a  $(1,2,2)$  mode. Near the peak walking speed in the superwalking region,

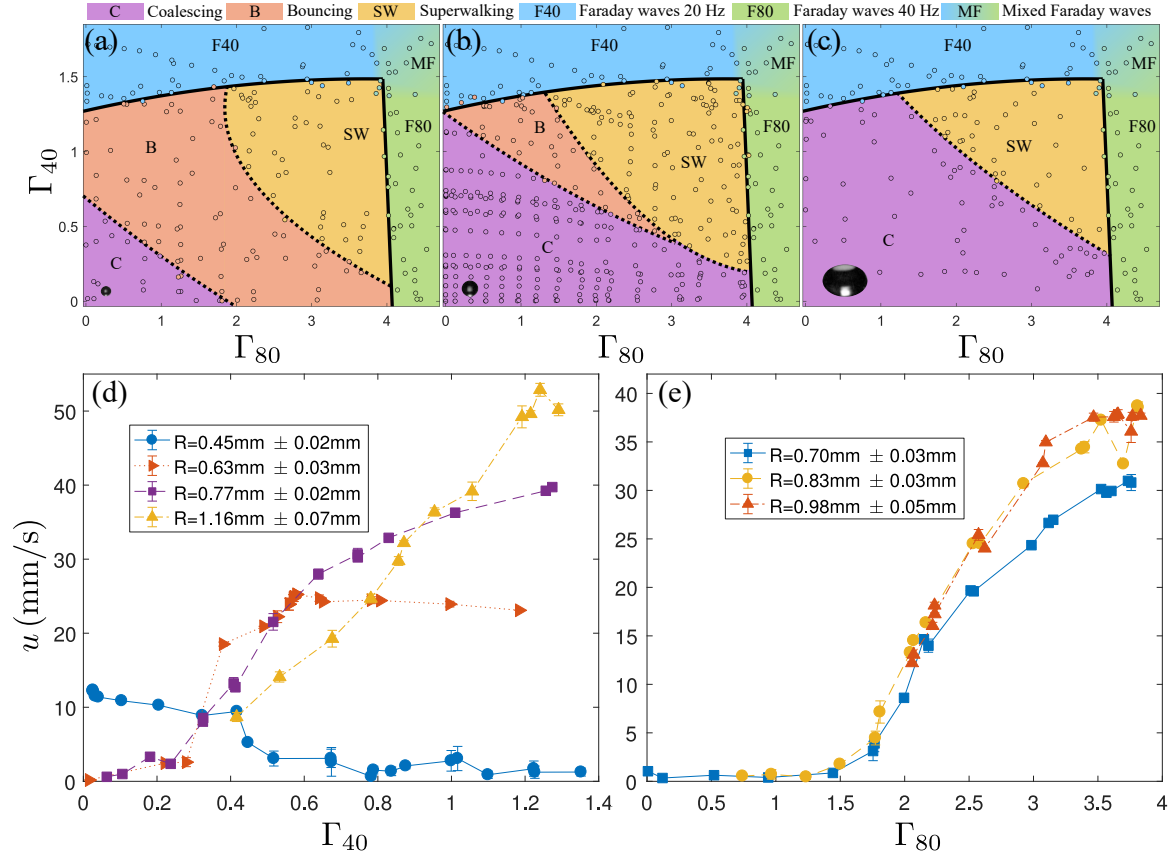


Figure 3.6 : Different behaviours occurring in the  $(\Gamma_{80}, \Gamma_{40})$  parameter space for a fixed phase difference  $\Delta\phi = 130^\circ$  and three different droplet radii: (a)  $R = 0.6 \pm 0.05$  mm, (b)  $R = 0.8 \pm 0.05$  mm, and (c)  $R = 1.0 \pm 0.05$  mm. (d) Speed as a function of  $\Gamma_{40}$  for droplet radii  $R = 0.45$  mm,  $R = 0.63$  mm,  $R = 0.77$  mm and  $R = 1.16$  mm. (e) Speed as a function of  $\Gamma_{80}$  for droplet radii  $R = 0.70$  mm,  $R = 0.83$  mm and  $R = 0.98$  mm.

both  $R = 0.54$  mm and  $R = 0.60$  mm droplets bounce in a  $(1,2,1)^H$  mode while the  $R = 0.83$  mm droplet always bounces in a  $(1,2,2)$  mode in the superwalking region. The maximum speed occurs in the vicinity of  $\Delta\phi \approx 140^\circ$ , a value that does not appear to vary significantly with  $\Gamma_{80}$ ,  $\Gamma_{40}$ , or droplet radius  $R$ .

### 3.4.3 Effect of varying the acceleration amplitudes

Figures 3.6(a-c) show the different regimes observed in the  $(\Gamma_{80}, \Gamma_{40})$  parameter space for a fixed phase difference  $\Delta\phi = 130^\circ$  and three different droplet radii. Parametrically forcing a bath of liquid simultaneously at two different frequencies  $f$  and  $f/2$  may result in a Faraday instability with either  $f/2$  or  $f/4$  waves depending on the amplitudes of the two frequencies and the phase difference  $\Delta\phi$  between them [83]. We find that

driving the bath at 80 Hz and 40 Hz delays the onset of 20 Hz Faraday waves when the driving acceleration  $\Gamma_{80}$  is large. The onset of the 40 Hz Faraday waves is not significantly affected. For large  $\Gamma_{40}$  and  $\Gamma_{80}$ , both 40 Hz and 20 Hz Faraday waves appear to be excited simultaneously. Below the Faraday threshold, we find coalescing (C), bouncing (B), and superwalking (SW) regions with the extent of each region dependent on droplet size. For a relatively small droplet, figure 3.6(a), the extent of the bouncing and superwalking regions is large. The bouncing region progressively decreases with an increase in droplet size (see figures 3.6(a)-(c)). For a larger droplet, figure 3.6(c), the bouncing region disappears and the droplet may either coalesce or walk. For even larger droplets, the superwalking region also vanishes. We also find that just above the 80 Hz-driving Faraday threshold, unlike walkers, superwalkers still walk steadily with their motion guided by the globally excited nonlinear Faraday waves. In the parameter regime where global Faraday waves are not excited, droplets always appear to trigger decaying 40 Hz Faraday waves, as illustrated by the similarity in wavelengths in figure 3.1. In Chapter 4 we will derive an expression for the wave field of a superwalker and show that the dominant contribution is indeed from the 40 Hz waves.

Figure 3.6(d-e) provides further insight into the relationship between the walking speed and the peak acceleration amplitudes  $\Gamma_{40}$  and  $\Gamma_{80}$  for different-sized droplets. In figure 3.6(d) the walking speed as a function of  $\Gamma_{40}$  is shown for four different sized droplets. The smallest droplet ( $R = 0.45$  mm) is a  $(2,1)^H$  walker for single-frequency driving. Adding the subharmonic frequency barely impacts its speed up to a threshold  $\Gamma_{40}$  value, beyond which the walking speed drops precipitously and the droplet switches to a chaotic mode. A slightly larger droplet of  $R = 0.63$  mm is a bouncer for a single-frequency driving and remains so for small  $\Gamma_{40}$ . Beyond a threshold  $\Gamma_{40}$  value, the droplet begins to walk and does so with increasing speed before plateauing for moderately large  $\Gamma_{40}$ . A medium-sized droplet of  $R = 0.77$  mm exhibits similar behaviour but its speed continues to increase with  $\Gamma_{40}$ . The largest droplet of  $R = 1.16$  mm coalesces at low  $\Gamma_{40}$  and directly begins to superwalk beyond a threshold value of  $\Gamma_{40}$  with its speed increasing almost linearly with  $\Gamma_{40}$  and reaching a maximum speed of approximately 50 mm/s. Figure 3.6(e) shows the speed as a function of  $\Gamma_{80}$  for three different droplet radii. The trend for all three droplet sizes is similar with the speed increasing with  $\Gamma_{80}$ . We note that the largest droplet, a jumbo superwalker, only exists in the superwalking regime and coalesces at lower  $\Gamma_{80}$ .

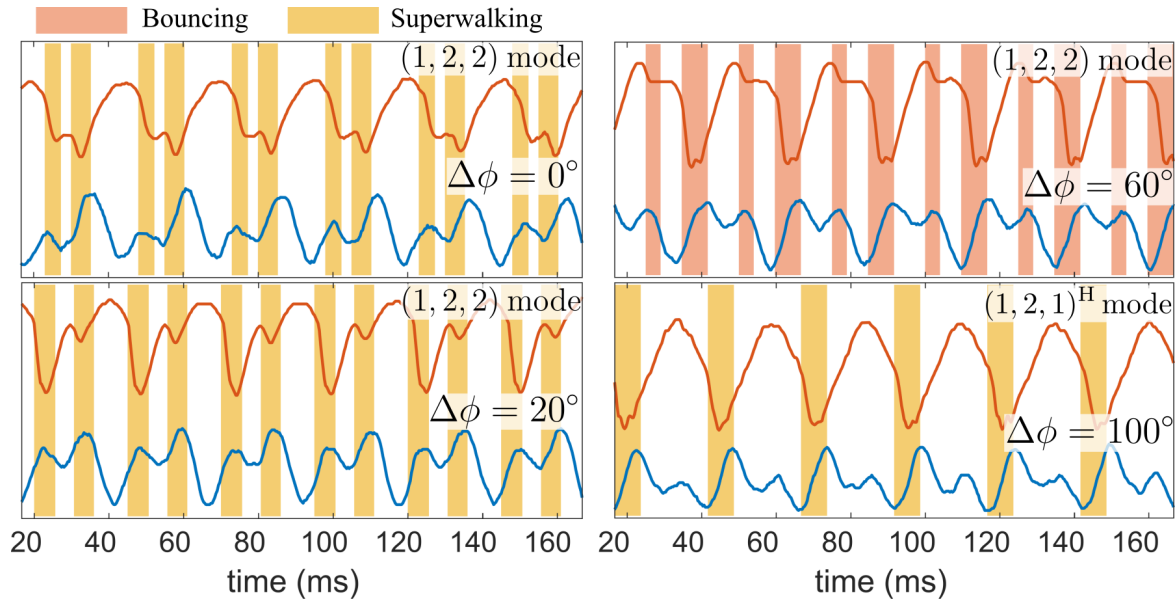


Figure 3.7 : Vertical motion of a fixed point on the droplet (red curve) and the bath motion (blue curve) as a function of time (in milliseconds) showing the different bouncing modes for different phase differences  $\Delta\phi$  at  $\Gamma_{80} = 3$  and  $\Gamma_{40} = 0.8$  for a droplet of radius  $R = 0.60 \pm 0.01$  mm. The contact interval is indicated by the shaded regions.

### 3.5 Contact with the underlying wave field

The details of the contact between the droplet and the underlying wave field are crucially important for the droplet dynamics. However, for large droplets that barely lift off the fluid surface and undergo significant internal deformations, it becomes exceedingly difficult to quantify the nature and duration of the contact. Moreover, due to the imaging limitation of our experiments, we were only able to do qualitative analysis of the bouncing motion from the high speed videos and use that to estimate the contact time. Figure 3.7 shows the droplet's vertical motion (red curve) and the bath motion (blue curve) at different phase differences  $\Delta\phi$  for a fixed droplet size and at fixed values of  $\Gamma_{80}$  and  $\Gamma_{40}$ . The vertical motion of the bath (blue curve) was obtained by tracking the motion of a fixed point on the edge of the bath. The droplet's vertical position (red curve) was obtained by tracking a fixed bright spot on the droplet. Since the droplet deforms significantly during contact, this method does not capture the vertical trajectory well during contact which is indicated by the shaded region. The contact region was determined by visual inspection of the sequence of images from the high speed videos. Moreover, since the imaging plane in the high speed videos was not aligned with droplet's vertical motion, the vertical co-ordinate is not a representative of

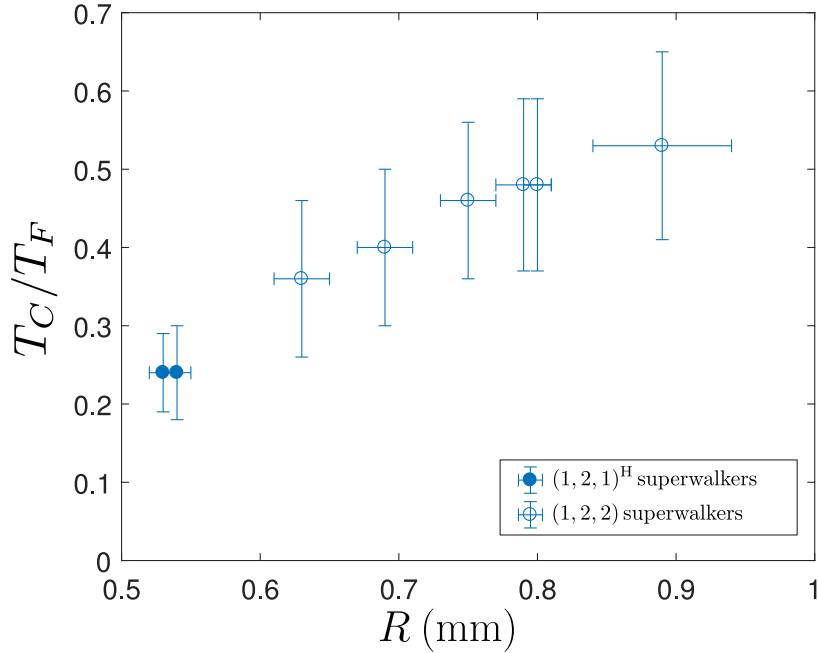


Figure 3.8 : Total contact time ( $T_C$ ) relative to the Faraday period ( $T_F$ ) for different sized droplets. The contact time was calculated by visual inspection of the high speed videos of superwalkers. Filled circles represent  $(1,2,1)^H$  superwalkers while empty circles represent  $(1,2,2)$  superwalkers. Here the other parameters were fixed to  $\Gamma_{80} = 3.8$ ,  $\Gamma_{40} = 0.6$  and  $\Delta\phi = 130^\circ$ .

the vertical scale of the droplet's motion. From the qualitative bouncing modes shown in figure 3.7 we identify that for a droplet in the  $(1,2,1)^H$  mode, it stays in contact with the bath for the entire upward motion of the larger peak in the bath motion. Moreover, for the droplet in the  $(1,2,2)$  mode we see two contacts per bouncing period. We also note that the  $(1,2,2)$  mode shown for  $\Delta\phi = 0^\circ$ , has the two contact regions in one bouncing period very close to each other. Hence, it is not clear where such a mode is truly a  $(1,2,2)$  mode or a  $(1,2,1)^L$  mode.

By calculating the contact time through visual inspection of high speed videos for different sized droplets, we can obtain an approximation of the contact time with the bath as a function of the droplet size as shown in figure 3.8. Note the large vertical error bars that take into account the large uncertainty in our visual inspection method. For droplets with radius  $R \gtrsim 0.9$  mm, our imaging resolution was insufficient to determine their contact time but they appeared to be in contact for the entire bouncing period.

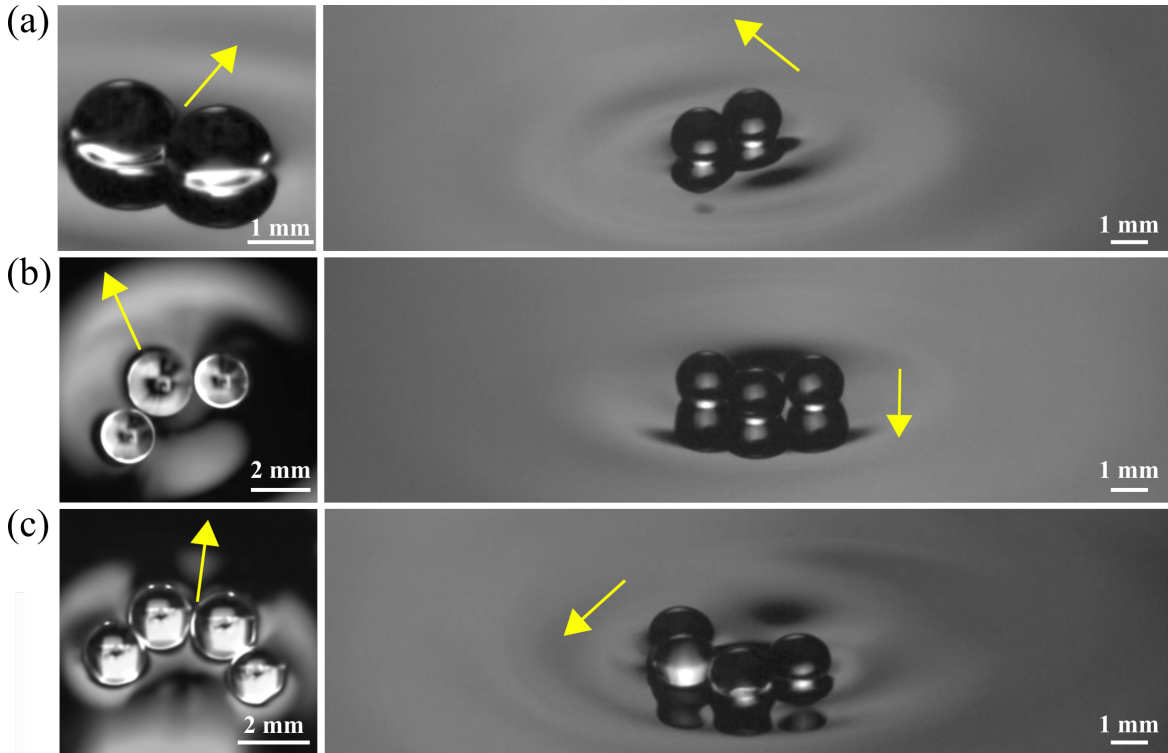


Figure 3.9 : Tightly bound states of superwalking droplets. (a) Doublet, (b) Triplet and (c) Quadruplet states of superwalking droplets with symmetric droplet configurations where the aggregate follows a straight line trajectory. For videos, see Supplemental Videos S2, S3 and S4 of [53].

### 3.6 Interactions of multiple superwalkers

Like walkers, multiple superwalkers can interact with each other through their underlying wave field. Moreover, due to their large inertia, superwalkers can also have direct droplet-droplet interactions with other superwalkers. These interactions lead to a variety of novel stationary and dynamic configurations, a selection of which are illustrated in figures 3.9 – 3.13 (for videos see Supplemental Material of [53]). We note that for walkers, since their typical bouncing frequency is half the driving frequency, two walkers can have either in-phase or out-of-phase interactions. Conversely, for superwalkers, the typical bouncing frequency is same as the overall driving frequency, and hence we only observe in-phase interactions for superwalkers.

Two superwalkers can bind into a tight pair in which the droplets are separated only by a very thin air layer (see figure 3.9(a)). If the droplets have different size then they traverse a circular path, while a pair of identical droplets traverses a straight path. Similar states exist for staggered three-droplet and four-droplet configurations where

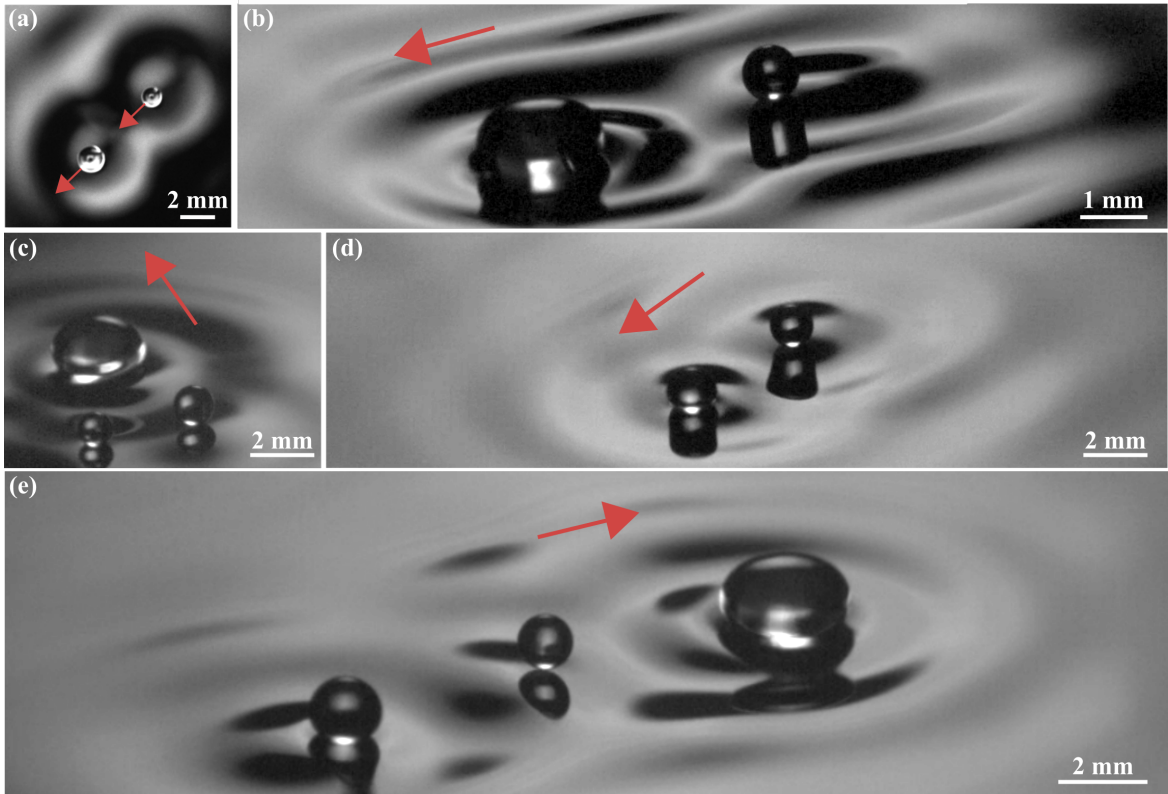


Figure 3.10 : Chasing pair of superwalkers. (a) Top view and (b) side view of a typical pair of chasers with mismatched droplets. (c) Chasers with three droplets where the leading large droplet drags behind two smaller droplets in a staggered configuration. (d) Less common chasing pair where both droplets are similar in size. (e) Chasers with three droplets where the leading large droplet drags two smaller droplets in a collinear configuration. For videos, see Supplemental Videos S5 and S6 of [53].

if the droplet configurations are symmetric then the group traverses a straight line trajectory (see figures 3.9(b) and (c)), while asymmetric droplet configurations lead to circular trajectories. These states are typically observed at relatively low driving acceleration or low memory.

We have observed another type of bound pair called chasers (see figure 3.10), which have previously been found numerically for identical droplets with single-frequency driving [63, 55] and experimentally in an effectively one-dimensional confined annular geometry [14]. Here we observe chasers in free space where two droplets walk one behind the other at a constant speed. For droplets of differing size, the larger droplet leads and drags the smaller one in its wake (see figures 3.10(a) and (b)). Chasing pairs of superwalkers are robust and ubiquitous at high memory, and the larger the size disparity between the two droplets, the more stably bound they are. Particularly disparate

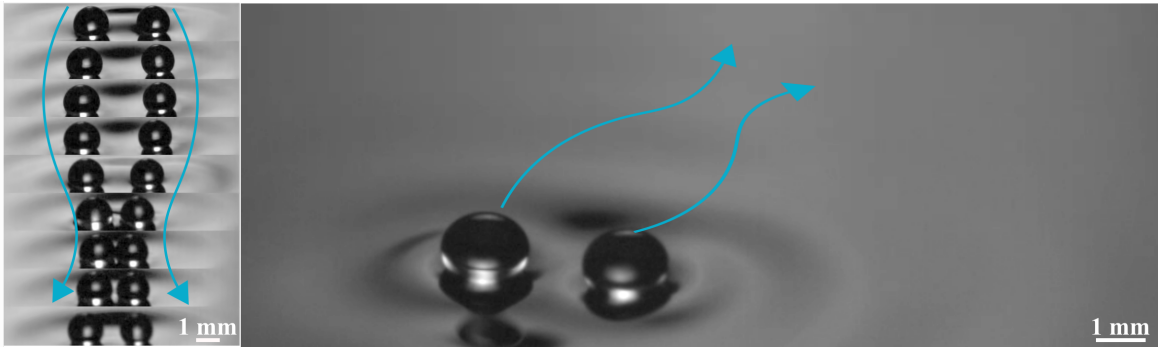


Figure 3.11 : Promenading pair of superwalkers. In this bound state, supewalkers can walk side by side on parallel trajectories with sideways oscillations where droplets bounce off each other at their closest approach. For a video, see Supplemental Video S7 of [53].

pairs can survive collisions with other droplets and even with the bath's walls. Less commonly, we have observed chasers with similar droplet size (see figure 3.10(d)) and aggregates consisting of three chasing droplets either in a staggered (see figure 3.10(c)) or a collinear configuration (see figure 3.10(e)). We note that chasing pairs are different from ratcheting pairs of walkers reported by Eddi et al. [12] and Galeano-Rios et al. [13]. Ratcheting motion typically occurs below the walking threshold and the pair travels slowly, while we find that chasers only appear at high memory and are an order of magnitude faster. We also observe ratcheting pairs with superwalkers at very low memory.

Two superwalkers can form a state reminiscent of promenading pairs of walkers, where the droplets walk in parallel with sideways oscillations [9, 10, 55]. Promenading pairs of walkers remain physically separated at all times due to the wave barrier formed as they approach one another. In contrast, promenading pairs of superwalkers undergo droplet-droplet collisions, bouncing off one another as shown in figure 3.11. The centre of mass of identical promenading superwalkers follows a straight path while that of even slightly mismatched superwalkers tends to follow a circular trajectory.

Two superwalkers may also form loosely bound orbiting pairs (see figure 3.12(a)) similar to walkers [6, 89, 11] where two droplets orbit about their common centre of rotation. A novel feature for orbiting superwalkers is that we have occasionally observed intermittent reversals of the orbiting direction for mismatched droplets. We also observe tightly bound orbiting pairs of mismatched superwalkers. With an extreme size imbalance, giant droplets that would coalesce with the bath in isolation can persist if accompanied by a smaller orbiting satellite droplet, see figure 3.12(b). More exotic orbiting superwalkers have also been observed such as orbits with three superwalkers

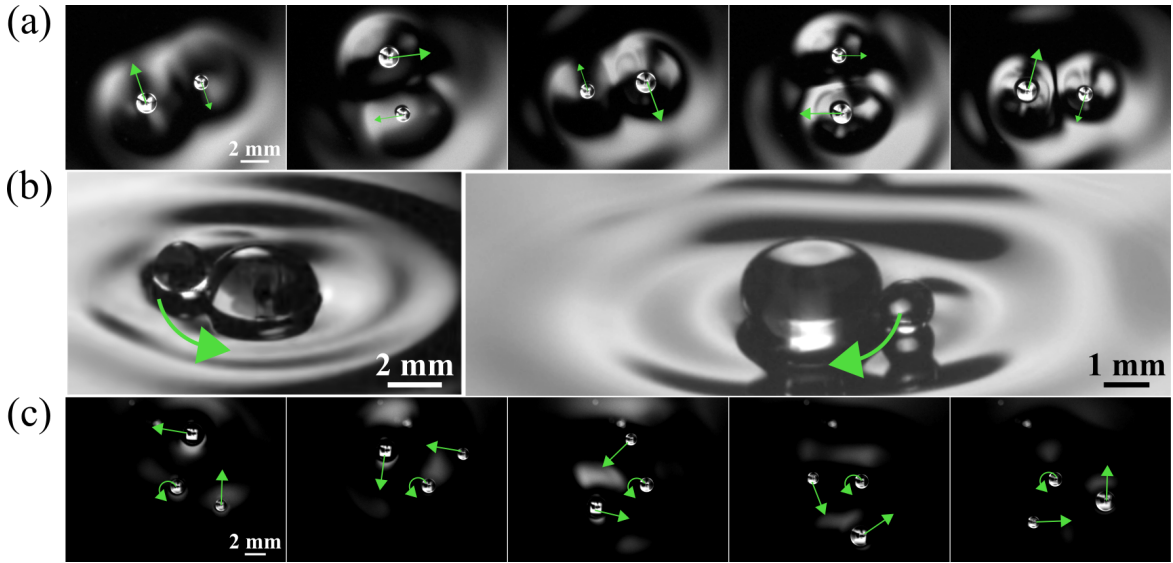


Figure 3.12 : Orbiting superwalkers. (a) Loosely bound orbiting pair of superwalkers where the two droplets rotate about their common centre of rotation. (b) Tightly bound orbiting pair where a relatively small satellite droplet orbits around a giant droplet (for a video, see Supplemental Video S8 of [53]). (c) Orbit with three superwalkers where a big and a small droplet orbit a central medium-sized wobbling droplet. For panels (a) and (c), snapshots of the droplets at different locations in the orbit are shown.

where a big and a small droplet orbit around a central medium-sized wobbling droplet (see figure 3.12(c)).

When many superwalkers are present, the inter-droplet interactions favour crystalline droplet configurations for relatively low driving accelerations. If the value of  $\Gamma_{40}$  is progressively increased while keeping  $\Gamma_{80}$  fixed, see figure 3.13, the crystal initially begins to jiggle. Similar jiggling of a droplet crystal has been observed for single frequency driving on decreasing the frequency or increasing the number of droplets [93]. Increasing  $\Gamma_{40}$  further results into disintegration of the droplet crystal but droplets may still remain bounded in two- and three-droplet configurations. Ultimately, at highest  $\Gamma_{40}$ , the droplets begin to superwalk at high speed, bouncing off each other elastically like billiard balls. The observed dynamics are reminiscent of solid-liquid-gas phase transitions with the forcing amplitude acting as a temperature parameter. This behaviour is robust with respect to interchanging the roles of  $\Gamma_{40}$  and  $\Gamma_{80}$ , and are associated with crossing the phase boundary between bouncing (B) and superwalking (SW).

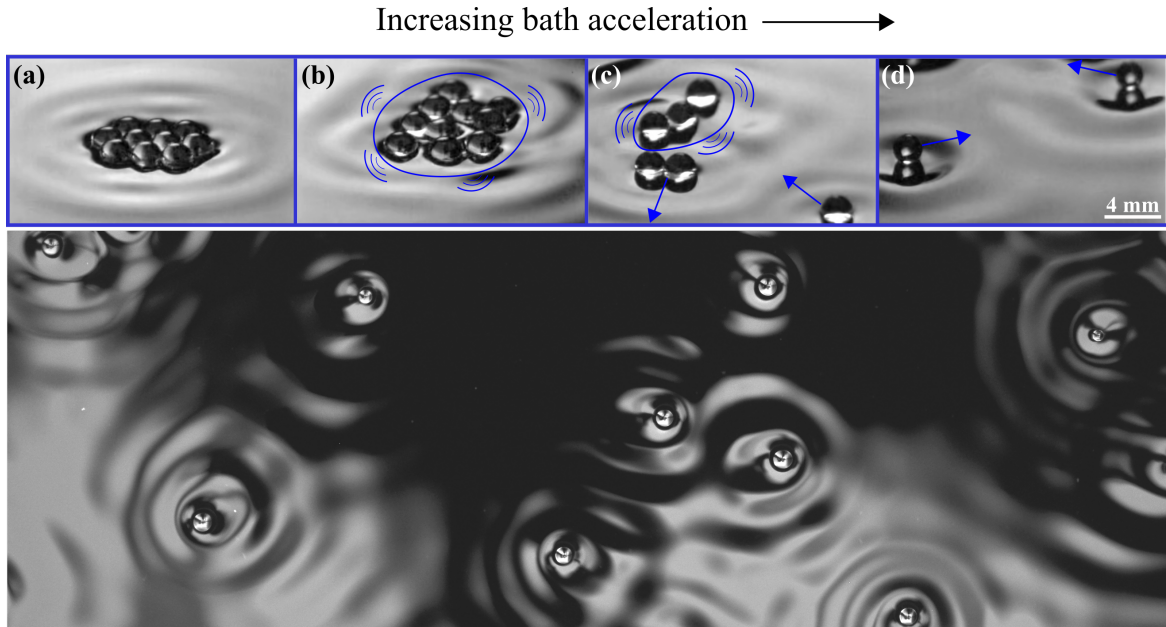


Figure 3.13 : Interactions of many superwalkers. Many superwalkers self-organise into (a) a tightly bound crystal-like configuration at low memory. (b) As the memory is progressively increased the aggregate starts to jiggle. (c) Further increase in memory leads to disintegration of the aggregate but droplets may still remain bound in two- and three-droplet configurations. (d) At the highest memory, the droplets begin to superwalk at high speed, bouncing off each other elastically like billiard balls. Bottom panel shows many superwalkers interacting at high memory. For a video, see Supplemental Video S9 of [53].

### 3.7 Bubble-droplets

Large two-component *bubble-droplets*, which are partly liquid and partly air, may be created with ease using a syringe filled with silicone oil and containing an air bubble. When such a bubble-droplet is placed on the liquid bath driven at two frequencies as prescribed in this chapter, we get two qualitatively different types of dynamics. If the proportion of air is appreciable, then the bubble-droplet bounces with an additional pendulum motion, tumbling back and forth (see figure 3.14(a)). If the air only occupies a small proportion of the droplet, then the bubble-droplet walks much like a superwalker but at a reduced speed with respect to an air-free droplet (see Fig. 3.14(b)). Such bubble superwalkers form bound states similar to air-free superwalkers (see figures 3.14(c) and (d)). The bubble-droplets open up a new parameter space to explore in the system of walking droplet. By controlling the amount of air (or liquid) in the droplet, the inertia of the droplet can be reduced while keeping the droplet size fixed allowing for bigger droplets that move slowly compared to air-free superwalkers.

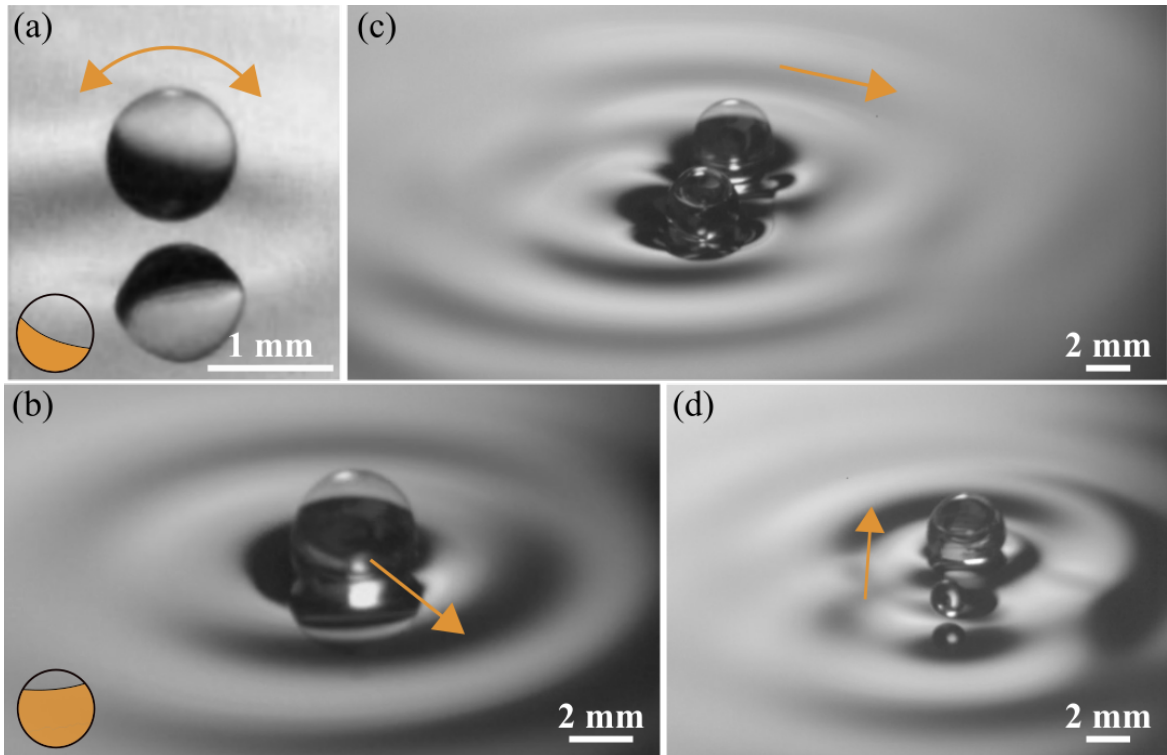


Figure 3.14 : Bubble-droplets that are partly filled with silicone oil and partly air. (a) If the bubble-droplet is dominated by air, it tumbles back and forth and undergoes pendulum-like motion (for a video, see Supplemental Video S11 of [53]). (b) Bubble-superwalker: A bubble-droplet that is mostly filled with silicone oil with a small amount of air walks much like a superwalker but at a reduced speed compared to the air-free droplet. Multiple bubble-superwalkers form bound states akin to regular superwalkers such as (c) tightly bound superwalking pairs and (d) chasing pairs.

### 3.8 Conclusion

We have introduced a new class of walking droplets, coined superwalkers, enabled by adding a subharmonic driving signal to a periodically driven walking-droplet system. We found that these superwalkers can be more than twice the size and walk at more than triple the speed of typical single-frequency driven walkers. The superwalking behaviour of a given sized droplet varies as the acceleration amplitudes  $\Gamma_{80}$  and  $\Gamma_{40}$  and the phase difference  $\Delta\phi$  between the two driving frequencies are varied. The variation in the superwalking behaviour with the acceleration amplitudes is expected as it controls the decay time of damped Faraday waves generated by the droplet, however the sensitivity of the superwalking behaviour to the phase difference  $\Delta\phi$  is intriguing. Interactions of multiple superwalkers give rise to novel static and dynamic multi-droplet bound states as well as emergent many droplet behaviours. This introductory study

of superwalkers uncovers a wealth of new phenomena that need to be studied in more detail both experimentally and numerically. As a first step, in the next chapter, we start by developing a theoretical model for superwalking droplets. Using this model, we attempt to uncover the underlying mechanism resulting in the superwalking phenomenon and build a foundation on which further studies of superwalkers can take place.

# Chapter 4

## Emergence of superwalking droplets: a numerical approach

In this chapter, we extend the previously established theoretical models for walkers driven by a single frequency to superwalkers driven by two frequencies in order to understand the emergence of superwalking behaviour. We explore the vertical and horizontal dynamics of superwalkers and show that driving the bath at two frequencies with an appropriate phase difference raises every second peak and lowers the intermediate peaks in the vertical periodic motion of the fluid surface. This allows large droplets that could otherwise not walk to leap over the intermediate peaks, resulting in superwalking droplets whose vertical dynamics is qualitatively similar to normal walkers. We find that the droplet's vertical and horizontal dynamics are strongly influenced by the relative height difference between successive peaks of the bath motion, a parameter that is controlled by the phase difference. Comparison of our simulated superwalkers with the experimental results presented in Chapter 3 shows good agreement for small- to moderate-sized superwalkers.

This chapter is based on the following published paper:

R. N. Valani, J. Dring, T. Simula and A. C. Slim, *Emergence of superwalking droplets*, Journal of Fluid Mechanics **906**, A3 (2021).

### 4.1 Introduction

In Chapter 3, we described characteristics of superwalkers observed in experiments when a bath of silicone oil is driven with two frequencies  $f = 80$  Hz and  $f/2 = 40$  Hz and a

relative phase difference  $\Delta\phi$ . It was found that superwalkers can be significantly larger than walkers with radii up to 1.4 mm and walking speeds up to 50 mm/s. Intriguingly, the walking speed and the vertical dynamics of superwalkers are strongly dependent on the phase difference  $\Delta\phi$ , with peak superwalking speed occurring near  $\Delta\phi = 140^\circ$ , while near  $\Delta\phi = 45^\circ$  they only bounce or may even coalesce. Moreover, for a fixed phase difference, smaller superwalkers typically behave very similarly to walkers, with their speed increasing with their size and impacting the surface once every two up-and-down cycles of the bath. Conversely, the speed of larger superwalkers decreases with size. These large superwalkers appear to impact the bath twice every two up-and-down cycles of the bath and have prolonged contact with the bath, with the largest ones hardly lifting from the surface. Using sophisticated numerical simulations, Galeano-Rios et al. [68] were able to replicate superwalking behaviour for a single droplet of moderate radius  $R = 0.68$  mm, and reported a good match in the superwalking speed between their simulation and our experimental results presented in Chapter 3. Although our experimental study in Chapter 3 and the simulations of Galeano-Rios et al. [68] describe the characteristics of superwalkers, an understanding of the mechanism that enables superwalking is still lacking. In this chapter, our aim is to understand this underlying mechanism by adapting the theoretical models used for walkers driven with a single frequency, to superwalkers driven with two frequencies.

## 4.2 Theoretical setup

To simulate superwalkers, we couple previously established models of vertical and horizontal dynamics of Moláček and Bush [57, 85] along with a new model for the wave field of a superwalker to understand and rationalise superwalking. As shown schematically in figure 2.1 and described in Section 2.1, consider the setup of a droplet of mass  $m$  and radius  $R$  bouncing on a bath of liquid of density  $\rho$ , kinematic viscosity  $\nu$  and surface tension  $\sigma$ . The bath is driven vertically at two frequencies  $f$  and  $f/2$  with acceleration  $\gamma(t) = \Gamma_f g \sin(\Omega t) + \Gamma_{f/2} g \sin(\Omega t/2 + \Delta\phi)$ . Here  $\Gamma_f$  and  $\Gamma_{f/2}$  are dimensionless accelerations amplitudes and  $\Omega = 2\pi f$  is the angular frequency. We simulate the vertical droplet dynamics using the improved linear spring model of Moláček and Bush [57] as described in equations (2.1) and (2.3) adapted for two-frequency driving. To describe the horizontal dynamics of the walking droplet, we use the model of Moláček and Bush [85] for which the horizontal equation of motion is given by equation (2.11).

### 4.3 Waves excited under two-frequency driving

To form a complete model to simulate superwalkers, the vertical and horizontal dynamics equations (2.3) and (2.11), need to be coupled to the free surface deformation  $h(\mathbf{x}, t)$  created by the droplet's impact. This free surface  $z = h(\mathbf{x}, t)$  is calculated as the linear superposition of all the individual waves generated by the droplet on its previous bounces

$$h(\mathbf{x}, t) = \sum_n h_n(\mathbf{x}, t),$$

where  $h_n(\mathbf{x}, t)$  is the wave field generated by the  $n$ th bounce at location  $\mathbf{x}_n$  and time  $t_n$ . The individual waves generated by the droplet on each bounce are localised, damped standing Faraday waves. Various different models of the wave field have been developed for walkers [84, 85, 62, 86] and they are described in section 2.4.2. To derive the form of the surface waves generated by a single impact of a droplet on a bath driven at two frequencies  $f$  and  $f/2$ , we closely follow the approach of Tadrict et al. [86] who derived the wave form for single impact of a droplet under single frequency driving as given in equation (2.10).

We consider an incompressible, Newtonian liquid in a bath that is infinitely large in horizontal extent and infinitely deep. The bath is subjected to periodic vertical vibrations that result in a modulation of the effective gravity in the frame of the bath  $g^*(t) = g[1 + \Gamma_f \sin(\Omega t) + \Gamma_{f/2} \sin(\Omega t/2 + \Delta\phi)]$ . For notational clarity, we will refer to specific frequencies  $f = \Omega/2\pi = 80$  Hz and  $f/2 = 40$  Hz, but the derivation is general. The evolution of the liquid is governed by the incompressible Navier-Stokes equations,

$$\nabla \cdot \mathbf{v} = 0 \quad \text{and} \quad \frac{\partial \mathbf{v}}{\partial t} + (\mathbf{v} \cdot \nabla) \mathbf{v} = -\frac{1}{\rho} \nabla P - g^*(t) \hat{\mathbf{k}} + \nu \nabla^2 \mathbf{v},$$

where  $\mathbf{v}(\mathbf{r}, t)$  is the velocity field,  $P(\mathbf{r}, t)$  is the pressure field relative to atmospheric pressure,  $\mathbf{r} = (x, y, z)$  is the position vector,  $\hat{\mathbf{k}}$  is a unit vector in the  $z$  direction,  $\rho$  is the density and  $\nu$  is the kinematic viscosity. We consider small perturbations from the stationary equilibrium state  $\mathbf{v} = \mathbf{0}$ ,  $P = -\rho g^*(t)z$  and  $h = 0$ . We linearise the above equations about this equilibrium state with pressure perturbation  $p(\mathbf{r}, t)$  and velocity perturbation  $\mathbf{v}(\mathbf{r}, t)$  resulting in the following linearised equation:

$$\frac{\partial \mathbf{v}}{\partial t} - \nu \nabla^2 \mathbf{v} = -\frac{1}{\rho} \nabla p. \quad (4.1)$$

Due to the incompressibility of the liquid, the pressure perturbation  $p$  satisfies

$$\nabla^2 p = 0. \quad (4.2)$$

Assuming that the liquid is only weakly perturbed, the absence of tangential stress at the free surface combined with the incompressibility condition gives the following equation for the vertical component of the liquid velocity  $v_z$  at  $z = 0$ :

$$\frac{\partial^2 v_z}{\partial z^2}(x, y, 0, t) = \left( \frac{\partial^2}{\partial x^2} + \frac{\partial^2}{\partial y^2} \right) v_z(x, y, 0, t). \quad (4.3)$$

The pressure boundary condition requires

$$p(x, y, 0, t) = 2\nu\rho \frac{\partial v_z}{\partial z}(x, y, 0, t) - \sigma \left( \frac{\partial^2}{\partial x^2} + \frac{\partial^2}{\partial y^2} \right) h(x, y, t) + \rho g^*(t) h(x, y, t) + P^{\text{ext}}(x, y, t),$$

and the kinematic boundary condition implies

$$\frac{\partial h}{\partial t} = v_z(x, y, 0, t), \quad (4.4)$$

where  $h(x, y, t)$  is the free surface perturbation,  $\sigma$  is the coefficient of surface tension,  $P^{\text{ext}}(x, y, t)$  is the pressure exerted by the droplet on the free surface through the intervening air layer and  $\hat{\mathbf{n}}$  is the unit normal out of the liquid. Assuming that the pressure distribution imparted by the droplet during contact is uniform in the contact region we get

$$P^{\text{ext}}(x, y, t) = P^{\text{ext}}(t) = F_N(t)/\pi w^2, \quad (4.5)$$

where  $w$  is the effective radius of the contact area and  $F_N(t)$  is the normal force as described in equation (2.3). Since the bath has infinite horizontal extent, we can simplify the equations using the Fourier transform defined as follows for an arbitrary variable  $X(x, y, \tau)$ :

$$X_{\mathbf{k}}(\tau) = \int_0^\infty \int_0^\infty X(x, y, \tau) \exp[-i(k_x x + k_y y)] dx dy,$$

where  $\mathbf{k} = (k_x, k_y)$  is the horizontal wave vector with  $k = |\mathbf{k}|$ . Applying the Fourier transform to equation (4.2) we get

$$\frac{\partial^2 p_{\mathbf{k}}}{\partial z^2}(z, t) = k^2 p_{\mathbf{k}}(z, t).$$

The solution of this equation is given by  $p_{\mathbf{k}}(z, t) = p_{\mathbf{k}}(0, t) e^{kz}$  with the boundary conditions  $p_{\mathbf{k}}(-\infty, t) = 0$  and

$$p_{\mathbf{k}}(0, t) = 2\nu\rho \frac{\partial v_{z,\mathbf{k}}}{\partial z}(0, t) + [\rho g^*(t) + \sigma k^2] h_{\mathbf{k}}(t) + P_{\mathbf{k}}^{ext}(t).$$

Applying the Fourier transform to the linearized Navier-Stokes equation (4.1) we get,

$$\begin{aligned} \left( \frac{\partial}{\partial t} - \nu \frac{\partial^2}{\partial z^2} + \nu k^2 \right) v_{z,\mathbf{k}}(z, t) = & - \left( 2\nu \frac{\partial v_{z,\mathbf{k}}}{\partial z}(0, t) + \left[ g^*(t) + \frac{\sigma}{\rho} k^2 \right] h_{\mathbf{k}}(t) \right) k e^{kz} \\ & - \frac{k}{\rho} P_{\mathbf{k}}^{ext}(t) e^{kz}, \end{aligned} \quad (4.6)$$

with boundary conditions

$$\frac{\partial h_{\mathbf{k}}}{\partial t}(t) = v_{z,\mathbf{k}}(0, t) \quad \text{and} \quad \frac{\partial^2 v_{z,\mathbf{k}}}{\partial z^2}(0, t) = -k^2 v_{z,\mathbf{k}}(0, t), \quad (4.7)$$

obtained from equations (4.4) and (4.3) respectively. For the remainder of the derivation, we will use dimensionless time  $\tau = \Omega t/2$  for ease of comparison with the equations of Tadrict et al. [86], and will revert back to the dimensional time  $t$  in the final expressions. Using this non-dimensional time we make the following change of variables as done in Tadrict et al. [86],

$$w_{\mathbf{k}} = \frac{2}{\Omega} v_{z,\mathbf{k}}, \quad \Pi_{\mathbf{k}} = \frac{4k}{\Omega^2 \rho} P_{\mathbf{k}}^{ext}, \quad \gamma_{\mathbf{k}} = \frac{4\nu k^2}{\Omega} \quad \text{and} \quad \omega_{\mathbf{k}}^2 = \frac{4(gk + (\sigma/\rho)k^3)}{\Omega^2}.$$

Using this new notation equations (4.6) and (4.7) become,

$$\begin{aligned} \left( \frac{\partial}{\partial \tau} - \frac{\gamma_{\mathbf{k}}}{2k^2} \frac{\partial^2}{\partial z^2} + \frac{\gamma_{\mathbf{k}}}{2} \right) w_{\mathbf{k}}(z, \tau) = & - \left( \frac{\gamma_{\mathbf{k}}}{k} \frac{\partial w_{\mathbf{k}}}{\partial z}(0, \tau) + \left[ \frac{4\Gamma_f g k}{\Omega^2} \sin(2\tau) + \frac{4\Gamma_{f/2} g k}{\Omega^2} \sin(\tau + \Delta\phi) + \omega_{\mathbf{k}}^2 \right] h_{\mathbf{k}}(\tau) \right) e^{kz} \\ & - \Pi_{\mathbf{k}}(\tau) e^{kz}, \end{aligned} \quad (4.8)$$

and

$$\frac{\partial h_{\mathbf{k}}}{\partial \tau}(\tau) = w_{\mathbf{k}}(0, \tau) \quad \text{and} \quad \frac{\partial^2 w_{\mathbf{k}}}{\partial z^2}(0, \tau) = -k^2 w_{\mathbf{k}}(0, \tau). \quad (4.9)$$

Now the Laplace transform is defined as follows:

$$X_{\mathbf{k},s} = \int_0^\infty X_{\mathbf{k}}(\tau) e^{-s\tau} d\tau.$$

Taking Laplace Transform of equations (4.8) and (4.9) results in

$$\begin{aligned} & \left( s - \frac{\gamma_k}{2k^2} \frac{\partial^2}{\partial z^2} + \frac{\gamma_k}{2} \right) w_{\mathbf{k},s}(z) = \\ & - \left( \frac{\gamma_k}{k} \frac{\partial w_{\mathbf{k},s}}{\partial z}(0) + \omega_k^2 h_{\mathbf{k},s} + \frac{2\Gamma_{f g k}}{i\Omega^2} (h_{\mathbf{k},s-2i} - h_{\mathbf{k},s+2i}) + \frac{2\Gamma_{f/2 g k}}{i\Omega^2} (h_{\mathbf{k},s-i} e^{i\Delta\phi} - h_{\mathbf{k},s+i} e^{-i\Delta\phi}) \right) e^{kz} \\ & - \Pi_{\mathbf{k},s} e^{kz}, \end{aligned}$$

and

$$s h_{\mathbf{k},s} = w_{\mathbf{k},s}(0) \quad \text{and} \quad \frac{\partial^2 w_{\mathbf{k},s}}{\partial z^2}(0) = -k^2 w_{\mathbf{k},s}(0).$$

Following Tadrict et al. [86], the solution to this differential equation can be expressed as,

$$w_{\mathbf{k},s} = [-\gamma_k e^{\sqrt{1+2s/\gamma_k} k z} + (s + \gamma_k) e^{kz}] h_{\mathbf{k},s},$$

provided that  $h_{\mathbf{k},s}$  satisfies

$$f_k(s) h_{\mathbf{k},s} + \frac{2\Gamma_{80 g k}}{i\Omega^2} (h_{\mathbf{k},s-2i} - h_{\mathbf{k},s+2i}) + \frac{2\Gamma_{40 g k}}{i\Omega^2} (h_{\mathbf{k},s-i} e^{i\Delta\phi} - h_{\mathbf{k},s+i} e^{-i\Delta\phi}) + \Pi_{\mathbf{k},s} = 0, \quad (4.10)$$

for the transformed free surface  $h_{\mathbf{k},s}$ . Furthermore,

$$f_k(s) = (s + \gamma_k)^2 - \gamma_k^{3/2} \sqrt{\gamma_k + 2s} + \omega_k^2.$$

This function and all its derivatives obey  $f_k(\bar{z}) = \overline{f_k(z)}$  where the overline denotes complex conjugation. The last term of equation (4.10) describes the transformed pressure distribution from droplet's impact  $\Pi_{\mathbf{k},s} = (4k/\Omega^2 \rho) P_{\mathbf{k},s}^{\text{ext}}$ . Using the definition of the Fourier Transform and the assumption of uniform pressure distribution during contact with  $wk \ll 1$  we get,  $P_{\mathbf{k},s}^{\text{ext}} = P^{\text{ext}}(s) \int_0^w J_0(kr) r dr \approx F_N(s)/2\pi$  with  $r = \sqrt{x^2 + y^2}$ . Hence we obtain

$$\Pi_{\mathbf{k},s} = \frac{2k}{\pi\Omega^2 \rho} F_N(s), \quad (4.11)$$

where  $P^{\text{ext}}(s)$  and  $F_N(s)$  are the Laplace transforms of  $P^{\text{ext}}(\tau)$  and  $F_N(\tau)$  respectively. We note that equation (4.10) reduces to equation (2.2) of Tadrict et al. [86] on setting  $\Gamma_{40} = 0$ , with the caveat that our driving is a sine function while Tadrict et al. [86] use a cosine. We have chosen a sine function for driving for the sake of consistency with the experiments results presented in the Chapter 3.

We first consider Faraday waves in the absence of external pressure perturbations, which reduces equation (4.10) to

$$f_k(s)h_{\mathbf{k},s} + \frac{2\Gamma_{80}gk}{i\Omega^2}(h_{\mathbf{k},s-2i} - h_{\mathbf{k},s+2i}) + \frac{2\Gamma_{40}gk}{i\Omega^2}(h_{\mathbf{k},s-i}e^{i\Delta\phi} - h_{\mathbf{k},s+i}e^{-i\Delta\phi}) = 0. \quad (4.12)$$

Due to the periodic driving of the system, a Floquet ansatz is appropriate in the time domain. The form we assume and its corresponding Laplace transform are given by [94]

$$h_{\mathbf{k}}(\tau) = \sum_{l=-\infty}^{\infty} h_{\mathbf{k}}^{(l)} e^{il\tau} e^{\delta_k \tau} \quad \text{and} \quad h_{\mathbf{k},s} = \sum_{l=-\infty}^{\infty} \frac{h_{\mathbf{k}}^{(l)}}{s - il - \delta_k}. \quad (4.13)$$

Here  $\delta_k$  is a complex perturbation whose real part vanishes when the Faraday instability threshold is reached. Substituting this form into (4.12), we obtain

$$\sum_{l=-\infty}^{\infty} h_{\mathbf{k}}^{(l)} \left[ \frac{f_k(s)}{s - il - \delta_k} - i\Gamma_{80}\beta_k \left( \frac{1}{s - i(l+2) - \delta_k} - \frac{1}{s - i(l-2) - \delta_k} \right) - i\Gamma_{40}\beta_k \left( \frac{1}{s - i(l+1) - \delta_k} e^{i\Delta\phi} - \frac{1}{s - i(l-1) - \delta_k} e^{-i\Delta\phi} \right) \right] = 0,$$

with  $\beta_k = 2gk/\Omega^2$ . Using the Heaviside cover-up method [95] yields an infinite dimensional linear system  $\mathbf{A}\mathbf{h} = \mathbf{0}$  coupling the Floquet components together [82, 96, 94, 86]. Here  $\mathbf{A}$  is the pentadiagonal matrix

$$\mathbf{A} = \begin{bmatrix} \ddots & & & & & & & \\ \ddots & f_k(-2i + \delta_k) & \Upsilon_k & \alpha_k & 0 & 0 & \dots \\ \ddots & \bar{\Upsilon}_k & f_k(-1i + \delta_k) & \Upsilon_k & \alpha_k & 0 & \dots \\ \dots & \bar{\alpha}_k & \bar{\Upsilon}_k & f_k(\delta_k) & \Upsilon_k & \alpha_k & \dots \\ \dots & 0 & \bar{\alpha}_k & \bar{\Upsilon}_k & f_k(1i + \delta_k) & \Upsilon_k & \ddots \\ \dots & 0 & 0 & \bar{\alpha}_k & \bar{\Upsilon}_k & f_k(2i + \delta_k) & \ddots \\ \dots & \vdots & \vdots & \vdots & \ddots & \ddots & \ddots \end{bmatrix},$$

with  $\alpha_k = i\Gamma_{80}\beta_k$  and  $\Upsilon_k = i\Gamma_{40}\beta_k e^{-i\Delta\phi}$ , and  $\mathbf{h}$  is a vector of the Floquet components  $h_{\mathbf{k}}^{(l)}$ . To obtain non-trivial solutions of this linear system requires

$$\det(\mathbf{A}) = 0. \quad (4.14)$$

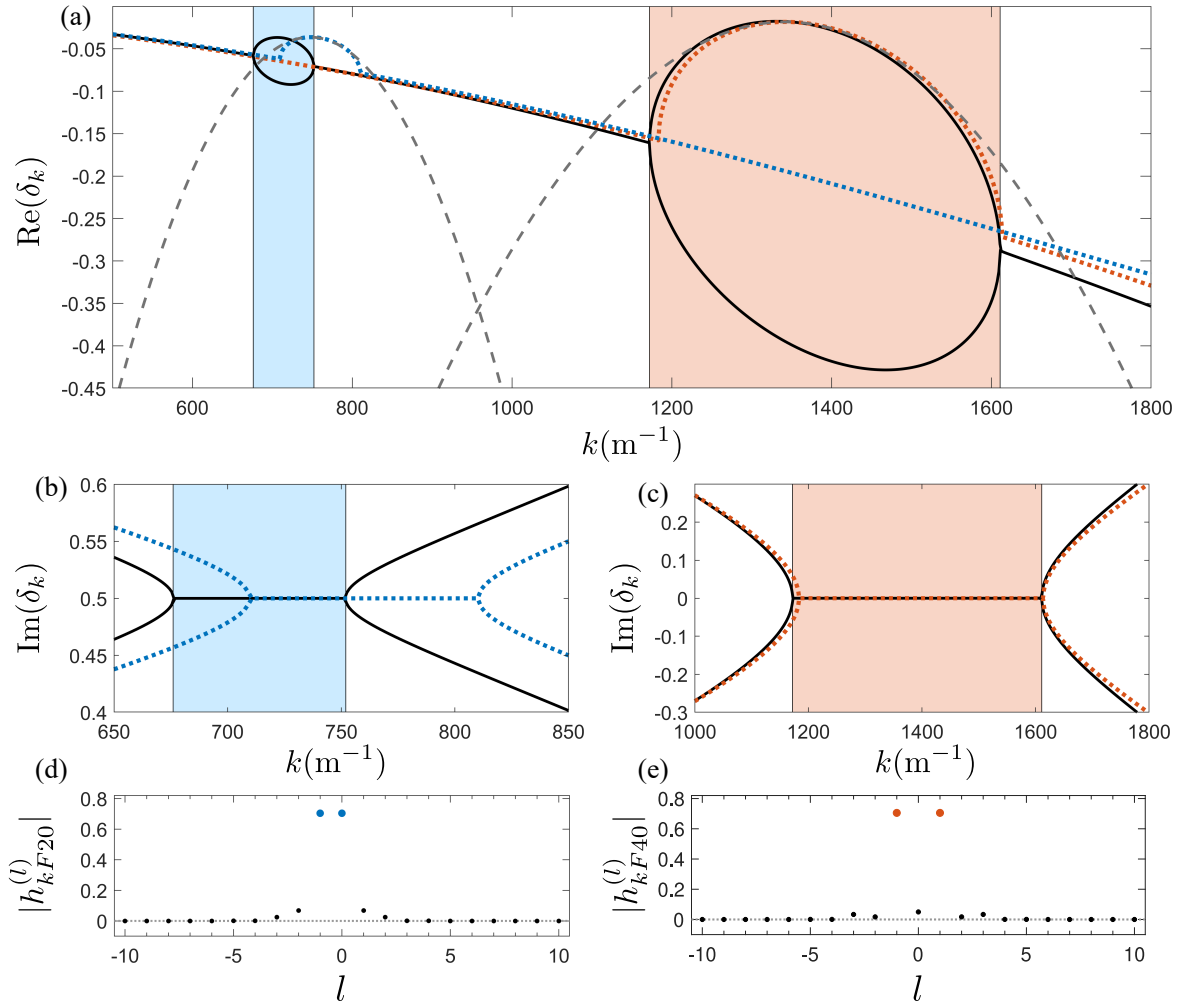


Figure 4.1 : Properties of two-frequency, damped Faraday waves. (a) Decay rate  $\text{Re}(\delta_k)$  as a function of wavenumber  $k$  for  $\Gamma_{80} = 3.8$ ,  $\Gamma_{40} = 0.6$  and  $\Delta\phi = 130^\circ$  using a 21-mode truncation corresponding to  $|l| \leq 10$  (solid black curve). The blue and red dotted curves show the decay rate of the slowly decaying wave using the two-mode approximation  $\text{Re}(\delta_{k20}^+)$  in the blue Faraday window and the two-mode approximation  $\text{Re}(\delta_{k40}^+)$  in the red Faraday window respectively. The grey dashed curves are second-order approximations to these decay rates at the peak values in each Faraday window. Panels (b) and (c) show the dispersion relation  $\text{Im}(\delta_k)$  in the two Faraday windows. In (d) and (e), the magnitude of the amplitudes  $h_{kF40}^{(l)}$  and  $h_{kF20}^{(l)}$  of the different modes  $l$  are shown at the most unstable wavenumbers in each Faraday window using the 21-mode truncation, with the dominant modes coloured. These correspond to the eigenvectors of  $\mathbf{A}\mathbf{h} = \mathbf{0}$  with eigenvalue 0. Note that these amplitudes only yield information about the relative values of each mode.

### 4.3.1 Decay rate of damped Faraday waves

Solving equation (4.14) for fixed  $\Gamma_{80}$ ,  $\Gamma_{40}$  and  $\Delta\phi$ , we obtain  $\delta_k$  as a function of the wavenumber  $k$ . Below the Faraday instability threshold, this corresponds to a decay rate for the waves  $\text{Re}(\delta_k)$  and a dispersion relation  $\text{Im}(\delta_k)$ . Results for typical parameter values of superwalkers are shown in figure 4.1. Figure 4.1(a) shows the numerically converged  $\text{Re}(\delta_k)$  as a function of  $k$  (solid curves). We see two different Faraday windows, one in which the waves are locked at  $\text{Im}(\delta_k) = 1/2$  (the blue-shaded region in figures 4.1(a) and (b)) and one in which waves are locked at  $\text{Im}(\delta_k) = 0$  (the red-shaded region in figures 4.1(a) and (c)). In each of these windows, we see two different branches for the decay rate  $\text{Re}(\delta_k)$ , an upper branch corresponding to a slowly decaying wave and a lower branch corresponding to a more rapidly decaying wave.

To obtain analytical forms of these results, we truncate the infinite dimensional matrix equation to a few dominant modes. For the  $\text{Im}(\delta_k) = 0$  (red) Faraday window in figure 4.1(a), we find that the dominant contribution to the amplitude is from the two modes with  $l = \pm 1$  (see figure 4.1(e)) corresponding to a frequency of  $\pm 40$  Hz. Denoting the decay rate in this Faraday window by  $\text{Re}(\delta_{k40})$  and using this two-mode approximation, equation (4.14) reduces to

$$f_k(-i + \text{Re}(\delta_{k40}))f_k(i + \text{Re}(\delta_{k40})) - |\alpha_k|^2 = 0.$$

We can obtain a good approximation to this decay rate by following an approach similar to Section 2.2.2 of Tadrst et al. [86] and expanding the function  $f_k(\pm i + \text{Re}(\delta_{k40}))$  to second order in the small decay rate  $\text{Re}(\delta_{k40})$  to get

$$\text{Re}(\delta_{k40}^\pm) = -\frac{b_k(i)}{2a_k(i)} \left( 1 \mp \sqrt{1 - \frac{4a_k(i)c_k(i, \alpha_k)}{b_k^2(i)}} \right), \quad (4.15)$$

where the functions

$$\begin{aligned} a_k(u) &= \dot{f}_k(u)\dot{f}_k(-u) + \frac{1}{2}\ddot{f}_k(u)f_k(-u) + \frac{1}{2}\ddot{f}_k(-u)f_k(u), \\ b_k(u) &= \dot{f}_k(u)f_k(-u) + \dot{f}_k(-u)f_k(u), \\ c_k(u, Z) &= f_k(u)f_k(-u) - |Z|^2. \end{aligned}$$

Here  $\text{Re}(\delta_{k40}^+)$  and  $\text{Re}(\delta_{k40}^-)$  correspond to the decay rates of the slowly and quickly decaying wave respectively. This approximation for the slowly decaying wave  $\text{Re}(\delta_{k40}^+)$  is shown as a red, dotted curve in figure 4.1(a). We can further approximate this decay

rate near the most unstable wavenumber  $k_{F40}$  by

$$\text{Re}(\delta_{k40}^+) \approx \text{Re}(\delta_{F40}^+) - D_{40}(k - k_{F40})^2, \quad (4.16)$$

where  $\text{Re}(\delta_{F40}^+) = \lim_{k \rightarrow k_{F40}} \text{Re}(\delta_{k40}^+)$  and  $D_{40} = -\frac{1}{2}d^2\text{Re}(\delta_{k40}^+)/dk^2|_{k=k_{F40}}$  is the diffusion coefficient, both of which can be calculated from equation (4.15). This approximation of  $\text{Re}(\delta_{k40}^+)$  is shown as a grey, dashed curve in figure 4.1(a).

We follow a similar approach to obtain an analytical expression for the decay rate in the  $\text{Im}(\delta_k) = 1/2$  (blue) Faraday window in figure 4.1(a). In this window, the dominant contribution is from the  $l = -1$  and  $0$  modes (see figure 4.1(d)), corresponding to frequencies  $\pm 20$  Hz. Using this two-mode approximation and denoting the decay rate by  $\text{Re}(\delta_{k20})$ , equation (4.14) reduces to

$$f_k(-i/2 + \text{Re}(\delta_{k20}))f_k(i/2 + \text{Re}(\delta_{k20})) - |\Upsilon_k|^2 = 0.$$

A good approximation for this decay rate is obtained by expanding the function  $f_k(\pm i/2 + \text{Re}(\delta_{k20}))$  to second order, giving us

$$\text{Re}(\delta_{k20}^\pm) = -\frac{b_k(i/2)}{2a_k(i/2)} \left( 1 \mp \sqrt{1 - \frac{4a_k(i/2)c_k(i/2, \Upsilon_k)}{b_k^2(i/2)}} \right), \quad (4.17)$$

where  $\text{Re}(\delta_{k20}^+)$  and  $\text{Re}(\delta_{k20}^-)$  correspond to the decay rates of the slowly and quickly decaying wave respectively. We can further approximate  $\text{Re}(\delta_{k20}^+)$  near the most unstable wavenumber  $k_{F20}$  by

$$\text{Re}(\delta_{k20}^+) \approx \text{Re}(\delta_{F20}^+) - D_{20}(k - k_{F20})^2, \quad (4.18)$$

where  $\text{Re}(\delta_{F20}^+) = \lim_{k \rightarrow k_{F20}} \text{Re}(\delta_{k20}^+)$  and  $D_{20} = -\frac{1}{2}d^2\text{Re}(\delta_{k20}^+)/dk^2|_{k=k_{F20}}$  is the diffusion coefficient corresponding to this Faraday window. These approximations of  $\text{Re}(\delta_{k20}^+)$  from equations (4.17) and (4.18) are shown in figure 4.1(a) as a blue dotted and a grey dashed curve respectively.

### 4.3.2 Faraday instability thresholds

When  $\text{Re}(\delta_k) > 0$  for any wavenumber  $k$ , growing Faraday waves are predicted. For two-frequency driving at  $f$  and  $f/2$ , either  $f/2$  Faraday waves or  $f/4$  Faraday waves can emerge depending on the relative strength of the acceleration amplitudes and the phase difference [? 53]. The marginal stability curves representing the acceleration amplitudes

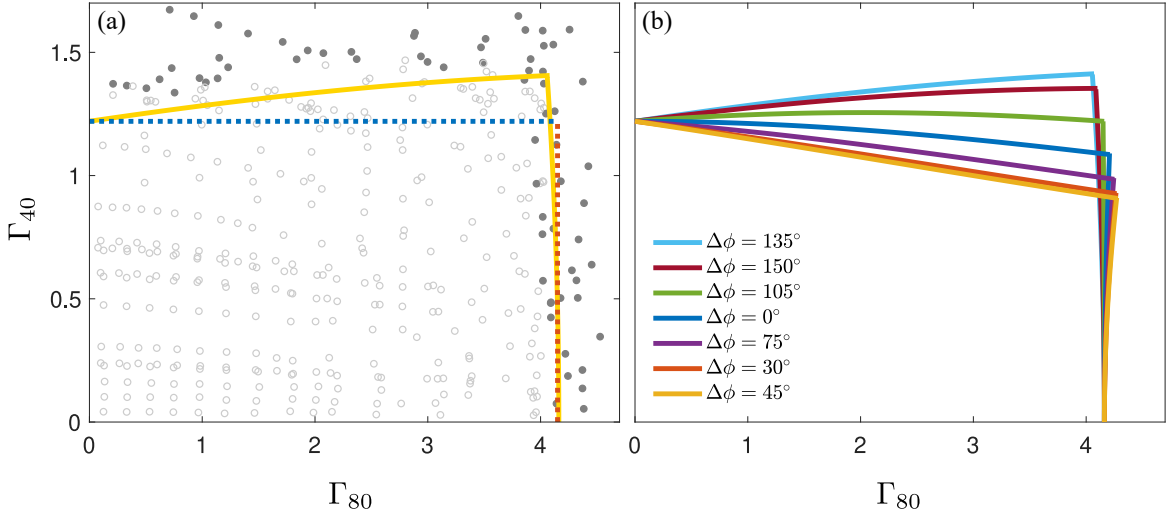


Figure 4.2 : Faraday threshold curves for two-frequency driving. (a) Comparison of the Faraday threshold curves for  $\Delta\phi = 130^\circ$  obtained using 21 modes (solid yellow curves) and using the two-mode approximations (dotted curves) together with the experimental results (circles) presented in figure 3.6. For the latter, empty circles indicate that flat liquid surfaces were observed while filled circles indicate that Faraday waves were observed. (b) Faraday thresholds for different values of the phase difference  $\Delta\phi$  using a 21-mode calculation.

at onset of Faraday waves,  $\Gamma_{F80}$  and  $\Gamma_{F40}$ , can be found by setting  $\text{Re}(\delta_k) = 0$  when solving equation (4.14). From figure 4.1(a), we see two Faraday windows where  $\text{Re}(\delta_k)$  can potentially cross zero corresponding to either the  $f/2$  instability of frequency 40 Hz or the  $f/4$  instability of frequency 20 Hz. Figure 4.2(a) shows the comparison of the numerically converged marginal stability curve obtained using a 21-mode truncation (yellow solid curve) and the two-mode approximation for the 20 Hz (blue dashed curve) and 40 Hz (red dashed curve) Faraday waves, with the experimental results from Chapter 4 (circles). Figure 4.2(b) shows the numerically converged marginal stability curves at different phase differences  $\Delta\phi$ . We note that changes in  $\Delta\phi$  cause appreciable changes in the 20 Hz Faraday threshold.

### 4.3.3 Amplitude and phase shift of damped Faraday waves

In figures 4.1(d) and (e), the relative amplitudes of the Floquet modes are shown for the slowest decaying modes in the 20 Hz and 40 Hz Faraday windows respectively. We now turn to calculating these amplitudes for our reduced-mode approximations and use these to obtain expressions for the wave profile generated by a single bounce of a droplet.

Using the two-mode approximation for the 40 Hz window, we can write the Floquet ansatz in equation (4.13) as

$$h_{\mathbf{k}}(\tau) \approx \left( h_k^{(-1)} e^{-i\tau} + h_k^{(1)} e^{i\tau} \right) e^{\delta_k \tau}, \quad (4.19)$$

and the infinite dimensional linear system  $\mathbf{A}\mathbf{h} = \mathbf{0}$  reduces to a  $2 \times 2$  matrix system  $\mathbf{A}_2 \mathbf{h}_2 = \mathbf{0}$ . Since the determinant of the matrix  $\mathbf{A}_2$  is zero, we obtain the amplitudes  $\mathbf{h}_2$  from the null space vector, which gives  $h_k^{(-1)} = c \xi_{40}^\pm$  with  $\xi_{40}^\pm = i\sqrt{\alpha_k/f_k(-i + \delta_{k40}^\pm)}$  and  $h_k^{(1)} = \overline{h_k^{(-1)}}$ , where  $c$  is a free parameter. Substituting this solution into equation (4.19) and using  $\text{Im}(\delta_{k40}^\pm) = 0$  in this window, we obtain the wave forms

$$h_{\mathbf{k}40}^\pm(\tau) = c \left[ \xi_{40}^\pm e^{-i\tau} + \bar{\xi}_{40}^\pm e^{i\tau} \right] e^{\text{Re}(\delta_{k40}^\pm)\tau}.$$

Thus, the total wave field in this Faraday window can be represented as

$$h_{\mathbf{k}40}(\tau) = \zeta_{40}^+ e^{\text{Re}(\delta_{k40}^+)\tau} \cos(\tau + \theta_{k40}^+) + \zeta_{40}^- e^{\text{Re}(\delta_{k40}^-)\tau} \cos(\tau + \theta_{k40}^-), \quad (4.20)$$

where

$$\theta_{k40}^\pm = \arctan \left( \frac{-\text{Im}(\xi_{40}^\pm)}{\text{Re}(\xi_{40}^\pm)} \right). \quad (4.21)$$

and  $\zeta_{40}^\pm = 2c|\xi_{40}^\pm|$ . These equations (4.21) and (4.20) are equivalent to equations (2.47) and (2.48) of Tadrict et al. [86]. Similar to Section 2.3 of Tadrict et al. [86], we now continue by modelling the temporal profile of a droplet's impact by a delta function. The corresponding pressure and force exerted by the droplet on the liquid is then

$$\Pi_{\mathbf{k}}(\tau) = (2k/\pi\Omega^2\rho)F_N(\tau) = \delta(\tau - \tau_i)v_{\mathbf{k}}. \quad (4.22)$$

By integrating the time domain version of equation (4.10) across the delta kick, we find that  $v_{\mathbf{k}}$  corresponds to negative change of velocity of  $h_{\mathbf{k}}$  following impact. If the surface is perfectly flat and at rest before the impact, the wave profile is axisymmetric i.e.  $h_{\mathbf{k}}(\tau) = h_k(\tau)$ . Using the initial conditions as  $\tau \rightarrow \tau_i$  that  $h_{\mathbf{k}} = 0$  and  $\frac{\partial h_{\mathbf{k}}}{\partial \tau} = -v_{\mathbf{k}}$  we get  $\zeta_{40}^\pm = v_k \alpha_{40}^\pm$ , where

$$\alpha_{40}^\pm = \frac{-2 \cos(\tau_i + \theta_{k40}^\mp) e^{-\text{Re}(\delta_{k40}^\pm)\tau_i}}{(\text{Re}(\delta_{k40}^\pm) - \text{Re}(\delta_{k40}^\mp))(\cos(2\tau_i + \theta_{k40}^\pm + \theta_{k40}^\mp) + \cos(\theta_{k40}^\pm - \theta_{k40}^\mp)) - 2 \sin(\theta_{k40}^\pm - \theta_{k40}^\mp)}.$$

Taking a similar approach, we can obtain an equation for the wave field by using the two-mode approximation in the 20 Hz Faraday window. The two-mode approximation

of equation (4.13) gives

$$h_{\mathbf{k}20}^{\pm}(\tau) = (h_k^{(-1)} e^{-i\tau/2} + h_k^{(0)} e^{i\tau/2}) e^{\text{Re}(\delta_{k20}^{\pm})\tau}.$$

Solving for the null space of the matrix equation we get  $h_k^{(-1)} = c\xi_{20}^{\pm}$  with  $\xi_{20}^{\pm} = i\sqrt{\Upsilon_k/f_k(-i/2 + \text{Re}(\delta_{k20}^{\pm}))}$  and  $h_k^{(0)} = \overline{h_k^{(-1)}}$ , where  $c$  is a free parameter. For this we obtain the amplitudes

$$h_{\mathbf{k}20}^{\pm}(\tau) = c(\xi_{20}^{\pm} e^{-i\tau/2} + \bar{\xi}_{20}^{\pm} e^{i\tau/2}) e^{\text{Re}(\delta_{k20}^{\pm})\tau}.$$

Hence, we can express the total wave field for this Faraday window as

$$h_{\mathbf{k}20}(\tau) = \zeta_{20}^+ e^{\text{Re}(\delta_{k20}^+) \tau} \cos(\tau/2 + \theta_{k20}^+) + \zeta_{20}^- e^{\text{Re}(\delta_{k20}^-) \tau} \cos(\tau/2 + \theta_{k20}^-), \quad (4.23)$$

where

$$\theta_{k20}^{\pm} = \arctan\left(\frac{-\text{Im}(\xi_{20}^{\pm})}{\text{Re}(\xi_{20}^{\pm})}\right). \quad (4.24)$$

Using the same initial conditions as for 40 Hz waves we get  $\zeta_{20}^{\pm} = v_k \alpha_{20}^{\pm}$ , where

$$\alpha_{20}^{\pm} = \frac{-2 \cos(\tau_i/2 + \theta_{k20}^{\mp}) e^{-\text{Re}(\delta_{k20}^{\pm})\tau_i}}{(\text{Re}(\delta_{k20}^{\pm}) - \text{Re}(\delta_{k20}^{\mp}))(\cos(\tau_i + \theta_{k20}^{\pm} + \theta_{k20}^{\mp}) + \cos(\theta_{k20}^{\pm} - \theta_{k20}^{\mp})) - 2 \sin(\theta_{k20}^{\pm} - \theta_{k20}^{\mp})}.$$

#### 4.3.4 Wave field of a superwalker

For late times after the impact,  $\tau \gg \tau_i$ , and when the acceleration amplitudes are close to their respective Faraday thresholds,  $\Gamma_{80} \lesssim \Gamma_{F80}$  and  $\Gamma_{40} \lesssim \Gamma_{F40}$ , the wave field is dominated by the slowly decaying Faraday waves from both the 40 Hz and 20 Hz modes. Hence, we can approximate the final wave field generated by the impact of the droplet as

$$h_{\mathbf{k}}(\tau) = \alpha_{40}^+ v_k e^{\text{Re}(\delta_{k40}^+) \tau} \cos(\tau + \theta_{k40}^+) + \alpha_{20}^+ v_k e^{\text{Re}(\delta_{k20}^+) \tau} \cos(\tau/2 + \theta_{k20}^+).$$

Transforming back to the spatial domain with an inverse Fourier transform yields

$$h(x, y, \tau) = \frac{1}{2\pi} \int_0^{\infty} \int_0^{\infty} h_{\mathbf{k}}(\tau) \exp[i(k_x x + k_y y)] dk_x dk_y.$$

Since the wave profile is radially symmetric, the above inverse Fourier transform reduces to an inverse Hankel transform,

$$h(x, y, \tau) = \int_0^\infty h_{\mathbf{k}}(\tau) J_0(kr) k dk.$$

Hence the wave profile in the real space is given by

$$\begin{aligned} h(x, y, \tau) &= \int_0^\infty B_{k40}^+ v_k e^{\operatorname{Re}(\delta_{k40}^+)(\tau - \tau_i)} \cos(\tau + \theta_{k40}^+) J_0(kr) k dk \\ &+ \int_0^\infty B_{k20}^+ v_k e^{\operatorname{Re}(\delta_{k20}^+)(\tau - \tau_i)} \cos(\tau/2 + \theta_{k20}^+) J_0(kr) k dk, \end{aligned}$$

where  $B_{k40}^+ = \alpha_{40}^+ e^{\operatorname{Re}(\delta_{k40}^+) \tau_i}$  and  $B_{k20}^+ = \alpha_{20}^+ e^{\operatorname{Re}(\delta_{k20}^+) \tau_i}$ . Using the second order expansion for  $\operatorname{Re}(\delta_{k40}^+)$  and  $\operatorname{Re}(\delta_{k20}^+)$  in equations (4.16) and (4.18), we get the following approximation to the above integral in the limit  $\tau \rightarrow \infty$  (for details see Appendix C of [86])

$$\begin{aligned} h(x, y, \tau) &= \tilde{A}_{40}^{(0)}(\tau_i) \frac{\cos(\tau + \theta_{F40}^+)}{\sqrt{\tau - \tau_i}} J_0(k_{F40} |\mathbf{x} - \mathbf{x}_i|) \exp \left[ -\frac{\tau - \tau_i}{2\pi \operatorname{Me}_{40}} - \frac{|\mathbf{x} - \mathbf{x}_i|^2}{4D_{40}(\tau - \tau_i)} \right] \\ &+ \tilde{A}_{20}^{(0)}(\tau_i) \frac{\cos(\tau/2 + \theta_{F20}^+)}{\sqrt{\tau - \tau_i}} J_0(k_{F20} |\mathbf{x} - \mathbf{x}_i|) \exp \left[ -\frac{\tau - \tau_i}{2\pi \operatorname{Me}_{20}} - \frac{|\mathbf{x} - \mathbf{x}_i|^2}{4D_{20}(\tau - \tau_i)} \right], \end{aligned}$$

where  $\mathbf{x}_i$  is the location of the impact and the memory parameters  $\operatorname{Me}_{40}$  and  $\operatorname{Me}_{20}$  are given by  $\operatorname{Me}_{40} = -1/2\pi \operatorname{Re}(\delta_{F40}^+)$  and  $\operatorname{Me}_{20} = -1/2\pi \operatorname{Re}(\delta_{F20}^+)$ . Furthermore,

$$\tilde{A}_{40}^{(0)} = k_{F40} \sqrt{\frac{\pi}{D_{40}}} v_k B_{F40}^+(\tau_i) \text{ and } \tilde{A}_{20}^{(0)} = k_{F20} \sqrt{\frac{\pi}{D_{20}}} v_k B_{F20}^+(\tau_i).$$

To include a finite contact time, we follow the suggestion in Tadrst et al. [86] of using Duhamel's principle and the approach used in Appendix A.4 of Moláček and Bush [85], and integrate the impulse response with a time varying impact signal  $\Pi_{\mathbf{k}}(\tau)$ . This results in replacing the amplitude coefficients  $\tilde{A}_{40}^{(0)}$  and  $\tilde{A}_{20}^{(0)}$  by

$$\begin{aligned} \tilde{A}_{40} &= k_{F40} \sqrt{\frac{\pi}{D_{40}}} \int_{\tau_n^i}^{\tau_n^c} B_{F40}^+(\tau') \Pi_{\mathbf{k}}(\tau') d\tau', \\ \tilde{A}_{20} &= k_{F20} \sqrt{\frac{\pi}{D_{20}}} \int_{\tau_n^i}^{\tau_n^c} B_{F20}^+(\tau') \Pi_{\mathbf{k}}(\tau') d\tau'. \end{aligned}$$

We change the dimensionless time  $\tau$  back to dimensional time  $t$  and replace  $\Pi_{\mathbf{k}}(t)$  by  $(2k/\pi\Omega^2\rho)F_N(t)$  using equation (4.11). We also replace the initial contact time  $t_i$  and

location of contact  $\mathbf{x}_i$  by their weighted average values  $t_n$  and  $\mathbf{x}_n$  as given in equation (2.9), and replace the dimensionless amplitudes  $\tilde{A}_{40}$  and  $\tilde{A}_{20}$  by  $A_{40} = \sqrt{2/\Omega}\tilde{A}_{40}$  and  $A_{20} = \sqrt{2/\Omega}\tilde{A}_{20}$  giving us

$$\begin{aligned} A_{40} &= \sqrt{\frac{2\pi}{\Omega^3 D_{40}} \frac{k_{F40}^2}{\pi\rho}} \int_{t_n^i}^{t_n^c} B_{F40}^+(t') F_N(t') dt', \\ A_{20} &= \sqrt{\frac{2\pi}{\Omega^3 D_{20}} \frac{k_{F20}^2}{\pi\rho}} \int_{t_n^i}^{t_n^c} B_{F20}^+(t') F_N(t') dt', \end{aligned} \quad (4.25)$$

and results in the wave field equation,

$$\begin{aligned} h_n^{(\text{SW})}(\mathbf{x}, t) &= A_{40} \frac{\cos(\Omega t/2 + \theta_{F40}^+)}{\sqrt{t - t_n}} J_0(k_{F40}|\mathbf{x} - \mathbf{x}_n|) \exp\left[-\frac{t - t_n}{T_F \text{Me}_{40}} - \frac{T_F |\mathbf{x} - \mathbf{x}_n|^2}{8\pi D_{40}(t - t_n)}\right] \\ &+ A_{20} \frac{\cos(\Omega t/4 + \theta_{F20}^+)}{\sqrt{t - t_n}} J_0(k_{F20}|\mathbf{x} - \mathbf{x}_n|) \exp\left[-\frac{t - t_n}{T_F \text{Me}_{20}} - \frac{T_F |\mathbf{x} - \mathbf{x}_n|^2}{8\pi D_{20}(t - t_n)}\right]. \end{aligned} \quad (4.26)$$

The interpretation of equation (4.26) is that a droplet bouncing under the prescribed two-frequency driving excites two dominant waves at wavenumbers  $k_{F40}$  and  $k_{F20}$ , corresponding to frequencies of 40 Hz and 20 Hz. These waves decay in time at rates  $\text{Re}(\delta_{F40}^+)$  and  $\text{Re}(\delta_{F20}^+)$ , which determine the corresponding memory parameters  $\text{Me}_{40} = -1/2\pi\text{Re}(\delta_{F40}^+)$  and  $\text{Me}_{20} = -1/2\pi\text{Re}(\delta_{F20}^+)$ . The waves also spread diffusively with diffusion coefficients  $D_{40}$  and  $D_{20}$  and have phase shifts  $\theta_{F40}^+$  and  $\theta_{F20}^+$ .

### 4.3.5 Comparison of a superwalker and a walker wave field

Comparing the superwalker wave field in equation (4.26) to that of a walker derived by Tadrict et al. [86] and presented in equation (2.10) leads to two key observations: (i) both models have a wave at frequency  $f/2 = 40$  Hz. We note that Tadrict et al. [86] derived equation (2.10) by considering a cosine form of driving while we have considered a sine form of driving to be consistent with our experiments. This results in a constant shift of  $\pi/4$  in the phase shift  $\theta_F^+$  in equation (2.10) which has been taken into account when comparing results. (ii) An additional wave of frequency  $f/4 = 20$  Hz appears in the wave field of a superwalker. However, in the region of  $(\Gamma_{80}, \Gamma_{40})$  parameter space where superwalking is realised, typically the amplitude of the 40 Hz wave,  $A_{40}$ , is 4 to 8 times that of the 20 Hz wave,  $A_{20}$ . Thus in general, our new two-frequency wave model is not appreciably different from the single-frequency model of Tadrict et al. [86]. This

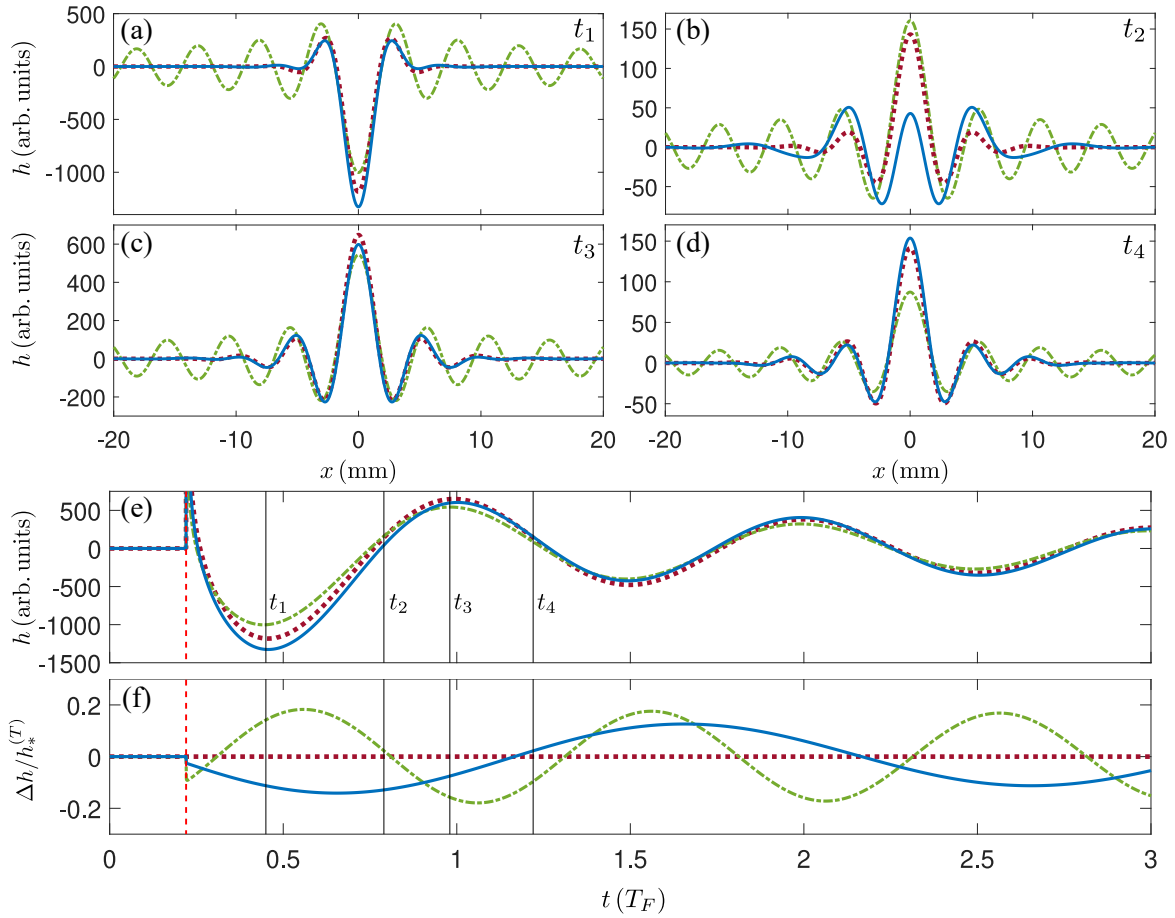


Figure 4.3 : Comparison of the wave fields generated by an instantaneous impact at  $x = 0$  and at time  $t_i = 0.22 T_F$  for typical superwalker parameter values. The wave fields from the Moláček and Bush [85] model (green dashed-dotted curve), Tadrst et al. [86] model (maroon dotted curve) and the superwalker model of this work (blue solid curve) are shown at times (a)  $t_1 = t_i + 0.23 T_F$ , (b)  $t_2 = t_i + 0.57 T_F$ , (c)  $t_3 = t_i + 0.76 T_F$  and (d)  $t_4 = t_i + 1.00 T_F$ . The evolution of the absolute wave height  $h$  at  $x = 0$  from an impact at  $t_i$  (vertical red dashed line) is shown in (e) and the relative wave height  $\Delta h/h_*^{(T)}$  with respect to the Tadrst et al. [86] model is shown in (f). Here  $h_*^{(T)}$  is the wave field from Tadrst et al. [86] model in (2.10) excluding the cosine term to avoid singularities in  $\Delta h/h_*^{(T)}$ , and  $\Delta h = h^{(SW)} - h^{(T)}$  or  $h^{(M)} - h^{(T)}$ . The parameters are  $\Gamma_{80} = 3.8$ ,  $\Gamma_{40} = 0.6$  and  $\Delta\phi = 130^\circ$ .

is illustrated further in figure 4.3 where the wave fields predicted using the models of Moláček and Bush [85] in equation (2.8), Tadrst et al. [86] in equation (2.10) and the superwalker wave field in equation (4.26) are shown for an instantaneous impact at time  $0.22 T_F$ , corresponding to the typical impact phase for superwalkers, with an appreciable  $\Gamma_{f/2}$  component. The waves from our new two-frequency model (4.26)

and the single-frequency [86] model (2.10) are quantitatively similar (figures 4.3(a) and (c-e)), except near times when the overall wave field is quite flat and is changing rapidly (figure 4.3(b)). The comparison with the single-frequency [85] model appears poorer, however the difference is primarily in the far-field and arises from the absence of diffusive spatial decay in this model. In the near-field region of primary interest for walking, all three models are quantitatively similar with a maximum relative error of around 20% as shown in figures 4.3(e) and (f). Moreover, as shown in figure 4.3(f), the relative height difference at the impact location between the waves of Moláček and Bush [85] model and Tadríst et al. [86] model is sinusoidal due to the added phase shift of  $\theta_F^+ \approx -4^\circ$  in the Tadríst et al. [86] model for the chosen parameters in figure 4.3, and the relative height difference at the impact location between the superwalker wave and that of Tadríst et al. [86] reveals the added 20 Hz wave in the superwalker wave field. Overall these results suggest that the wave fields observed for two-frequency and single-frequency driving remain very similar, an observation that we made qualitatively from experimental images of superwalkers' wave field in Chapter 3. We present results using our new two-frequency model, but note that results using either the Moláček and Bush [85] model or the Tadríst et al. [86] model are comparable; we provide details in Section 4.5.4.

## 4.4 Numerical method and parameter values

As observed in experiments, solitary superwalkers walk at a constant speed in straight line trajectories. Hence to simulate a superwalker, we proceed by restricting the domain of horizontal motion to the  $x$  direction only. To solve this system numerically, we discretise equations (2.1) and (2.11) using the Leap-frog method [97], a modified version of the Euler method where the new horizontal and vertical positions are calculated using the old velocities and then the new velocities are calculated using the new positions. Converting the second order differential equation for the vertical dynamics in equation (2.1) into a system of two first order ordinary differential equations and discretising using the Leap-frog method we get,

$$z_d(t_{i+1}) = z_d(t_i) + \Delta t v_d(t_i),$$

and

$$v_d(t_{i+1}) = v_d(t_i) + \frac{\Delta t}{m} [-m(g + \gamma(t_{i+1})) + F_N(t_{i+1})],$$

where  $v_d(t) = \dot{z}_d(t)$ , and

$$F_N(t_{i+1}) = H(-\bar{z}_d(t_{i+1})) \max(-k\bar{z}_d(t_{i+1}) - b\bar{v}_d(t_i), 0).$$

Here  $\bar{z}_d(t_{i+1}) = z_d(t_{i+1}) - h(x_d(t_{i+1}), t_{i+1})$  and  $\bar{v}_d(t_i) = v_d(t_i) - \frac{\partial h}{\partial t}(x_d(t_{i+1}), t_{i+1})$ . The total wave height beneath the droplet  $h(x_d(t_{i+1}), t_{i+1})$  is calculated by keeping the waves from the last 100 impacts of the droplet and discarding the earlier ones, which have typically decayed to below  $10^{-5}$  of their initial amplitude. Similarly, the second order equation (2.11) governing the horizontal dynamics takes the following form,

$$x_d(t_{i+1}) = x_d(t_i) + \Delta t u_d(t_i),$$

and

$$u_d(t_{i+1}) = u_d(t_i) + \frac{\Delta t}{m} \left[ -D_{tot}(t_{i+1})u_d(t_i) - F_N(t_{i+1}) \frac{\partial h}{\partial x}(x_d(t_{i+1}), t_{i+1}) \right],$$

where  $u_d(t) = \dot{x}_d(t)$  and  $D_{tot}(t) = D_{mom}(t) + D_{air}$ . The simulations were performed with a fixed time step of  $\Delta t = T_F/100$  and initialised with  $x_d = 0$  mm,  $u_d = 1$  mm/s,  $v_d = 0$  mm/s and six different equally spaced vertical positions  $z_d = (0, 2, 4, 6, 8, 10)R$ . Multiple initial conditions were used so that different modes existing at the same parameter values are likely to be captured.

The physical parameters were fixed to match our experiments in Chapter 3:  $\rho = 950$  kg/m<sup>3</sup>,  $\nu = 20$  cSt,  $\sigma = 20.6$  mN/m and  $f = 80$  Hz. There are three adjustable parameters in the model: the spring constant of the bath  $k_s$ , the damping coefficient of the bath  $b$  and the dimensionless contact drag coefficient  $C$ . The dimensionless parameters corresponding to  $k_s$  and  $b$  are  $K = k_s/m\omega_d^2$  and  $B = b/m\omega_d$ , where  $\omega_d = \sqrt{\sigma/\rho R^3}$  is the droplet's characteristic internal vibration frequency [57]. For walkers, appropriate values were determined by fitting to experimental data [57, 85] and typical values are  $K = 0.59$  and  $B = 0.48$  [61], and  $C = 0.17$  [85]. For superwalkers, we also set  $C = 0.17$ , but adjust  $K$  and  $B$  to best fit the available experimental data. The details of this fit are described in Appendix B. We use both constant values of  $K = 0.70$  and  $B = 0.60$ , as well as allowing the parameter  $K$  to vary with droplet radius  $R$  according to

$$K = 1.06\sqrt{\text{Bo}} + 0.37 \quad (4.27)$$

with a fixed  $B = 0.60$ , where  $\text{Bo} = \rho g R^2 / \sigma$  is the Bond number of the droplet. We refer the reader to Appendix B for more details on how this relationship was obtained.

We note that these values give a good match with our experiments; however, the qualitative behaviour of the results remains unchanged for a range of  $K$  and  $B$  values. The vertical bouncing dynamics are crucially important for the existence and characteristics of superwalkers. To describe the vertical dynamics of superwalkers, we use the bouncing modes notation introduced in Section 3.3. Moreover, to distinguish the two different styles of  $(1, 2, 1)$  bouncing,  $(1, 2, 1)^H$  and  $(1, 2, 1)^L$ , we use the method prescribed in Galeano-Rios et al. [68] and classify the droplets that have two peaks in the normal force during contact as  $(1, 2, 1)^L$  while those that have only one peak as  $(1, 2, 1)^H$ .

## 4.5 Emergence of superwalking

To illustrate the emergence of superwalking and its relationship with normal walking, we begin by describing the dynamics of a relatively small normal walker with the bath driven at a single frequency of  $f = 80$  Hz and acceleration amplitude  $\Gamma_{80} = 3.8$  (compared to a Faraday threshold  $\Gamma_{F80} = 4.15$ ). This results in a normal walker that is bouncing in a  $(2, 1)^H$  mode (see figure 4.4(a)). The  $(2, 1)$  bouncing mode is crucial for walking as the droplet is bouncing at the same frequency as the frequency of the subharmonic Faraday waves that emerge beyond the Faraday instability threshold. Thus the droplet's bouncing is in resonance with the damped Faraday waves it generates and with which it interacts. For slightly larger droplets (see figure 4.4(b)), the same  $(2, 1)^H$  bouncing mode is maintained but the height of the bounces are reduced, while for larger droplets still, the bounces reduce in height to such an extent that the droplet can no longer leap over the second peak in the bath's motion. For the chosen parameters, this results in the droplet transitioning to a chaotic bouncing mode and no longer walking (figure 4.4(c)).

In contrast, figure 4.4(d) shows the vertical dynamics of the same-sized droplet as in figure 4.4(c) with the addition of the subharmonic frequency  $f/2 = 40$  Hz and amplitude  $\Gamma_{40} = 0.6$  (compared to a Faraday threshold  $\Gamma_{F40} = 1.22$ ) at a phase difference of  $\Delta\phi = 130^\circ$ . This additional subharmonic driving raises every second peak and lowers the intermediate peaks in both the bath's and the waves' motion. This allows the bigger droplet to clear every second peak in the bath's motion and settle in a  $(1, 2, 1)^H$  bouncing mode, effectively identical to the  $(2, 1)^H$  mode for a walker, and results in the emergence of a superwalker. This jump from a walker to a superwalker is shown schematically on the speed-size curve in figure 4.4(e).

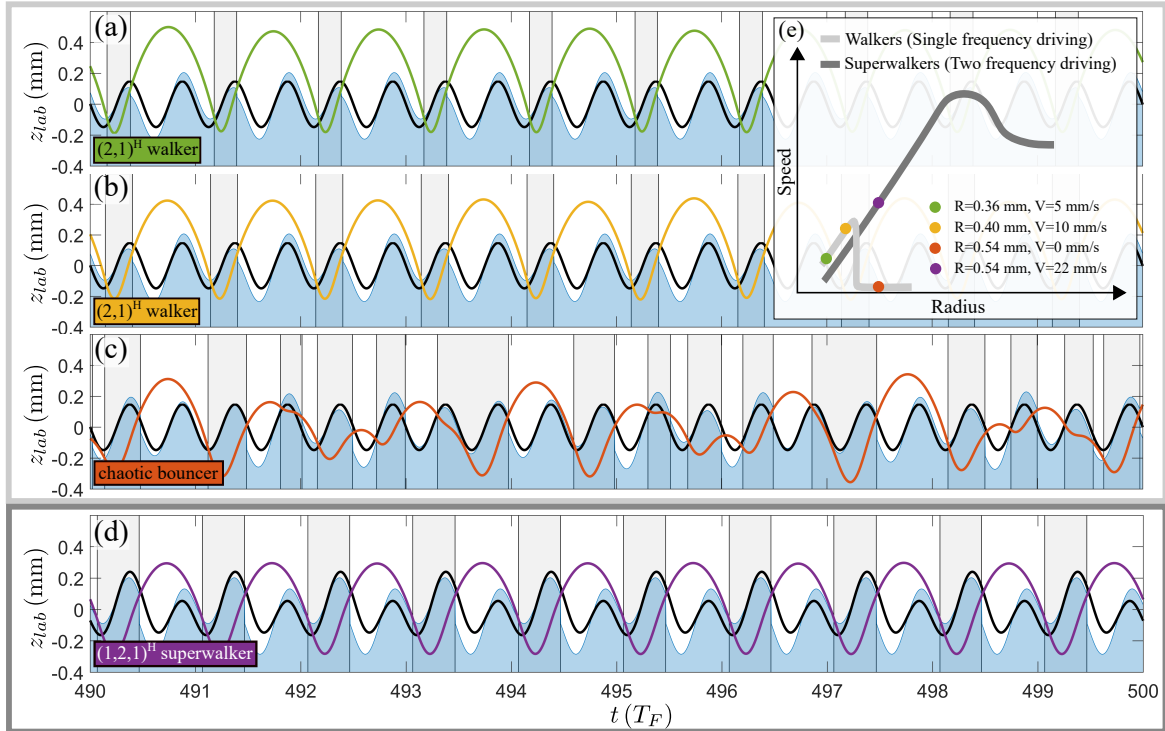


Figure 4.4 : Emergence of a superwalker. Panels (a)-(c): Vertical dynamics of a walker of radius (a)  $R = 0.36$  mm and (b)  $R = 0.40$  mm bouncing in a  $(2, 1)^H$  mode, and a bigger non-walking droplet of radius (c)  $R = 0.54$  mm bouncing in a chaotic mode. Here the bath is driven at a single frequency of  $f = 80$  Hz with acceleration amplitude  $\Gamma_{80} = 3.8$ . Panel (d): Vertical dynamics of a superwalker of radius  $R = 0.54$  mm bouncing in a  $(1, 2, 1)^H$  mode. Here the bath is driven at  $f = 80$  Hz and  $f/2 = 40$  Hz with phase difference  $\Delta\phi = 130^\circ$  and acceleration amplitudes  $\Gamma_{80} = 3.8$  and  $\Gamma_{40} = 0.6$ . In panels (a)-(d), the solid black curves indicate the bath motion,  $\mathcal{B}(t) = -(\Gamma_{fg}/\Omega^2) \sin(\Omega t) - (4\Gamma_{f/2g}/\Omega^2) \sin(\Omega t/2 + \Delta\phi)$ , the coloured curves represent the motion of the south pole of the droplet,  $z_d(t) + \mathcal{B}(t)$ , and the filled blue regions illustrate the motion of the liquid surface,  $h(\mathbf{x}_d, t) + \mathcal{B}(t)$ , all in the lab frame. The grey regions indicate times at which the droplet is in contact with the bath. Panel (e) shows a schematic of the speed-size characteristics for the droplets in panels (a)-(d). Here the values of the parameters  $K$  and  $B$  are both fixed to 0.70 and 0.60 respectively.

#### 4.5.1 Importance of the phase difference

The phase difference between the two driving frequencies controls the relative height of the two peaks in one full cycle of the periodic bath motion, equivalently two up-and-down cycles, and it is therefore a crucial parameter for the emergence of superwalking. Figure 4.5(a) shows the walking speed  $u$  as a function of the phase difference  $\Delta\phi$  for a fixed-sized droplet that is too large to walk with single-frequency driving (the largest droplet shown in figure 4.4). The different vertical modes at different  $\Delta\phi$  are shown in

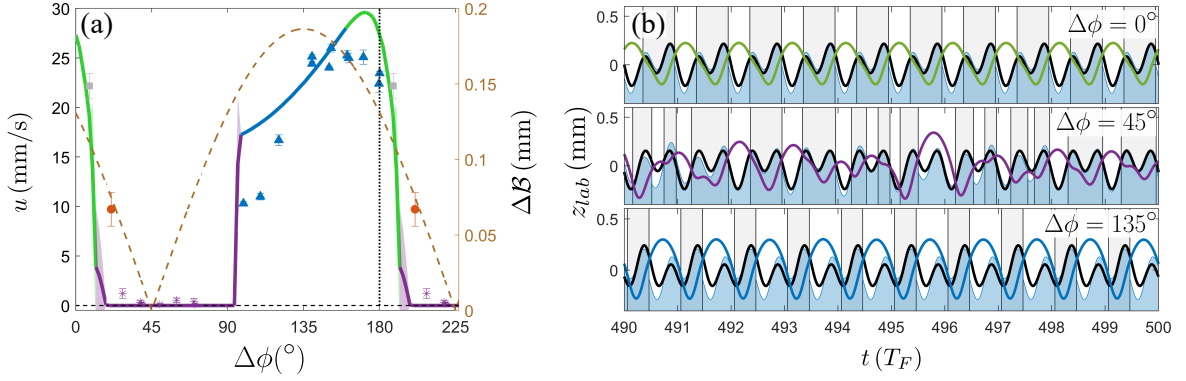


Figure 4.5 : Effect of phase difference on superwalking behaviour. (a) Walking speed  $u$  as a function of the phase difference  $\Delta\phi$  for a superwalker of radius  $R = 0.54$  mm with  $\Gamma_{80} = 3.8$  and  $\Gamma_{40} = 0.6$ . The solid curve represents results from numerical simulations with colours indicating different bouncing modes:  $(1, 2, 1)^L$  in green,  $(1, 2, 1)^H$  in blue, and chaotic in purple. The experimental results from figure 3.5(a) are shown by points, with the style of marker indicating the bouncing modes:  $(1, 2, 2)$  are red circles,  $(1, 2, 1)^H$  are blue triangles, transition between a  $(1, 2, 1)^H$  and a  $(1, 2, 2)$  mode are grey squares, and chaotic are purple asterisks. The dashed curve indicates the height difference  $\Delta\mathcal{B}$  between consecutive peaks in one period of the bath motion. The data to the right of the vertical dotted line is repeated. Panel (b) shows bouncing modes obtained for different values of  $\Delta\phi$  from panel (a). In this panel, the grey regions indicate times at which the droplet is in contact with the bath. The parameters  $K$  and  $B$  are fixed to 0.70 and 0.60 respectively.

figure 4.5(b). Depending on the phase difference, the droplet either bounces without walking or it superwalks. In the bouncing regime,  $20^\circ \lesssim \Delta\phi \lesssim 90^\circ$ , the droplet's vertical dynamics appear chaotic. This can be attributed to the height difference  $\Delta\mathcal{B}$  between successive peaks in the bath's motion being small (see dashed curve in figure 4.5(a)) and hence the droplet behaves similarly to the single frequency case (see figure 4.4(c)). Conversely, regions of high superwalking speed are associated with a large height difference  $\Delta\mathcal{B}$  between the two peaks in the bath's motion and a droplet can easily settle in a  $(1, 2, 1)$  bouncing mode.

The predicted speeds from the numerical simulations agree well with experiments. The chaotic mode in the bouncing regime and the  $(1, 2, 1)^H$  bouncing mode in the superwalking regime are also observed at parameter values comparable to those in experiments. The numerically observed  $(1, 2, 1)^L$  superwalkers were not reported in experiments, instead  $(1, 2, 2)$  modes were observed at the corresponding parameter values. However, as noted in Section 3.3, it is difficult to distinguish between a  $(1, 2, 1)^L$  and a  $(1, 2, 2)$  mode experimentally. Hence, it is not clear whether all the  $(1, 2, 2)$

superwalkers we reported in experiments are truly  $(1, 2, 2)$  superwalkers or if some may in fact be  $(1, 2, 1)^L$  superwalkers.

### 4.5.2 Speed-size characteristics of superwalking droplets

In the size range for which walkers exist, their walking speed typically increases with their size [85]. For superwalkers, we observed two trends in experimental results presented in Chapter 3: an ascending branch for smaller superwalkers where the speed increases with size, followed by a descending branch for larger superwalkers where the speed decreases with size. Figure 4.6 shows the speed-size characteristics of simulated superwalkers at  $\Gamma_{80} = 3.8$  and  $\Delta\phi = 130^\circ$  for a range of  $\Gamma_{40}$  values.

We begin by focusing on the comparison for the ascending branch. Figure 4.6 shows simulated speeds for constant  $K = 0.70$  and  $B = 0.60$  (grey curves) as used in the simulations shown in figures 4.4 and 4.5, and  $K$  linearly increasing function of droplet radius as in equation (4.27) with a fixed  $B = 0.60$  (coloured curves). We refer the reader to Appendix B for details on this linear relationship. Both the superwalking speed and the bouncing mode are captured well for both combinations for small- to moderate-sized superwalkers, and this is generally true for a broad range of  $K$  and  $B$  values (see Appendix B). By allowing  $K$  to vary linearly with the droplet radius  $R$  (coloured curve), we obtain a better fit for droplets on the ascending branch at relatively high  $\Gamma_{40}$  values (see figure 4.6(e)). Focusing on the vertical dynamics for this fit when  $\Gamma_{40} = 0.6$  (see figure 4.6(a)), we find that superwalkers on this branch universally impact the bath once every two up and down cycles of the bath's motion. For the smallest superwalkers, the amplitude of the bounces is chaotic. As the droplet size increases, there is a transition to a  $(2, 4, 2)$  mode in a narrow region near  $R = 0.51$  mm. Beyond this, the droplets bounce in a  $(1, 2, 1)^H$  mode for the remainder of the ascending branch. This agrees well with our experimental results where chaotic and  $(1, 2, 1)^H$  bouncing modes were also observed on the ascending branch.

Simulations of larger droplets that lie on the descending branch in experiments reveal that the model is unable to capture the larger superwalkers. We have explored different constant values of  $K$  and  $B$  as well as varying  $K$  and  $B$  as a function of  $R$  but were unable to obtain a better fit to the experimental superwalking speeds on this branch than the relatively poor fits shown in figure 4.6. However, we note that the bouncing modes predicted from simulations on the descending branch are comparable with experimental observations. For the curves shown, the superwalkers on the descending branch bounce typically bounces in a  $(1, 2, 1)^L$  mode. Although only

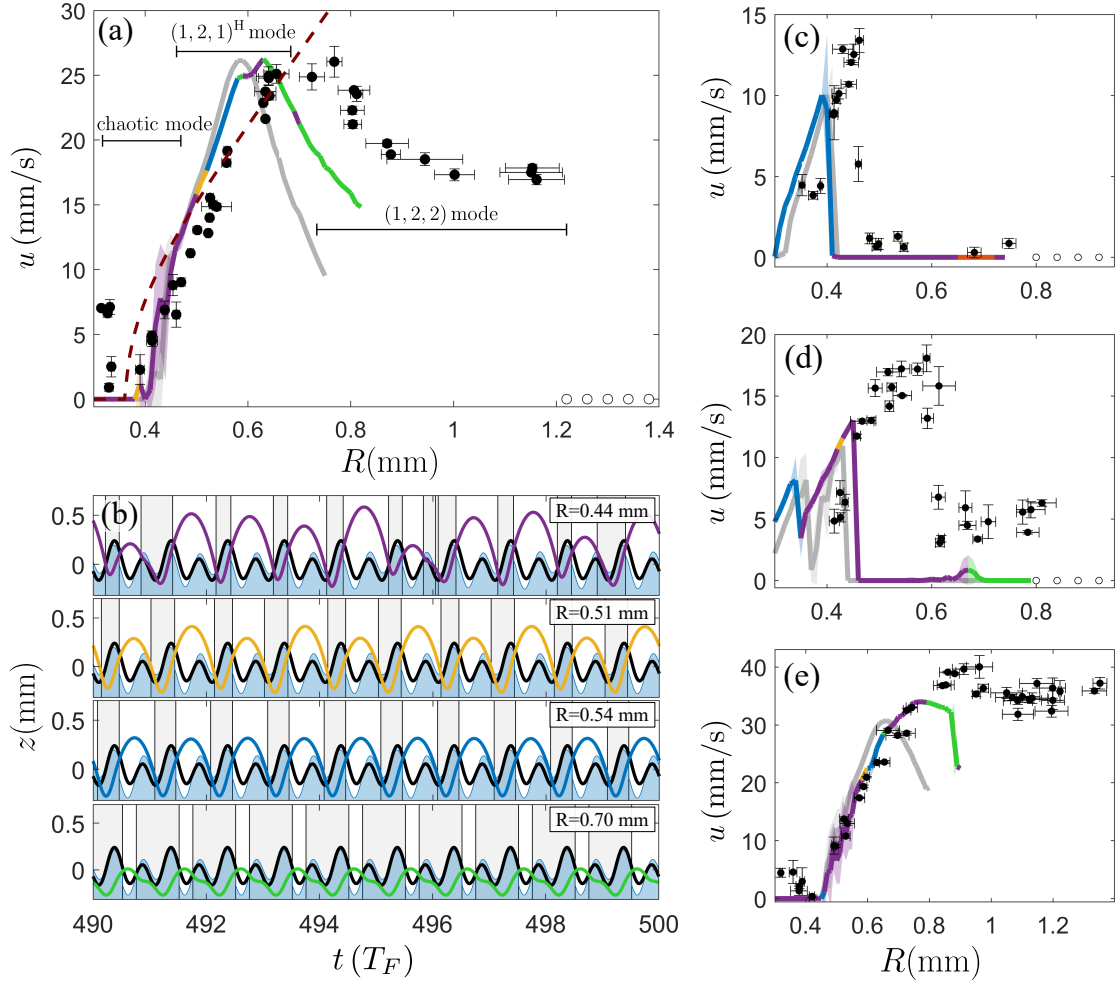


Figure 4.6 : Speed-size characteristics of superwalkers at  $\Gamma_{80} = 3.8$  and  $\Delta\phi = 130^\circ$ . (a) Comparison of the speed-size characteristics at  $\Gamma_{40} = 0.6$  of droplets from numerical simulations (solid curves) with the experimental results from figures 3.3 and 3.4 (black circles with empty circles indicating coalescence) and the stroboscopic model of Oza et al. [88] (dashed curve) presented in equation (2.15) with same parameter values as used in figure 3.3. The black horizontal bars indicate where different bouncing modes in experiments were observed. Panel (c), (d) and (e) show the speed-size characteristics at  $\Gamma_{40} = 0$ ,  $\Gamma_{40} = 0.3$  and  $\Gamma_{40} = 1$  respectively. In each panel the grey curve is for fixed parameter values of  $K = 0.70$  and  $B = 0.60$ , and multicoloured curve represents when  $K$  is varied as a linear function of the droplet radius  $R$  according to equation (4.27) with a fixed  $B = 0.60$ . The colours on this curve represent a chaotic bouncing mode in purple,  $(2,4,2)$  mode in yellow,  $(1,2,1)^H$  mode in blue,  $(1,2,1)^L$  mode in green and  $(1,2,2)$  mode in red. Termination of the solid curves indicate coalescence. The typical bouncing modes from panel (a) at different droplet radii are shown in panel (b). In this panel, the grey regions indicate times at which the droplet is in contact with the bath.

the  $(1, 2, 2)$  mode was reported in experiments, as previously mentioned,  $(1, 2, 1)^L$  and  $(1, 2, 2)$  are similar and have been difficult to distinguish in experiments.

### 4.5.3 Dynamics in the acceleration amplitudes parameter space

By fixing the phase difference  $\Delta\phi$  and the droplet radius  $R$ , we can explore the vertical and horizontal dynamics of a droplet in the parameter space formed by the two acceleration amplitudes  $\Gamma_{80}$  and  $\Gamma_{40}$ . We choose a droplet radius of  $R = 0.60$  mm and a phase difference of  $\Delta\phi = 130^\circ$  to compare the results from numerical simulations with our experiments. Figure 4.7(a) shows the region of parameter space where bouncing (lighter shades) and superwalking (darker shades) are observed as well as the bouncing modes (different colours) observed in those regions. Regions of bouncing (empty circles) and superwalking (filled circles) that were identified in our experiments are also shown. We find an excellent agreement in the transition boundary from bouncing to superwalking. Moreover, we identify that the superwalking region is dominated by the  $(1, 2, 1)$  bouncing mode with a  $(1, 2, 1)^L$  mode when  $\Gamma_{40}$  is small and a  $(1, 2, 1)^H$  mode when  $\Gamma_{40}$  is large. In contrast, the bouncing mode is nearly independent of  $\Gamma_{80}$  at a fixed  $\Gamma_{40}$  except at relatively high  $\Gamma_{80}$  values.

To understand how the superwalking speed  $u$  changes as a function of  $\Gamma_{40}$ , we show a slice of the  $(\Gamma_{80}, \Gamma_{40})$  parameter space at  $\Gamma_{80} = 3.8$  in figure 4.7(b) with corresponding bouncing modes in figure 4.7(c). We find that the walking speed is initially zero for all  $\Gamma_{40} \lesssim 0.3$  before increasing rapidly with  $\Gamma_{40}$  to a peak value near  $\Gamma_{40} = 0.7$  and then marginally decreasing. This illustrates the rather abrupt rise in walking speed that occurs once the asymmetry between the heights of succeeding peaks in the bath's and waves' motion is sufficient. Comparison of this numerically simulated walking speed  $u$  versus acceleration amplitude  $\Gamma_{40}$  curve with that obtained from our experiments for a droplet radius of  $R = (0.63 \pm 0.03)$  mm, shows good agreement highlighting the success of the present model for small- to moderate-sized superwalkers.

### 4.5.4 Comparison of different droplet models

Our current model works well for small- to moderate-sized droplets but does not capture the superwalking behaviour of large droplets. In an attempt to capture the large superwalkers, we have explored superwalkers using alternative models for the vertical dynamics, the wave field generated, and adding droplet deformations to the model presented in this chapter. Comparison of these models with the model presented

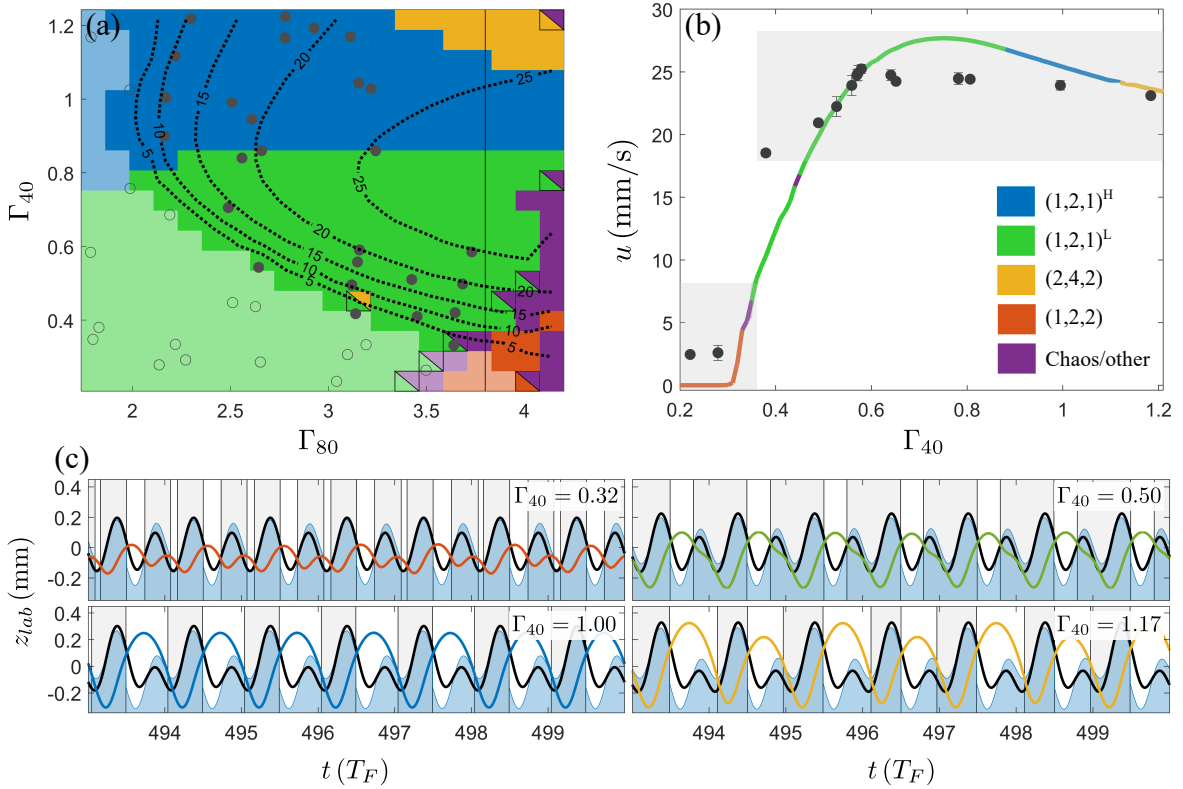


Figure 4.7 : Superwalking behaviour in the  $(\Gamma_{80}, \Gamma_{40})$  parameter space. (a) Bouncing modes shown as different colours for a droplet of radius  $R = 0.60$  mm in the  $(\Gamma_{80}, \Gamma_{40})$  parameter space with multiple colours at the same  $(\Gamma_{80}, \Gamma_{40})$  values indicating multiple bouncing modes that were observed at the same  $(\Gamma_{80}, \Gamma_{40})$  values. The lighter shade of each colour indicates bouncing and the darker shade is where superwalking is observed with walking speed indicated by dotted constant speed contours in mm/s. The markers indicate bouncing (empty circles) and superwalking (filled circles) for a droplet of radius  $R = (0.60 \pm 0.05)$  mm from our experimental results presented in figure 3.6. (b) A vertical slice of the parameter space in panel (a) (solid line) showing walking speed  $u$  as a function of  $\Gamma_{40}$  at a fixed  $\Gamma_{80} = 3.8$ . The solid curve is the result from simulations with colours indicating bouncing modes and the filled black markers are the experimental walking speeds for a droplet of radius  $R = (0.63 \pm 0.03)$  mm. The grey shaded region indicates the jump in walking speed for this droplet when  $\Gamma_{40}$  is appreciable. The different bouncing modes at different  $\Gamma_{40}$  values are shown in panel (c) with the grey regions in this panel indicating contact with the bath. The phase difference is fixed to  $\Delta\phi = 130^\circ$ . The parameters  $K$  and  $B$  are fixed to 0.70 and 0.60 respectively.

in this paper and the experimental results for a typical speed-size curve of superwalkers is presented in figure 4.8.

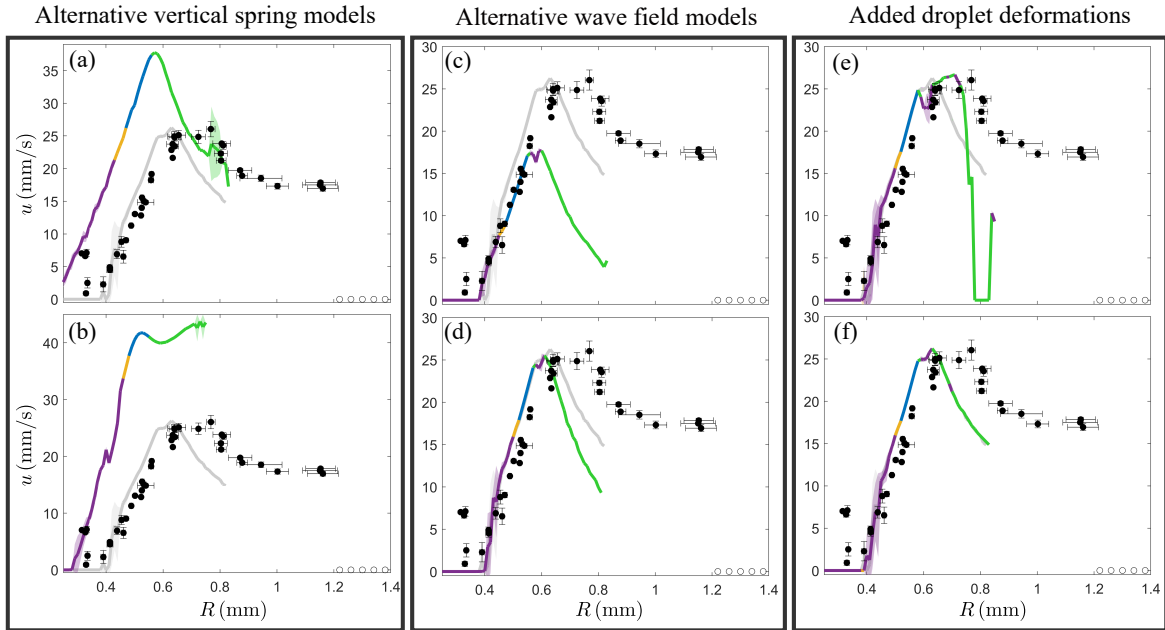


Figure 4.8 : Comparison of the speed-size characteristics of different models at  $\Gamma_{80} = 3.8$ ,  $\Gamma_{40} = 0.6$  and  $\Delta\phi = 130^\circ$ . In each panel, the black circles are experimental results, grey curves are the results from figure 4.6(a) using the model presented in this paper and the coloured curves are results from different models stated below with the colour indicating bouncing modes using the same conventions as in figure 4.6. Termination of the solid curves indicate coalescence. Results of using two alternative vertical spring models, a simple linear spring model and the logarithmic spring model of Moláček and Bush [57], are shown in (a) and (b), respectively. Results obtained using a wave field from the model of Moláček and Bush [85] and Tadríst et al. [86] are shown in (c) and (d), respectively. Results obtained by adding droplet deformation based on Blanchette [75] and Gilet et al. [76] are shown in (e) and (f), respectively. For the grey curves and the coloured curves in all panels except (b), the linear spring model was used for the vertical dynamics with the parameters  $K$  defined according to equation (4.27) and a fixed  $B = 0.60$ .

Apart from the linear spring model used in this work, two alternative spring models for the vertical dynamics of a bouncing droplet were presented by Moláček and Bush [57]: (i) a simple linear spring model that does not restrict the normal force to be positive i.e., without the maximum condition in equation (2.3) (see equation (2.2)), and (ii) a logarithmic spring model, which can be implemented by replacing equation (2.1) with equation (2.4) when the droplet is in contact with the bath, and using,  $m\ddot{z}_d = -m[g + \gamma(t)]$ , when the droplet is in the air. We fixed the parameter values in the logarithmic spring model to  $C_1 = 2$ ,  $C_2 = 12.5$  and  $C_3 = 1.4$  which are typical values used for walkers [57]. Coupling these vertical dynamics models with the wave

field and the horizontal dynamics used in this chapter, we obtain the speed-size curves presented in figures 4.8(a) and (b). Both these models capture the qualitative features on the ascending branch but overpredict the walking speeds. Moreover, they do not capture the superwalking behaviour of larger droplets.

Using the wave field of a walker from the Moláček and Bush [85] model presented in equation (2.8) and the Tadrict et al. [86] model presented in equation (2.10) in place of the superwalker wave field that was used in this work, we obtain the speed-size curves shown in figures 4.8(c) and (d). These curves also show good match with the experiments on the ascending branch. We note that for a droplet in a  $(1, 2, 1)^H$  bouncing mode, the subsequent bounces would occur one Faraday period after the initial impact. At this time, there is approximately a 10% difference in the amplitudes between the three models, and a slightly greater difference in the gradients (see figure 4.3). This would suggest a comparable difference in the walking speeds. However, although in figure 4.8(c), the peak of the speed-size curve from the wave model of Moláček and Bush [85] only goes up to approximately 17 mm/s for the present choice of  $K$  and  $B$  values, we obtain a better fit to the experimental results by alternate choices of parameters  $K$  and  $B$ . Hence by tuning the  $K$  and  $B$  values and using the wave model of Moláček and Bush [85], we can obtain good fit to the experimental data which is comparable to the fit obtained from the superwalker wave model. Speed-size curve from the wave model of Tadrict et al. [86] is identical to the curve from the superwalker wave model on the ascending branch. On the descending branch, we see that lower speeds are obtained from the Tadrict et al. [86] model compared to the superwalker wave field. This shows that the added 20 Hz waves seems to slightly speed up larger droplets on the descending branch in  $(1, 2, 1)^L$  bouncing mode.

Finally, to account for droplet deformations, we couple the droplet deformation models of Blanchette [75] (see equation (2.6)) and Gilet et al. [76] (see equation (2.7)) presented in Section 2.3 to the theoretical model presented in this chapter. We choose the parameters for these models as stated in Section 2.3. Coupling these droplet deformation models to the theoretical model presented in this chapter results in the speed-size curves shown in figures 4.8(e) and (f). We see that the model of Gilet et al. [76] seems to have an insignificant effect on the speed-size characteristics with the curves completely overlapping each other. The model of Blanchette [75] increases the walking speed of droplets in a small neighbourhood around  $R = 0.7$  mm but the model is still unable to capture the large superwalkers.

## 4.6 Discussion and conclusion

We have studied the dynamics of bouncing droplets on a vibrating liquid bath under two-frequency driving using the theoretical model of Moláček and Bush [57, 85] and a new model for the wave field to understand the emergence of superwalkers. We have shown that two-frequency driving at  $f$  and  $f/2$  with an appropriately chosen phase difference  $\Delta\phi$  lifts every second peak and lowers the intermediate peaks in the bath's motion. This allows larger droplets to bounce in a resonant  $(1, 2, 1)$  mode where they can efficiently excite damped subharmonic Faraday waves that enable them to superwalk. We note that superwalking would not be expected for two arbitrary frequency combinations, as the lowering of every second peak is crucial for them to remain in a  $(1, 2, 1)$  mode. For example, for two frequency driving at  $f = 80$  Hz and  $4f/5 = 64$  Hz, Sampara and Gilet [92] reported chaotic bouncing modes with irregular walking at typical speeds of only 5 mm/s.

We have shown that the phase difference  $\Delta\phi$  plays a crucial role in the dynamics of superwalking droplets because it controls the relative amplitudes of two succeeding peaks in one full cycle of the bath's motion. Fast superwalking occurs for phase differences between  $130^\circ$  and  $180^\circ$  where there is a larger difference between these amplitudes, while phase differences around  $45^\circ$ , where the amplitude difference between succeeding peaks is small, correspond to stationary bouncing or coalescence.

On comparing the speed-size characteristics of simulated superwalkers with the experimental results, we find excellent agreement on the ascending branch, with  $(1, 2, 1)^H$  superwalkers primarily observed. These observations also explain the good agreement noted in Chapter 3 between superwalking speeds obtained in experiments and those predicted using the stroboscopic model of Oza et al. [88] (dashed curve in figure 4.6(a)). The latter is a reduced form of the full Moláček and Bush [57, 85] model predicated on a  $(2, 1)^H$  bouncing mode and our two-frequency model would reduce to essentially the same model for such modes.

The superwalking speed of larger superwalkers is not captured well by the current model. This suggests that the model does not include the fundamental mechanism that allows the largest superwalkers to walk, and even exist. Indeed, we noted in Chapter 3 that the largest superwalkers on the descending branch undergo significant internal deformations [53]. We incorporated deformation of the droplets by modelling them as a vertical spring following Blanchette [75] and Gilet et al. [76], and find this to have a limited effect on the speed-size curve. Using the nonlinear logarithmic spring model of Moláček and Bush [85] for the vertical dynamics resulted in no better success. Another observation made in Chapter 3 was that larger superwalkers have a prolonged

---

contact time with the bath. This prolonged contact time, potentially in combination with internal deformation, may change the wave field in the vicinity of the droplet and the long time approximation of the standing wave field in equation (4.26) may break down. Perhaps a more refined modelling of the system that incorporates the detailed contact interaction between the droplet and the bath, the wave evolution and droplet deformations might be required to capture the behaviour of these larger superwalkers.



# Chapter 5

## Stop-and-go motion (SGM) of superwalkers

In this chapter, we explore a novel behaviour exhibited by superwalkers that we call stop-and-go motion (SGM). In this phenomenon, the droplet cycles periodically between pure bouncing (stop) and superwalking (go) resulting in a new type of locomotion in the system of walking droplets. We present the experimental observations and investigate the SGM numerically. Different types of SGM such as back-and-forth, forth-and-forth and random walk-like motion are observed.

The experimental observation of SGM presented in this chapter is based on the following published paper:

R. N. Valani, A. C. Slim and T. Simula, *Superwalking Droplets*, Physical Review Letters **123** 024503 (2019).

### 5.1 Introduction

Intermittent locomotion where organisms alternate between active propulsion and passive phases is frequently encountered in the natural world [98–100]. Examples include unicellular organisms such as ciliates, insect larvae and adults, reptiles, birds and mammals. Terrestrial organisms that exhibit intermittent locomotion typically come to a complete stop during the passive phase, but organisms in air or water may continue to glide forward during the passive phase resulting into a continuous variable speed motion [98]. Intermittent locomotion has also been identified in inanimate self-propelled particles such as microswimmers powered by chemical activity where

self-interaction of the swimmer with its long-lived chemical wake results in intermittent locomotion [101]. In this chapter, we show that intermittent locomotion can also be realised in the system of superwalking droplets when the two driving frequencies are slightly detuned giving rise to a *stop-and-go motion* (SGM). We present the experimental observation and explore this SGM numerically using the theoretical model for superwalkers established in Chapter 4.

## 5.2 SGM: experimental observation

At single frequency driving with amplitude  $\Gamma_f$  and frequency  $f$ , a given size walker has a fixed walking speed. Conversely, for a given size superwalker driven at two frequencies  $f$  and  $f/2$  with fixed acceleration amplitudes  $\Gamma_f$  and  $\Gamma_{f/2}$ , the droplet can have a range of walking speeds as a function of the phase difference  $\Delta\phi$ . Depending on this  $\Delta\phi$ , the droplet can either be in the superwalking, pure bouncing or the coalescence regime. Smaller superwalkers either superwalk or bounce depending on  $\Delta\phi$  while larger superwalkers can coalesce as well for a band of  $\Delta\phi$  values (see figure 3.5). By slightly detuning the two driving frequencies to  $f$  and  $f/2 + \epsilon$ , the driving acceleration of the bath takes the form

$$\gamma(t) = \Gamma_f g \sin(2\pi ft) + \Gamma_{f/2+\epsilon} g \sin(\pi ft + \Delta\phi(t)),$$

where  $\Delta\phi(t) = 2\pi\epsilon t$ , with  $\epsilon$  being the amount of detuning. For  $2\epsilon/f \ll 1$ , this form of the driving can be well approximated as driving the bath at frequencies  $f$  and  $f/2$  with a slowly varying phase difference  $\Delta\phi(t)$ .

An interesting dynamical phenomenon is observed in experiments with superwalkers when the driving frequencies are slightly detuned, for example with  $f = 80$  Hz and  $f/2 + \epsilon = 39.5$  Hz driving (for a video see Supplemental Video S10 of [53]). We observe that the droplets perform a *stop-and-go motion* (SGM) in which the droplets walk for a while, then stop abruptly, then walk again, and so on (see figure 5.1). Such motion arises because the small value of  $2\epsilon/f$  results in a continuously varying phase difference  $\Delta\phi(t)$  that causes the droplet to periodically traverse the pure bouncing (stop) and superwalking (go) regimes in speed versus phase difference space (see figure 3.5). SGM is typically observed in experiments for small- to moderate-sized superwalkers for which the coalescence regime in figure 3.5 does not exist or it exists for a narrow range of  $\Delta\phi$  values, so even if a coalescence regime is encountered, coalescence may be avoided if such a regime is traversed quickly enough.

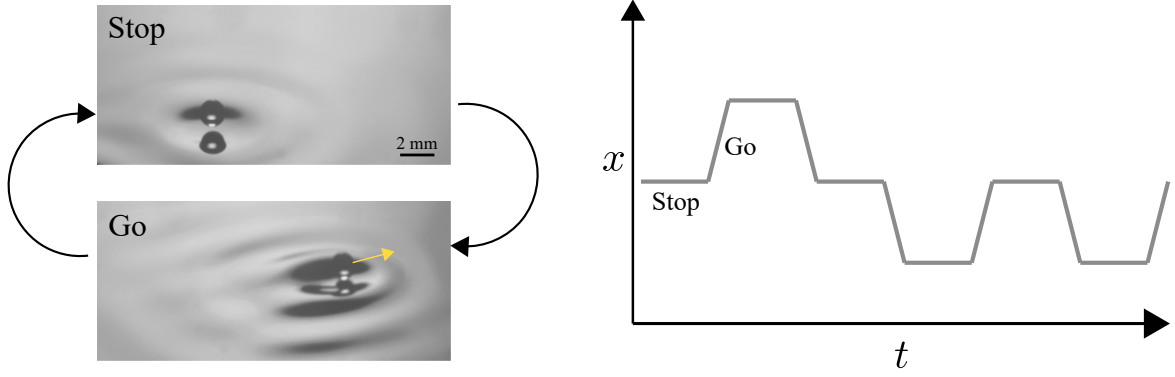


Figure 5.1 : Stop-and-go motion (SGM) of superwalking droplets. *Left panel:* In experiments with superwalking droplets, if the two driving frequencies  $f$  and  $f/2$  are slightly detuned, then it results in a SGM for small- to moderate- sized superwalkers where a droplet alternates periodically between pure bouncing (stop) and superwalking (go) modes of motion. *Right panel:* Schematic of a position-time graph of a droplet undergoing SGM.

### 5.3 Theoretical model

To model the SGM for superwalking droplets, we use the theoretical model for superwalkers developed in Chapter 4. We assume that the detuning  $\epsilon \ll f/2$  which ensures that the phase difference evolution  $\Delta\phi(t)$  is slow so that the evolution can be approximated as a “quasi-static” process and we can use the theoretical model developed in Chapter 4 for a constant phase difference. Due to the evolving phase difference  $\Delta\phi(t)$ , the decay rates of waves  $\text{Re}(\delta_{F40}^+(t))$  and  $\text{Re}(\delta_{F20}^+(t))$ , the diffusion coefficients  $D_{40}(t)$  and  $D_{20}(t)$  and the phase shifts  $\theta_{F40}^+(t)$  and  $\theta_{F20}^+(t)$  will all vary with time. Moreover, the prefactors,

$$A_{40}^p = \sqrt{\frac{2\pi}{\Omega^3 D_{40}} \frac{k_{F40}^2}{\pi\rho}} \quad \text{and} \quad A_{20}^p = \sqrt{\frac{2\pi}{\Omega^3 D_{20}} \frac{k_{F20}^2}{\pi\rho}},$$

of the amplitudes of the wave generated by a superwalker presented in equation (4.25) are now also functions of time. Hence, they are replaced by a weighted average over the contact duration as follows:

$$A_{40}^{avg} = \frac{\int_{t_n^i}^{t_n^c} A_{40}^p(t') F_N(t') dt'}{\int_{t_n^i}^{t_n^c} F_N(t') dt'},$$

$$A_{20}^{avg} = \frac{\int_{t_n^i}^{t_n^c} A_{20}^p(t') F_N(t') dt'}{\int_{t_n^i}^{t_n^c} F_N(t') dt'}.$$

We numerically simulate superwalkers using the same numerical scheme as described in Section 4.4. The bath is driven with acceleration

$$\gamma(t) = \Gamma_f g \sin(2\pi ft) + \Gamma_{f/2} g \sin(\pi ft + \Delta\phi(t)),$$

with a fixed  $f = 80$  Hz,  $f/2 = 40$  Hz,  $\Gamma_f = 3.8$ ,  $\Gamma_{f/2} = 0.6$  and  $\Delta\phi(t) = 2\pi\epsilon t$ . The horizontal motion in simulations was restricted to  $x$  direction only. The simulations were performed with a time step of  $\Delta t = T_F/100$  and initialised with  $x_d = 0$  mm,  $u_d = 1$  mm/s,  $v_d = 0$  mm/s and three different equally spaced vertical positions  $z_d = (0, 5, 10)R$ .

## 5.4 Emergence of SGM

We start by presenting results for a typical detuning of  $\epsilon = -0.5$  Hz and a typical droplet of radius  $R = 0.54$  mm for which the speed versus phase difference curve was presented in figure 4.5 and also shown in figure 5.2. We observe a SGM in simulations for these parameters and the walking speed and bouncing modes for one cycle of the SGM are shown in figures 5.2(a) and (c) respectively. By comparing in figure 5.2 the speed for a constant phase difference (coloured curve) with that obtained from an evolving phase difference (black curve) in the SGM, we see that the ‘stop’ phase in the SGM occurs in the bouncing regime while the high superwalking speed in the ‘go’ phase occurs in the superwalking regime. Moreover, the peak speed obtained in one cycle of the SGM is shifted from the peak that occurs for simulations at a constant phase difference presumably due to the inertia of the droplet. The time taken to traverse one cycle of the speed versus phase difference diagram i.e.  $\Delta\phi = 0^\circ$  to  $180^\circ$  is given by  $T = 1/2|\epsilon| = 1$  s. Moreover, for the chosen detuning of  $\epsilon = -0.5$  Hz  $< 0$ , the phase differences in figure 5.2(a) are traversed from right to left i.e., from  $\Delta\phi = 180^\circ$  to  $\Delta\phi = 0^\circ$ . We note that from figure 5.2(b), the bath motion at  $\Delta\phi = 180^\circ$  is same as  $\Delta\phi = 0^\circ$  but shifted. Hence for constant phase difference simulations, we get the same results for  $\Delta\phi = 0^\circ$  and  $\Delta\phi = 180^\circ$ .

Observing the bouncing modes for one cycle of the SGM we see that the droplet is continuously trying to adjust to the bouncing modes that are realised at different phase differences. We find that in the accelerating phase of the SGM the droplet is in a  $(1, 2, 1)^L$  bouncing mode while near the peak walking speed in the SGM, the droplet transitions to a  $(1, 2, 1)^H$  bouncing mode. Once the droplet enters the bouncing regime,

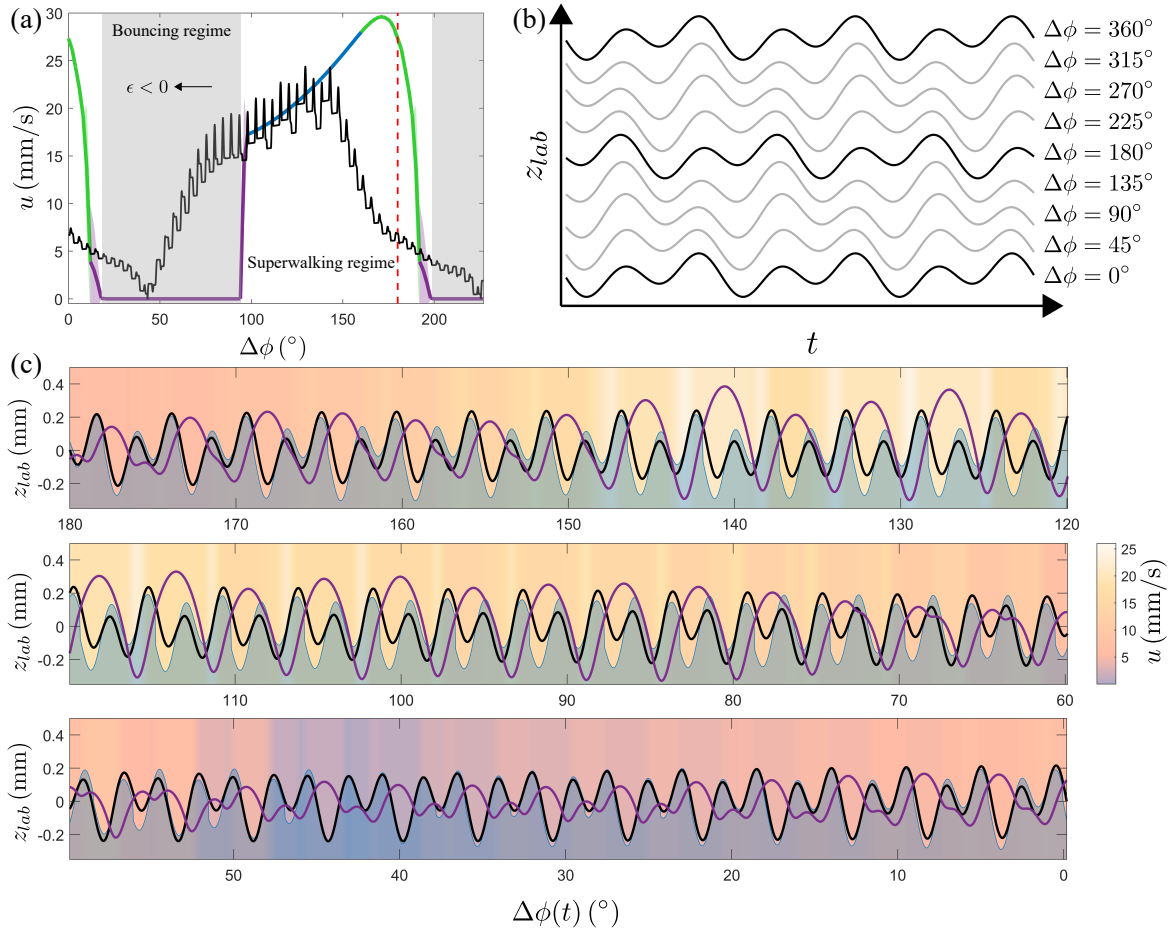


Figure 5.2 : SGM in numerical simulations for a droplet of radius  $R = 0.54$  mm with detuning  $\epsilon = -0.5$  Hz. (a) Walking speed  $u$  as a function of the phase difference  $\Delta\phi$  from constant phase difference superwalker simulations from Chapter 4 (coloured curve) and evolving phase difference SGM simulations (black curve). The different colours represent the bouncing modes as in figure 4.5. The data from the coloured curve after the vertical dashed red line is repeated. The bouncing regime (grey region) and the superwalking regime are also shown. A positive detuning corresponds to traversing the phase differences from left to right while a negative detuning corresponds to traversal in the opposite direction. Panel (b) shows the bath motion for different phase difference  $\Delta\phi$ . Panel (c) shows the vertical dynamics of the droplet for one cycle of the SGM with  $\Delta\phi(t) = 2\pi\epsilon t$ . The black solid curve is the bath motion, filled blue region is the wave motion and the solid blue curve is the motion of the south pole of the droplet. The coloured background shows the walking speed.

it loses resonance to the  $(1, 2, 1)^H$  bouncing and transitions to a chaotic bouncing mode before accelerating again to start the next cycle.

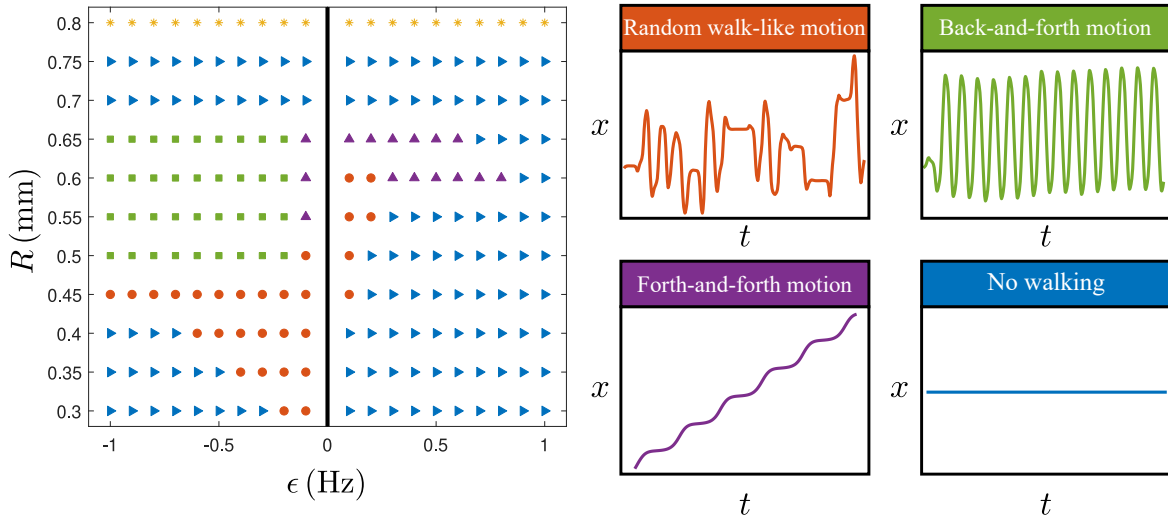


Figure 5.3 : Various types of SGM in the  $(\epsilon, R)$  parameter space. Four distinct types of dynamics are observed in the  $(\epsilon, R)$  parameter space: (i) random walk-like motion (red circles) where the droplet performs SGM with erratic switches in direction, (ii) back-and-forth (green squares) SGM where the droplet switches direction after each cycle, (iii) forth-and-forth (purple triangles) SGM where the droplet moves in the same direction after each cycle and (iv) No walking (blue triangles) where the droplet bounces but does not propel horizontally. We also observe that large droplets coalesce (yellow asterisks).

### 5.4.1 Parameter space exploration of the SGM

We have simulated droplets in the parameter space formed by the detuning  $\epsilon$  and the droplet radius  $R$  to explore the SGM. The parameter space plot along with a schematic of the different behaviours observed is shown in figure 5.3. We observe four qualitatively different types of dynamics in the  $(\epsilon, R)$  parameter space: (i) random walk-like SGM, (ii) back-and-forth SGM, (iii) forth-and-forth SGM and (iv) no walking.

In the random walk-like SGM, the droplet appears to switch chaotically between forward and backward superwalking after each cycle of the SGM. Moreover, the distance travelled in each cycle of the SGM varies significantly. A typical trajectory of this motion is shown in figures 5.4(a) and (b). In back-and-forth SGM, intriguingly, the droplet switches its walking direction after each cycle of the SGM. A typical trajectory of this motion is shown in figures 5.4(c) and (d). Conversely, in forth-and-forth SGM, the droplet maintains the same walking direction after each cycle of the SGM. A typical trajectory of this motion is shown in figures 5.4(e) and (f). We have observed random walk-like SGM and back-and-forth SGM frequently in experiments while forth-and-forth SGM has only been observed occasionally.

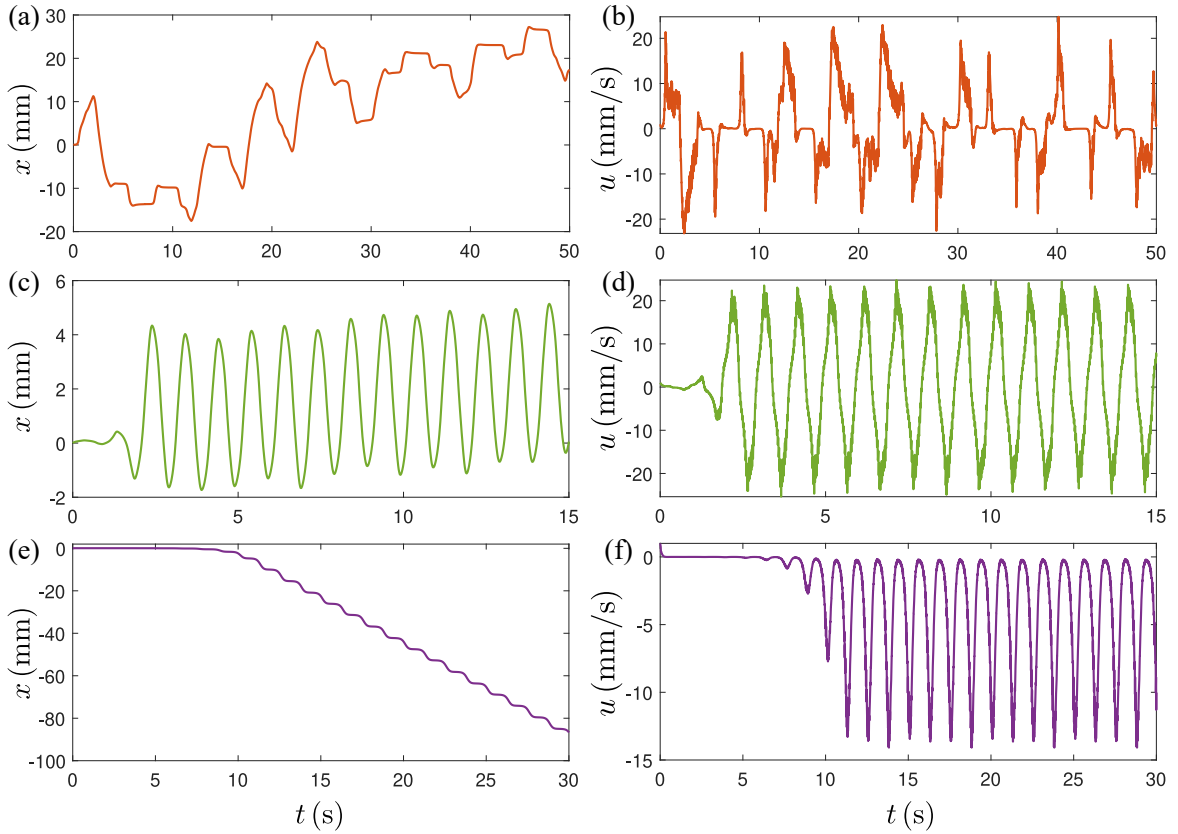


Figure 5.4 : Trajectories showing the three different types of SGM. Position-time and velocity-time plots for (a,b) random walk-like SGM for  $R = 0.45$  mm and  $\epsilon = -0.2$  Hz, (c,d) back-and-forth SGM for  $R = 0.55$  mm and  $\epsilon = -1$  Hz and (e,f) forth-and-forth SGM for  $R = 0.6$  mm and  $\epsilon = 0.4$  Hz.

In the parameter space diagram in figure 5.3 we see that relatively small droplets cannot walk under this prescribed driving or undergo random walk-like SGM for small negative detuning. Medium sized droplets show a wide range of stop-and-go behaviour including back-and-forth and forth-and-forth motion. Large droplets cease to perform walking and very large droplets coalesce with the bath and cannot even bounce.

### 5.4.2 Back-and-forth SGM

We have observed back-and-forth SGM in experiments for single and multiple superwalkers. To understand the emergence of this motion, we analyse the vertical dynamics and the horizontal force,  $F_H(t) = -F_N(t)\nabla h(\mathbf{x}_d, t)$ , acting on a droplet for the duration of one cycle of the back-and-forth motion during which the droplet reverses its walking direction. Figures 5.5(a) and (b) show respectively the vertical dynamics of the droplet and the horizontal force  $F_H$  acting on the droplet during one back-and-forth cycle

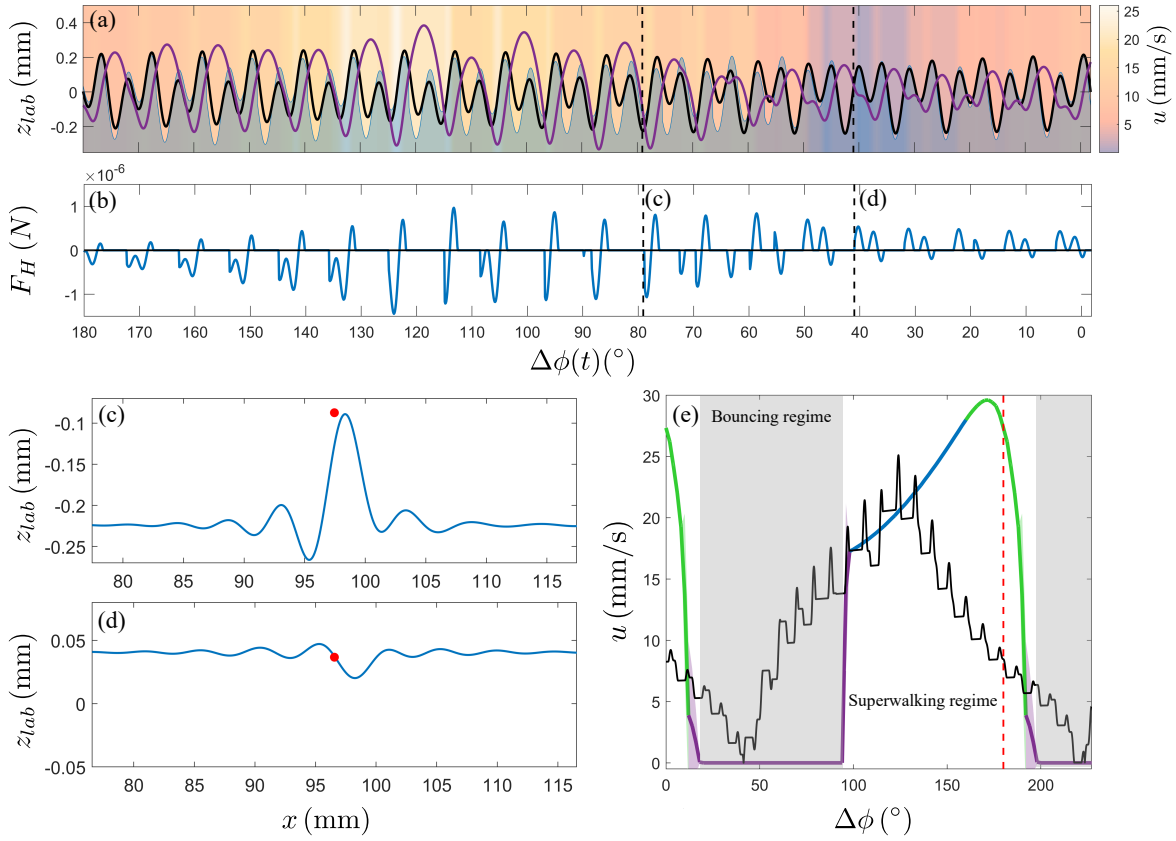


Figure 5.5 : Back-and-forth SGM of a superwalker for  $R = 0.54$  mm and  $\epsilon = -1$  Hz. (a) Vertical dynamics and (b) the horizontal force  $F_H$  acting on the droplet for one cycle of the back-and-forth SGM. Frames (c) and (d) show, respectively, snapshots of the wave field (blue curve) and the location of the south pole of the droplet (red circle) just when the droplet is about to contact the wave field before and after the droplet reverses its walking direction. The snapshots are taken at the times indicated by the vertical dashed lines in panels (a) and (b). Panel (e) shows the speed versus phase difference for constant phase difference simulations from Chapter 4 and the evolving phase difference SGM simulations. The different colours represent the different bouncing modes as in figure 4.5. The data from the coloured curve after the vertical dashed red line is repeated.

along with the corresponding superwalking speed in figure 5.5(e). We find that at the start of the cycle at a phase difference  $\Delta\phi(t) = 180^\circ$ , the two peaks in one cycle of the bath motion are asymmetrical in amplitude with, say, the right peak being the smaller one and the left peak being the larger one. As the phase difference evolves, the amplitudes of the two peaks become similar near  $\Delta\phi(t) = 45^\circ$  after which the peaks again become asymmetrical in amplitude with the left peak becoming the smaller one and the right peak becoming the larger one (see figures 5.5(a) and 5.2(b)). During this

exchange in position of the bigger and smaller peaks, the droplet undergoes a change in the bouncing phase where it contacts the underlying wave field at the opposite phase of the oscillation for the next SGM cycle and this results in a kick in the opposite direction from its direction of motion. Subsequent persistent kicks in the direction opposite to its walking direction eventually drives the droplet to reverse its walking direction. Figures 5.5(c) and (d) show, respectively, snapshots of the droplet just when it contacts the underlying wave field before and after it reverses the walking direction. As it can be seen that the droplet contacts the underlying waves at opposite phase resulting in the droplet landing on opposite sides of the peak and the corresponding horizontal forces acting in opposite directions. This change in the direction of the kicks is also evident from the evolution of the horizontal force  $F_H$  in figure 5.5(b).

## 5.5 Discussion and conclusion

We have observed a new type of intermittent locomotion, SGM, that emerges when a bath is driven simultaneously at frequencies  $f$  and  $f/2 + \epsilon$  with a small detuning  $\epsilon$ . In both experiments and simulations, we observe a SGM where the droplet periodically traverses the bouncing and the superwalking regimes in the speed versus phase difference space. This SGM is a complex nonlinear phenomenon with multiple timescales such as the bouncing time scale of the droplet, the memory time scale associated with decay of Faraday waves, the longer time scale introduced by the detuning and the inherent time scale of the droplet dynamics.

By doing numerical simulations in the  $(\epsilon, R)$  parameter space, we find three different types of SGM. These include uncorrelated SGM where superwalking direction and the distance travelled appear to vary chaotically, and correlated SGM, where either a back-and-forth or a forth-and-forth SGM is observed. In experiments, the random walk-like motion and the back-and-forth motion has been observed frequently while the forth-and-forth motion has only been observed occasionally.

Investigating this back-and-forth motion in detail reveals that the switch in the walking direction that occurs every cycle is due to the droplet changing the bouncing phase and impacting the underlying oscillating wave field at the opposite phase. This results in the wave field imparting horizontal force on the droplet in the opposite direction to its motion, which eventually reverses the direction of motion. We note that such reversals of motion due to reversal of the bouncing phase have also been demonstrated in the system of single-frequency driven walkers where a pulse in the

driving signal was engineered to change the bouncing phase of the droplet (see figure 1 of [102]). Here we see this behaviour arising as an emergent phenomenon.

The form of the detuning we have considered here results in a phase difference evolving linearly in time  $\Delta\phi(t) = 2\pi\epsilon t$ , but we can engineer any time-dependent function  $\Delta\phi(t)$  that slowly varies in time, allowing an exploration of the various different types of locomotion.

## Part II

# Generalised Pilot-Wave Dynamics



# Chapter 6

## Pilot-wave dynamics of two droplets

In this chapter, we take the stroboscopic pilot-wave model of Oza et al. [88] and investigate the dynamics of two interacting identical, in-phase bouncing droplets theoretically and numerically. A remarkably rich range of behaviours is encountered as a function of the two system parameters, the ratio of inertia to drag and the ratio of wave forcing to drag. We explore these rich behaviours and the bifurcations between them through analytic and numerical linear stability analyses and through fully nonlinear numerical simulations.

This chapter is based on the following published paper:

R. N. Valani and A. C. Slim, *Pilot-wave dynamics of two identical, in-phase bouncing droplets*, *Chaos* **28**, 096114 (2018).

### 6.1 Introduction

Interactions of multiple, single-frequency driven bouncing and walking droplets are dominated by their underlying wave fields and result in rich static and dynamical behaviours. Multiple bouncing droplets can form bound states where the droplets remain stationary at discrete distances apart [6] and many bouncing droplets interactions give rise to various lattice structures [7, 8]. Two walkers can interact to form dynamical bound states such as parallel walkers [6], promenading pairs that oscillate towards and away from one-another while parallel walking [6, 9, 10], orbiting pairs [6, 10, 11] and ratcheting pairs [12, 13]. Theoretical studies on interactions of multiple walkers

have focused on explaining these particular modes observed in experiments. A study of the full range of dynamics of the two-droplet system as a function of the different parameters has been lacking.

In this chapter we take the stroboscopic model of Oza et al. [88] that was described in Section 2.6 as a theoretical pilot-wave model and explore the behaviours observed for a simple extension from one walker to two identical, in-phase bouncing and walking droplets. Although the Oza et al. [88] model is predicated on a  $(2, 1)^H$  bouncing mode for single-frequency driven walkers, it was shown in Chapters 3 and 4 that the  $(1, 2, 1)^H$  bouncing mode of two-frequency driven superwalkers is effectively similar to the  $(2, 1)^H$  bouncing mode for walkers. Hence, we expect this model to potentially capture the dynamic states of two identical superwalkers as well. However, we note that inertia dominated superwalkers primarily interact via short range droplet-droplet interactions which this model fails to capture as it does not incorporate finite size effects of the droplet. Hence, aspects of the bound states of two superwalkers that are dominated by droplet-droplet interactions may not be captured. We also note the two simplified assumptions of the model that may break down for both walkers and superwalkers when extending this model to two interacting droplets: (i) this model neglects the transient wave and assumes a zeroth order  $J_0$  Bessel function standing wave field generated by the droplet. This structure of the wave field provides a good approximation in the near-field (within two Faraday wavelengths) but overpredicts the wave in the far-field (see figure 2.5 and figure 9 of Milewski et al. [62]). (ii) The model also assumes a constant impact phase for the droplet. This assumption breaks down for interacting walkers and thus far this has only been addressed using an empirical fix for the particular system being considered [89, 10, 61]. For analytical tractability, we use this simple extension, however, we show that despite the simplifying assumptions of constant impact phase and the structure of the wave field, we are able to capture two-droplet states that are observed in experiments including parallel walkers, promenading pairs and orbiting pairs. Moreover, by exploring the dynamics of two droplets using this model in a generalised pilot-wave framework i.e. stepping well outside the parameter regimes accessible in experiments, we also uncover a rich array of more exotic dynamics such as regularly and chaotically switching walkers, wandering walkers and intriguing closed-loop trajectories in regions of parameter space where wave forcing and/or inertia play a significant role.

## 6.2 Theoretical formulation

We start by extending the trajectory equation of a single walker developed by Oza et al. [88] and presented in equation (2.15), to two interacting walkers. The dimensionless positions of the droplets in the horizontal plane are  $\mathbf{x}_1 = (x_1, y_1)$  and  $\mathbf{x}_2 = (x_2, y_2)$ . The horizontal motion is described by the pair of integro-differential equations

$$\kappa \ddot{\mathbf{x}}_i + \dot{\mathbf{x}}_i = -\beta \nabla h(\mathbf{x}, t)|_{\mathbf{x}=\mathbf{x}_i(t)}, \quad (6.1)$$

for  $i = 1, 2$ , where the dimensionless height of the interface

$$h(\mathbf{x}, t) = \int_{-\infty}^t J_0(|\mathbf{x} - \mathbf{x}_1(s)|) e^{-(t-s)} ds + \int_{-\infty}^t J_0(|\mathbf{x} - \mathbf{x}_2(s)|) e^{-(t-s)} ds, \quad (6.2)$$

and dots indicate differentiation with respect to dimensionless time  $t$ . The left hand side of equation (6.1) comprises an inertial term  $\kappa \ddot{\mathbf{x}}_i$  and an effective drag term  $\dot{\mathbf{x}}_i$ . The right hand side of the equation captures the forcing of the droplets by the waves they have generated. Each impact generates a wave modelled as an axisymmetric Bessel function  $J_0(|\mathbf{x}|)$  centred at the point of impact and decaying exponentially in time. Since this model takes into account the waves generated from all the previous impacts, the shape of the interface is calculated through integration of waves generated from all the previous bounces of both droplets. At each impact, the droplet receives a horizontal kick proportional to the gradient of the interface at that point.

For the details of the non-dimensionalisation, we refer the reader to Section 2.6. However, we note that the length scale has been chosen to be the inverse Faraday wavenumber  $1/k_F$  and the time scale has been chosen to be  $T_F \text{Me}$ , where  $T_F$  is the Faraday period and  $\text{Me}$  is the memory parameter which represents the proximity to the Faraday threshold [88]. In these units, the Faraday wavelength is  $2\pi$  and the Faraday period is  $1/\text{Me}$ . For the parameter space under consideration, this memory typically varies in the range  $1 \lesssim \text{Me} \lesssim 20$ . The dimensionless parameters  $\kappa$  and  $\beta$  follow directly from Section 2.6 and are referred to as the dimensionless mass and the memory force coefficient respectively. We note that  $\kappa\beta \sim \text{Me}$  and hence one can obtain curves in the  $\beta$ - $\kappa$  parameter space along which memory is constant. The parameters  $\kappa$  and  $\beta$  may be usefully interpreted as the ratios of inertia to drag and wave forcing to drag respectively. Thus for small  $\kappa$ , the droplets' motion responds effectively immediately to the wave forcing. For large  $\kappa$ , it responds more slowly and a more sustained forcing is required to modify the motion. In such regimes, the droplets are likely to overshoot their equilibria and oscillations are expected.

This model can be extended to two identical out-of-phase bouncing droplets by appropriately switching the signs of the wave forcing term on the right hand side of equations (6.1) and (6.2) for the two droplets. Moreover, two droplets of different sizes can be modelled by using different  $\kappa$  and  $\beta$  for each droplet. This study focus on the dynamics of two identical, in-phase bouncing droplets.

We numerically integrate equations (6.1) using the Leap-Frog method [97], a modified version of the Euler method where the new horizontal and vertical positions of the droplet are calculated using the old velocities and then the new velocities are calculated using the new positions. The dimensionless time step is fixed to  $\Delta t = 2^{-6}$  unless stated otherwise. The details of the numerical method are provided in Appendix C.

### 6.3 Parameter space description

We begin with a summary of the rich dynamics observed on varying  $\beta$  and  $\kappa$ . Figure 6.1 shows the behaviour at  $t = 1000$  for droplets initiated at  $t = 0$  as parallel walkers with noise. Specifically, the initial positions were taken as  $\mathbf{x}_1 = (0, 0)$  and  $\mathbf{x}_2 = (\mathcal{D}_1(\beta), 0)$  and the initial velocities as  $\dot{\mathbf{x}}_1 = (\delta_1, \mathcal{U}_1(\beta) + \delta_2)$  and  $\dot{\mathbf{x}}_2 = (\delta_3, \mathcal{U}_1(\beta) + \delta_4)$ , where  $\mathcal{D}_1(\beta)$  and  $\mathcal{U}_1(\beta)$  are the distance between the two droplets and the velocity of each droplet in the parallel walking state (described in Section 6.6), and each  $\delta_i$  is a random perturbation uniformly selected between  $-0.1$  and  $0.1$ . For  $t < 0$ , the droplets were assumed to be in the unperturbed parallel walking state. Simulations for  $\kappa \leq 0.225$  have been performed using a timestep of  $\Delta t = 2^{-8}$  while  $\Delta t = 2^{-6}$  was used for all the other simulations because we find that the changes in the boundaries separating different behaviours using a smaller timestep is not significant on the scale of the parameter space plot.

For  $\kappa < 1$ , where drag exceeds inertia, a bifurcation from stationary states (yellow) to walking states occurs at  $\beta = 2$ , as for a single droplet [88]. For  $\kappa > 1$ , where inertia exceeds drag, the droplets are stationary for very small wave forcing  $\beta$ , before starting to oscillate towards and away from one another about fixed positions for  $\beta$  in a region below and very slightly above 2 ( $\beta \lesssim 2.1$ ). We term this latter behaviour *inline oscillations* (blue). For  $\beta > 2$ , we observe a variety of walking motions. For  $\kappa < 1$  and moderate  $\beta$ , the droplets perform a parallel walk at constant velocity. These states have been observed experimentally and are referred to as *parallel walkers* (red) [6]. For larger  $\beta$ , the droplets oscillate, predominantly towards and away from one another, while walking. These states have also been observed experimentally and have

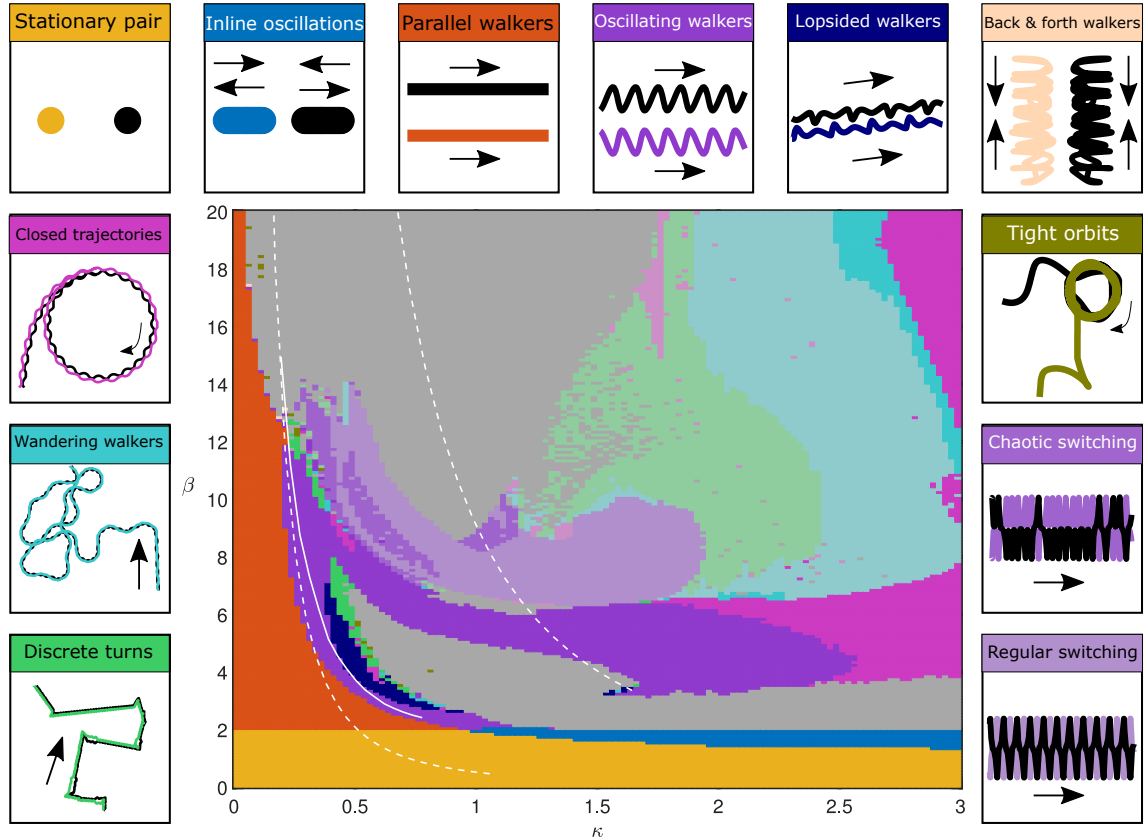


Figure 6.1 : Behaviours observed in the  $\beta$ - $\kappa$  parameter space at  $t = 1000$  from simulations initiated at  $t = 0$  as parallel walkers with noise. We explore the parameter space region  $0 < \kappa \leq 3$  and  $0 < \beta \leq 20$  with resolution  $\Delta\kappa = 0.025$  and  $\Delta\beta = 0.1$ . Simulations for  $\kappa \leq 0.225$  have been performed using a time step of  $\Delta t = 2^{-8}$  while  $\Delta t = 2^{-6}$  was used for all the other simulations as the changes in the boundaries separating the different regions by using a smaller time step are not significant on this scale. In grey regions the droplets have become unbound. The coloured regions correspond to the various states depicted in the surrounding trajectory plots. For oscillating walkers (purple), discrete-turning walkers (green), wandering walkers (cyan), and closed trajectories (pink), the darker shaded regions have non-switching oscillating walkers and the lighter regions have regularly switching walkers. The intermediate shade for oscillating walkers exhibit some form of chaotic switching. We note that the back-and-forth walkers (beige) may only be transient behaviour as we find that in our simulations, some of the back-and-forth walkers ultimately either settle into a tight orbit (olive) or become unbound. The region between the faint dashed white curves indicates where existing experimental setups may be able to perform experiments (see also figure 7.3). The solid white curve is the transect along which Arbelaiz et al. [10] observed oscillating walkers for in-phase bouncing droplets at the closest inter-droplet distance  $\mathcal{D}_1$ .

been referred to as promenading pairs [9, 10]. We refer to them as *oscillating walkers* (dark purple) to simplify classification. Upon further increasing  $\beta$ , these oscillating walkers tend to unbind. More intricate oscillating walkers such as *regular switching walkers* (light purple) and *chaotic switching walkers* (intermediate purple) that are reminiscent of promenading pair of superwalkers (see figure 3.11) are also observed. Other exotic dynamics such as *lopsided walkers* (navy blue), *back-and-forth walkers* (beige), *discrete-turning walkers* (green), *continuously turning walkers* (sky blue) and *closed trajectories* (pink) are observed for larger  $\beta$  and  $\kappa$ . These various states are explored in the next sections: stationary states in Section 6.4, inline oscillations in Section 6.5, parallel walkers in Section 6.6, oscillating walkers in Section 6.7 and more exotic, wandering states in Section 6.8. Despite the initial conditions being those of parallel walkers, we also very occasionally observe the droplets binding into tight orbits for large  $\beta$  and very small  $\kappa$ . We refer the reader to Oza et al. [89] for more details on this state.

## 6.4 Stationary states

We begin by exploring stationary states. Consider two droplets a distance  $d$  apart. We look for equilibrium states of the system such that the droplets remain stationary at this distance. Substituting  $\mathbf{x}_1 = (0, 0)$  and  $\mathbf{x}_2 = (d, 0)$  into equation (6.1), we obtain the constraint

$$J_1(d) = 0. \quad (6.3)$$

We denote the discrete solutions of this equation by  $d = \mathcal{D}_n$ , where  $\mathcal{D}_n$  is the  $n$ th zero of the Bessel function  $J_1(\cdot)$ . At these equilibrium distances, the second droplet sits either at a trough (odd  $n$ ) or a crest (even  $n$ ) of the wave field generated by the first droplet ( $J'_0(d) = -J_1(d) = 0$ ). We will focus on the first four distances  $\mathcal{D}_1 \approx 3.83$ ,  $\mathcal{D}_2 \approx 7.02$ ,  $\mathcal{D}_3 \approx 10.17$  and  $\mathcal{D}_4 \approx 13.32$ .

### 6.4.1 Linear stability analysis

To investigate the stability of these stationary states, we consider a general perturbation to the droplets:  $\mathbf{x}_1 = (0, 0) + \epsilon(x_{11}(t), y_{11}(t))$  and  $\mathbf{x}_2 = (d, 0) + \epsilon(x_{21}(t), y_{21}(t))$ . Substituting these forms into equation (6.1) and linearizing the resulting equations, we

obtain the matrix equation

$$\begin{bmatrix} \dot{\mathbf{X}}_1 \\ \dot{\mathbf{Y}}_1 \\ \dot{\mathbf{X}}_2 \\ \dot{\mathbf{Y}}_2 \end{bmatrix} = \begin{bmatrix} \mathbf{\Omega} & \mathbf{O} & \boldsymbol{\chi} & \mathbf{O} \\ \mathbf{O} & \mathbf{\Theta} & \mathbf{O} & \mathbf{O} \\ \boldsymbol{\chi} & \mathbf{O} & \mathbf{\Omega} & \mathbf{O} \\ \mathbf{O} & \mathbf{O} & \mathbf{O} & \mathbf{\Theta} \end{bmatrix} \begin{bmatrix} \mathbf{X}_1 \\ \mathbf{Y}_1 \\ \mathbf{X}_2 \\ \mathbf{Y}_2 \end{bmatrix}, \quad (6.4)$$

where

$$\mathbf{X}_i = \begin{bmatrix} x_{i1} \\ \dot{x}_{i1} \\ X_{i1} \end{bmatrix}, \quad \mathbf{Y}_i = \begin{bmatrix} y_{i1} \\ \dot{y}_{i1} \\ Y_{i1} \end{bmatrix},$$

for  $i = 1, 2$ :

$$\mathbf{\Omega} = \frac{1}{2\kappa} \begin{bmatrix} 0 & 2\kappa & 0 \\ \beta(1 + 2J'_1(d)) & -2 & -\beta \\ 2\kappa & 0 & -2\kappa \end{bmatrix},$$

$$\boldsymbol{\chi} = \frac{1}{\kappa} \begin{bmatrix} 0 & 0 & 0 \\ 0 & 0 & -\beta J'_1(d) \\ 0 & 0 & 0 \end{bmatrix}, \quad \mathbf{\Theta} = \frac{1}{2\kappa} \begin{bmatrix} 0 & 2\kappa & 0 \\ \beta & -2 & -\beta \\ 2\kappa & 0 & -2\kappa \end{bmatrix},$$

and  $\mathbf{O}$  is the  $3 \times 3$  matrix of zeroes. Derived variables  $X_{i1}$  and  $Y_{i1}$  are given by

$$X_{i1} = \int_{-\infty}^t x_{i1}(s)e^{-(t-s)} ds, \quad Y_{i1} = \int_{-\infty}^t y_{i1}(s)e^{-(t-s)} ds.$$

The solutions of equation (6.4) are proportional to  $e^{\lambda t}$ , with the complex growth rates  $\lambda$  given by the eigenvalues of the right-hand-side matrix. The characteristic polynomial of this matrix factorises in a convenient manner as

$$\det(\lambda \mathbf{I} - \mathbf{\Theta})^2 \det(\lambda \mathbf{I} - \mathbf{\Omega} - \boldsymbol{\chi}) \det(\lambda \mathbf{I} - \mathbf{\Omega} + \boldsymbol{\chi}) = 0,$$

where each of the sub-determinants corresponds to a distinct eigenmode of the system. Thus,

$$\det(\lambda \mathbf{I} - \mathbf{\Theta}) = \lambda^3 + \frac{\kappa + 1}{\kappa} \lambda^2 - \frac{\beta - 2}{2\kappa} \lambda,$$

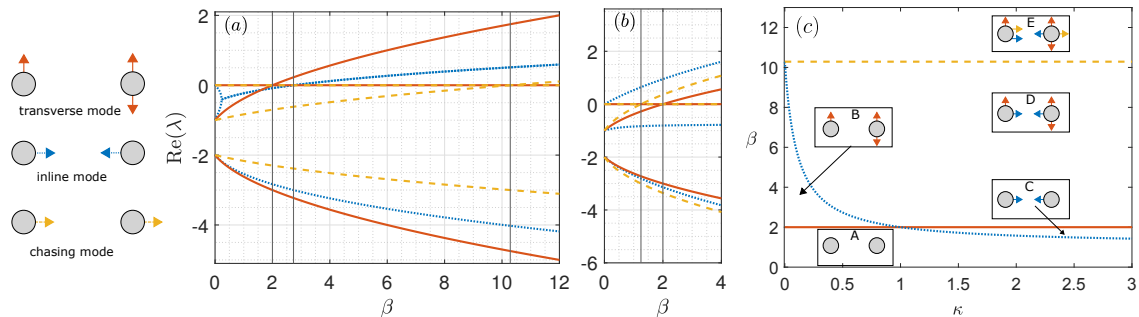


Figure 6.2 : Stationary pairs: Linear growth rates of perturbations  $\text{Re}(\lambda)$  as a function of memory parameter  $\beta$  for droplets (a) the first stationary distance  $d = \mathcal{D}_1$  apart and (b) the second stationary distance  $d = \mathcal{D}_2$  apart. Perturbation modes are distinguished as transverse (red, solid curves), inline (blue, dotted curves) or chasing (yellow, dashed curves). The vertical lines shows the  $\beta$  values at which the eigenvalues cross  $\text{Re}(\lambda) = 0$ . The dimensionless mass  $\kappa = 0.5$ . (c) Stability diagram in the  $\beta$ - $\kappa$  parameter space for the first stationary distance  $d = \mathcal{D}_1$ . Region A is stable to any small perturbation. Regions B and C are unstable to transverse and inline perturbations respectively. Region D is unstable to both inline and transverse perturbations while Region E is also unstable to chasing modes perturbations.

is the characteristic polynomial corresponding to perturbations perpendicular to the line joining the droplets called the *transverse mode*,

$$F_i(\lambda) := \det(\lambda \mathbf{I} - \mathbf{\Omega} + \mathbf{\chi}) = \lambda^3 + \frac{\kappa + 1}{\kappa} \lambda^2 - \frac{\beta(2J_1'(d) + 1) - 2}{2\kappa} \lambda - \frac{2J_1'(d)\beta}{\kappa}, \quad (6.5)$$

corresponds to inline perturbations of the droplets towards or away from one other called the *inline mode* and

$$\det(\lambda \mathbf{I} - \mathbf{\Omega} - \mathbf{\chi}) = \lambda^3 + \frac{\kappa + 1}{\kappa} \lambda^2 - \frac{\beta(2J_1'(d) + 1) - 2}{2\kappa} \lambda,$$

corresponds to inline perturbations of the droplets in the same direction called the *chasing mode*.

Figures 6.2(a) and (b) shows the growth rates as a function of the memory force parameter  $\beta$  for the two smallest stationary distances at a fixed  $\kappa = 0.5$ . For  $d = \mathcal{D}_1$ , when  $\beta < 2$ , the real parts of all the non-trivial eigenvalues are negative indicating that the two-droplet system is stable for general small perturbations. When  $\beta \geq 2$ , an eigenvalue for each distinct mode becomes positive at different  $\beta$  values. Note that there are also two zero eigenvalues, which correspond to invariants of the equilibrium state.

Transverse perturbations become unstable at  $\beta = 2$  independent of  $\kappa$ . This bifurcation value is identical to that for a single droplet's bouncing-to-walking transition [88]. This is not a coincidence: for transverse perturbations, the order- $\epsilon$  forcing to each droplet arises only from the droplet's own wave field while the contribution from the other droplet's wave field is of higher order. Thus the linearised equations for the two droplets decouple and reduce to those of a single droplet. The eigenvalues of the transverse mode are purely real. At the onset of instability, parallel walkers emerge if the droplets are perturbed in the same transverse direction, while orbiting states emerge if the droplets are perturbed in the opposite transverse direction. The parallel walking state will be explored in Section 6.6.

For the inline mode, a pair of complex conjugate eigenvalues become unstable at

$$\beta_n^i = \left( \frac{1}{2} - J_1'(\mathcal{D}_n) \left( \frac{\kappa - 1}{\kappa + 1} \right) \right)^{-1}. \quad (6.6)$$

At the onset of this instability, the droplets oscillate towards and away from one another with angular frequency

$$\omega_n = \sqrt{\frac{1}{2\kappa} (2 - \beta(2J_1'(\mathcal{D}_n) + 1))}.$$

These oscillations, termed inline oscillations, are discussed in Section 6.5.

For the chasing mode, the eigenvalues are purely real and an eigenvalue becomes unstable at

$$\beta_n^c = \frac{2}{2J_1'(\mathcal{D}_n) + 1},$$

independent of  $\kappa$ . For  $d = \mathcal{D}_1$ , this corresponds to  $\beta_1^c \approx 10.29$ . In this mode, the droplets walk one behind another in the same direction at a constant speed. These chasers are explored briefly in Section 6.9.

Figure 6.2(c) summarises the linear stability of stationary states at  $d = \mathcal{D}_1$ . There are regions where only the walking or the inline oscillating mode is unstable while the chasing mode bifurcation only takes place where both inline and transverse modes are unstable. The bifurcations from stationary states to parallel walking and stationary states to inline oscillations match with the states observed numerically in figure 6.1.

From figure 6.2(b) it is clear that at  $d = \mathcal{D}_2$ , one eigenvalue for inline perturbations always has positive real part and therefore any perturbations will drive the system away from the stationary state. Considering only the eigenvalues corresponding to inline perturbations for distances  $\mathcal{D}_{2n}$  given in equation (6.5) and by invoking Descartes' rule of sign, we can deduce the existence of one positive root of this cubic equation. Thus

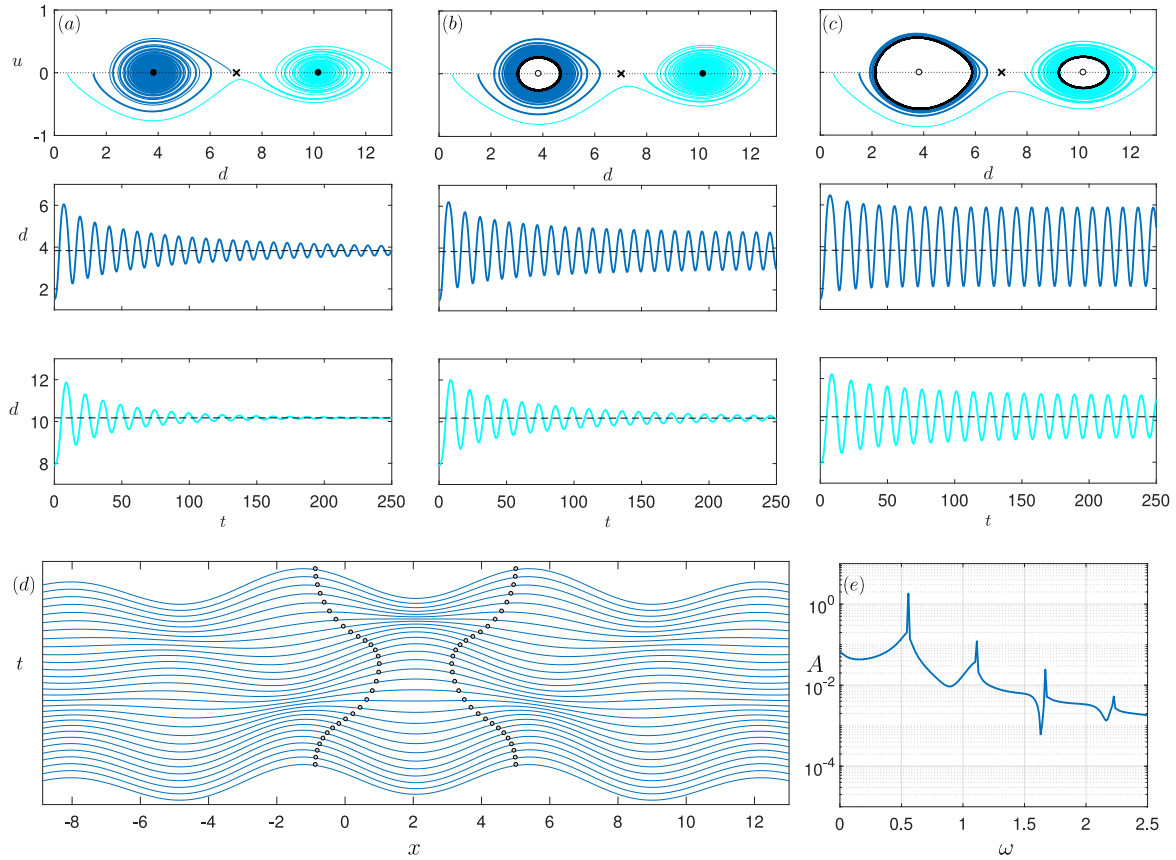


Figure 6.3 : Inline oscillations:  $u$ - $d$  phase plane at  $\kappa = 2$  and (a)  $\beta = 1.5$ , (b)  $\beta = 1.6$  and (c)  $\beta = 1.75$ . (a) At  $\beta = 1.5$ , both  $d = \mathcal{D}_1$  and  $d = \mathcal{D}_3$  are stable spirals (filled black circles) while  $d = \mathcal{D}_2$  is a saddle (black cross). (b) At  $\beta=1.6$ ,  $d = \mathcal{D}_3$  is still a stable spiral while at  $d = \mathcal{D}_1$ , an unstable spiral (empty black circles) has emerged with an enclosing limit cycle. (c) At  $\beta=1.75$ , limit cycles exist at both  $\mathcal{D}_1$  and  $\mathcal{D}_3$ . The two panels below the phase plane plot shows the distance between the droplets as a function of time for the thick solid curve trajectories in the phase plane. For  $\beta=1.75$ , panel (d) shows cross-sections of the wave field (blue curves) generated by the droplets and droplet positions (grey circles) at different instants over one period of the limit cycle at  $\mathcal{D}_1$  and panel (e) shows the fast Fourier transform (FFT) of the distance between the two droplets indicating that the oscillations are dominated by a single frequency.

the equilibrium distances  $\mathcal{D}_{2n}$  are always unstable to inline perturbations, as expected since one droplet is sitting on the crest of the other's wave field at these distances and small perturbations will result in kicks away from the equilibrium.

## 6.5 Inline oscillations

In a sliver of parameter space with inertia exceeding drag,  $\kappa > 1$ , and small wave forcing  $\beta \lesssim 2.1$ , inline oscillations are observed with droplets oscillating towards and away from one another (see figure 6.1). In experiments, inline oscillations have been observed for walkers [61] and we have also observed them in experiments with superwalkers. Here we explore the nature of the oscillations using our theoretical model.

The phase space for the one-dimensional inline motion of the droplets is two dimensional with the velocity  $u(t)$  of the first drop and the distance  $d(t)$  between the droplets sufficient to fully describe the system. The evolution of the phase-space portrait with increasing wave forcing  $\beta$  at fixed  $\kappa = 2$  is shown in figure 6.3. Note that, from equation (6.6), the  $\beta$  value at which different distances  $\mathcal{D}_n$  with  $n$  odd become unstable are a function of  $\kappa$ . For  $0 < \kappa < 1$ , the cascade of instability goes from larger to smaller distances as  $\beta$  increases, while for  $\kappa > 1$  it goes from smaller to larger distances. For  $\kappa = 1$ , all the distances become unstable at the same value  $\beta_n^i = 2$ . For  $\kappa = 2$ , the onset of inline oscillations occurs at  $\beta_1^i = 1.577$  for  $\mathcal{D}_1$  and  $\beta_3^i = 1.715$  for  $\mathcal{D}_3$ . Thus at  $\beta = 1.5$  (see figure 6.3(a)) there are stable spirals at  $\mathcal{D}_1$  and  $\mathcal{D}_3$  and a saddle at the unstable distance  $\mathcal{D}_2$ . If the droplets are perturbed inline when placed near a distance  $\mathcal{D}_1$  or  $\mathcal{D}_3$  apart, the oscillations will decay and the droplets will settle back into the stationary distance. As the parameter  $\beta$  is increased beyond  $\beta_1^i$ , the stable spiral at  $\mathcal{D}_1$  undergoes an apparent supercritical Hopf bifurcation and changes into an unstable spiral with an encompassing limit cycle (see figure 6.3(b)). Now the droplets either perform limit cycle oscillations corresponding to motion towards and away from one another around  $\mathcal{D}_1$  or settle into the second stable distance  $\mathcal{D}_3$ . On further increasing  $\beta$  beyond  $\beta_3^i$ , the stable spiral at  $\mathcal{D}_3$  also undergoes a supercritical Hopf bifurcation as shown for  $\beta = 1.75$  in figure 6.3(c). Eventually, as  $\beta$  is increased beyond 1.90, the limit cycle at  $\mathcal{D}_1$  vanishes in an apparent homoclinic bifurcation, followed by the one at  $\mathcal{D}_3$  at  $\beta = 2.01$ .

In simulations, inline oscillations are observed with rapidly increasing separation  $\mathcal{D}_n$  as  $\beta$  is increased for fixed  $\kappa \gtrsim 1.3$ . The droplets unbind in these simulations when  $\beta \approx 2.1$ . For  $1 < \kappa \lesssim 1.3$ , as  $\beta$  is increased for a fixed  $\kappa$ , the inline oscillations at  $\mathcal{D}_1$  bifurcate into oscillating walkers before unbinding near  $\beta \approx 2.2$ .

Figure 6.3(d) shows a representative example of the positions of the droplets along with cross-sections of their wave field for one cycle of inline oscillations. When the droplets are at their maximum separation, the wave field gradient ensures a kick towards each other. As the droplets travel towards each other, they pass their mean distance and reach a minimum separation with wave field gradient such that the droplets receive

a kick away from each other. In this way, the droplets oscillate towards and away from one another. Note that the oscillations are dominated by a single frequency (see figure 6.3(e)) and a single Fourier mode expansion approximates the oscillations reasonably well near the bifurcation.

## 6.6 Parallel walking

For  $\kappa < 1$  and  $\beta > 2$ , a parallel walking state emerges in which the droplets walk at constant speed in the direction perpendicular to the line joining them. Parallel walkers have been observed in experiments with walkers [6]. For superwalkers, although we do not observe a parallel walking state as described here, we do observe a similar state where two droplets form a tight pair and walk parallel side by side in a direction perpendicular to the line joining them (see figure 3.9(a)).

Consider two parallel walking droplets moving at constant speed  $u$  and separated by a distance  $d$ . By substituting  $\mathbf{x}_1 = (0, ut)$  and  $\mathbf{x}_2 = (d, ut)$  in equation (6.1), we arrive at the pair of integral equations

$$\int_0^\infty \frac{J_1(\sqrt{u^2 z^2 + d^2})}{\sqrt{u^2 z^2 + d^2}} e^{-z} dz = 0,$$

and

$$\frac{u}{\beta} = \frac{\sqrt{1+u^2} - 1}{u\sqrt{1+u^2}} + \int_0^\infty \frac{uz e^{-z}}{\sqrt{u^2 z^2 + d^2}} J_1(\sqrt{u^2 z^2 + d^2}) dz.$$

These can be solved numerically and have infinitely many solutions  $u = \mathcal{U}_n(\beta)$ ,  $d = \mathcal{D}_n(\beta)$  for  $n \in \mathbb{N}$ , which are functions of  $\beta$  but independent of  $\kappa$ . The first four such solutions are shown in figure 6.4. Note that droplets in the first and third solutions walk slightly slower than a single droplet while the second and fourth walk slightly faster.

### 6.6.1 Linear stability analysis

To understand the stability of this mode, we use an approach similar to that used by Oza et al. [88] to explore single-droplet walking. The linear stability analysis of parallel walkers with a varying impact phase based on empirical observations has been performed by Arbeláiz et al. [10]. Consider a perturbation to the equilibrium solution  $\mathbf{x}_1 = (\epsilon x_{11}(t)H(t), ut + \epsilon y_{11}(t)H(t))$  and  $\mathbf{x}_2 = (d + \epsilon x_{21}(t)H(t), ut + \epsilon y_{21}(t)H(t))$ , with

the Heaviside step function  $H(\cdot)$  included to introduce the perturbation at  $t = 0$ . Substituting this form into equation (6.1), linearising and taking Laplace transforms of the resulting equations, we obtain the matrix equation

$$\mathbf{A}_{PW}(s)\mathbf{X}(s) = \mathbf{X}_0(s).$$

Here

$$\mathbf{X}(s) = \begin{bmatrix} X_{11}(s) \\ Y_{11}(s) \\ X_{21}(s) \\ Y_{21}(s) \end{bmatrix} = \mathcal{L}[\mathbf{x}(t)] = \mathcal{L} \begin{bmatrix} x_{11}(t) \\ y_{11}(t) \\ x_{21}(t) \\ y_{21}(t) \end{bmatrix},$$

$$\mathbf{X}_0(s) = (s + 1)\mathbf{x}(0) + \dot{\mathbf{x}}(0),$$

and

$$\mathbf{A}_{PW}(s) = (\kappa s^2 + s)\mathbf{l}_4 + \beta\mathbf{K},$$

with  $\mathbf{l}_4$  the  $4 \times 4$  identity matrix. Moreover,

$$\mathbf{K} = \mathcal{L} \begin{bmatrix} p_1(u, 0, t) & 0 & f_0^1(u, d, t; d^2) & -f_1^0(u, d, t; d) \\ 0 & f_2^1(u, 0, t; 1) & -f_1^0(u, d, t; d) & f_2^1(u, d, t; 1) \\ f_0^1(u, d, t; d^2) & f_1^0(u, d, t; d) & p_1(u, 0, t) & 0 \\ f_1^0(u, d, t; d) & f_2^1(u, d, t; 1) & 0 & f_2^1(u, 0, t; 1) \end{bmatrix}$$

$$- \int_0^\infty \begin{bmatrix} p_1(u, 0, z) + f_0^0(u, d, z; d^2) & -f_1^0(u, d, z; d) & 0 & 0 \\ -f_1^0(u, d, z; d) & f_2^1(u, 0, z; 1) + q_2(u, d, z) & 0 & 0 \\ 0 & 0 & p_1(u, 0, z) + f_0^0(u, d, z; d^2) & f_1^0(u, d, z; d) \\ 0 & 0 & f_1^0(u, d, z; d) & f_2^1(u, 0, z; 1) + q_2(u, d, z) \end{bmatrix} dz,$$

with the functions

$$p_m(u, d, z) = m \frac{J_1(\sqrt{u^2 z^2 + d^2})}{\sqrt{u^2 z^2 + d^2}} e^{-z},$$

$$q_n(u, d, z) = \frac{(uz)^n}{\sqrt{u^2 z^2 + d^2}} \left( \frac{J_1(\sqrt{u^2 z^2 + d^2})}{\sqrt{u^2 z^2 + d^2}} \right)' e^{-z}$$

and  $f_n^m(u, d, z; \sigma) = p_m(u, d, z) + \sigma q_n(u, d, z)$ .

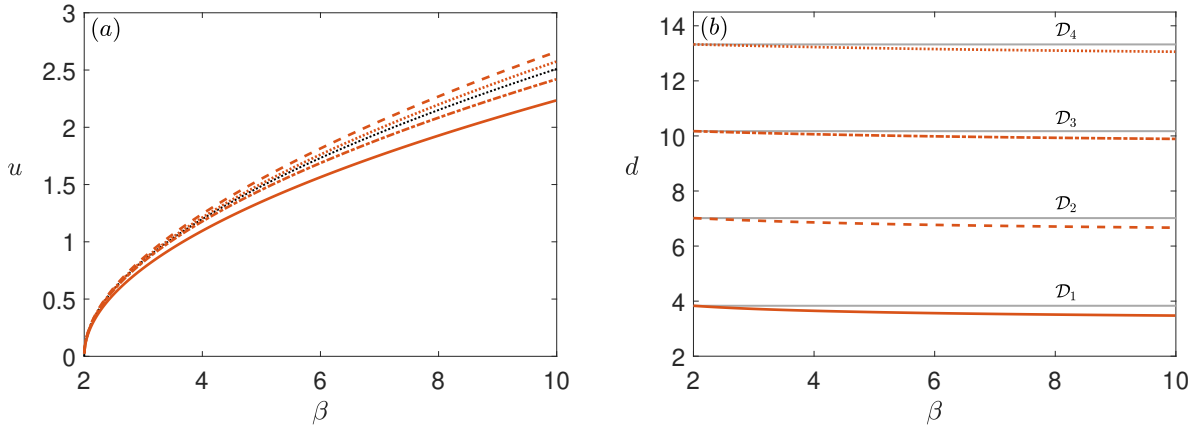


Figure 6.4 : Parallel walkers: First four equilibrium (a) walking speeds  $u = \mathcal{U}_n(\beta)$  and (b) separations  $d = \mathcal{D}_n(\beta)$  as a function of  $\beta$  corresponding to  $n = 1$  (solid curves), 2 (dashed curves), 3 (dashed-dotted curves) and 4 (dotted curves). Based on the linear stability analysis, the distances  $\mathcal{D}_1(\beta)$  and  $\mathcal{D}_3(\beta)$  are stable while  $\mathcal{D}_2(\beta)$  and  $\mathcal{D}_4(\beta)$  are unstable. The black curve in (a) represents the solution for a single walker. The grey lines in (b) are the corresponding stationary state equilibrium distances.

The growth rates of this linear stability problem correspond to the poles of  $\mathbf{X}(s)$ . The functions  $p^n(u, d, z)$  and  $q^n(u, d, z)$  decay exponentially as  $z \rightarrow \infty$ , and so all the functions in the matrix equation above are analytic in the region  $\text{Re}(s) \geq 0$ . Hence finding the growth rates reduces to determining the roots of  $\det(\mathbf{A}_{PW}(s)) = 0$ . This was done by simultaneously setting the real and imaginary parts of  $\det(\mathbf{A}_{PW}(s)) = 0$  using a modified secant method [103]. The initial guess for the modified secant method was scanned in the region  $-1 < \text{Re}(s) \leq 1$  and  $-3 \leq \text{Im}(s) \leq 3$  in steps of 0.1 and the perturbation fraction was chosen to be  $10^{-4}$ . We find that the distances  $\mathcal{D}_2(\beta)$  and  $\mathcal{D}_4(\beta)$  are always unstable while  $\mathcal{D}_1(\beta)$  and  $\mathcal{D}_3(\beta)$  are stable for a range of  $\beta$  and  $\kappa$  values. Figures 6.5(a) and (b) show the real and imaginary part of the numerically calculated poles as  $\beta$  varies for  $\kappa = 0.5$  for droplets a distance  $\mathcal{D}_1(\beta)$  apart. The first mode to become unstable is a complex conjugate pair indicating an oscillatory mode emerges at the bifurcation. Note that the zero eigenvalue reflects the invariant properties of the base state.

Figure 6.5(c) shows the stability diagram for parallel walkers in the  $\beta$ - $\kappa$  parameter space at a distance  $\mathcal{D}_1(\beta)$  apart. The state is stable for a large window of  $\beta$  when  $\kappa$  is small, with the  $\beta$  window reducing as the inertia  $\kappa$  increases. The stable region corresponds well with the region where parallel walkers are observed in simulations, suggesting that the bifurcations away from parallel walking are supercritical.

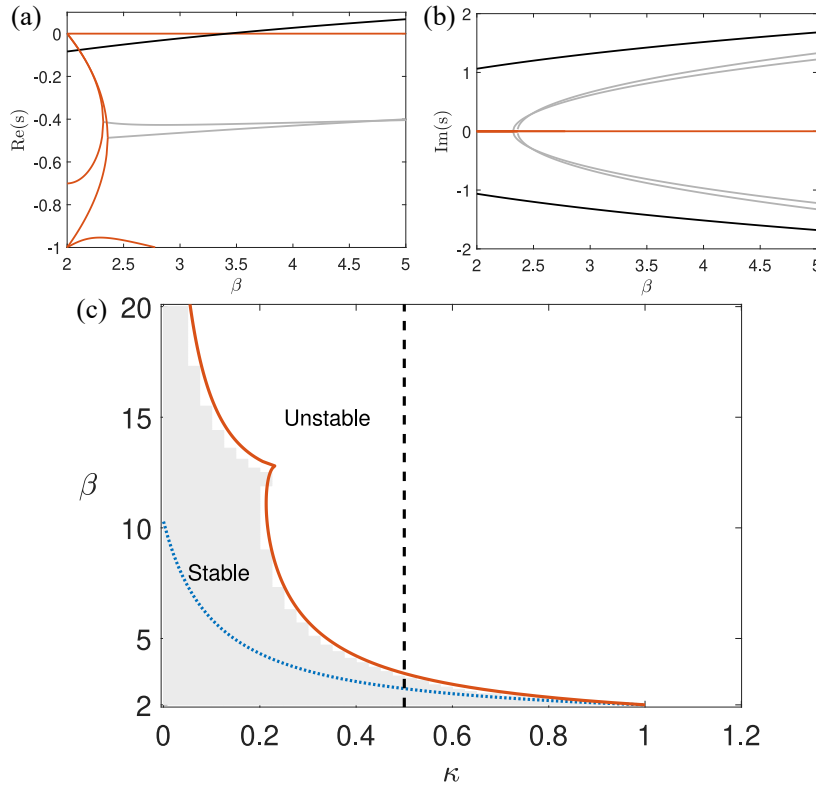


Figure 6.5 : Parallel walkers: (a) Real and (b) Imaginary part of the poles as functions of  $\beta$  at  $\kappa = 0.5$  for the first parallel walking solution  $(\mathcal{D}_1(\beta), \mathcal{U}_1(\beta))$ . Red curves show purely real poles. The black curve indicates the pole (complex conjugate) which first crosses  $\text{Re}(s) = 0$  resulting the bifurcation from parallel walkers to oscillating walkers. The grey curves indicate other complex conjugate poles. (c) Stability diagram of parallel walkers in the  $\beta$ - $\kappa$  parameter space for the first parallel walking solution  $d = \mathcal{D}_1(\beta)$  and  $u = \mathcal{U}_1(\beta)$ . The red curve divides the parameter space into an unstable region (above and to the right) and a stable region. The vertical dashed line corresponds to  $\kappa = 0.5$ . The grey shading indicates the region where parallel walkers are observed in figure 6.1 where a reduced time step of  $\Delta t = 2^{-8}$  was used for simulations with  $\kappa \leq 0.225$  and  $\Delta t = 2^{-6}$  for all the other simulations. It can be seen that the shaded region nearly coincides with the analytical bifurcation curve (red curve). The blue dotted curve indicates the bifurcation from stationary states to inline oscillations from figure 6.2(c).

Note that different modes are the first to become unstable across the two stability curves shown that meet at  $\kappa \approx 0.23$ . For  $\kappa \gtrsim 0.23$  (lower curve), simulations suggest the bifurcation results in oscillating walkers as shown in figure 6.1, while for  $\kappa \lesssim 0.23$  back-and-forth walkers are observed just above the bifurcation curve. These often become unbound in simulations.

## 6.7 Oscillating walkers

Parallel walkers bifurcate into oscillating walkers, as observed in the parameter space plot in figure 6.1. In this mode, the droplets oscillate towards and away from one another while walking. This state has been observed experimentally for walkers [9, 10] and for superwalkers (see figure 3.11).

The first mode to appear when parallel walkers bifurcate into oscillating walkers has symmetric motion of the droplets relative to the trajectory of their centre of mass. In figure 6.6, we plot the numerically simulated trajectory of such walkers, along with the underlying wave field, near the bifurcation from parallel walking. When the droplets are relatively far apart, the wave field of each droplet is discernible. However, when the droplets approach each other, their combined wave field generates a wave barrier. Note that the oscillations are primarily in the direction along the line joining the two droplets, although small oscillations also appears in the walking direction. These two components of the oscillations are completely out of phase. As  $\beta$  is increased for fixed  $\kappa$  for these walkers, the amplitude of the oscillations grows until a new, lopsided oscillating mode appears, as described below in Section 6.7.1.

Oscillating walkers that don't directly bifurcate from parallel walkers also appear for  $\beta$  values immediately above the tongue of unbound states at moderately small  $\beta$  and moderately large  $\kappa$  where inertia is too large for the droplets to be contained by the relatively weak wave field. These are similar in structure to those bifurcating from parallel walkers, except that as  $\beta$  increases their amplitude continues to increase, their inertia is sufficient to overcome the central wave barrier and they begin interchanging positions, as described below in Section 6.7.2.

### 6.7.1 Lopsided walkers

At moderately small  $\beta$ , symmetrically oscillating parallel walkers bifurcate to an asymmetrically oscillating mode as shown in figure 6.7. These asymmetries can be pronounced as shown, or can be more subtle with standard oscillations that are no longer perpendicular to the direction of motion. In all cases, the centre of mass of the two-droplet system now also oscillates. Where these modes are observed, they switch from an initial symmetrically oscillating state. Except near the  $\beta$  value where this mode is first observed, this switch is accompanied by an abrupt change in average direction of walking. This abrupt change in direction is a pre-cursor to discrete-turning walkers described in Section 6.8.2.

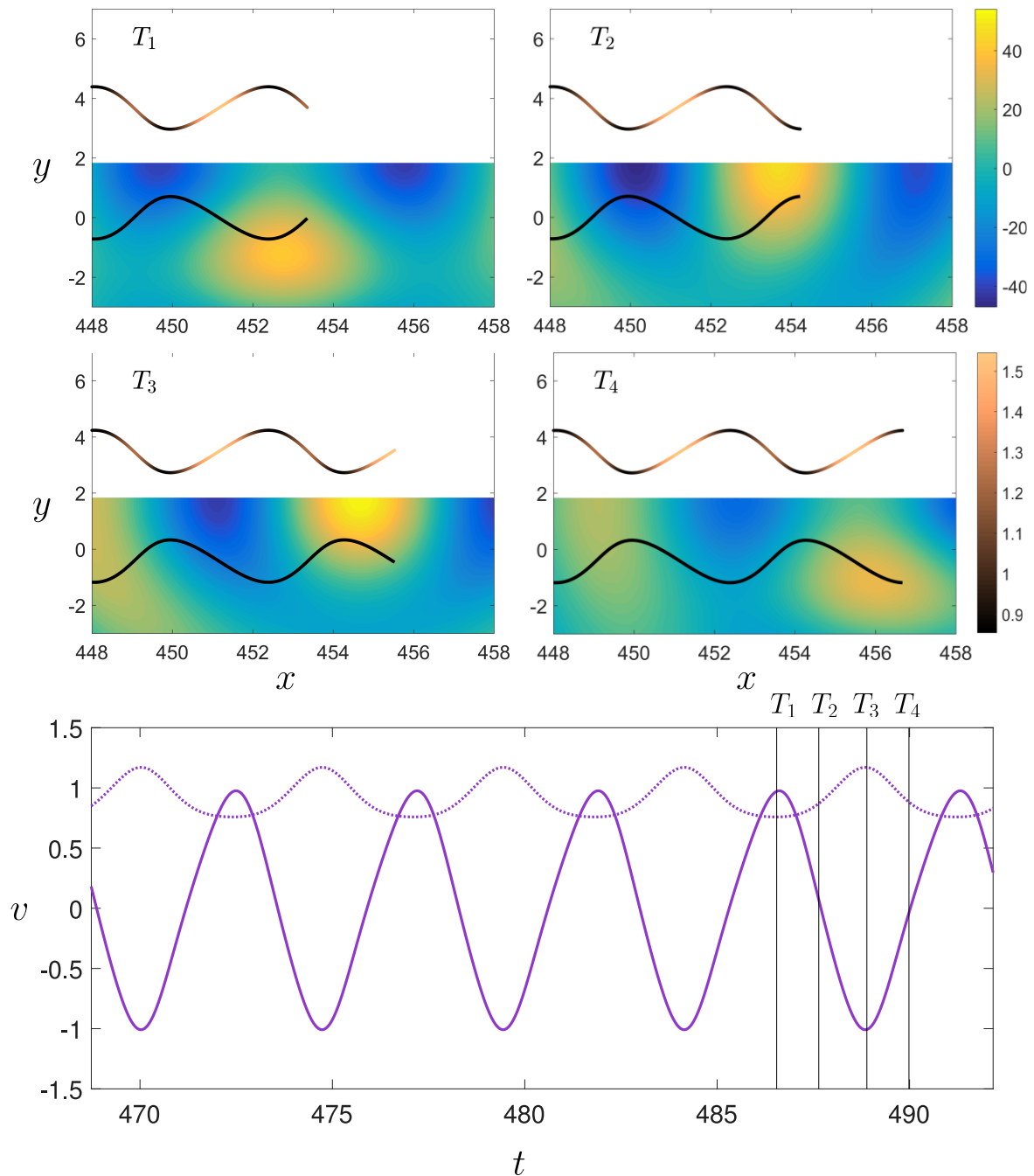


Figure 6.6 : Oscillating walkers: Droplet locations (curves), walking speed (shading on the curve in the upper half plane) and wave field elevation (colour maps in the lower half plane) at the instant of minimum forward velocity ( $T_1$ ), an intermediate time ( $T_2$ ), the instant of maximum forward velocity ( $T_3$ ) and a final intermediate time ( $T_4$ ) for  $\beta = 3.6$  and  $\kappa = 0.5$ . The bottom panel shows the inline (solid curve) and transverse (dotted curve) velocities of the droplet in the lower half plane.

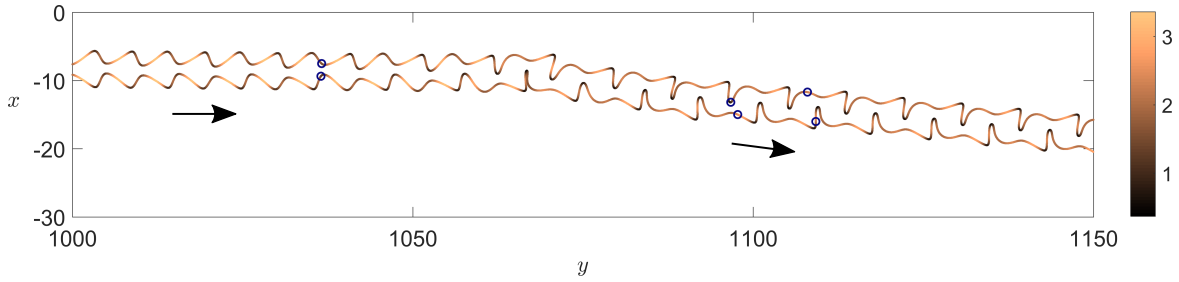


Figure 6.7 : Lopsided oscillating walkers: Trajectory for lopsided oscillating walkers for  $\kappa = 0.4$  and  $\beta = 6.7$ . The colour bar shows the speed of the droplets at the given location on the trajectory. In this simulation, the oscillating walker began in a symmetrically oscillating mode and made an abrupt turn on emergence of asymmetric oscillations. Circles show the positions of the droplets at a few different instances in time.

### 6.7.2 Switching walkers

In a tongue of parameter space in the range  $7 \lesssim \beta \lesssim 12$  and  $0.4 \lesssim \kappa \lesssim 1.8$ , switching walkers are observed. These are symmetrically oscillating walkers whose amplitude is sufficient to result in the droplets interchanging positions.

Intertwined regions of periodic and chaotic switching are found and shown in figure 6.8. There are two main types of periodic switching: In the first, the amplitude of oscillations is constant and switching taking place periodically. In the second, the amplitude changes periodically in addition to the periodic switching. Typical trajectories for each type are shown in figures 6.8(a) and (b). In most of the periodic switching trajectories, the droplets switch after every oscillation although higher-period switching is also observed.

Switching of droplets also occurs in a chaotic fashion. The chaos can either be just in the amplitude with regular switching or in both the amplitude and the switching of the oscillating walkers as shown in figures 6.8(c) and (d) respectively. Figures 6.8(e) and (f) show the first return map of the maximum distance  $d_{k+1}$  as a function of  $d_k$  for the chaotic trajectories shown. The return map is multi-valued when there is chaos in both amplitude and switching, while it is single valued for the case when there is chaos only in the amplitude. Moreover, the former seems to show hints of stretching and folding similar to a Smale horseshoe map [104].

We emphasise that such modes are unphysical because the two droplets occupy the same location as they cross their centre line. However, in the physical system, this may correspond to droplets bouncing off each other rather than switching, and this has been observed for promenading pairs of superwalkers (see figure 3.11). To capture

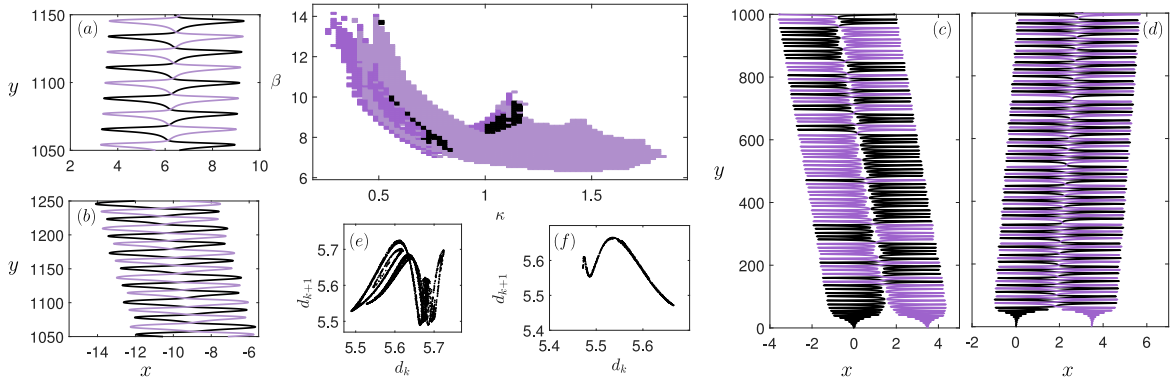


Figure 6.8 : Switching walkers: (center panel) Parameter space diagram for switching walkers indicating periodic switching and periodic (and constant) amplitude changes (light purple), periodic switching and chaotic amplitude changes (black) and chaotic switching and chaotic amplitude changes (purple). Representative trajectory plots show (a) periodic switching with constant amplitude ( $\kappa = 0.5$  and  $\beta = 9.4$ ), (b) periodic switching with amplitude changes repeating every 3 oscillations ( $\kappa = 1.2$  and  $\beta = 9.7$ ), (c) chaotic amplitude modulations and chaotic switching ( $\kappa = 0.5$  and  $\beta = 9.1$ ) and (d) chaotic amplitude modulation and regular switching ( $\kappa = 0.575$  and  $\beta = 9.9$ ). (e,f) First return map of the maximum distance  $d_{k+1}$  in the  $k + 1$ st oscillation as a function of the maximum distance  $d_k$  in the  $k$ th oscillation for trajectories (c,d). The map is single-valued for trajectories with chaos only in the amplitude, while it is multi-valued for trajectories with chaos in both amplitude and switching.

this, perhaps the interaction between two nearly touching droplets would need to be included in the governing model.

## 6.8 Wandering walkers

More exotic behaviours are observed in the simulations once they begin to deviate from on-average straight-line walking. A detailed analysis of these is beyond the scope, but here we describe some of the more interesting features.

### 6.8.1 Back-and-forth walkers

These are rare states found for small inertia,  $\kappa < 0.25$ , and occur shortly after parallel walkers become unstable. The droplets in these trajectories walk as oscillating walkers but they reverse their direction of walking after several oscillations (see figure 6.9). This type of dynamics seems to be unstable and although observed at intermediate times in most of the simulations in this region of parameter space, the droplets usually unbind before the end of the simulation.

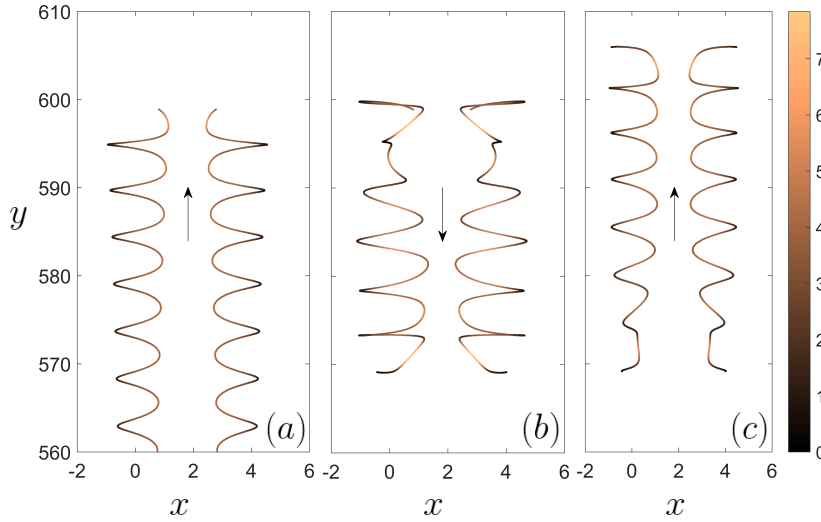


Figure 6.9 : Back-and-forth walkers: Trajectory of back-and-forth oscillating walkers at  $\kappa = 0.1$  and  $\beta = 15.1$ . (a) Initial motion for  $0 < t \lesssim 210.9$ , (b) the pair reverse their direction for  $210.9 \lesssim t \lesssim 226.5$  and (c) reverse it again for  $226.5 \lesssim t \lesssim 242.2$ . The colour bar indicates the speed of the droplets.

## 6.8.2 Discrete-turning walkers

The bifurcations from parallel walkers to (symmetrically) oscillating walkers to lopsided walkers culminate in discrete-turning walkers in a narrow region near  $0.4 \lesssim \kappa \lesssim 0.6$  and  $3 \lesssim \beta \lesssim 8$ . In this regime, the two droplets perform repeated quantised turns after walking in an on-average straight line for some distance. Figure 6.10(a) shows a typical trajectory. In Figures 6.10(b) and (c), we show two phase-space projections illustrating the lead-up to discrete-turning walkers with variables of the distance  $d$  between the two droplets, the speed  $u$  of the droplets in the direction of the line joining them and  $\cos(\theta)$  the cosine of the angle between the velocity of the centre of mass and the line joining the droplets. Relevant equilibria of the  $\mathcal{D}_1$  and  $\mathcal{D}_2$  parallel walking modes and the  $\mathcal{D}_2$  chasing mode (see Section 6.9) are indicated as black filled circles and crosses. In the trajectory shown in figure 6.10(a), the droplets start out as symmetrically oscillating walkers and make multiple discrete turns before settling into a stable lopsided motion. The limit cycle associated with walkers oscillating symmetrically around the  $\mathcal{D}_1$  equilibrium is shown by the purple curves and the stable lopsided walkers are shown by the navy blue curves. Turns are shown in yellow. When a pair of symmetrically oscillating walkers attempts to transition from the symmetric mode to the lopsided, it gets flung towards the chasing fixed point in the phase space as shown in figure 6.10(c). This fixed point being unstable, brings the droplets back to

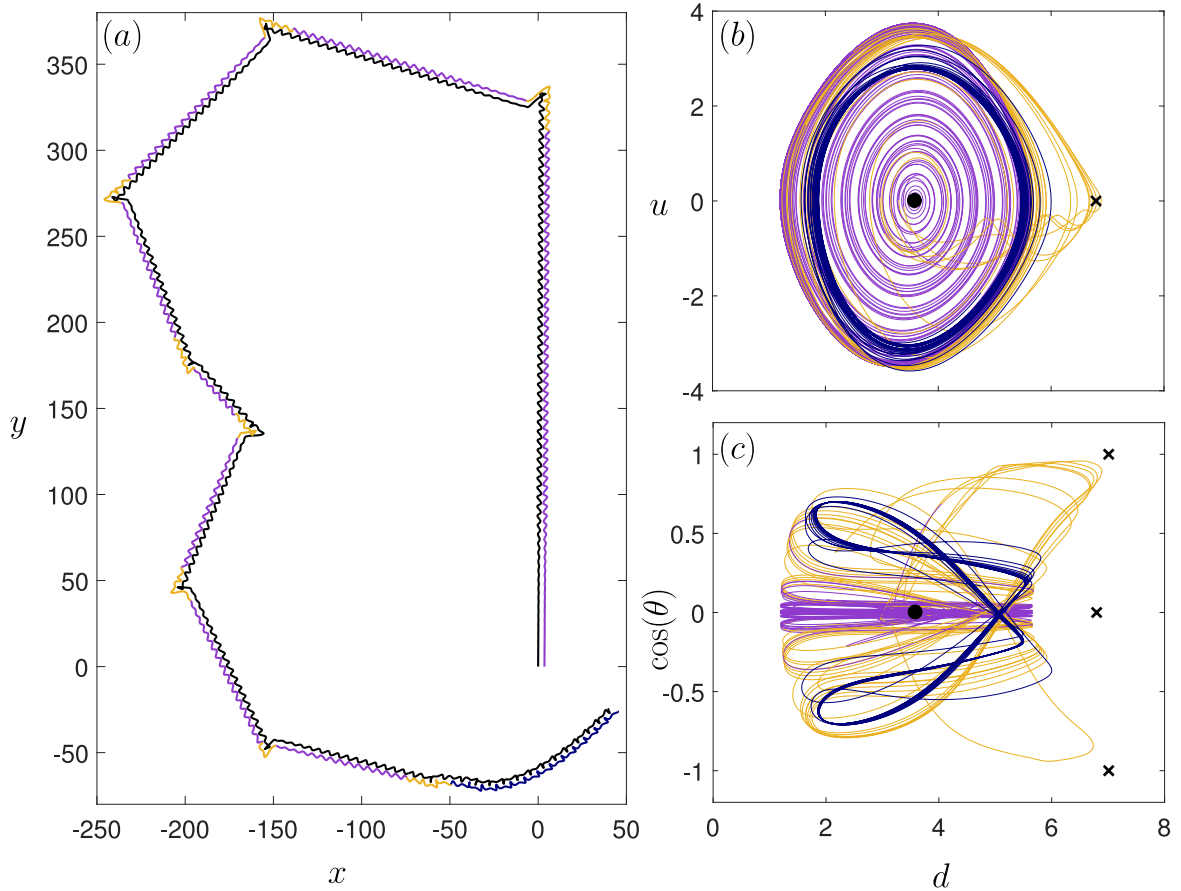


Figure 6.10 : Emergence of discrete turning walkers: (a) Trajectory at  $\kappa = 0.5$  and  $\beta = 5.3$  showing symmetrically oscillating walkers (purple) making multiple discrete turns and eventually settling into a lopsided mode (navy blue). The transient behaviour during the discrete turns is shown as yellow. Projections of phase space dynamics in (a)  $u$ - $d$  and (b)  $\cos(\theta)$ - $d$  plane where  $u$  is the speed of the droplet in the direction of the line joining the droplets,  $d$  is the distance between the droplets and  $\cos(\theta)$  is the cosine of the angle between the velocity of the centre of mass and the line joining the droplets. Relevant equilibria of the  $\mathcal{D}_1$  (black filled circle) and  $\mathcal{D}_2$  (black cross) parallel walking modes and the  $\mathcal{D}_2$  (black cross) chasing mode (see Section 6.9) are indicated.

the symmetrically oscillating walkers mode at  $\mathcal{D}_1$ . This loop near the chasing fixed point in the phase space corresponds to the actual turn in the trajectory.

As  $\beta$  is increased, it appears that the loops towards the chasing mode begin to dominate and the two droplets briefly chase one another before decaying either to the  $\mathcal{D}_1$  or the  $\mathcal{D}_3$  parallel walking fixed point. When it goes to the  $\mathcal{D}_3$  parallel walking fixed point, it is accompanied by a turn which is nearly right angled and then cascades back to the parallel walking distance  $\mathcal{D}_1$  as symmetrically oscillating walkers. We call these right-angled discrete turning walkers and they are shown in figure 6.11.

The underlying wave field shows that the turns are due to one of the walkers being reflected from a wave barrier. On studying the statistics of the turning angles, we find a strong peak near  $90^\circ$  (figure 6.11(d)), which is also evident from the trajectories. Nearly right-angled turns are observed for all simulations in this region. At larger scales, the trajectory appears like a random walk (figure 6.11(a)). By calculating the mean squared displacement as a function of time for an ensemble of simulations at  $\kappa = 0.5$  and  $\beta = 6$ , we find a sub-diffusive exponent of  $0.815 \pm 0.002$ . Such discrete turning behaviour has been observed for a single floating water droplet on the surface of a vertically vibrated bath of high-viscosity silicone oil [105].

A region of discrete-turning walkers is also observed in a small window at  $\kappa \approx 0.4$  and  $\beta \approx 11$ . These behave similarly, except they tend to walk in straight lines for longer before abruptly turning. A larger region of discrete-turning walkers is observed between  $1 \lesssim \kappa \lesssim 2.5$  and  $\beta \gtrsim 7$ . These are switching walkers and a typical trajectory is shown in figure 6.12(a). Note that in these trajectories, the droplets do not necessarily occupy the same location at the same time.

Discrete-turning walkers are not always stable. When they are unstable, they typically unbind (as indicated in the mixed grey/green region in figure 6.1), although occasionally they cascade into tight orbits. These are reminiscent of cascades from oscillating walkers to orbits that have been observed in experiments with walkers [10].

### 6.8.3 Continuously turning walkers

For larger inertia, these abrupt discrete turns become smoothed, as shown in the progression of trajectories for increasing  $\kappa$  and fixed  $\beta$  in figure 6.12. For sufficiently large inertia, the turns become a series of loops and eventually closed circles. Note that for  $\kappa \lesssim 2.5$ , the droplets switch positions. Although their trajectories cross, they do not necessarily occupy the same position at the same time.

### 6.8.4 Closed trajectories and nearly closed trajectories

Remarkably, we find that initially parallel walkers travelling in a straight line can ultimately settle into closed trajectories. Such states are primarily observed at high inertia as indicated by the pink region in the parameter space plot figure 6.1. In this region, the trajectories are circles, as shown in a representative plot in figure 6.12(d).

Circular closed trajectories also appear near  $0.4 \lesssim \kappa \lesssim 0.6$  and  $\beta \approx 4$  or  $\beta \approx 9$ . In the former region, the droplet mode is a lopsided oscillation as shown in figure 6.13(a), while in the latter it is a symmetric oscillation. Rare regular polygons also appear in

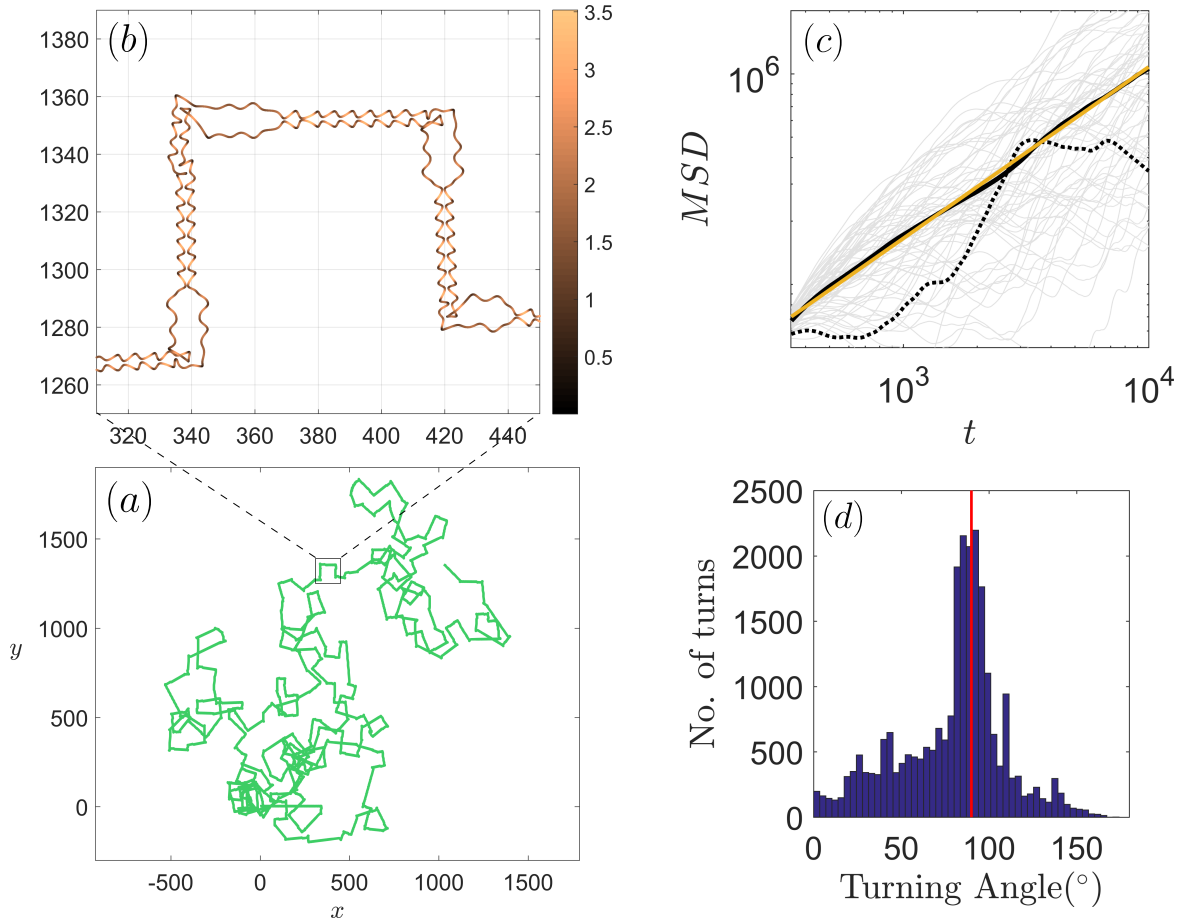


Figure 6.11 : Right-angled discrete-turning walkers: (a) Trajectory at  $\kappa = 0.5$  and  $\beta = 6$  indicating random walk-like behaviour. (b) Focusing on individual turns indicates that oscillating walkers at  $\mathcal{D}_1$  temporarily go to  $\mathcal{D}_3$  before cascading back to  $\mathcal{D}_1$ . The colour bar indicates the speed of the droplets. (c) Mean squared displacement (MSD) versus time: individual trajectories are shown as light grey curves, the trajectory in (a) is shown as the black dotted curve and the ensemble average over 160 simulations (at  $\kappa = 0.5$  and  $\beta = 6$  with noise in initial conditions) is shown as the solid black curve. Curve fitting suggests the diffusion exponent is  $0.815 \pm 0.002$  (solid yellow line), indicating sub-diffusive behaviour. (d) Distribution of turning angles from the ensemble of simulations indicates a strong peak near  $90^\circ$  (red vertical line).

isolation in the parameter space, including a hexagon (figure 6.13(c)), an octagon (not shown) and a nonagon (figure 6.13(d)). In the closed-trajectory region near  $\kappa \approx 1.8$  and  $\beta \gtrsim 15$ , smoothed star-shaped trajectories are observed such as the exterior of an enneagram (see figure 6.13(b)). Polygonal orbits have been previously observed for diametrically opposed orbiting walkers [89], but the closed trajectories we observe here are much larger in extent. We note that these polygonal structures are very sensitive

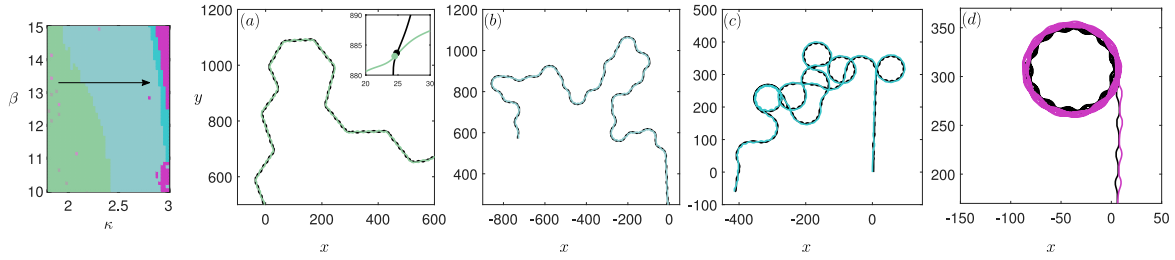


Figure 6.12 : Wandering walkers:  $\beta$ - $\kappa$  parameter space plot along with a progression of trajectories at fixed  $\beta = 13$  showing the transition from discrete-turning walkers to closed trajectories. (a) Discrete-turning walkers at  $\kappa = 1.9$  become (b) continuously turning walkers at  $\kappa = 2.5$  leading to (c) circular loops at  $\kappa = 2.825$  and eventually (d) stable circular trajectories at  $\kappa = 3$ . The droplets are not always side-by-side during this wandering motion, this is shown in inset of (a) where the droplets do not reach the crossing point simultaneously.

to the numerical time step chosen, and we have not been able to reproduce them at smaller time steps although we can reliably reproduce them with different initial conditions. We think this is because the parameters at which they form change slightly with the modified time step and we have not been able to find the exact values at which they reappear.

Intriguingly, in all closed trajectories, only the waves from the previous two oscillations of the droplets have not decayed to less than a tenth of their initial value (estimated from the location of the droplets two units of time earlier, where the exponential decay of the amplitude is  $e^{-2} \approx 1/10$ ). In particular for the polygonal paths, this suggests that the waves from the previous turn are not directly contributing to the next turn. However, a “memory” of the previous turn is retained by the system as shown in figure 6.13(e): the droplets are not walking symmetrically with the inner droplet on a turn leading its partner along the edges.

## 6.9 Chasers

Consider two in-phase droplets chasing one another in one-dimensional motion at a constant speed  $u$  and maintaining a constant separation  $d$ :  $\mathbf{x}_1 = (ut, 0)$  and  $\mathbf{x}_2 = (ut + d, 0)$ . Substituting these forms into equation (6.1), we obtain the following pair of equations:

$$u = \beta \left( \int_0^\infty J_1(uz) e^{-z} dz + \int_0^\infty J_1(uz \mp d) e^{-z} dz \right). \quad (6.7)$$

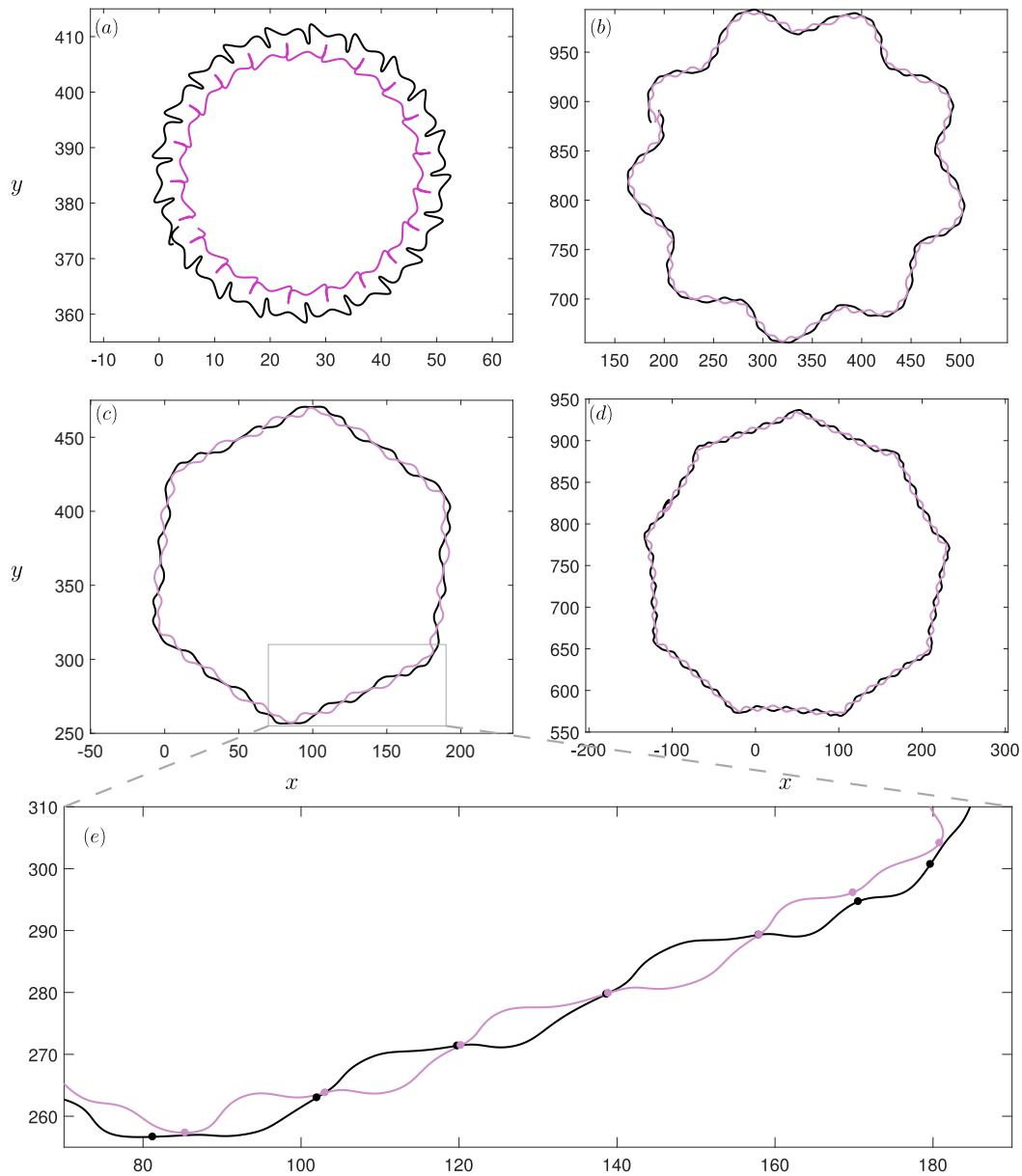


Figure 6.13 : Closed trajectories: (a) Closed circles with lopsided walkers for  $\kappa = 0.6$  and  $\beta = 4$ , (b) exterior of an enneagram for  $\kappa = 1.875$  and  $\beta = 18$ , (c) hexagon for  $\kappa = 1.85$  and  $\beta = 14.2$ , and (d) nonagon for  $\kappa = 1.575$  and  $\beta = 16$ . The polygonal structures were only traversed two or three times before the end of a simulation (only one traverse is plotted to show the structure), except for the hexagon where we have extended the simulation to 43 traverses. In all cases, some precession was apparent. (e) One side of the hexagon showing that the droplets are not always side-by-side and hence do not always approach the crossing point simultaneously.

Here the first integral represents the force on the droplet due to its own wave field while the second integral is the force from the other droplet's wave field.

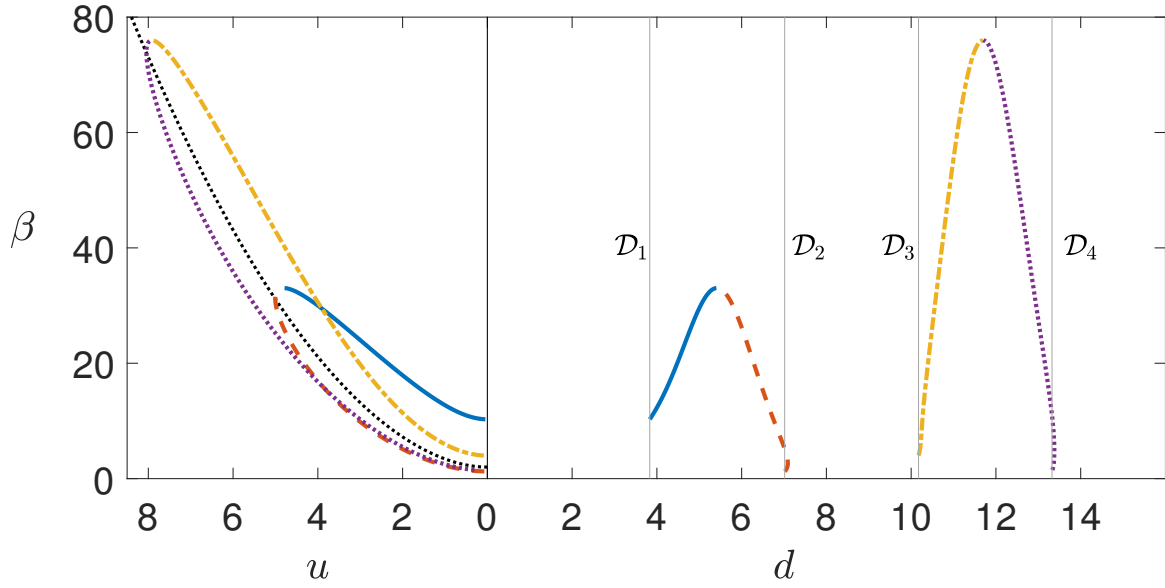


Figure 6.14 : Chasers: Equilibrium solutions  $u = \mathfrak{U}_n(\beta)$  and  $d = \mathfrak{D}_n(\beta)$  for  $n = 1$  (solid blue curve), 2 (dashed red curve), 3 (dashed-dotted yellow curve) and 4 (dotted purple curve). The black dotted curve shows the speed for a single walker. The grey vertical lines are the stationary state equilibrium distances.

Figure 6.14 shows the numerical solutions of equation (6.7) as a function of  $\beta$  (solutions are independent of  $\kappa$ ). There are infinitely many solution pairs  $u = \mathfrak{U}_n(\beta)$  and  $d = \mathfrak{D}_n(\beta)$ . Each solution pair only exists for a window of  $\beta$  values. The solution first emerges from the corresponding stationary state solution at  $\beta = \beta_n^c$  with  $\mathfrak{U}_n = 0$  and  $\mathfrak{D}_n = \mathcal{D}_n$ . Pairs of solution pairs coincide and annihilate one another in a saddle-node bifurcation at the upper end of the window.

### 6.9.1 Linear stability analysis

To understand the stability of this mode, we consider a general perturbation to a pair of droplets in the chasing mode applied at  $t = 0$  as follows:  $\mathbf{x}_1 = (ut + \epsilon x_{11}(t)H(t), \epsilon y_{11}(t)H(t))$  and  $\mathbf{x}_2 = (ut + d + \epsilon x_{21}(t)H(t), \epsilon y_{21}(t)H(t))$ , similar to the analysis for parallel walkers. Substituting this form into equation (6.1) and linearising, we find

$$\kappa\ddot{x}_{i1} + \dot{x}_{i1} = \beta \left[ \left( \int_0^\infty (J'_1(uz) + J'_1(uz \mp d))e^{-z} dz \right) x_{i1}(t) - \int_0^\infty J'_1(uz)x_{i1}(t-z)H(t-z)e^{-z} dz - \int_0^\infty J'_1(uz \mp d)x_{j1}(t-z)H(t-z)e^{-z} dz \right]$$

$$\kappa\ddot{y}_{i1} + \dot{y}_{i1} = \beta \left[ \left( \int_0^\infty \left( \frac{J_1(uz)}{uz} + \frac{J_1(uz \mp d)}{uz \mp d} \right) e^{-z} dz \right) y_{i1}(t) - \int_0^\infty \frac{J_1(uz)}{uz} y_{i1}(t-z)H(t-z)e^{-z} dz - \int_0^\infty \frac{J_1(uz \mp d)}{uz \mp d} y_{j1}(t-z)H(t-z)e^{-z} dz \right]$$

for  $i = 1, j = 2$  with the negative signs, and  $i = 2, j = 1$  with the positive signs.

On taking Laplace transforms of both sides, the equations can be rewritten in the matrix form

$$\mathbf{A}_{\text{chase}}(s)\mathbf{X}(s) = \mathbf{X}_0(s),$$

where

$$\mathbf{X}(s) = \begin{bmatrix} X_{11}(s) \\ Y_{11}(s) \\ X_{21}(s) \\ Y_{21}(s) \end{bmatrix}, \quad \mathbf{X}_0(s) = (s+1)\mathbf{x}(0) + \dot{\mathbf{x}}(0),$$

and

$$\mathbf{A}_{\text{chase}}(s) = (\kappa s^2 + s)\mathbf{I}_4 + \beta\mathbf{K}(s).$$

Here  $x_{i1}(t)$  and  $y_{i1}(t)$  are the dynamical variables in the time domain and  $X_{i1}(s)$  and  $Y_{i1}(s)$  are the dynamical variable in Laplace space with

$$\mathbf{K}(s) = \begin{bmatrix} \mathbf{B}(s) - \mathbf{A}_- & 0 & \mathbf{C}_-(s) & 0 \\ 0 & \mathbf{E}(s) - \mathbf{D}_- & 0 & \mathbf{F}_-(s) \\ \mathbf{C}_+(s) & 0 & \mathbf{B}(s) - \mathbf{A}_+ & 0 \\ 0 & \mathbf{F}_+(s) & 0 & \mathbf{E}(s) - \mathbf{D}_+ \end{bmatrix},$$

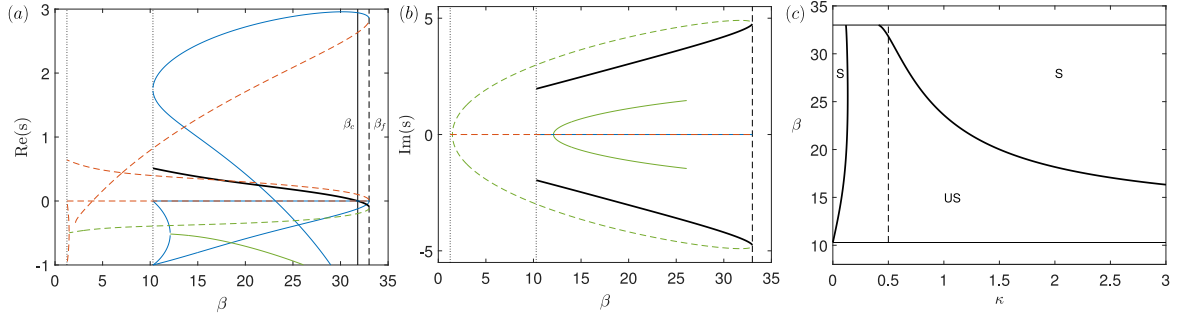


Figure 6.15 : Chasers: Plot of the (a) real and (b) imaginary part of the poles as a function of  $\beta$  at  $\mathfrak{D}_1(\beta)$  (solid curves) and  $\mathfrak{D}_2(\beta)$  (dashed curves) with  $\kappa = 0.5$ . The vertical black dotted lines correspond to the start of solution at  $\mathfrak{D}_1(\beta)$  and  $\mathfrak{D}_2(\beta)$  while the vertical black dashed line corresponds to the end of the chasing solution at  $\beta = \beta_f$ . Poles with imaginary parts are shown in green. The thick black solid curve corresponds to the pole from inline perturbation for which  $\text{Re}(s) < 0$  for  $\beta_c < \beta < \beta_f$  where  $\beta_c$  (vertical black solid line) is where it first crosses  $\text{Re}(s) = 0$ . This pole is a complex conjugate as indicated by the thick black curves in (b) and its stability in the  $\beta$ - $\kappa$  parameter space is shown in (c) where the stable and unstable regions are indicated by S and US respectively. The dashed vertical line at  $\kappa = 0.5$  in (c) corresponds to the plots in (a) and (b).

and

$$\begin{aligned}
 A_{\mp} &= \int_0^{\infty} (J_1'(uz) + J_1'(uz \mp d)) e^{-z} dz, \\
 D_{\mp} &= \int_0^{\infty} \left( \frac{J_1(uz)}{uz} + \frac{J_1(uz \mp d)}{uz \mp d} \right) e^{-z} dz, \\
 B(s) &= \mathcal{L} \left\{ J_1'(ut) e^{-t} \right\}, \quad C_{\mp}(s) = \mathcal{L} \left\{ J_1'(ut \mp d) e^{-t} \right\}, \\
 E(s) &= \mathcal{L} \left\{ \frac{J_1(ut)}{ut} e^{-t} \right\} \quad \text{and} \quad F_{\mp}(s) = \mathcal{L} \left\{ \frac{J_1(ut \mp d)}{ut \mp d} e^{-t} \right\},
 \end{aligned}$$

where  $\mathcal{L}$  is the Laplace transform operator.

Figures 6.15(a) and (b) shows the real  $\text{Re}(s)$  and imaginary  $\text{Im}(s)$  part of the poles of  $\mathbf{X}(s)$  as a function of  $\beta$  for chasing walkers at distance  $\mathfrak{D}_1(\beta)$  and  $\mathfrak{D}_2(\beta)$  with  $\kappa = 0.5$ . Note that the zero eigenvalue reflects the invariant properties of the base state. There is always a transverse mode with  $\text{Re}(s) > 0$  for both  $\mathfrak{D}_1(\beta)$  and  $\mathfrak{D}_2(\beta)$  indicating that the chasers are always unstable for general perturbations. This hold true for all  $\kappa$ . For  $\mathfrak{D}_1(\beta)$ , we see that the only unstable eigenvalue (complex conjugate) corresponding to the inline perturbation crosses  $\text{Re}(s) = 0$  around  $\beta = \beta_c \approx 31$  indicating that droplets are stable to inline perturbations for  $\beta_c < \beta < \beta_f$  and chasers will be realised

if restricted to only one space dimension, where  $\beta_f$  is where the chasing solution terminates. A stability diagram in the  $\beta$ - $\kappa$  parameter space indicating the stable and unstable region to inline perturbations at  $\mathfrak{D}_1(\beta)$  is shown in figure 6.15(c).

Although in our analysis, we find that chasers are unstable to general perturbations, Durey and Milewski [63] in their theoretical analysis found that two-droplet trains (equivalent to chasers) are unstable for identical, in-phase droplets with general perturbations but can become stable for out-of-phase droplets. We also note that chasers have been observed in experiments with superwalkers where the droplets bounce in-phase (see figure 3.10). Moreover, by adding a spatial decay to the wave in the theoretical model presented in this chapter, we are able to observe chasers in numerical simulations for in-phase droplets as will be shown in Chapter 7.

## 6.10 Conclusion

In this chapter, we have taken the stroboscopic mode of Oza et al. [88] as a theoretical pilot-wave description and explored the remarkable range of possible behaviours for a pair of droplets initially walking in parallel. With increasing inertia  $\kappa$  and/or wave forcing  $\beta$ , the droplets' motion gains degrees of freedom, commencing from a stationary pair where drag dominates both inertia and wave forcing. The droplets first gain a single translational degree of freedom, either oscillating in place for larger  $\kappa$  or parallel walking at constant speed and constant separation for larger  $\beta$ . For larger  $\beta$  and moderate  $\kappa$ , both modes are apparent and the droplets oscillate towards and away from one another with their centre of mass moving in a straight line. For larger  $\beta$  still, the droplets perform this motion with random changes in direction by  $180^\circ$  before gaining an additional degree of freedom with increased  $\kappa$  by taking discrete turns of less than  $180^\circ$  while walking. With sufficient inertia, these turns eventually become continuous. Surprisingly, we find that droplets only unbind if the wave forcing  $\beta$  is large and inertia  $\kappa$  is moderately small or in a narrow tongue where  $\beta$  is small and  $\kappa$  moderately large. For large  $\beta$  and  $\kappa$ , the states observed at long times are intriguing: closed trajectories with effective diameters many tens of Faraday wavelengths and many times the wavelengths of the droplets' oscillations towards and away from one another. These closed trajectories can be either regular polygons or circles.

Our investigation has reproduced the states that have been observed experimentally such as inline oscillations, orbiting droplets, parallel walkers and symmetrically oscillating walkers (promenading pairs). Our simulations agree quantitatively with where oscillating walkers have been observed (white curve in figure 6.1) except at the

highest memories. Parameters for existing experimental setups are restricted to a wedge of parameter space between the white dashed curves in figure 6.1. Besides the experimentally observed states, we predict switching modes, discrete-turning walkers and closed circular trajectories in this region. Switching walkers are unlikely to be observed in the form described here and the droplets might either bounce off one-another, coalesce, or possibly continue walking as a condensed pair (as seen for superwalkers in figures 3.9 and 3.11). The important facet of an evolving impact phase in experiments may modify or even suppress any turning mode. It would be interesting to explore whether any of the behaviours are realised.

# Chapter 7

## Two-droplet correlations

In this chapter, we present a numerical study of two-droplet pair correlations for in-phase droplets walking on a vibrating bath. Two such walkers are launched toward each other at an angle with different initial path differences. As they approach each other, their underlying waves may overlap and the droplets have a non-zero probability of forming a two-droplet bound state. The likelihood of such pairing is quantified by measuring the probability of finding the droplets in a bound state at late times. Three generic types of two-droplet correlations are observed: promenading, orbiting, and chasing pair of walkers. For certain parameters, the droplets may become correlated for certain initial path differences and remain uncorrelated for others, while in other cases, the droplets may never produce droplet bound states. These observations pave the way for further studies of strongly correlated multi-droplet behaviours in the hydrodynamical quantum analogues of walking and superwalking droplets.

This chapter is based on the following published paper:

R. N. Valani, A. C. Slim and T. Simula, *Hong–Ou–Mandel-like two-droplet correlations*, *Chaos* **28**, 096104 (2018).

### 7.1 Introduction

In quantum mechanical systems, particle correlations are of fundamental importance. The Einstein–Podolsky–Rosen paradox [106] and the Hanbury Brown and Twiss effect [107] are vivid demonstrations of non-classical correlations. Quantum correlations that have no classical counterpart can also be revealed using the Hong–Ou–Mandel (HOM) two-photon interference experiment [108]. In the classic optical HOM effect,

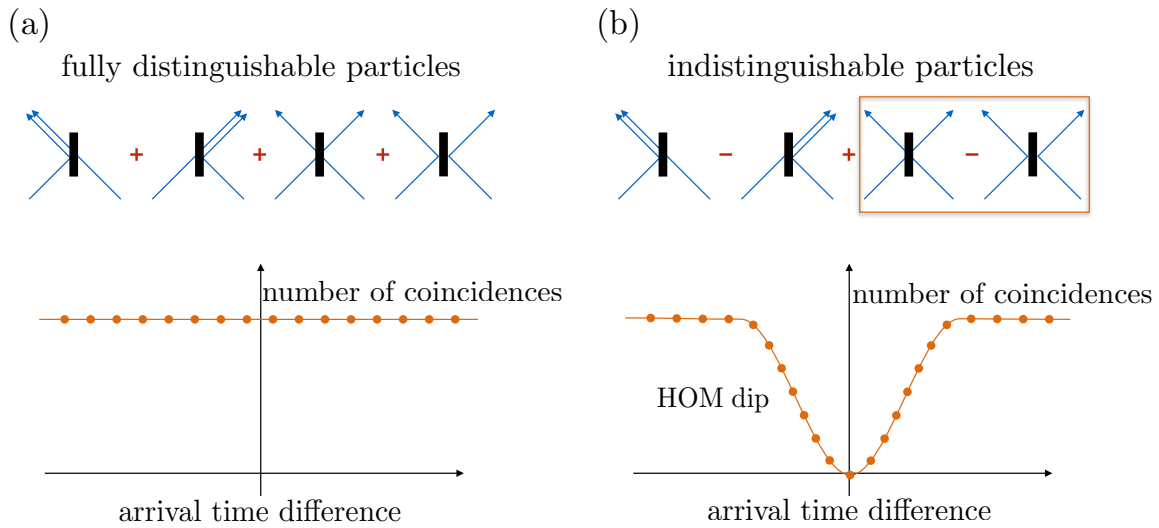


Figure 7.1 : Hong–Ou–Mandel interference of photons. (a) Two distinguishable photons (blue arrows) may be combined in a beam splitter (black bar) in four ways with equal probabilities and the probability of coincident detection (one photon leaving on each side of the beam splitter) is independent of the delay in the time of arrival of the photons at the beam splitter. (b) Two indistinguishable photons may also be combined in a beam splitter in four ways but the quantum amplitudes of ‘neither is reflected’ and ‘both are reflected’ interfere destructively such that no coincident detection is possible when the photon arrival time difference vanishes. This results in the Hong–Ou–Mandel dip in the coincidence detection probability as a function of the time of arrival of the photons at the beam splitter.

illustrated in figure 7.1, two photons (blue arrows) arrive at a ‘50/50’ beam splitter. A single photon, when incident on such a beam splitter, has a 50% probability of being reflected and a 50% probability of being transmitted. When two photons are incident, four possibilities arise: (1) the photon coming from the left is reflected and the photon arriving from the right is transmitted, (2) the photon coming from the right is reflected and the photon arriving from the left is transmitted, (3) both photons are transmitted, and (4) both photons are reflected. Two detectors (not shown) are placed far behind the beam splitter, one on the left and the other on the right side, and record coincident photon pairs (one photon detected by each detector). The normalised number of coincidence detections are recorded as a function of the difference in time of arrival of the photons. If the photons are fully distinguishable (see figure 7.1(a)), all four possibilities occur with equal probabilities and whether the photons pass through the beam splitter simultaneously or one after another is irrelevant. However, if the photons are indistinguishable (see figure 7.1(b)), their quantum mechanical description shows that the last two of the four possible outcomes cancel out—the photons interfere

destructively—and the probability of coincident detection vanishes [109]. One way to continuously ‘tune the level of indistinguishably’ is to vary the distance of the photon sources from the detector and thereby the difference in the photon arrival times. This results in the HOM *dip* shown in figure 7.1(b) whose characteristic width is determined by the size of the wavepacket of the photons. The HOM effect has a classical analogue and a HOM dip is also observable using classical light sources. However, the maximum visibility of the HOM dip cannot exceed 0.5 (the coincidence detection rate at the deepest point of the dip cannot be less than 0.5 of the maximum coincidence detection rate) for classical waves or particles [110]. As such, the HOM effect can be used for drawing a distinction between classical and quantum correlations. More recently, the HOM interference has been observed for photons that always pass through the beam splitter at different times [111] and by using atoms instead of photons [112]. Also, a variant of the HOM experiment in the absence of beam splitters has also been proposed [113].

Inspired by the atomic and optical HOM phenomena, we have performed numerical experiments with two droplets to study their spatiotemporal correlations. Nevertheless, we emphasise that, unlike photons, our droplets are interacting particles and cannot be indistinguishable in the quantum mechanical sense. A simple thought experiment is sufficient to demonstrate this: filling one of the droplets with dye will facilitate tracking the exact paths of the two droplets yet the results presented here would be unaffected by such particle tagging.

## 7.2 Theoretical model

Consider two identical walkers of mass  $m$  and radius  $R$ . The positions (in units of  $k_F^{-1} = \lambda_F/2\pi$ , where  $\lambda_F$  is the Faraday wavelength) of the two droplets in the horizontal plane are given by  $\mathbf{x}_1 = (x_1, y_1)$  and  $\mathbf{x}_2 = (x_2, y_2)$ . To study two-droplet correlations, we describe the horizontal motion of the droplets using the extension of the stroboscopic model of Oza et al. [88] presented in chapter 6 with an added spatial damping that was introduced in the improved stroboscopic model of Oza et al. [89]. We restrict our exploration of two-droplets correlations to in-phase bouncing droplets. The dimensionless equations of horizontal motion for two droplets are thus

$$\kappa \frac{d^2 \mathbf{x}_i}{dt^2} + \frac{d\mathbf{x}_i}{dt} = -\beta \nabla h(\mathbf{x}, t) \Big|_{\mathbf{x}_i} \quad \text{for } i = 1, 2, \quad (7.1)$$

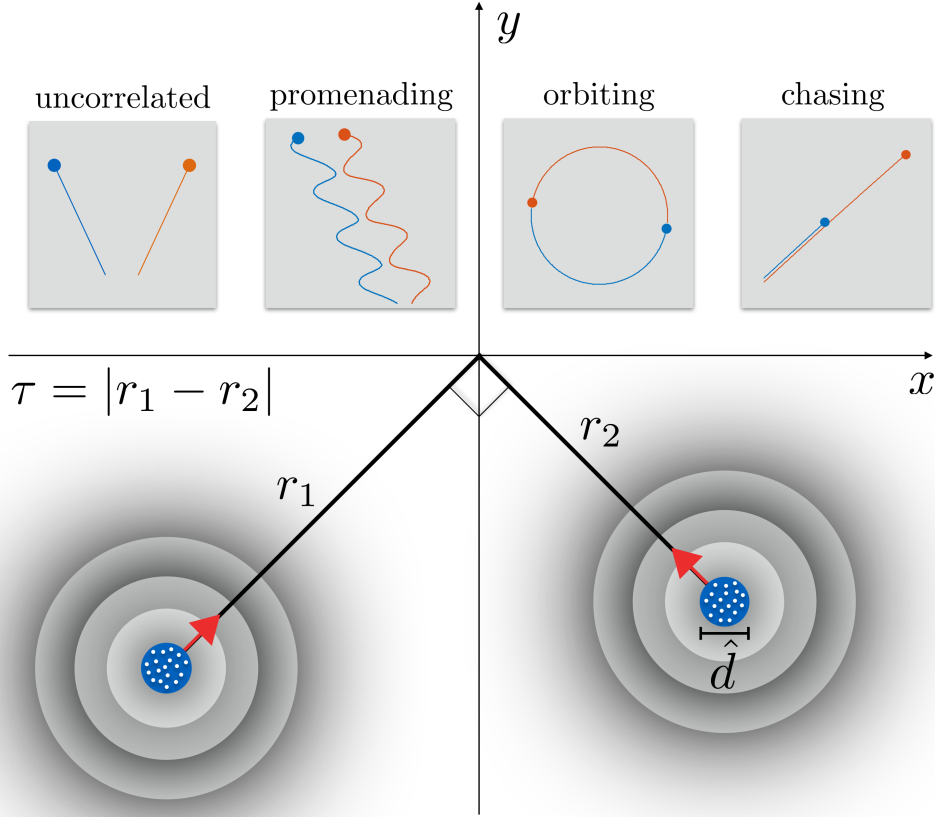


Figure 7.2 : Schematic diagram of the numerical setup. Two identical droplets with a dimensionless diameter  $\hat{d} = 2R/\lambda_F$  each and an initial path difference  $\tau$  are launched towards each other at an angle. The initial centre of mass positions (white dots) of the droplets are randomly chosen within a disk of diameter  $\hat{d}$ . The initial velocities have constant magnitude  $u$  and are always oriented toward the origin. Four generic types of behaviours are observed at late times (top sketches): (i) uncorrelated, (ii) promenading correlations, (iii) orbiting correlations, and (iv) chasing correlations.

with wave field

$$h(\mathbf{x}, t) = \int_{-\infty}^t J_0(|\mathbf{x} - \mathbf{x}_1(s)|) e^{-G_1(\mathbf{x}, t, s)} ds + \int_{-\infty}^t J_0(|\mathbf{x} - \mathbf{x}_2(s)|) e^{-G_2(\mathbf{x}, t, s)} ds, \quad (7.2)$$

and spatial and temporal decay envelope

$$G_j(\mathbf{x}, t, s) = \hat{\alpha} \frac{|\mathbf{x} - \mathbf{x}_j(s)|^2}{t - s + \text{Me}^{-1}} + (t - s) \text{ for } j = 1, 2.$$

The dimensionless parameters  $\kappa$ ,  $\text{Me}$  and  $\beta$  follow directly from the stroboscopic model for a single walker developed by Oza et al. [88] and are given by  $\kappa = m/DT_F\text{Me}$ ,  $\beta = mgAk_F^2T_F\text{Me}^2/D$  and  $\text{Me} = T_d/T_F(1 - \Gamma_f/\Gamma_F)$ , while the parameter  $\hat{\alpha} = \alpha/k_F^2T_F\text{Me}$  follows from Oza et al. [89]. We note that  $\kappa\beta \sim \text{Me}$  and hence one can obtain curves in the  $\beta$ - $\kappa$  parameter space along which memory is constant. Here time has been non-dimensionalised using the scale  $T_F\text{Me}$ .

### 7.2.1 System parameters

We restrict our exploration of the parameter space by fixing the parameters to the typical values for experiments [88, 89, 10] in addition to limiting to in-phase droplets. We consider a fixed forcing frequency of  $f = 80$  Hz and consider droplets of diameter in the range  $0.6 \text{ mm} \leq 2R \leq 1 \text{ mm}$  that are typically found in experiments with walkers [51]. In accordance with the experiments on orbiting [89] and promenading [10] pairs, the fluid density is chosen to be  $\rho = 949 \text{ kg/m}^3$ , fluid viscosity  $\nu = 20 \text{ cSt}$ , surface tension  $\sigma = 20.6 \times 10^{-3} \text{ N/m}$ ,  $\lambda_F = 4.75 \text{ mm}$ ,  $\Gamma_F = 4.2$ ,  $T_d = 1/54.9 \text{ s}$ , viscosity of air  $\mu_a = 1.84 \times 10^{-5} \text{ kg/ms}$  and density of air  $\rho_a = 1.2 \text{ kg/m}^3$ . We choose a constant impact phase of  $\sin(\Phi) = 0.2$ . The dimensionless drag coefficient  $C$  depends weakly on system parameters [85] and is shown to vary over the range  $0.17 \leq C \leq 0.33$ . In our numerical experiments we consider the two extreme values  $C = 0.17$  and  $0.33$ . From the remainder of this chapter, we will use dimensionless quantities in the results with the length scale chosen as the Faraday wavelength  $\lambda_F$  and the time scale as  $T_F\text{Me}$ .

### 7.2.2 Numerical experiments

Figure 7.2 (not to scale) shows the setup of our numerical experiments. Two in-phase walkers are initially placed at distances  $r_1$  and  $r_2$  from the origin and at equal angles from the  $y$ -axis. If the droplets were travelling at constant speed, the difference  $\tau = |r_1 - r_2|$  would be proportional to the difference in their time of arrival at the origin. To limit the size of the parameter space to be explored, we have fixed the average angle between the droplets' trajectories to  $90^\circ$ . However, we note that the detailed dynamics of the droplets are quite sensitive to the choice of this initial impact angle. In the numerical simulations, the droplets are point particles and the blue disk indicates the non-dimensional diameter  $\hat{d} = 2R/\lambda_F$  in the range  $0.13 \leq \hat{d} \leq 0.21$  corresponding to the diameters in the range  $0.6 \leq 2R \leq 1 \text{ mm}$  of the physical droplet. The visible size of the wavepacket produced by the droplet's impact is a few times  $\lambda_F$ . We assume an initial uncertainty in the centre of mass of the droplets' positions (white

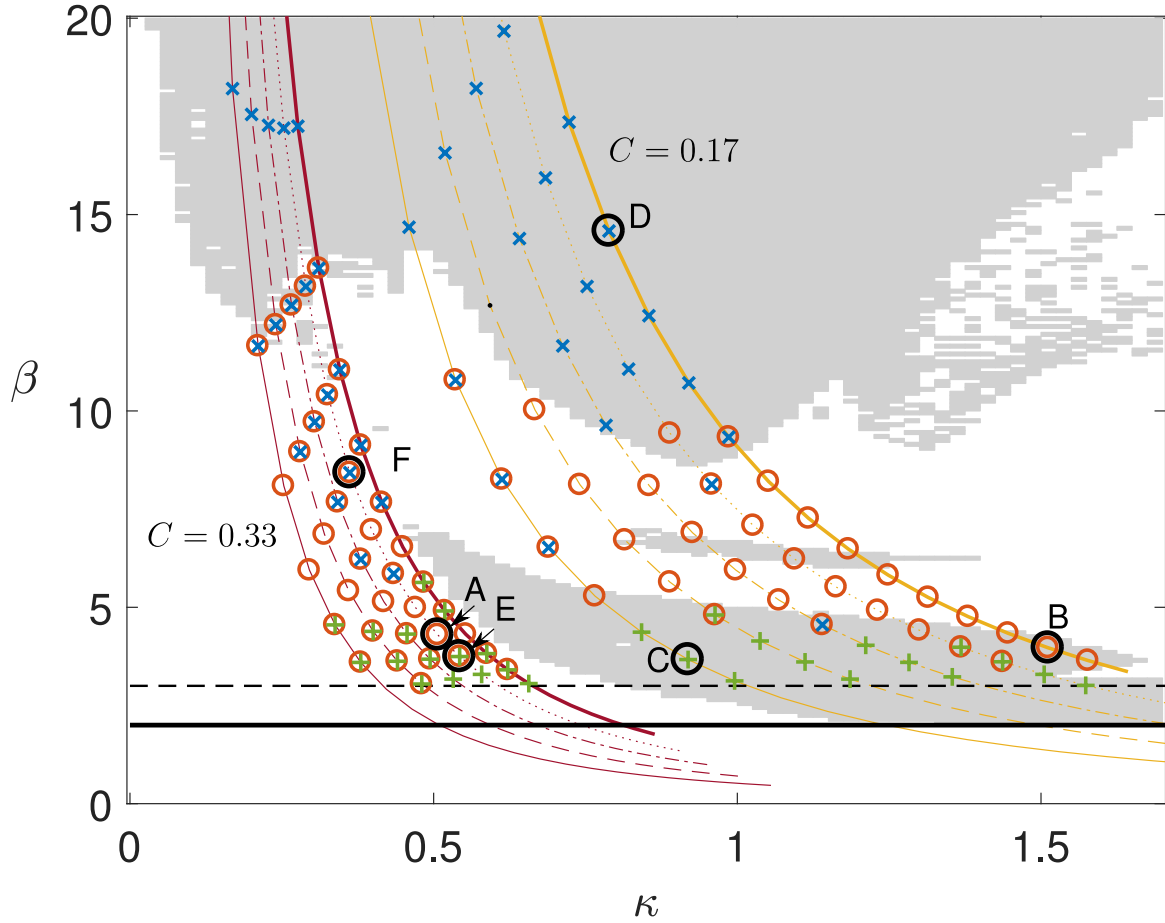


Figure 7.3 : The  $\beta$ - $\kappa$  parameter space considered in the numerical experiments. The two sets of curves correspond to dimensionless drag coefficients  $C = 0.17$  (yellow) and  $C = 0.33$  (dark red). Each of the five curves of the same colour corresponds to droplets of diameters  $2R = 0.6$  mm (solid),  $0.7$  mm (dashed),  $0.8$  mm (dashed-dotted),  $0.9$  mm (dotted) and  $1$  mm (thick solid). Light grey shaded regions correspond to parallel walkers that unbind at long times in simulations with  $\hat{\alpha} = 0$ , while white regions correspond to parallel walkers that remain as stable droplet pairs at long times, see figure 6.1. The black horizontal line indicates the walking threshold  $\beta = 2$ . All simulations were performed for  $\beta \geq 3$  (black dashed line) to ensure that the walking speed of the droplet is sufficiently high so that a single walker would travel at least  $2r_1$  by the end of the simulation,  $t = 250$ . The markers indicate the three different types of correlations observed: promenading (red  $\circ$ ), orbiting (green  $+$ ) and chasing (blue  $\times$ ) pairs of walkers. Simulations with only uncorrelated walkers are shown as a black dot. Markers indicate the correlations observed with probability greater than 20% for simulations with path differences  $0 \leq \tau \leq 18/2\pi$ .

dots in figure 7.2). This is modelled by drawing random numbers from a uniform distribution within a disk of the same diameter as a droplet,  $\hat{d}$ . The droplets are

launched at constant speed  $u$ , corresponding to the stable walking speed of an isolated droplet given by the stroboscopic model for a single walker [88], and are directed towards the origin. The detection occurs at time  $t = 250$ , during which a droplet travelling at speed  $u$  would travel a distance of at least  $2r_1$ . This cut-off point of  $t = 250$  has been chosen to ensure that any transient dynamics of droplet pairs have decayed and the droplets have settled either into a stable uncorrelated state or one of the correlated bound states. We numerically integrate the equations of motion in equation (7.1) using the same numerical method as in Chapter 6 (see Appendix C) with a dimensionless timestep of  $\Delta t = 2^{-6}$ .

We vary the proximity to the Faraday threshold,  $\Gamma_f/\Gamma_F$ , which traces out a curve for a droplet of fixed diameter in the  $\beta$ - $\kappa$  parameter space. Figure 7.3 shows two sets of such curves in the  $\beta$ - $\kappa$  parameter space. Each curve corresponds to a fixed value of the dimensionless drag coefficient  $C$  and the dimensionless droplet diameter  $\hat{d}$ . Increasing  $\Gamma_f/\Gamma_F$  increases  $\beta$  and decreases  $\kappa$ .

### 7.3 Two-droplet correlations

Two walkers are launched towards each other with varying path differences in the range  $0 \leq \tau \leq 18/2\pi$ . This is done by fixing the distance  $r_1 = 100/2\pi$  of the first droplet and changing the distance of the second droplet  $r_2$  in the range  $82/2\pi \leq r_2 \leq 100/2\pi$ . Each droplet is set to have an uncertainty in the initial position of its centre of mass. The droplets' initial positions are thus determined by drawing random numbers from a uniform distribution within a disk of diameter  $\hat{d}$ . We observe four generic behaviours: (i) In the majority of cases the droplets remain uncorrelated and travel along straight lines in different directions. (ii) The droplets pair up into promenading walkers where the droplets are walking parallel with sideways oscillations. More exotic promenading walkers also arise as shown in the parameter space study of two droplets in Chapter 6. We refer to all of these as promenading correlations. (iii) The droplets form a two-droplet orbiting pair referred to as orbiting correlations. (iv) The droplets pair up in a chasing mode where they are walking one behind the other. These are referred to as chasing correlations. In experiments with walkers, promenading and orbiting pairs are common and have been studied in detail [89, 10]. Chasers have previously been identified in a bounded domain where walkers are confined into an annular region [14] but free chasers have not been reported previously in experiments. However, we have occasionally observed free chasers at relatively high memory in experiments with

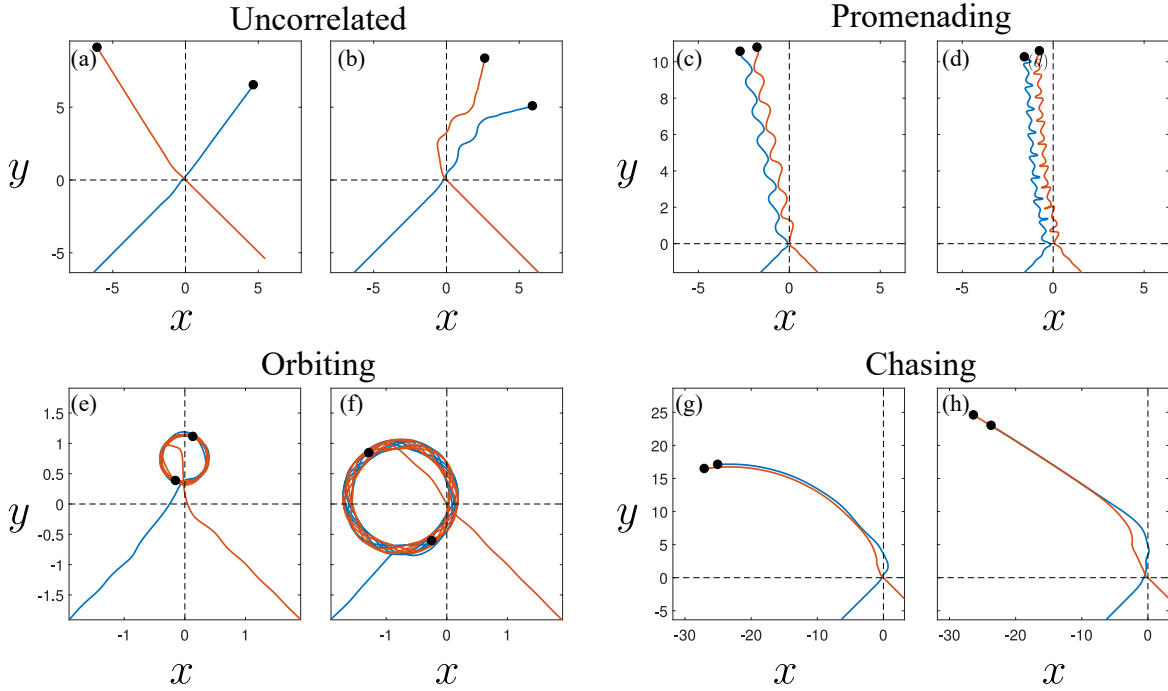


Figure 7.4 : Typical two-droplet trajectories: Uncorrelated trajectories whose interdroplet distance diverges with time are shown in (a) and (b) with parameter values same as figure 7.5(b) and path differences  $\tau = 2.71$  and  $\tau = 1.51$  respectively. Promenading correlations with symmetrical oscillations (c) at  $\tau = 0.40$  and other parameters same as figure 7.5(f), and asymmetrical oscillations (d) at  $\tau = 0.16$  and other parameters same as figure 7.5(e). Orbiting correlations of smaller diameter (e) at  $\tau = 0.95$  and larger diameter (f) at  $\tau = 1.99$  with other parameters same as figure 7.5(c). Chasing correlations with a circular path (g) at  $\tau = 2.71$  and other parameters same as figure 7.5(f), and on a straight line (h) at  $\tau = 1.25$  and other parameters same as figure 7.5(d). The axes are in units of the Faraday wavelength  $\lambda_F$ .

walkers. Moreover, they are ubiquitous in experiments with mismatched superwalkers and less common for identical superwalkers (see figure 3.10).

Typical realisations of the two droplet bound states and uncorrelated trajectories are summarised in figure 7.4. For the uncorrelated trajectories, two walkers may travel straight through the interaction region when their underlying waves interact weakly as shown in figure 7.4(a), or unbind after a short interaction as depicted in figure 7.4(b). Two walkers can also reflect off each other and end up uncorrelated. The first type of bound state we observe are *promenading walkers*. We observe two generic types of oscillating modes for this state: (i) a symmetrical mode, figure 7.4(c), in which droplets perform symmetric sideways oscillations while walking in parallel and their centre of mass follows a straight line trajectory, and (ii) an asymmetric mode,

figure 7.4(d), in which oscillations are lopsided and the centre of mass oscillates. The second type of bound state we observe in simulations are *orbiting walkers*. In this state, the two walkers orbit around their common centre of rotation. We observe two types of orbiting correlations: (i) In the first type, the droplets are in a smaller tight orbit at an inter-droplet distance of  $d_{12}^o \approx 0.8$ , figure 7.4(e), while in the second type (ii) the droplets are orbiting at a larger inter-droplet distance of  $d_{12}^o \approx 1.8$  figure 7.4(f). These larger orbits are sometimes accompanied by radial oscillations. The third kind of correlation we observe are *chasers*. In this state, the droplets are chasing one after another and are travelling at a constant speed and a fixed inter-droplet distance. We classify the chasers into two types: (i) those which follow a circular path, figure 7.4(g), and (ii) those which walk on a straight line trajectory, figure 7.4(h). Straight-line chasers are found to have inter-droplet distances of  $d_{12}^c \approx 3$  and  $d_{12}^c \approx 4$ , while the chasers which follow a circular path are more tightly bound with inter-droplet distances  $d_{12}^c \approx 1.3$  and  $d_{12}^c \approx 2$ . Moreover, the trailing walker is offset sideways from the leading walker in this latter case.

To understand the probabilistic properties of the emergence of two-walker correlations, we have studied the statistics of the two-droplet bound states by simulating many trajectories with similar initial conditions. On studying the final state of the droplets as functions of the path difference  $\tau$ , we find regions of correlated and uncorrelated behaviours. The parameter space chosen for the results presented is summarised in figure 7.3. The light grey region in the background corresponds to where initially parallel walkers unbind at late times in simulations with  $\hat{\alpha} = 0$ , while white regions correspond to where initially parallel walkers remain in a bound state at late times (see figure 6.1). We primarily observe orbiting and chasing correlations, and uncorrelated behaviour for parameters in the light grey region, consistent with promenading walkers being unstable there. However, we do sometimes observe promenading walkers near the edges of the light grey region, which may be because the simulations here are relatively short or may result from  $\hat{\alpha} \neq 0$ . On traversing one of the curves corresponding to  $C = 0.17$  (low drag), we find that the low memory region (small  $\beta$ ) is dominated by orbiting correlations with the emergence of promenading correlations at mid-memory and then only chasing correlations at high memory (large  $\beta$ ). On the other hand, traversing a curve for  $C = 0.33$  (high drag), we find both promenading and orbiting correlations at low memory, promenading and chasing correlations at mid-memory and only chasing correlations at high memory. At even higher memories corresponding to  $\beta > 20$ , we either observe chasing correlations or uncorrelated walkers.

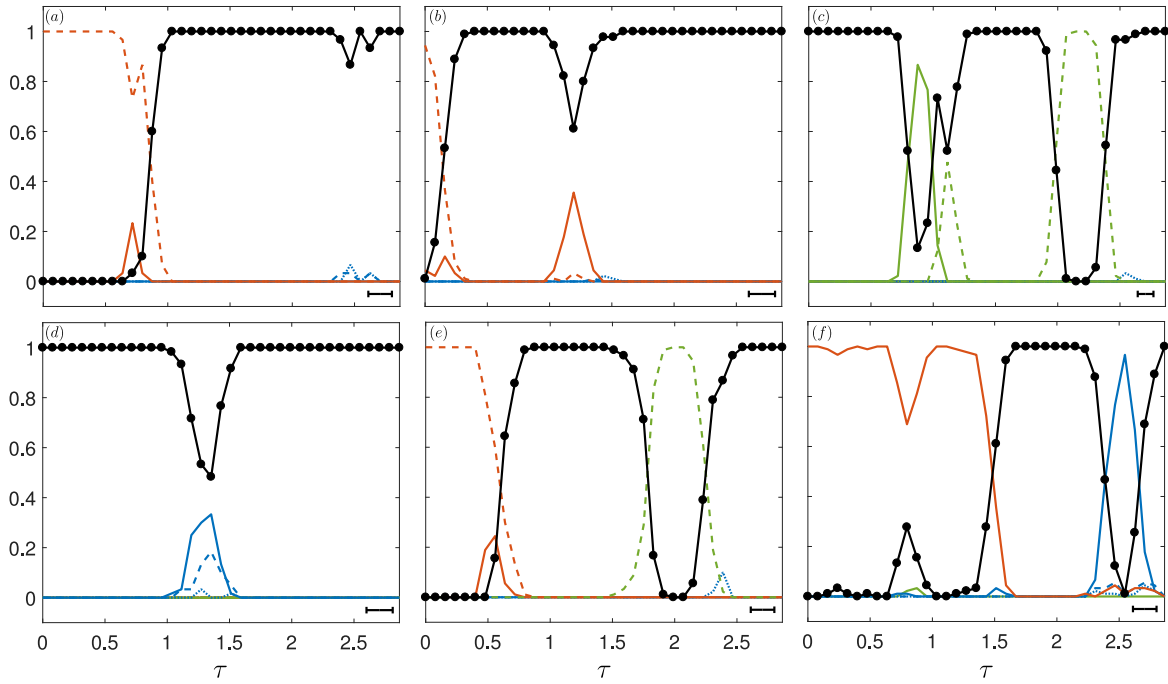


Figure 7.5 : Probability of different correlations as a function of the path difference  $\tau$  (in units of Faraday wavelength  $\lambda_F$ ). The six plots (a)-(f) correspond to the six points A-F in the  $\beta$ - $\kappa$  parameter space plot in figure 7.3. The parameter values for these are, (a)  $\hat{d} = 0.19$  and  $\Gamma_f/\Gamma_F = 0.86$ , (b)  $\hat{d} = 0.21$  and  $\Gamma_f/\Gamma_F = 0.77$ , (c)  $\hat{d} = 0.13$  and  $\Gamma_f/\Gamma_F = 0.88$ , (d)  $\hat{d} = 0.21$  and  $\Gamma_f/\Gamma_F = 0.88$ , (e)  $\hat{d} = 0.19$  and  $\Gamma_f/\Gamma_F = 0.85$  and (f)  $\hat{d} = 0.19$ ,  $\Gamma_f/\Gamma_F = 0.9$ . Thick black lines indicate the probability of uncorrelated walkers while the coloured lines show probabilities of each of the different types of correlations: the symmetrical (red solid line) and asymmetrical (red dashed line) modes of promenading walker correlations, smaller (green solid line) and larger (green dashed line) diameter orbiting correlations, circular-path chasing correlations with inter-droplet distance  $d_{12} \approx 2$  (blue solid line) and straight-line chasing correlations with inter-droplet distance  $d_{12} \approx 3$  (blue dashed line) and  $d_{12} \approx 4$  (blue dotted line). Each data point has a statistical uncertainty of  $1/\sqrt{90}$  since each data point is obtained by averaging over 90 trajectories with slightly different initial conditions due to uncertainty in the initial positions of the droplets resulting from their non-zero size. The horizontal black bar indicates the diameter of each droplet.

Figure 7.5 shows the probabilities of droplets being correlated or uncorrelated at  $t = 250$  as functions of the path difference  $\tau$ . If the walkers end up in any of the droplet bound states at the end of the simulation, we classify them as correlated, while if the droplets are found to be separated by a distance exceeding 30 and moving in different directions, we classify them as uncorrelated. The thick black solid lines in figure 7.5 shows the probability of uncorrelated walkers while the coloured lines show

the probabilities of each different types of correlations. Every dip in the black curves corresponds to a certain type of two-droplet correlation. Each of the data points comprises an ensemble average over 90 simulated trajectories. The  $\beta$ - $\kappa$  parameter values used for obtaining the data in figure 7.5 are indicated in figure 7.3 as A-F. In figure 7.5(a), we observe a single dominant dip arising from the asymmetrical mode of promenading correlations (red dashed line) for  $0 < \tau \lesssim 1$ . Figures 7.5(b) and (c) comprise of two dips. Figure 7.5(b) has two dips arising from the asymmetrical and symmetrical (red solid line) modes of promenading walkers correlation for  $\tau \approx 0$  and  $\tau \approx 1.2$ , respectively. The two dips in figure 7.5(c) arise from the smaller (green solid line) and the larger (green dashed line) diameter orbiting correlations. The dip near  $\tau \approx 1$  comprises of both types of orbiting correlations while the dip near  $\tau \approx 2.2$  emerges only from the larger diameter orbiting correlation. Figure 7.5(d) has a single dip near  $\tau \approx 1.3$  but it is dominated by a mixture of both straight-line (blue dashed line) chasing correlations with inter-droplet distance  $d_{12}^c \approx 3$  as well as circular-path (blue solid line) chasing correlations with inter-droplet distance  $d_{12}^c \approx 2$ . Figures 7.5(e) and (f) each have two dips arising from two different types of correlations. Dips in figure 7.5(e) arise from the asymmetrical mode of promenading walkers correlations and larger diameter orbiting correlations, while the dips in figure 7.5(f) are from the symmetrical mode of promenading walker correlations and circular path chasing correlations.

## 7.4 Conclusion

We have considered the non-Markovian dynamics of pairs of walking droplets with crossing paths that are initially separated by a large inter-droplet distance. We have studied the probability that the droplets remain unbound as a function of their path difference to the common origin. We have found three generic classes of two-droplet correlations: promenading, orbiting and chasing, that are identified as dips in figure 7.5.

Our numerical experiments correspond to a hydrodynamic analogue of the Hong–Ou–Mandel (HOM) two-photon interference experiment without a beam splitter. One of the limitations of the hydrodynamic pilot-wave model used in this study is the assumption of a constant impact phase. If one were to study these phenomena experimentally, the modulations of the impact phase may occur and may result in either enhancement or suppression of correlation dips. Another feature we observe here is that the correlation dips are very sensitive to the system parameters and an experimental realisation of

this setup may result in quantitatively different correlation dips, but we do expect the qualitative features of the correlation dips to persist.

To achieve a closer analogue of the HOM interference experiment, a hydrodynamic equivalent of a 50/50 beam splitter would need to be implemented. An *ad hoc* numerical implementation of a beam splitter can be realised by reversing the  $x$ -component of the droplets' velocity along with their memories with a 50% probability once the droplets enter a spatial 'beam splitter region'. On testing this idea, we found that the qualitative features of the two-droplet correlation dips persist.

In summary, we have demonstrated a richness in the reaction dynamics of two walkers paving the way to further studies of many-droplet correlated behaviours of these curious non-Markovian dynamical systems.

# Chapter 8

## Unsteady dynamics of a walking droplet

In this chapter, we explore the unsteady dynamics of a single walking droplet using the stroboscopic model of Oza et al. [88] with different wave fields. We find that for small inertia and large wave forcing, the steady walking motion of a droplet becomes unstable and unsteady dynamics emerge. We study the unsteady dynamics of the droplet by restricting its motion to one horizontal dimension. We uncover a variety of unsteady motions such as random walk-like motion, oscillating walker and self-trapped oscillations of the droplet. We explore the chaotic nature of these unsteady motions as well as their statistical behaviour.

### 8.1 Introduction

A single walker or a superwalker travels in a straight line at a constant speed unless it encounters obstacles or other droplets. However, in simulations it has been shown that in the very high memory regime, which is currently not accessible in experiments, the linear motion of the droplet becomes unstable and the droplet's dynamics becomes bimodal where it erratically switches between phases of linear motion and diffusive motion [114]. This bimodal motion shows analogies with the run-and-tumble motion that is ubiquitous in swimming micro-organisms. For example, the motion of *Escherichia coli* in a nutrient-filled medium is known to display the 'run-and-tumble' dynamics [115]. Moreover, it has been observed that artificial droplet swimmers, that are used to mimic living microswimmers, can also display bimodal gait switching triggered by the interaction between the droplet and its self-generated chemical gradients [101]. This is reminiscent of gait-switching dynamics in biological organisms [116].

Recently, Durey et al. [117] explored this regime using the stroboscopic model of Oza et al. [88] by restricting the droplet's motion to one dimension and identified regimes in the parameter space where the droplet has a wavelike statistical signature. A regime where speed oscillations with the wavelength of the guiding wave arise when the droplet is perturbed from the steady walking state, and an unsteady regime where a random walk-like motion is observed in the high memory regime similar to Hubert et al. [114]. Sáenz et al. [23] in their experimental exploration of a hydrodynamic analogue of Friedel oscillations also showed that the emergent wavelike statistics arise from the inline oscillations of the walking droplet.

In this chapter, we revisit the unsteady walking regime using the stroboscopic model of Oza et al. [88] and explore the dynamics observed in the parameter space using different forms of the wave field. We start with the linear stability analysis of a single walking droplet in 2D in Section 8.2 and show that the perturbations to inline and transverse directions decouple. Thereon, we restrict the motion of the droplet to one horizontal dimension and explore the droplet's unsteady dynamics using three different forms of the wave field: a Bessel function wave field (Section 8.4), a Gaussian wave field (Section 8.5) and a sinusoidal wave field (Section 8.6). We focus on the nonlinear dynamics and the statistical behaviour in this unsteady regime and draw connections of the walking droplet dynamics with Lorenz equations, Langevin equation and deterministic diffusion.

## 8.2 Linear stability of a walking droplet in 2D

Following Oza et al. [88], we start by performing a linear stability analysis of the steady walking state in the stroboscopic model of Oza et al. [88] whose equation of motion is given in (2.15). This equation takes the following form for the motion in the  $x$  and  $y$  directions respectively,

$$\kappa\ddot{x}_d + \dot{x}_d = \beta \int_{-\infty}^t \frac{J_1\left(\sqrt{(x_d(t) - x_d(s))^2 + (y_d(t) - y_d(s))^2}\right)}{\sqrt{(x_d(t) - x_d(s))^2 + (y_d(t) - y_d(s))^2}} (x_d(t) - x_d(s)) e^{-(t-s)} ds, \quad (8.1)$$

$$\kappa\ddot{y}_d + \dot{y}_d = \beta \int_{-\infty}^t \frac{J_1\left(\sqrt{(x_d(t) - x_d(s))^2 + (y_d(t) - y_d(s))^2}\right)}{\sqrt{(x_d(t) - x_d(s))^2 + (y_d(t) - y_d(s))^2}} (y_d(t) - y_d(s)) e^{-(t-s)} ds. \quad (8.2)$$

Assuming a steady walking droplet with speed  $u$  and substituting  $\mathbf{x}_d = (ut, 0)$  in the above equations, we arrive at

$$u = \frac{1}{\sqrt{2}} \sqrt{-1 + 2\beta - \sqrt{1 + 4\beta}}.$$

We apply a general perturbation of the form  $\mathbf{x}_d = (x_d, y_d) = (ut, 0) + \epsilon H(t)(x_1(t), y_1(t))$  with  $H(\cdot)$  being the Heaviside step function used to introduce the perturbation at  $t = 0$ . Substituting in equations (8.1) and (8.2), and comparing  $O(\epsilon)$  terms on both sides of the equations we get,

$$\kappa \ddot{x}_1 + \dot{x}_1 = \beta \int_0^\infty J_1'(uz) [x_1(t) - x_1(t-z)H(t-z)] e^{-z} dz,$$

$$\kappa \ddot{y}_1 + \dot{y}_1 = \beta \int_0^\infty \frac{J_1(uz)}{uz} [y_1(t) - y_1(t-z)H(t-z)] e^{-z} dz.$$

Taking a Laplace transform of the above two equations results in following matrix equation

$$\mathbf{A}_W(s) \mathbf{X}(s) = \mathbf{X}_0(s),$$

where

$$\mathbf{X}(s) = \begin{bmatrix} X_1(s) \\ Y_1(s) \end{bmatrix} = \mathcal{L}[\mathbf{x}(t)] = \mathcal{L} \begin{bmatrix} x_1(t) \\ y_1(t) \end{bmatrix},$$

$$\mathbf{X}_0(s) = (s+1)\mathbf{x}(0) + \dot{\mathbf{x}}(0),$$

and

$$\mathbf{A}_W(s) = \begin{bmatrix} \mathbf{A}(s) & 0 \\ 0 & \mathbf{B}(s) \end{bmatrix}.$$

Here  $\mathcal{L}$  denotes the Laplace transform operator and

$$\mathbf{A}(s) = \kappa s^2 + s - \beta \left[ \int_0^\infty J_1'(uz) e^{-z} dz - \mathcal{L} \left\{ J_1'(ut) e^{-t} \right\} \right],$$

$$\mathbf{B}(s) = \kappa s^2 + s - \beta \left[ \int_0^\infty \frac{J_1(uz)}{uz} e^{-z} dz - \mathcal{L} \left\{ \frac{J_1(ut)}{ut} e^{-t} \right\} \right].$$

The poles of  $X_1(s)$  and  $Y_1(s)$  in the Laplace space correspond to the eigenvalues in physical space and are determined by  $\mathbf{A}_W(s) = 0$  which results in,

$$\mathbf{A}(s) \mathbf{B}(s) = 0.$$

Thus, we see that the linear stability equation for the perturbation in the direction of walking,  $\mathbf{A}(s) = 0$ , decouples from the equation of perturbation in the direction transverse to the walking,  $\mathbf{B}(s) = 0$ . Solving  $\mathbf{B}(s) = 0$  for transverse perturbation gives rise to a double pole at  $s = 0$  for  $Y_1(s)$  indicating that the droplet is neutrally stable to perturbations transverse to the direction of walking (see Oza et al. [88] for more details). However, solving  $\mathbf{A}(s) = 0$  for inline perturbations results in one of the poles crossing  $\text{Re}(s) = 0$  and resulting in a bifurcation we are interested in exploring in this chapter. Hence, we restrict the droplet's motion to 1D for the remainder of this chapter.

### 8.3 Generalised 1D stroboscopic model with an arbitrary wave form

The stroboscopic model of Oza et al. [88] describing the horizontal dynamics of a walking droplet with a  $J_0(\cdot)$  Bessel function form of the wave field was described in equation (2.15). We restrict ourselves to horizontal motion in only one direction and extend this model to an arbitrary spatial wave form  $F(x)$  resulting in the following general stroboscopic model

$$\kappa \ddot{x}_d + \dot{x}_d = -\beta \left. \frac{\partial h}{\partial x} \right|_{x=x_d}, \quad (8.3)$$

where

$$h(x, t) = \int_{-\infty}^t F(x(t) - x_d(s)) e^{-(t-s)} ds. \quad (8.4)$$

Combining these two equations we get,

$$\kappa \ddot{x}_d + \dot{x}_d = \beta \int_{-\infty}^t f(x_d(t) - x_d(s)) e^{-(t-s)} ds, \quad (8.5)$$

where  $f(x) = -F'(x)$ . The two parameters in this dimensionless equation of motion,  $\kappa$  and  $\beta$ , may be usefully interpreted as the ratio of inertia to drag and the ratio of wave forcing to drag respectively.

### 8.3.1 Steady walking solution

We look for a steady walking solution of the generalised stroboscopic model by substituting  $x = ut$  in equation (8.5) which results in the following equation

$$u = \beta \int_0^\infty f(uz) e^{-z} dz. \quad (8.6)$$

Provided that a solution to the above equation exists, one obtains the steady walking speed  $u$  of the droplet for a given parameter  $\beta$  and spatial wave form  $F(x)$ .

### 8.3.2 Linear stability analysis

To determine the stability of the steady walking solution in this generalised framework, we apply a perturbation of the form  $x_d(t) = ut + \epsilon x_1(t)H(t)$  to the steady walking solution with speed  $u$ . By substituting this in equation (8.5) and comparing  $O(\epsilon)$  terms on both sides we get,

$$\kappa \ddot{x}_1 + \dot{x}_1 = \beta \left[ x_1(t) \int_0^\infty f'(uz) e^{-z} dz - \int_0^\infty f'(uz) x_1(t-z) H(t-z) e^{-z} dz \right]. \quad (8.7)$$

The first integral on the right side can be simplified as:

$$\int_0^\infty f'(uz) e^{-z} dz = -\frac{f(0)}{u} + \frac{1}{u} \int_0^\infty f(uz) e^{-z} dz = -\frac{f(0)}{u} + \frac{1}{\beta}.$$

Substituting this in equation (8.7) and taking Laplace transform on both sides we get,

$$X_1(s) = \frac{\kappa(sx_1(0) + \dot{x}_1(0)) + x_1(0)}{\kappa s^2 + s - 1 + \beta[f(0)/u + g(s)]}, \quad (8.8)$$

where

$$g(s) = \mathcal{L} \left\{ f'(ut) e^{-t} \right\}.$$

Hence, the stability of the inline walking motion can be determined by finding the poles of  $X_1(s)$  in equation (8.8).

In this chapter we consider three different forms of the spatial wave field  $F(x)$ . We start by exploring the droplet dynamics using the Bessel wave field,  $F(x) = J_0(x)$ , that was used in the stroboscopic model of Oza et al. [88] in Section 8.4. This Bessel wave field has two key features: (i) spatial oscillations and (ii) a spatial decay. We analyse the effects of each of these features separately by considering two alternate forms of the wave field: a sinusoidal wave field of the form,  $F(x) = \cos(x)/2$ , which has oscillations

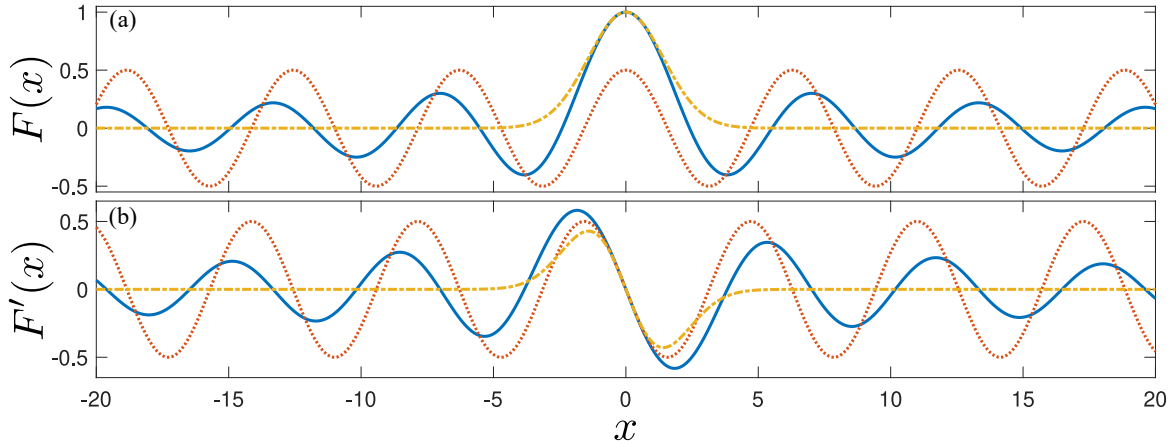


Figure 8.1 : (a) Comparison of the three different forms of the wave field considered in this chapter. A Bessel function wave field  $J_0(x)$  (blue solid curve), a sinusoidal wave field  $\cos(x)/2$  (red dotted curve) and a Gaussian wave field  $e^{-(x/2)^2}$  (yellow dashed-dotted curve). Comparison of their gradients are shown in panel (b).

but no spatial decay, and a Gaussian wave field of the form,  $F(x) = e^{-(x/2)^2}$ , which has spatial decay but no oscillations. We discuss the droplet dynamics emerging from the sinusoidal and the Gaussian form of the wave field in Sections 8.6 and 8.5 respectively. Both of these wave fields have been chosen such that the gradient matches with the Bessel function wave field at the location where the wave is created. A comparison of the three wave fields and their gradients is shown in figure 8.1.

## 8.4 Droplet dynamics with a Bessel wave field

### 8.4.1 Steady solution and linear stability analysis

Choosing a Bessel function form of the wave field,  $F(x) = J_0(x)$ , results in  $f(x) = -F'(x) = J_1(x)$  in equation (8.5). The steady walking solution obtained from equation (8.6) is then given by,

$$u = \frac{1}{\sqrt{2}} \sqrt{-1 + 2\beta - \sqrt{1 + 4\beta}}.$$

The equation for the walking speed is identical to the walking speed solution obtained for the 2D case considered in Section 8.2. This steady walking solution is realised for  $\beta > 2$  while for  $\beta \leq 2$ , the stationary droplet solution is stable. For large  $\beta$ , the above equation for the walking speed can be approximated by  $u \approx \sqrt{\beta}$ .

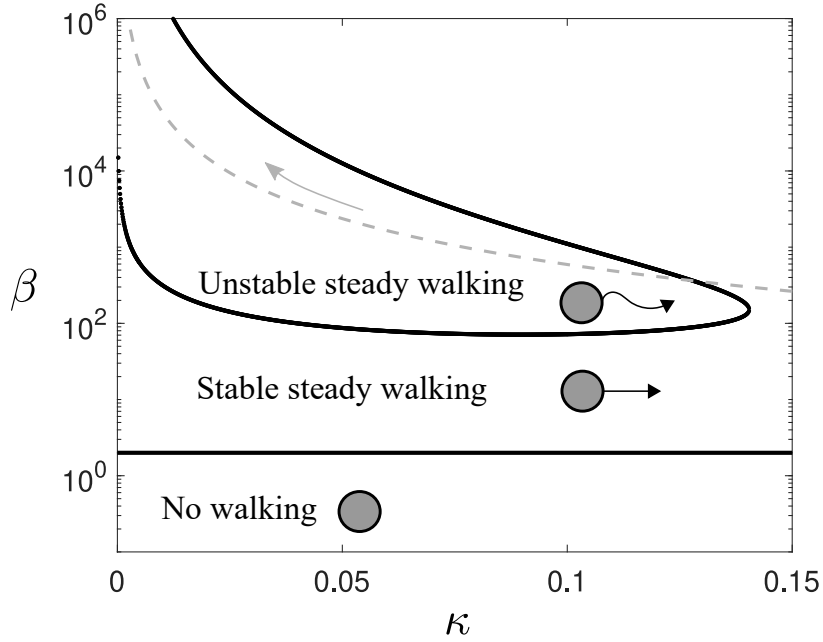


Figure 8.2 : Linear stability diagram in the  $(\kappa, \beta)$  parameter space for inline perturbations to the steady walking solution of a single droplet using the Bessel wave field. The grey dashed curve shows the path traversed in the parameter space for typical experimental parameters as the driving acceleration (or the memory) is increased.

The linear stability analysis requires solving for the poles of  $X_1(s)$  in equation (8.8) with  $f(0) = J_1(0) = 0$  and

$$g(s) = \mathcal{L} \left\{ J_1'(ut) e^{-t} \right\} = \frac{1}{2\sqrt{u^2 + (s+1)^2}} \left( 1 - \frac{u^2}{(s+1 + \sqrt{u^2 + (s+1)^2})^2} \right).$$

This results in solving the equation,

$$(\kappa s^2 + s - 1)\sqrt{u^2 + (s+1)^2} \left( s+1 + \sqrt{u^2 + (s+1)^2} \right) + \beta(s+1) = 0. \quad (8.9)$$

For small  $\kappa$  and large  $\beta$ , a complex pole of the above equation crosses  $\text{Re}(s) = 0$  resulting in the instability of the steady walking solution. We can find the stability boundary of the steady walking solution in the  $(\kappa, \beta)$  parameter space by making  $\text{Re}(s) = 0$  and substituting  $s = i\omega$  in equation (8.9). The linear stability diagram is shown in figure 8.2. We see that a ‘lobe’ shape region appears for small  $\kappa$  and large  $\beta$  where steady walking is unstable. For a fixed  $\kappa \lesssim 0.14$ , as  $\beta$  is increased, we get steady walking for small  $\beta$ , unsteady walking for moderately large  $\beta$  and intriguingly, we recover the steady walking state for very large  $\beta$ .

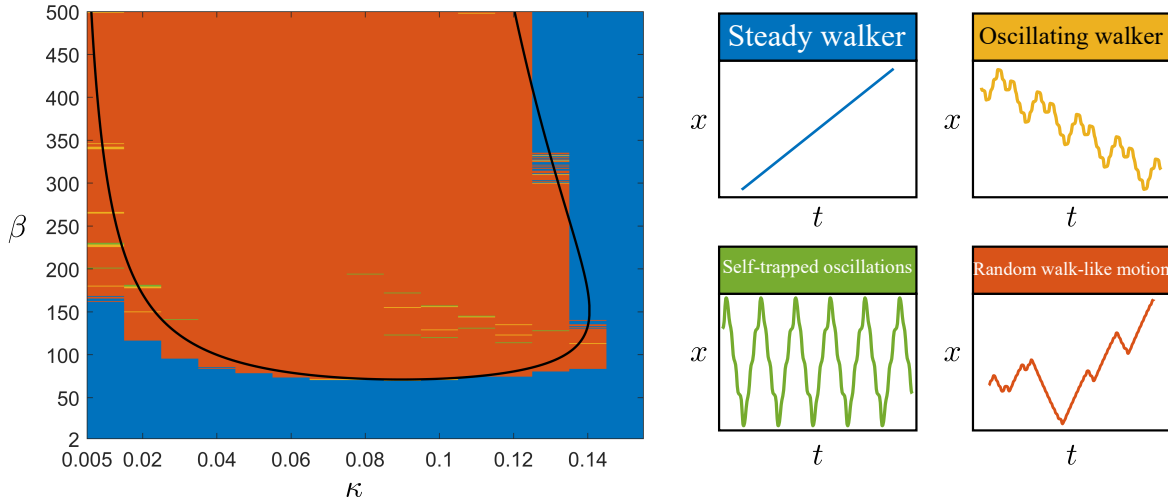


Figure 8.3 : Different dynamical behaviours observed in the  $(\kappa, \beta)$  parameter space at  $t = 1000$  from simulations initiated in the steady walking state at  $t = 0$ . We explore the parameter space region  $0.01 \leq \kappa \leq 0.15$  and  $0 < \beta \leq 500$  with resolution  $\Delta\kappa = 0.01$  and  $\Delta\beta = 1$ . We observe steady walking (blue), oscillating walker (yellow), self-trapped oscillations (green) and random walk-like motion (red). The solid black curve is the linear stability curve from figure 8.2 separating the steady walking and the unsteady walking regime.

### 8.4.2 Simulations in the parameter space

We have explored the unsteady dynamics of a walker with the Bessel wave field in the  $(\kappa, \beta)$  parameter space and the results are presented in figure 8.3. We numerically integrate equations (8.5) with the Bessel wave field using the same Leap-Frog method [97] as in Chapter 6, but we use an implicit Euler method to solve the velocity equation compared to the explicit Euler method used in Chapters 6 and 7 (see Appendix C for details). Moreover, the velocity for each implicit Euler step is solved using a secant method. We use an implicit method because the unsteady motion of the droplet arises in the parameter space region of very small  $\kappa$  and very large  $\beta$  where the integro-differential equation describing droplet's motion becomes a stiff equation. The dimensionless time step is fixed to  $\Delta t = 2^{-6}$ .

We identify four distinct dynamical regimes from simulations. We observed a steady walking solution where it is linearly stable as identified in figure 8.2. We observe that the unstable region identified in figure 8.2 is mainly dominated by random walk-like motion. A typical trajectory of the walker undergoing random walk-like motion is shown in figure 8.4(a). Here the droplet performs inline oscillations while walking and switches the walking direction erratically resulting in a random walk-like dynamics. By observing the time series of the droplet's velocity in figure 8.4(b), we see that the

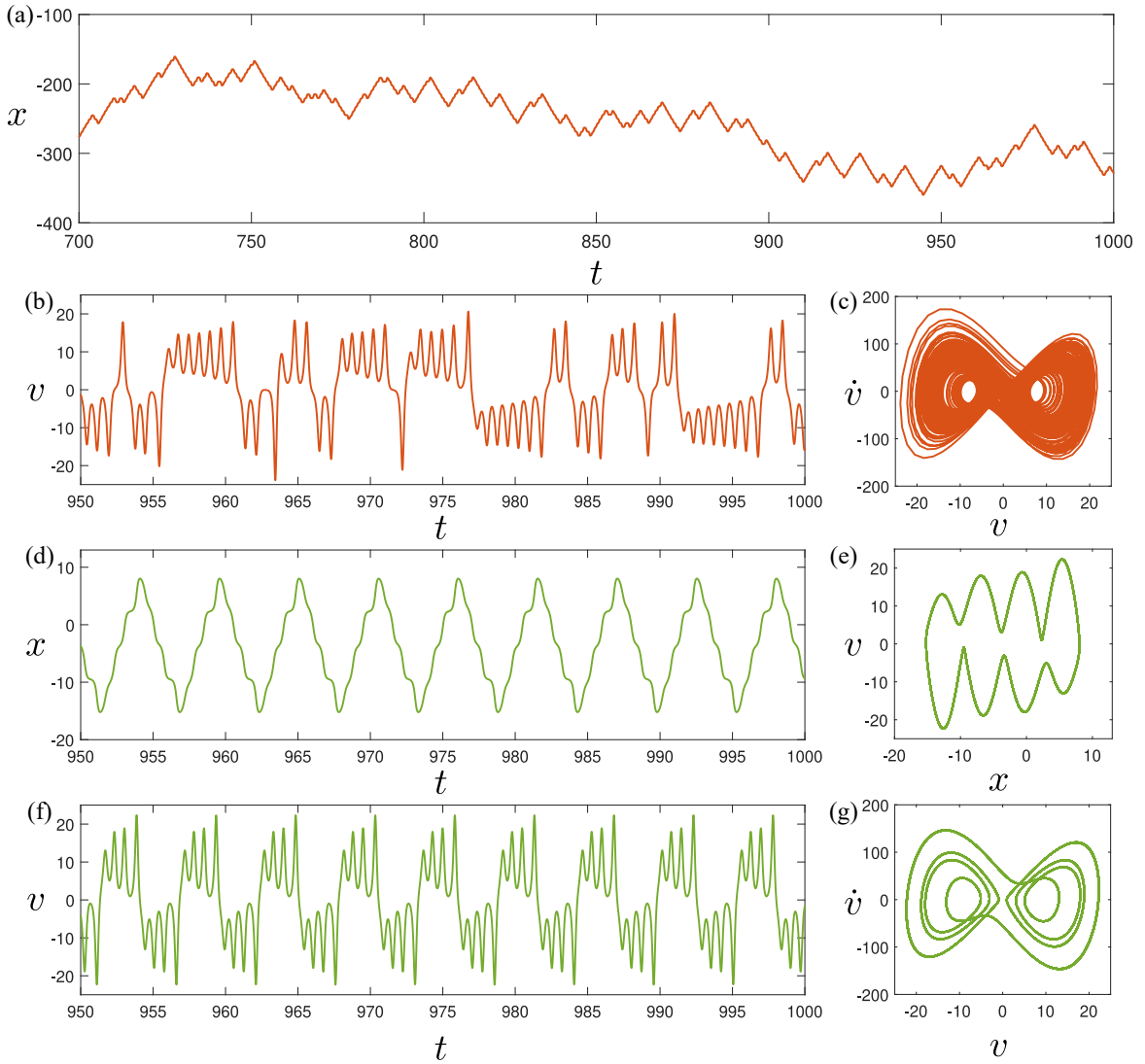


Figure 8.4 : Trajectories showing the random walk-like motion and the self-trapped oscillations of a droplet with a Bessel wave field. (a) Position-time plot and (b) velocity-time plot along with (c) phase space plot showing the projection of the chaotic attractor for the random walk-like motion of the droplet at  $\kappa = 0.13$  and  $\beta = 101$ . (d) Position time and (f) velocity-time plots along with the (e) velocity-position and (g) acceleration-velocity phase space plots for self-trapped oscillations of a droplet at  $\kappa = 0.13$  and  $\beta = 128$ .

erratic switches between positive and negative velocities correspond to switch in the walking direction the droplet. Moreover, the acceleration-velocity phase space plot (see figure 8.4(c)) reveals the projection of the underlying chaotic attractor.

In very small isolated regions of the parameter space, we observe oscillating walkers and self-trapped oscillations. In the oscillating walker state, the droplet walks in one

direction with inline oscillations. We refer the reader to the work of Durey et al. [117] who investigated the oscillating walker dynamics arising from a Bessel wave field in detail. For self-trapped oscillations, the droplet trapped itself under its self-generated wave field and performs periodic back-and-forth motion. A trajectory plot and a velocity time series of this motion is shown in figures 8.4(d) and (f) respectively. Moreover, the phase space dynamics shows closed loops due to the periodic nature of the oscillations (see figure 8.4(e) and (g)). We note that such self-trapped periodic oscillations were also observed by Durey [118] (see Section 5.2 of this work) using their discrete-time pilot-wave model.

## 8.5 Droplet dynamics with a Gaussian wave field

Choosing a Gaussian form of the wave field  $F(x) = e^{-(x/2)^2}$  results in  $f(x) = (x/2)e^{-(x/2)^2}$  in equation (8.5). The corresponding steady walking solution obtained from equation (8.6) is then given by

$$u = \frac{\beta u}{2} \int_0^\infty z e^{-(uz/2)^2 - z} dz = \frac{\beta}{u} \left( 1 - \frac{\sqrt{\pi} e^{1/u^2} \operatorname{erfc}(1/u)}{u} \right), \quad (8.10)$$

which in the limit of large  $\beta$ , scales as  $u \sim \sqrt{\beta}$ .

The linearly stability analysis results in solving for the poles of  $X_1(s)$  in equation (8.8) with  $f(0) = 0$  and

$$g(s) = \mathcal{L} \left\{ \left( -\frac{u^2 t^2}{4} + \frac{1}{2} \right) e^{-(ut/2)^2 - t} \right\}.$$

We find that for the Gaussian form of wave field considered here, the steady walking solution always remains stable. Hence we only get two qualitatively different behaviours when a Gaussian wave field is used: (i) No walking for  $\beta \leq 2$  and (ii) steady walking for  $\beta > 2$ . This suggests that perhaps, oscillations in the wave field are necessary for the steady walking motion of the droplet to become unstable.

## 8.6 Droplet dynamics with a sinusoidal wave field

### 8.6.1 Steady walking solution and linear stability analysis

Choosing a sinusoidal wave form,  $F(x) = \cos(x)/2$ , results in  $f(x) = \sin(x)/2$  and the steady walking solution using equation (8.6) is given by,

$$u = \frac{\beta}{2} \int_0^\infty \sin(uz) e^{-z} dz = \frac{\beta u}{2(1+u^2)},$$

which on solving for  $u$  gives,

$$u = \pm \sqrt{\frac{\beta}{2} - 1}.$$

By substituting  $f(0) = \sin(0)/2 = 0$  and

$$g(u, s) = \mathcal{L} \{f'(ut) e^{-t}\} = \frac{s+1}{2(u^2 + (s+1)^2)},$$

in equation (8.8), we get the following equation to solve for the poles of  $X_1(s)$ ,

$$(\kappa s^2 + s - 1)(2s^2 + 4s + \beta) + \beta(s+1) = 0. \quad (8.11)$$

To find the onset of instability of the steady walking solution in  $(\kappa, \beta)$  parameter space, we substitute  $s = i\omega$  in equation (8.11) and solving the resulting equation gives,

$$\beta = \frac{2(1+4\kappa)}{\kappa(1-2\kappa)}, \quad (8.12)$$

and

$$\omega^2 = \frac{\beta - 2}{2\kappa + 1}. \quad (8.13)$$

### 8.6.2 Reducing the integro-differential equation to a finite system of ODEs

For the sinusoidal wave field, we can rewrite integro-differential equation (8.5) as a finite system of ODEs. Substituting the sinusoidal wave field in equation (8.5) and using the addition formula for sine we get,

$$\kappa \frac{d^2 x_d}{dt^2} + \frac{dx_d}{dt} = \frac{\beta}{2} \sin(x_d(t)) \int_{-\infty}^t \cos(x_d(s)) e^{-(t-s)} ds - \frac{\beta}{2} \cos(x_d(t)) \int_{-\infty}^t \sin(x_d(s)) e^{-(t-s)} ds.$$

Now let  $y(t) = \int_{-\infty}^t \cos(x_d(s)) e^{-(t-s)} ds$  and  $z = \int_{-\infty}^t \sin(x_d(s)) e^{-(t-s)} ds$  then  $y$  and  $z$  are the solution of the following ODEs

$$\dot{y} + y = \cos(x_d(t)),$$

$$\dot{z} + z = \sin(x_d(t)).$$

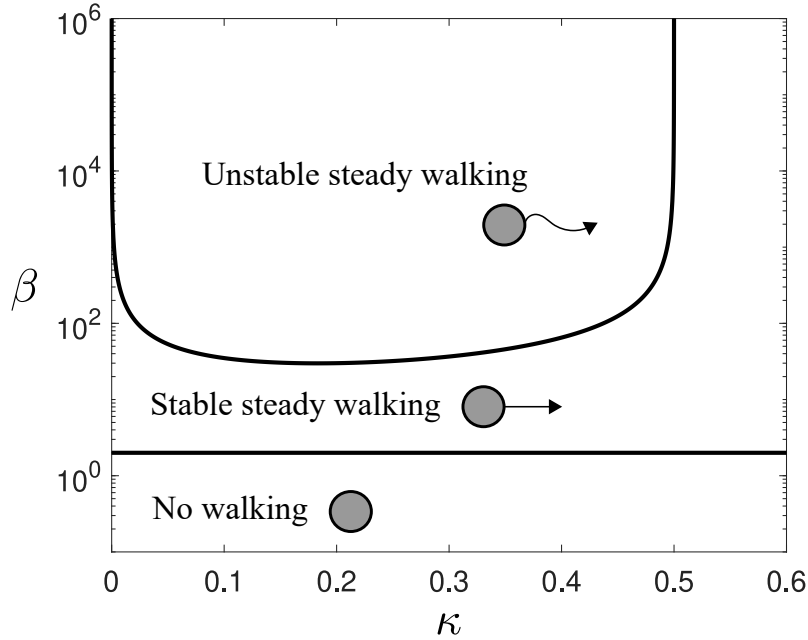


Figure 8.5 : Linear stability diagram in the  $(\kappa, \beta)$  parameter space for inline perturbations to the steady walking solution of a single droplet using the sinusoidal wave field.

Moreover, let  $\dot{x}_d = v_d$ , then we have the following set of ODEs:

$$\begin{aligned}
 \dot{x}_d &= v_d, \\
 \kappa \dot{v}_d + v_d &= \frac{\beta}{2} (y \sin(x_d) - z \cos(x_d)), \\
 \dot{y} + y &= \cos(x_d), \\
 \dot{z} + z &= \sin(x_d).
 \end{aligned} \tag{8.14}$$

### 8.6.3 Simulations in the parameter space

We have explored the dynamics of a droplet with a sinusoidal wave field numerically in the  $(\kappa, \beta)$  parameter space. We observed rich dynamical behaviour as shown in figure 8.6. The simulations were performed by solving equations (8.14) in MATLAB using the ode45 solver. We initialised the simulations assuming the droplet to be in the steady walking state resulting in the following initial conditions for the system of ODEs:  $x_d(0) = 0$ ,  $v_d(0) = u$ ,  $y(0) = 1/1 + u^2$  and  $z(0) = -u/1 + u^2$ . The simulations were run for a time  $t = 1000$ .

We observed four qualitatively different types of behaviours. As per the linear stability analysis, we observed steady walking for relatively small  $\beta$  at all  $\kappa$  values and

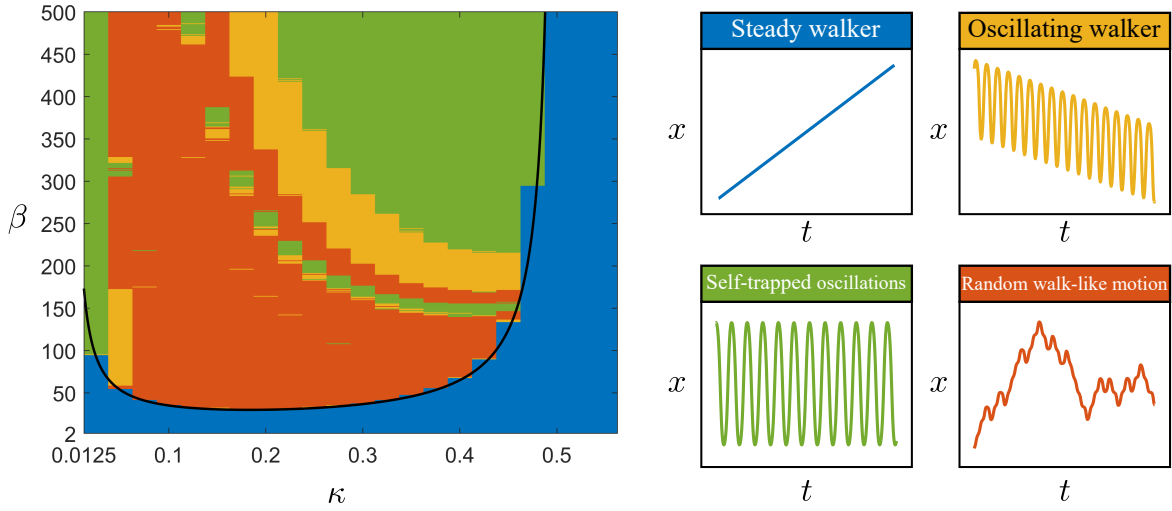


Figure 8.6 : Different dynamical behaviours observed in the  $(\kappa, \beta)$  parameter space at  $t = 1000$  from simulations initiated in the steady walking state at  $t = 0$  using the sinusoidal wave field. We explore the parameter space region  $0.025 \leq \kappa \leq 0.55$  and  $0 < \beta \leq 500$  with resolution  $\Delta\kappa = 0.025$  and  $\Delta\beta = 1$ . We observe steady walking (blue), oscillating walker (yellow), self-trapped oscillations (green) and random walk-like motion (red). The solid black curve is the linear stability curve from figure 8.5 separating the steady walking and the unsteady walking regime.

we also observe steady walking for large  $\kappa$  at all  $\beta$  values. For small  $\kappa$  and large  $\beta$ , we observed more exotic dynamics such as oscillating walker, self-trapped oscillations and random walk-like dynamics.

In the oscillating walker regime, the droplet performs inline oscillations in the direction of motion about some mean velocity. We note that the oscillating walkers observed here span a larger region in the parameter space compared to the small isolated regions of oscillating walkers obtained using the Bessel wave field.

We also find self-trapped oscillations similar to the one obtained for Bessel function wave field. However, we again find an extended region in the parameter space where these self-trapped oscillations are observed compared to small isolated regions of self-trapped oscillations in the Bessel wave field. This is presumably due to the absence of spatial decay in the sinusoidal wave field compared to the Bessel wave field, which enhances interference of the waves in the far-field. Two typical trajectories along with the phase-space plots are shown in figure 8.7. The type of oscillations can be different where we have observed a simple closed loop or a dumbbell shaped closed loops in phase space. We note that similar periodic oscillations were also observed by Moláček [119] in his exploration of the walker dynamics along a line in a central force with a sinusoidal wave field.

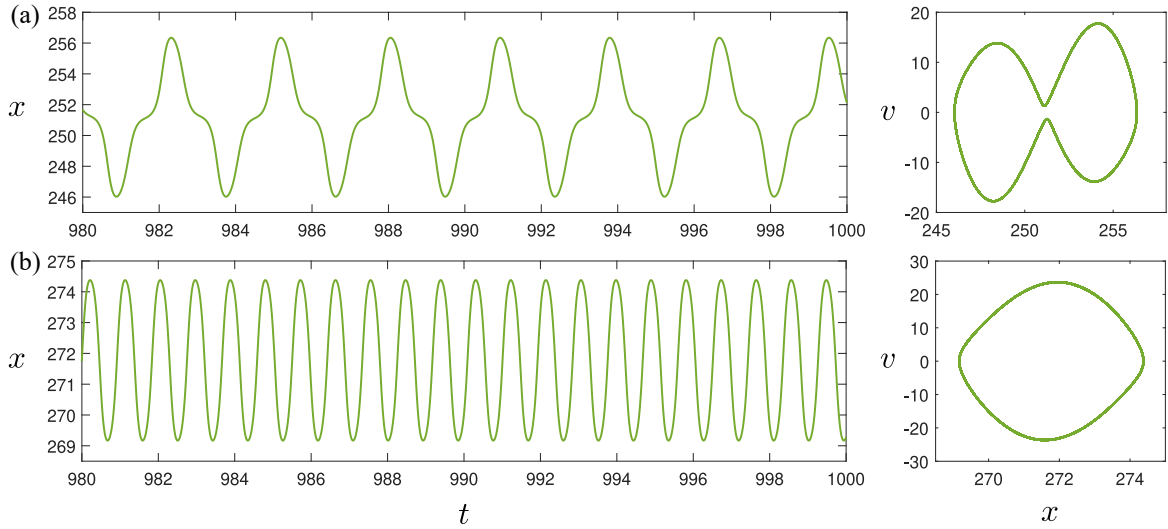


Figure 8.7 : Self-trapped oscillations of the walking droplet using the sinusoidal wave field. Self-trapped oscillations showing the back-and-forth motion of the droplet and the corresponding phase space plot for  $\kappa = 0.3$  and (a)  $\beta = 170$  and (b)  $\beta = 400$ .

We also observe the random-walk like dynamics of the walker similar to the one observed for the Bessel wave field. Here also the droplet performs a random walk-like motion where it switches its walking direction erratically. Since the sinusoidal wave field is simpler than the Bessel wave field, we explore the chaotic and statistical aspects of random walk-like motion mainly using the sinusoidal wave field in Sections 8.7 and 8.8 respectively.

## 8.7 Chaotic aspects of the unsteady dynamics

### 8.7.1 Lorenz system and the droplet's dynamics

One of the classic systems that exhibits chaotic behaviour is the celebrated Lorenz system [120] defined as follows:

$$\begin{aligned}\frac{dX}{dt} &= \sigma(Y - X), \\ \frac{dY}{dt} &= -XZ + rX - Y, \\ \frac{dZ}{dt} &= XY - bZ.\end{aligned}\tag{8.15}$$

This system has three fixed points: (i)  $X = Y = Z = 0$  (unstable), (ii)  $X = Y = \sqrt{b(r-1)}$  and  $Z = r-1$  (stable) and (iii)  $X = Y = -\sqrt{b(r-1)}$  and  $Z = r-1$  (stable)

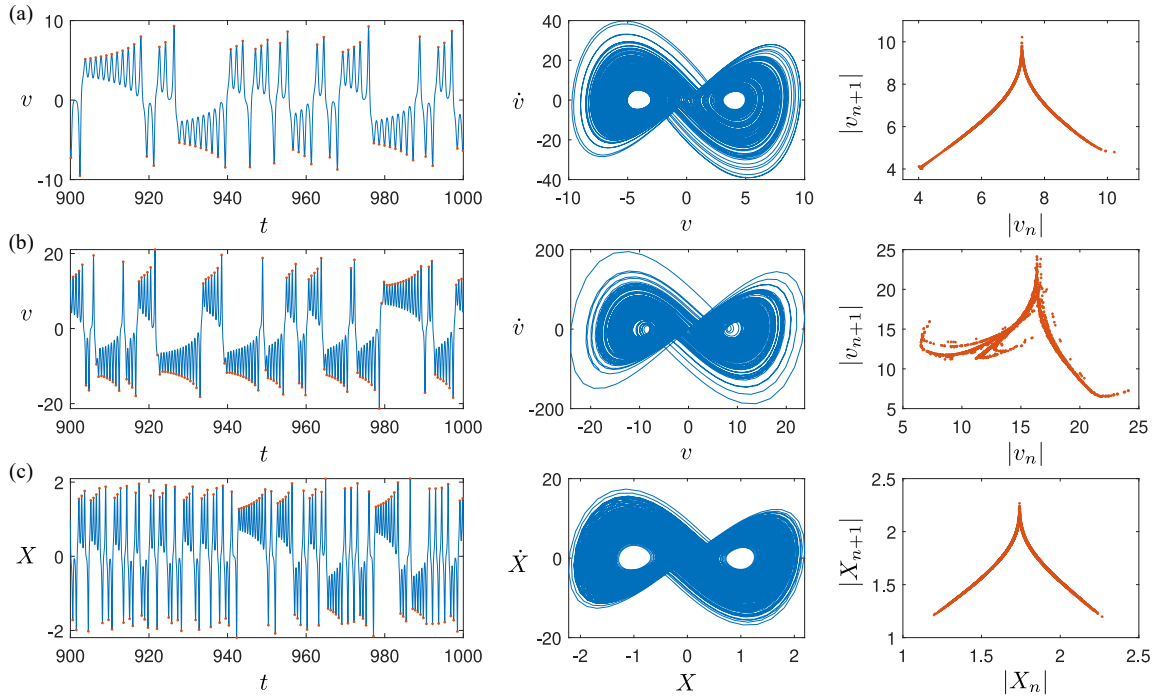


Figure 8.8 : Comparison of the chaotic behaviour in the droplet’s dynamics using (a) a sinusoidal wave field ( $\kappa = 0.2$ ,  $\beta = 35$ ) and (b) a Bessel wave field ( $\kappa = 0.1$ ,  $\beta = 90$ ) with (c) the Lorenz system ( $r = 28$ ,  $b = 8/3$ ,  $\sigma = 10$ ). For the droplet’s dynamics, the time series of velocity  $v$  is shown in the left panel, the projection of the chaotic attractor in the  $(v, \dot{v})$  phase space in the middle panel and the 1D return map for the maximum absolute velocity is shown in the right panel. For the Lorenz system, similar plots are shown for the variable  $X$ .

for  $1 < r < r_c$  with  $r_c = \sigma(\sigma + b + 3)/(\sigma - b - 1)$ . When  $r > r_c$ , all fixed points are unstable and the system exhibits either periodic or chaotic behaviour on a strange attractor [121].

Figure 8.8 shows a comparison of the chaotic behaviour from the Lorenz system with that from the unsteady regime of the droplet’s dynamics using a sinusoidal wave field and a Bessel wave field. The velocity time series for the droplet’s dynamics seems to have striking similarity with the time series for the variable  $X$  obtained from the Lorenz equation (see figure 8.8 (a)-(c) left panel). The phase space dynamics of the droplet in the  $(v, \dot{v})$  space reveals the projection of the underlying chaotic attractor which is very similar to the projection of the Lorenz attractor in the  $(X, \dot{X})$  space (see figure 8.8 (a)-(c) middle panel). A plot of the consecutive maxima of oscillations of  $|X|$  in the Lorenz system, i.e.  $|X_{n+1}|$  against  $|X_n|$ , results in the classic cusp map. Indeed, we see similar cusp maps for the consecutive maxima of the velocity oscillations  $|v|$  in the droplet’s dynamics as shown in the right panel of figure 8.8 (a)-(c).

Inspired by the above similarities between the Lorenz system and the droplet's dynamics, we further explore the connection between the two systems. Intriguingly, Takeyama [122] showed that the system of Lorenz equations in (8.15) can be recasted into an integro-differential equation for the variable  $X(t)$ . By eliminating the variable  $Y$  in equation (8.15) we get,

$$\ddot{X} + (1 + \sigma)X + \sigma(1 - r + Z)X = 0, \quad (8.16)$$

$$\dot{Z} + bZ = X(X + \dot{X}/\sigma). \quad (8.17)$$

We can further eliminate  $Z$  by solving equation (8.17) and substituting into equation (8.16). This results in the following integro-differential equation for  $X(t)$ ,

$$\ddot{X} + (1 + \sigma)\dot{X} + \sigma X \left[ 1 - r + \frac{1}{2\sigma}X^2 + \left(1 - \frac{b}{2\sigma}\right) \int_0^\infty X^2(t-z) e^{-bz} dz \right] = 0. \quad (8.18)$$

This equation describes the steady-state (far from the initial transient) chaotic dynamics of the Lorenz system defined in equation (8.15). In equation (8.18), we have dropped the terms due to the initial values that decay exponentially in time and assumed that the motion has started at an infinite past [122, 123]. If we assume that  $b$  is very large and approximate the exponential in the integral of equation (8.18) by a delta function, then the equation reduces to

$$\ddot{X} + (1 + \sigma)\dot{X} + \frac{dU}{dX} = 0,$$

with

$$U(X) = \sigma \left( \frac{1-r}{2} X^2 + \frac{1}{4b} X^4 \right).$$

This equation can be interpreted as one-dimensional motion of a particle with unit mass in a quartic potential well  $U(X)$  with friction coefficient  $1 + \sigma$  [122, 124]. For  $r > 1$ , the quartic potential well takes the form of a double-well potential with stable fixed points at  $X = \pm\sqrt{b(r-1)}$  and an unstable fixed point at  $X = 0$ . We can rewrite equation (8.18) as

$$\ddot{X} + (1 + \sigma)\dot{X} + \frac{dU}{dX} + \left( \sigma - \frac{b}{2} \right) X \int_0^\infty (X^2(t-z) - X^2(t)) e^{-bz} dz = 0. \quad (8.19)$$

The above equation can be interpreted as a particle of unit mass and a friction coefficient  $1 + \sigma$  in a potential well  $U(X)$  with an additional force that depends on the history of the motion. Without the memory term, the particle would stop in one

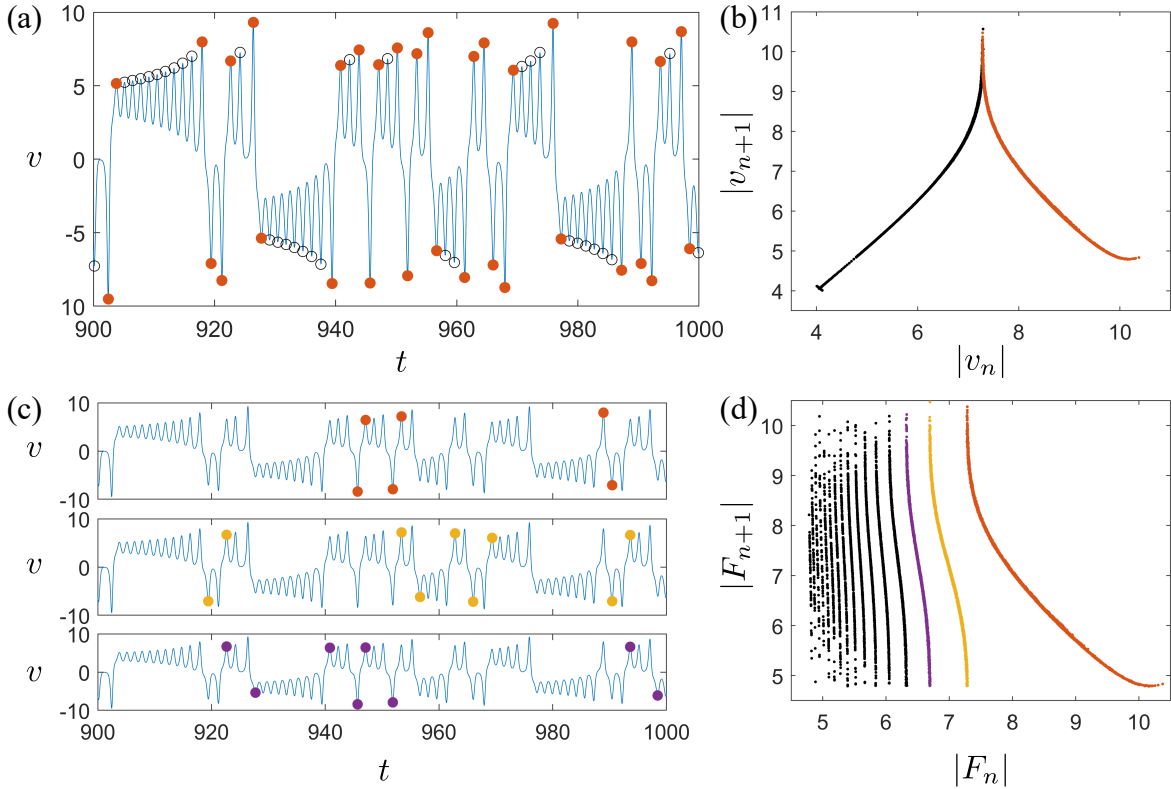


Figure 8.9 : Flip-flop process in the velocity time series of the droplet with a sinusoidal wave field at  $\kappa = 0.2$  and  $\beta = 35$ . (a) The velocity time series along with circles at the extrema of the oscillations are shown. The red filled circles indicate the extreme values before and after the flip. (b) Map of absolute value of consecutive extrema in the time series i.e. the absolute value of the consecutive circle in the left panel. The red and black branch corresponds to the red and black circles in the time series. (c) Same time series as in (a) but the markers now highlight the extreme values after a flip with a fixed number of  $N$  oscillations between them. The  $N = 0$  (red circles),  $N = 1$  (yellow circles) and  $N = 2$  (purple circles) are shown. (d) The map showing consecutive absolute values of the extrema after a flip with the  $N = 0$ ,  $N = 1$  and  $N = 2$  branch highlighted.

of the minima of the double-well potential  $U$  due to the damping force  $-(1 + \sigma)\dot{X}$ . The memory forcing sustains the particle motion. The particle oscillates in one of the minima with growing amplitude until it has sufficient energy to cross the barrier at  $X = 0$  [123, 125]. The unpredictability of this crossing behaviour results in the emergence of chaotic behaviour as shown in figure 8.8(c).

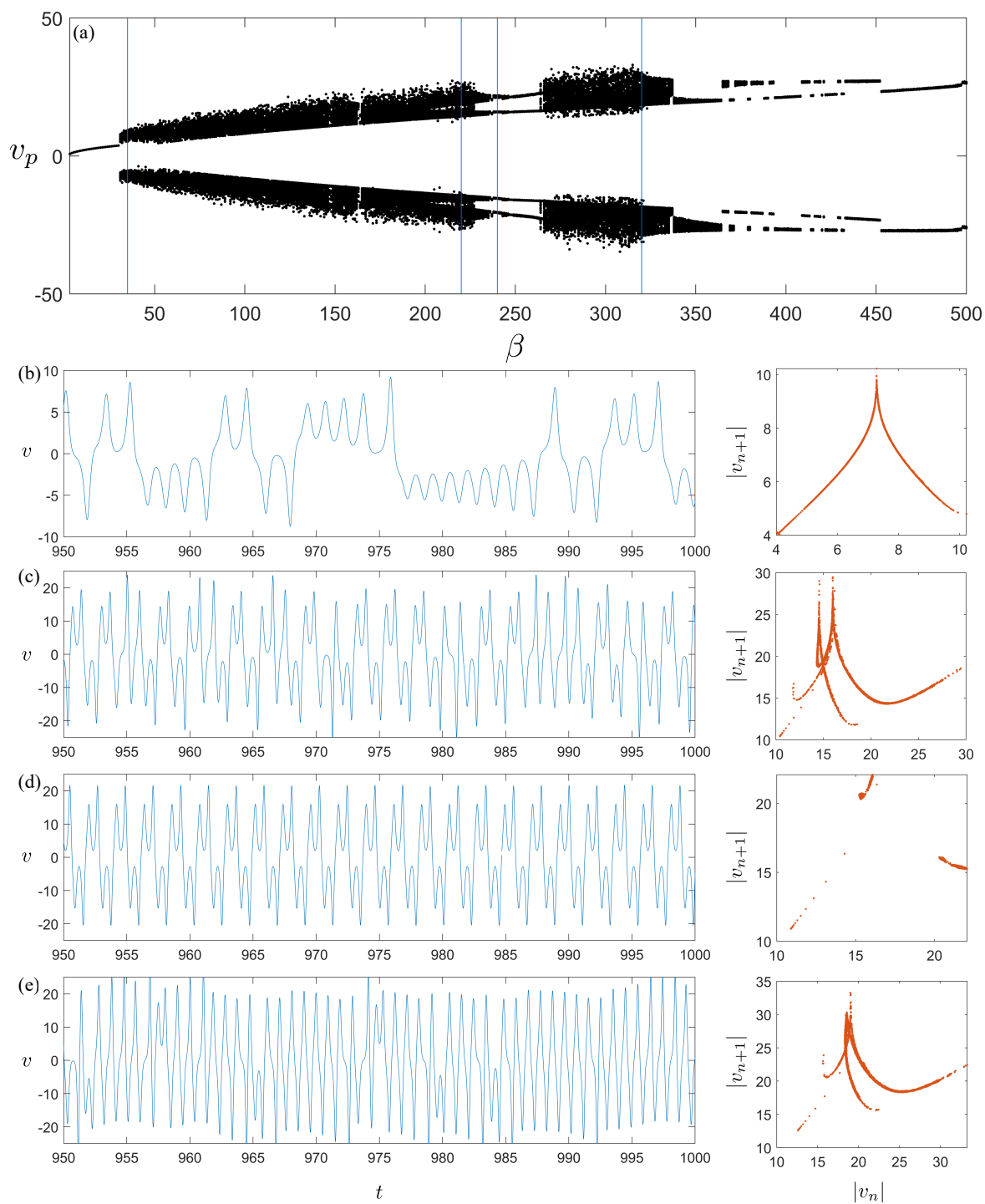


Figure 8.10 : (a) Velocity bifurcation diagram showing the peaks and troughs of the velocity time series as a function of the parameter  $\beta$  and a fixed  $\kappa = 0.2$ . The time series of velocity and the corresponding map for the maximum consecutive absolute values are shown for (b)  $\beta = 35$ , (c)  $220$ , (d)  $240$  and (e)  $320$ .

Now the integro-differential equation describing the motion of the droplet with a sinusoidal wave field from equation (8.5) is given by,

$$\kappa \ddot{x}_d + \dot{x}_d = \beta \int_0^\infty \sin(x_d(t) - x_d(t-z)) e^{-z} dz, \quad (8.20)$$

where we have changed the variable in the integral using  $z = t - s$ . By differentiating this equation with respect to time, we obtain the following integro-differential equation for the velocity of the droplet,

$$\kappa \ddot{v}_d + (1 + \kappa) \dot{v}_d + v_d \left[ 1 - \beta \int_0^\infty \cos(x_d(t) - x_d(t-z)) e^{-z} dz \right] = 0. \quad (8.21)$$

By comparing equations (8.18) and (8.21), we can see that both equations have similar structure with an inertia term, a damping term and a memory forcing term. Although the form of the memory forcing is different in the two equations, we see from figure 8.8 that they give rise to similar chaotic dynamics in regions of the parameter space hinting at a deeper connection between the two systems. We also refer the reader to the recent work of Durey [126] who have used the properties of Lorenz equations as a guide to explore the bifurcations and chaos in the droplet's dynamics with an equation that is equivalent to equation (8.20).

### 8.7.2 1D map of the velocity time series

We further explore the 1D cusp-like map obtained when the consecutive maximum values of absolute velocity are plotted against each other. As shown in figure 8.9, we find that the ascending branch on the cusp map corresponds to absolute extreme values of velocity oscillations when the droplet is moving in the same direction (black empty circles) while the descending branch corresponds to the absolute extreme values of velocity oscillations when a flip occurs in the velocity time series or equivalently the walking direction (red filled circles).

To analyse this further, we only look at the maximum absolute velocity after a flip occurs and plot their consecutive values against each other (see figure 8.9(c) and (d)). Here we find a band like structure similar to the Gauss map [127] with each band corresponding to a fixed number of  $N$  oscillations between flips. The branches corresponding to  $N = 0$  (red),  $N = 1$  (yellow) and  $N = 2$  (purple) are shown.

Figure 8.10(a) shows the velocity bifurcation diagram where the extreme values in the velocity time series  $v_p$  are plotted against the parameter  $\beta$ . The bifurcation diagram reveals regions of periodic and chaotic dynamics as a function of  $\beta$  for a fixed

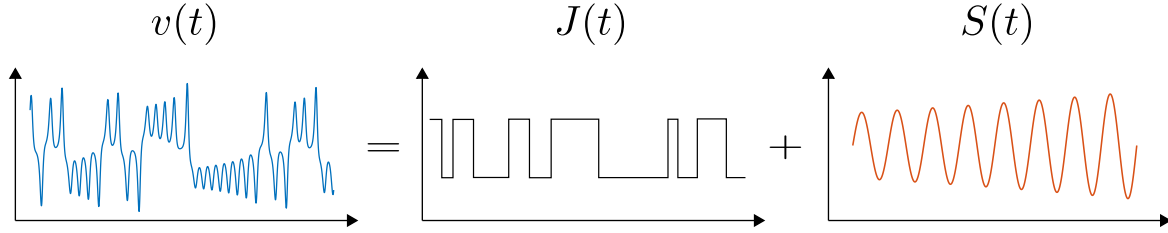


Figure 8.11 : Schematic showing that a typical velocity time-series  $v(t)$  of the droplet in the random walk-like regime can be thought of as a sum of a flip-flop process  $J(t)$  and an exponentially increasing sinusoidal  $S(t)$  which dictates the flip after the amplitudes reaches some threshold value [128].

$\kappa$ . Figure 8.10(b)-(e) shows the velocity time series and the 1D map of consecutive maximum values of absolute velocity at different  $\beta$  values. At low  $\beta$ , near the onset of the unsteady regime, we find that the map has a cusp like structure similar to that observed for a Lorenz map. At large  $\beta$ , we see folding taking place in the cusp map. Interspersed between the chaotic regimes are periodic regimes where the 1D map collapses to a compact region. For  $\beta \gtrsim 330$ , the droplet transitions from the chaotic regime to oscillating walker regime and then eventually to self-trapped oscillations.

## 8.8 Statistical aspects of the unsteady dynamics

### 8.8.1 Statistical properties of the flip-flop process

Aizawa [128] analysed the chaotic aspects of the Lorenz system by decomposing the time series in the Lorenz system into a flip-flop process and sinusoidal oscillations with increasing amplitude. As shown schematically in figure 8.11, we take a similar approach for the droplet's velocity time series and focus on the statistical aspects of the flip-flop process.

The flip-flop process in the droplet's velocity time series can also be thought of as the switches between the two attracting basins of the chaotic attractor projection shown in the middle panel of figures 8.8(a) and (b). Denoting the left and right attracting basins by  $L$  and  $R$  respectively, the dynamics of the flip-flop process will generate a sequence of states  $LLRRLR\dots$  for each trajectory (see figure 8.12(a) and (b)). The probability of being found in each state,  $L$  or  $R$ , is given by  $\Pr(L) = \Pr(R) = 1/2$ , due to the symmetry of the system. If the flip-flop process is Markovian, then the transition probabilities should be constant. Calling  $p$  the probability of flipping or

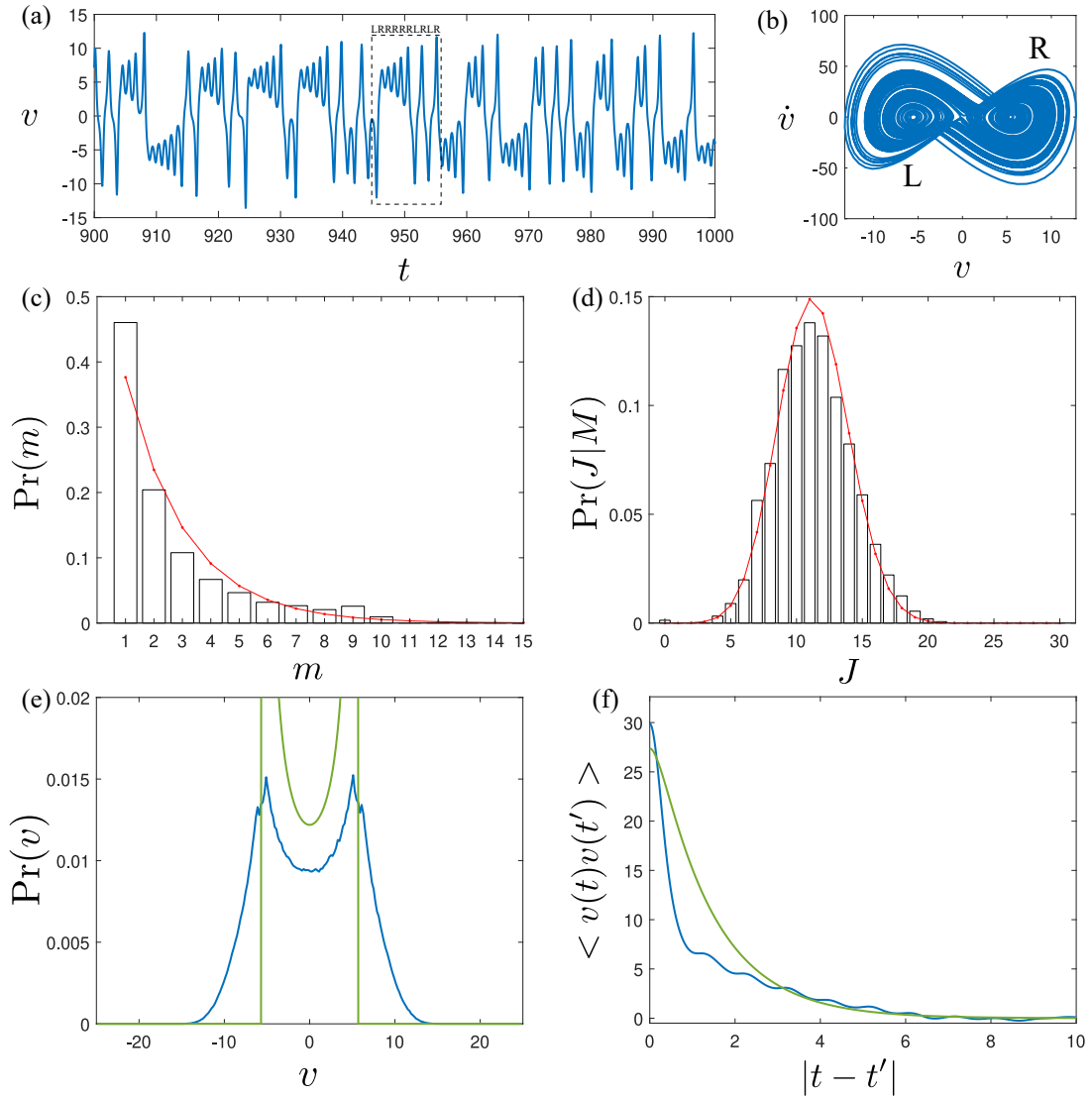


Figure 8.12 : Statistics of the flip-flop process for  $\kappa = 0.2$  and  $\beta = 65$  using the sinusoidal wave field. (a) Time series of velocity for a typical droplet's trajectory in the random walk-like regime using the sinusoidal wave field and (b) the corresponding projection of the chaotic attractor. The attractor has two basins that are labelled left 'L' and right 'R'. Panel (c) shows the probability distribution for having  $m$  oscillations between flips, while panel (d) shows the probability distribution for the number of jumps  $J$  in a given sequence of  $M$  steps. In both panels (c) and (d), the histogram is from the numerical simulations while the red curves are best fits obtained using equations (8.22) and (8.23) respectively. Panel (e) shows the stationary probability distribution for velocity while panel (f) shows the plot of velocity autocorrelation function. In both the panels, the blue curve is from numerical simulations while the green curve is the fit obtained by using Langevin model with dichotomous noise.

jump we have  $\Pr(L|R) = \Pr(R|L) = p$ , while the probability of not switching the state is given by  $\Pr(L|L) = \Pr(R|R) = 1 - p$  [129].

For a sequence  $LLRLRRLRRL\dots$ , one can generate a chain  $NJJJNJJNJ\dots$ , where  $J$  denotes an occurrence of a jump and  $N$  denotes no jump has occurred. If the process is Markovian, then the probability that the phase-space trajectory will execute  $m$  turns after entering a basin before it jumps out of the basin is given by the distribution [128, 129]

$$\Pr(m) = p(1 - p)^{m-1}. \quad (8.22)$$

Similarly, the probability that  $J$  jumps have occurred in a sequence of  $M$  turns is given by [128, 129]

$$\Pr(J|M) = \binom{M}{J} p^J (1 - p)^{M-J}. \quad (8.23)$$

We can estimate these probabilities from long enough chains of the flip-flop process from simulations by using

$$\Pr(m) = \frac{\sum_{k=1}^N \delta_{m,i_k}}{N} \quad \text{and} \quad \Pr(J|M) = \frac{\sum_{k=1}^T \delta_{J,J_k}}{T}. \quad (8.24)$$

Here  $\delta$  is the Kronecker delta,  $i_k$  represents number of turns executed in the basin between  $k - 1$ st and  $k$ th jump,  $N$  is the total number of jumps in the sample and  $J_k$  is the number of jumps occurring in each of the  $T$  sequences of  $M$  turns of the  $k$ th subdivided sample.

Figure 8.12(c) and (d) shows the comparison of these probability distribution calculated from ensemble average of 100 trajectories in the simulations (histograms) and the corresponding best fits of equations (8.22) and (8.23) for a typical  $\kappa$  and  $\beta$  value in the random walk-like regime. For the parameters chosen in figure 8.12, we obtain  $p = 0.376$ . We find a good fit at these parameters suggesting that Markovian approximation is reasonable in regions of the parameter space. However, we note that this is not always true in all the unsteady regimes of the parameter space.

We compare the equation of motion of the droplet, (8.5), with a Langevin-type equation that describes the motion of a particle under stochastic forcing [130],

$$\dot{q} + \gamma q = \xi(t). \quad (8.25)$$

Here  $q$  is the dynamical variable,  $\gamma$  is the friction coefficient and  $\xi(t)$  is the stochastic forcing. Comparing equation (8.25) with the droplet's equation of motion with a

sinusoidal wave field,

$$\dot{v}_d + \frac{1}{\kappa} v_d = \frac{\beta}{\kappa} \int_0^\infty \frac{1}{2} \sin(x_d(t) - x_d(t-z)) e^{-z} dz, \quad (8.26)$$

we see that the dynamical variable  $q$  is equivalent to the velocity  $v$  of the droplet, the friction coefficient  $\gamma$  is equivalent to  $1/\kappa$  and the stochastic forcing in equation (8.25) takes the place of memory forcing in the droplet's equation of motion. The time evolution of the memory force in the random walk-like regime of the walker is very similar to the velocity time series with the force switching erratically between positive and negative values with oscillations. We can crudely approximate the memory force time series for the droplet as a flip-flop process and ignore the oscillations. Then, the force time series of the droplet resembles a dichotomous process where the values of the force flips randomly between only two possible values. Hence if we choose the stochastic noise  $\xi(t)$  in equation (8.25) to be a dichotomous process, then we can compare the Langevin dynamics results with the numerical simulations of the droplet's dynamics. We assume that  $\xi(t)$  is a dichotomous process that will have only two possible values  $\pm\Delta$  with equal probability and jumps between them at a rate  $\lambda/2$  [130]. This form of the forcing has zero mean and autocorrelation

$$\langle \xi(t)\xi(t') \rangle = \Delta^2 e^{-\lambda|t-t'|}.$$

For the droplet's dynamics this value of  $\Delta$  can be approximated by  $\Delta \approx u/\kappa$  where  $u = \sqrt{\beta/2 - 1}$  is the steady walking speed for the sinusoidal wave field. For the Langevin equation described in (8.25), one can obtain an exact solution for the stationary probability distribution for the variable  $q$  [130] which gives,

$$P_{st}(q) = N(\Delta^2 - \gamma^2 q^2)^{\lambda/2\gamma - 1}, \quad (8.27)$$

where

$$N = \frac{\gamma \Gamma(1/2 + \lambda/2\gamma)}{\Delta^{\lambda/\gamma - 1} \Gamma(1/2) \Gamma(\lambda/2\gamma)}. \quad (8.28)$$

The corresponding autocorrelation function for the variable  $q$  in the stationary regime is

$$\langle q(t)q(t') \rangle = \frac{-\lambda\Delta^2}{\gamma(\gamma^2 - \lambda^2)} e^{-\gamma(t-t')} + \frac{\Delta^2}{\gamma^2 - \lambda^2} e^{-\lambda(t-t')}. \quad (8.29)$$

A comparison of the Langevin model results with the numerical results for the stationary probability distribution of droplet's velocity and the velocity autocorrelation

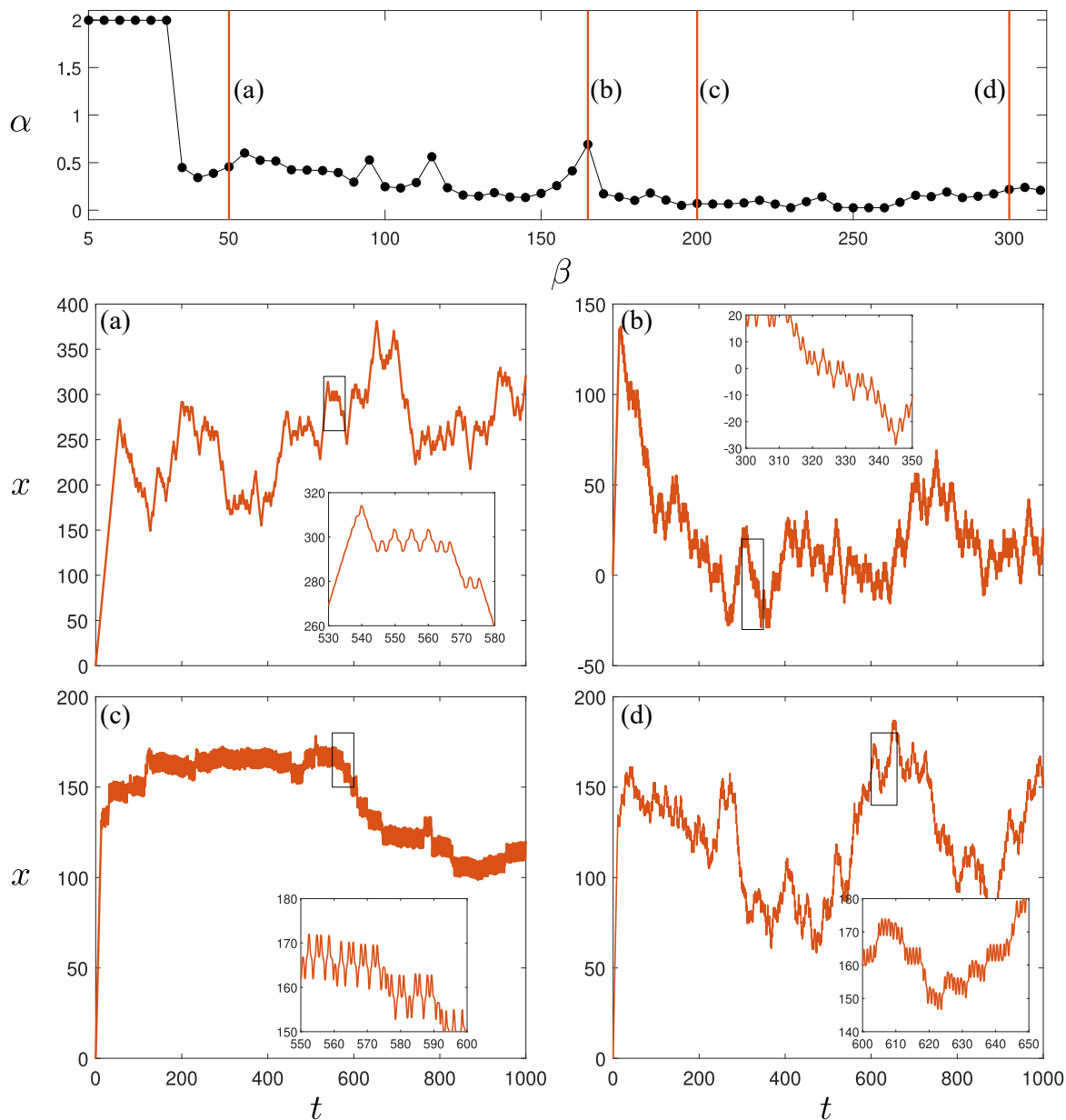


Figure 8.13 : Random-walk like dynamics of the droplet. Diffusive exponent  $\alpha$  as a function of the parameter  $\beta$  for a fixed  $\kappa = 0.2$ . Typical trajectories at (a)  $\beta = 50$ , (b) 100, (c) 200 and (d) 300 are shown.

function is shown in figures 8.12(e) and (f) respectively. We find that the Langevin model captures the qualitative features of both of these plots.

### 8.8.2 Analysis of the diffusion-like dynamics

In 1828, Robert Brown observed the erratic motion of small particles suspended in water. We now know this as Brownian motion. Brownian motion plays a key role in modelling of many random behaviours in nature and it is typically modelled by considering random impulsive forces acting on particles. However, numerous investigations have shown that the existence of Brownian-like motion from deterministic dynamics (also known as deterministic diffusion) in both discrete and continuous systems (see [131–134, 123, 135] and the reference therein). In particular, deterministic diffusion have been shown in differential delay equations [123, 136].

By investigating the trajectories in the random walk-like regime of the droplet with a sinusoidal wave field, we also obtain diffusion-like behaviour for the droplet. The diffusive behaviour of a system can be characterised by calculating how the mean squared displacement (MSD) scales with time i.e.,  $\text{MSD} \sim t^\alpha$  with  $\alpha$  the diffusive exponent. If  $\alpha = 2$  then the motion is ballistic while diffusive motion has  $0 < \alpha < 2$  with  $0 < \alpha < 1$  indicating sub-diffusive behaviour,  $\alpha = 1$  indicating diffusive motion and  $1 < \alpha < 2$  indicating super-diffusive behaviour. We calculate the diffusive exponent  $\alpha$  from an ensemble of 1000 trajectories with each trajectory run for  $t = 1000$ . We plot this diffusive exponent  $\alpha$  as a function of the parameter  $\beta$  for a fixed  $\kappa$  as shown in figure 8.13. We observe ballistic motion in the steady regime and in the random walk-like regime, the diffusive exponent drops below 1 indicating that the motion is sub-diffusive. Some typical trajectories in the random walk-like regime are shown in figures 8.13(a)-(d).

We also note that as previously described, the Lorenz system can be written as an integro-differential equation that describes a particle in a double-well potential. If the double-well potential is substituted by a periodic potential then diffusive behaviour like we see here is also obtained in the Lorenz system [123].

## 8.9 Conclusion

We have explored the unsteady dynamics of a walking droplet in the  $(\kappa, \beta)$  parameter space using the stroboscopic model of Oza et al. [88] with three different forms of the wave field: Bessel wave field, Gaussian wave field and sinusoidal wave field. Performing a linear stability analysis of the steady walking solution using a Gaussian wave field shows that the steady walking motion is stable in all of parameter space. Conversely, for the Bessel wave field and the sinusoidal wave field, the linear stability analysis shows regions in the parameter space where the steady walking solution becomes unstable and

a variety of unsteady motions are realised including oscillating walkers, self-trapped oscillations and random walk-like motion.

We have explored the chaotic dynamics of the droplet in the random walk-like regime and observed that the velocity evolution of the droplet has striking similarity with the evolution of the  $X$  variable in the Lorenz system and the projection of the chaotic attractor have similar structure. Moreover, the Lorenz equations can be recasted into an integro-differential equation that has similar form to the velocity equation for the droplet. This suggests a deeper connection between the two systems and warrants further investigation.

On exploring the statistical aspects of the droplet's velocity time series in the random walk-like regime, we find that in certain regions of the parameter space, the statistics of the chaotic switching in the walking direction of the droplet can be approximated by a Markovian process. Moreover, using the Langevin equation with a dichotomous noise we are able to capture the qualitative aspects of the stationary velocity distribution as well as the velocity autocorrelation function in the droplet's dynamics.

# Chapter 9

## Conclusions and outlook

In Part I of the thesis, we presented experimental and numerical results of a new class of self-propelled droplets, coined superwalkers, that emerge when a bath of liquid is simultaneously driven at a frequency and half that frequency with a relative phase difference between them. Superwalkers are bigger and faster than typical single-frequency driven walkers and they enable new types of inter-droplet interactions that give rise to a plethora of new multi-droplet behaviours.

We presented an experimental investigation of superwalking droplets in Chapter 3 where we characterised the dynamics of solitary superwalkers. We showed that superwalkers can be more than twice the size and walk at more than triple the speed of typical walkers. Moreover, the superwalking behaviour was found to be sensitive to the phase difference between the two driving frequencies which results in the droplets having bouncing, coalescence and superwalking regimes depending on this phase difference. We also noted that the inertia dominated superwalkers enable a new type of interaction between droplets, where the droplets can overcome the underlying wave field and can have short range droplet-droplet interactions. This results in novel dynamical bound states for few superwalkers and emergent behaviours when many superwalkers interact.

Single-frequency driven walkers have been shown to mimic several quantum analogues [51]. Thus, it would be interesting to revisit these experiments using superwalkers. Superwalkers provide an extra degree of freedom where the phase difference between the two driving signals can be used to tune the speed of the superwalkers. Thus, for example, in quantum corral analogues where a walker confined in a circular cavity displays wavelike statistics [35], it would be interesting to investigate the statistics of superwalkers and how those statistics change as a function of the superwalking speed which can be varied by varying the phase difference. This may give us new insights into the role of inertia in these hydrodynamic quantum analogues.

The observed collective dynamics of many superwalkers (see figure 3.13) are reminiscent of a solid-liquid-gas-like phase transition with the forcing amplitude acting as a temperature parameter. One can use the tools from statistical mechanics to characterise this phase transition behaviour. Moreover, it seems conceivable that in the ‘gas’ state, it may be possible to formulate an equilibrium statistical mechanics theory for superwalkers, as their motion in this regime is similar to that of an ideal gas of particles.

Superwalking droplets also constitute an example of active particles that extract energy from the vibrating bath and convert it to mechanical walking motion [137]. Specifically, superwalkers form a unique system of active particles that are dominated by inertia and can have both long-range interactions mediated by the underlying wave field as well as short-range droplet-droplet interactions. In the flourishing field of active matter, most of the focus have been towards studying systems where inertia of the active particles can be neglected. Emergent behaviours of inertia dominated active matter has not been explored much [137] and the superwalking droplets make a suitable system for such investigations.

In Chapter 4, we explored superwalking droplets numerically by adapting the previously established theoretical models for walkers to two-frequency driving and derived a new model for the superwalker wave field. We showed that superwalking emerges because driving the bath at two frequencies with an appropriate phase difference raises every second peak and lowers the intermediate peaks in the vertical periodic motion of the fluid surface allowing the large droplets to leap over intermediate peaks and settle in a resonant bouncing mode. We were successfully able to capture the experimentally observed superwalker characteristics for small- to moderate-sized superwalkers. Our model failed to capture the dynamics of large superwalkers. We suspect that to reproduce these large superwalkers in simulations, the droplet-wave interactions need to be modelled more accurately. Galeano-Rios et al. [68] have developed a model that provides a more complete description of the walking droplet system by detailed modelling of the droplet-wave interaction. Using their model, they have been able to capture the superwalking behaviour of a moderate sized droplet. It would be interesting to explore the large superwalkers using this model and to see if their characteristics are captured.

In Chapter 5, we presented a novel type of locomotion, stop-and-go motion (SGM), exhibited by superwalkers when the two driving frequencies are slightly detuned. Such motion arises because the small value of detuning results in a continuously varying phase difference that causes the droplet to periodically traverse the pure bouncing (stop)

---

and superwalking (go) regimes in speed versus phase difference space. By numerically exploring the SGM in the parameter space, we found three distinct types of motion. These are uncorrelated random walk-like motion where superwalking direction and the distance travelled appear to vary chaotically, and correlated motion, where either back-and-forth or forth-and-forth motion is observed. I plan to explore these behaviours in more detail in future to have a deeper understanding of the underlying mechanism that gives rise to correlated stop-and-go dynamics. Moreover, by engineering time dependent functions of the phase difference, one may be able to manipulate and control the motion of superwalking droplets.

In Part II of the thesis, we theoretically and numerically explored the dynamics and correlations of two droplets as well as the unsteady dynamics arising due to interfering memory of a single droplet using a stroboscopic model. We observed rich nonlinear dynamics for both a single droplet and droplet pairs that we have attempted to rationalise.

We began Part II of the thesis by exploring theoretically and numerically the dynamics of two identical, in-phase bouncing droplets and observed a rich range of behaviours. We captured the experimentally observed states such as parallel walkers and promenading pairs as well as more exotic dynamics such as wandering walkers and intriguing closed-loop trajectories. These more exotic trajectories have not been observed for walking droplets in experiments. However, we note that the spatial extent of some of these exotic trajectories, such as discrete turning walkers, is much larger than current experimental setups. Hence it would be interesting to explore the two-droplet dynamics systematically on a spatially extended experimental setup to see if any of these exotic behaviours are realised. Even with just two droplets, we get a rich range of exotic trajectories and hence it would be interesting to numerically explore the dynamics of many droplets as it may give rise to novel collective behaviours in walking droplets system.

A novel bound pair of droplets, called chasers, has been observed in experiments with superwalkers (see figure 3.10). For two identical, in-phase droplets we found the chasers to be unstable in Chapter 6. However, adding a spatial decay to the wave field in the stroboscopic model resulted in stable chasers for the same system in Chapter 7. Thus, it would be interesting to understand the dynamics of two identical droplets in a chasing pair in more detail. Moreover, the common chasing pairs observed with superwalkers in experiments are mismatched with the leading droplet being bigger than the trailing droplet. Hence, it would be interesting to explore different sized droplets in a chasing pair using the stroboscopic model.

In Chapter 7 we numerically studied the non-Markovian dynamics of pairs of walking droplets with crossing paths that are initially separated by a large inter-droplet distance. We have studied the probability that the droplets remain unbound as a function of their path difference to the common origin. We have found three generic classes of two-droplet correlations: promenading, orbiting and chasing, that are identified as dips in the probability plots. These numerical experiments correspond to a hydrodynamic analogue of the Hong–Ou–Mandel (HOM) two-photon interference experiment without a beam splitter. It will be interesting to explore such a setup of two-droplet correlations in experiments with walkers and superwalkers. It is known that for both classical waves and for classical particles the visibility of the HOM dip cannot exceed 50% [110]. It is therefore reasonable to assume the same to be true also for classical composite objects comprised of a droplet *and* a wave. To achieve a closer analogue of the HOM interference experiment, a hydrodynamic equivalent of a 50/50 beam splitter would need to be implemented. One such candidate could be a subsurface barrier with which a hydrodynamic analogue of quantum tunnelling has been demonstrated [44, 46, 45]. If the height and the width of such a barrier are suitably tuned, then in principle it should be possible to have a subsurface barrier reflect or transmit a single walker with a 50% probability. However, the reflection of a walker from a subsurface barrier is known to be sensitive to the incident angle and it might be difficult to overcome this subtlety in practice. Another scenario, motivated by the atomic HOM experiments [112], would be to direct the droplets through a grid barrier that would act as a Bragg diffraction grating for the droplets.

In Chapter 8, we explored the unsteady dynamics of a single droplet using different forms of the wave field in the stroboscopic model. We showed that for a Bessel wave field and a sinusoidal wave field, the steady walking motion of a single droplet becomes unstable for small inertia and large wave forcing and three distinct types of unsteady motions - oscillating walkers, self-trapped oscillations and random walk-like dynamics, are realised. On further exploring the chaotic dynamics of a walker in the random walk-like motion regime we found similarities in the chaos between the Lorenz system and the droplet's dynamics. Moreover, the Lorenz equations can be recast into an integro-differential equation that has a similar form to the velocity equation for the droplet. This suggests that we may be able to form deeper connections between these two system by studying the droplet's chaotic dynamics in more detail. Maybe, in some appropriate limit, the velocity equation of a walker reduces to the Lorenz equations allowing to form a robust connection between the two systems. Moreover, by studying the velocity statistics in the random walk-like regime, we found that in some regions

of the parameter space, the chaotic droplet dynamics can be well approximated by a Markovian process. Diffusion-like behaviour in deterministic systems, also known as deterministic diffusion [123, 125], has been known to arise in differential delay equations [136] where, similar to the droplet's trajectory equation in the stroboscopic model, the dynamics depend on the history. Applications of deterministic diffusion in modelling physical or biological phenomena that display stochastic behaviour may be interesting to explore because what is typically thought to be a signature of a random, nondeterministic process could well be a signature of a completely deterministic process [136].

Superwalkers open a new parameter regime to explore in the established area of walking droplets. They enable a new type of droplet-droplet interaction that gives rise to novel multi-droplet behaviours. Studying superwalkers may give us new insights in the areas of hydrodynamic quantum analogues and active matter. Moreover, integro-differential equations that model the dynamics of walking droplets give a rich range of dynamical behaviours. The study of droplet dynamics performed in this thesis lays the foundation for exploring hydrodynamic quantum analogues in a generalised pilot-wave framework.



# References

- [1] M. Faraday. On a peculiar class of acoustical figures; and on certain forms assumed by groups of particles upon vibrating elastic surfaces. *Philosophical Transactions of the Royal Society of London Series I*, 121:299–340, 1831.
- [2] T. B. Benjamin, F. J. Ursell, and G. I. Taylor. The stability of the plane free surface of a liquid in vertical periodic motion. *Proceedings of the Royal Society of London. Series A. Mathematical and Physical Sciences*, 225(1163):505–515, 1954.
- [3] J. Walker. Drops of liquids can be made to float on the liquid. What enables them to do so? *Scientific American*, 238(6):123–129, 1978.
- [4] Y Couder, E Fort, C-H Gautier, and A Boudaoud. From bouncing to floating: noncoalescence of drops on a fluid bath. *Physical Review Letters*, 94(17):177801, 2005.
- [5] Y. Couder, S. Protière, E. Fort, and A. Boudaoud. Dynamical phenomena: Walking and orbiting droplets. *Nature*, 437(7056):208–208, 2005.
- [6] S. Protière, A. Boudaoud, and Y. Couder. Particle–wave association on a fluid interface. *Journal of Fluid Mechanics*, 554:85–108, 2006.
- [7] S. Protière, Y. Couder, E. Fort, and A. Boudaoud. The self-organization of capillary wave sources. *Journal of Physics: Condensed Matter*, 17(45):S3529–S3535, 2005.
- [8] A. Eddi, A. Decelle, E. Fort, and Y. Couder. Archimedean lattices in the bound states of wave interacting particles. *Europhysics Letters*, 87(5):56002, 2009.
- [9] C. Borghesi, J. Moukhtar, M. Labousse, A. Eddi, E. Fort, and Y. Couder. Interaction of two walkers: Wave-mediated energy and force. *Physical Review E*, 90(6):063017, 2014.
- [10] J. Arbelaz, A. U. Oza, and J. W. M. Bush. Promenading pairs of walking droplets: Dynamics and stability. *Physical Review Fluids*, 3:013604, 2018.
- [11] S. Protière, S. Bohn, and Y. Couder. Exotic orbits of two interacting wave sources. *Physical Review E*, 78:036204, 2008.
- [12] A. Eddi, D. Terwagne, E. Fort, and Y. Couder. Wave propelled ratchets and drifting rafts. *Europhysics Letters*, 82(4):44001, 2008.

- 
- [13] C. A. Galeano-Rios, M. M. P. Couchman, P. Caldairou, and J. W. M. Bush. Ratcheting droplet pairs. *Chaos: An Interdisciplinary Journal of Nonlinear Science*, 28(9):096112, 2018.
- [14] B. Filoux, M. Hubert, and N. Vandewalle. Strings of droplets propelled by coherent waves. *Physical Review E*, 92(4):041004, 2015.
- [15] D. M. Harris, J. Moukhtar, E. Fort, Y. Couder, and J. W. M. Bush. Wavelike statistics from pilot-wave dynamics in a circular corral. *Physical Review E*, 88:011001, 2013.
- [16] T. Cristea-Platon, P. J. Sáenz, and J. W. M. Bush. Walking droplets in a circular corral: Quantisation and chaos. *Chaos: An Interdisciplinary Journal of Nonlinear Science*, 28(9):096116, 2018.
- [17] M. Durey, P. A. Milewski, and Z. Wang. Faraday pilot-wave dynamics in a circular corral. *Journal of Fluid Mechanics*, 891:A3, 2020.
- [18] T. Gilet. Dynamics and statistics of wave-particle interactions in a confined geometry. *Physical Review E*, 90:052917, 2014.
- [19] T. Gilet. Quantumlike statistics of deterministic wave-particle interactions in a circular cavity. *Physical Review E*, 93:042202, 2016.
- [20] Lucas D. Tambasco and J. W. M. Bush. Exploring orbital dynamics and trapping with a generalized pilot-wave framework. *Chaos: An Interdisciplinary Journal of Nonlinear Science*, 28(9):096115, 2018.
- [21] M. F. Crommie, C. P. Lutz, and D. M. Eigler. Imaging standing waves in a two-dimensional electron gas. *Nature*, 363(6429):524–527, 1993.
- [22] P. J. Sáenz, T. Cristea-Platon, and J. W. M. Bush. Statistical projection effects in a hydrodynamic pilot-wave system. *Nature Physics*, 14(3):315–319, 2018.
- [23] P. J. Sáenz, T. Cristea-Platon, and J. W. M. Bush. A hydrodynamic analog of Friedel oscillations. *Science Advances*, 6(20), 2020.
- [24] J. Friedel. Electronic structure of primary solid solutions in metals. *Advances in Physics*, 3(12):446–507, 1954.
- [25] K. Kanisawa, M. J. Butcher, H. Yamaguchi, and Y. Hirayama. Imaging of Friedel oscillation patterns of two-dimensionally accumulated electrons at epitaxially grown inas(111) *A* surfaces. *Physical Review Letters*, 86:3384–3387, 2001.
- [26] S. Perrard, M. Labousse, M. Miskin, E. Fort, and Y. Couder. Self-organization into quantized eigenstates of a classical wave-driven particle. *Nature Communications*, 5:3219, 2014.
- [27] S. Perrard, M. Labousse, E. Fort, and Y. Couder. Chaos driven by interfering memory. *Physical Review Letters*, 113:104101, 2014.

- [28] L. D. Tambasco, D. M. Harris, A. U. Oza, R. R. Rosales, and J. W. M. Bush. The onset of chaos in orbital pilot-wave dynamics. *Chaos: An Interdisciplinary Journal of Nonlinear Science*, 26(10):103107, 2016.
- [29] M. Labousse, S. Perrard, Y. Couder, and E. Fort. Build-up of macroscopic eigenstates in a memory-based constrained system. *New Journal of Physics*, 16(11):113027, 2014.
- [30] M. Labousse, A. U. Oza, S. Perrard, and J. W. M. Bush. Pilot-wave dynamics in a harmonic potential: Quantization and stability of circular orbits. *Physical Review E*, 93:033122, 2016.
- [31] K. M. Kurianski, A. U. Oza, and J. W. M. Bush. Simulations of pilot-wave dynamics in a simple harmonic potential. *Physical Review Fluids*, 2:113602, 2017.
- [32] M. Durey, P. A. Milewski, and J. W. M. Bush. Dynamics, emergent statistics, and the mean-pilot-wave potential of walking droplets. *Chaos: An Interdisciplinary Journal of Nonlinear Science*, 28(9):096108, 2018.
- [33] S. Perrard and M. Labousse. Transition to chaos in wave memory dynamics in a harmonic well: Deterministic and noise-driven behavior. *Chaos: An Interdisciplinary Journal of Nonlinear Science*, 28(9):096109, 2018.
- [34] E. Fort, A. Eddi, A. Boudaoud, J. Moukhtar, and Y. Couder. Path-memory induced quantization of classical orbits. *Proceedings of the National Academy of Sciences*, 107(41):17515–17520, 2010.
- [35] D. M. Harris and J. W. M. Bush. Droplets walking in a rotating frame: from quantized orbits to multimodal statistics. *Journal of Fluid Mechanics*, 739:444–464, 2014.
- [36] A. U. Oza, D. M. Harris, R. R. Rosales, and J. W. M. Bush. Pilot-wave dynamics in a rotating frame: on the emergence of orbital quantization. *Journal of Fluid Mechanics*, 744:404–429, 2014.
- [37] A. U. Oza, Ø. Wind-Willassen, D. M. Harris, R. R. Rosales, and J. W. M. Bush. Pilot-wave hydrodynamics in a rotating frame: exotic orbits. *Physics of Fluids*, 26(8):082101, 2014.
- [38] E. Fort and Y. Couder. Trajectory eigenmodes of an orbiting wave source. *Europhysics Letters*, 102(1):16005, apr 2013.
- [39] M. Labousse, S. Perrard, Y. Couder, and E. Fort. Self-attraction into spinning eigenstates of a mobile wave source by its emission back-reaction. *Physical Review E*, 94:042224, 2016.
- [40] A. U. Oza, R. R. Rosales, and J. W. M. Bush. Hydrodynamic spin states. *Chaos: An Interdisciplinary Journal of Nonlinear Science*, 28(9):096106, 2018.
- [41] A. Eddi, J. Moukhtar, S. Perrard, E. Fort, and Y. Couder. Level splitting at macroscopic scale. *Physical Review Letters*, 108(26):264503, 2012.

- [42] G. Pucci, P. J. Sáenz, L. M. Faria, and J. W. M. Bush. Non-specular reflection of walking droplets. *Journal of Fluid Mechanics*, 804:R3, 2016.
- [43] L. M. Faria. A model for Faraday pilot waves over variable topography. *Journal of Fluid Mechanics*, 811:51–66, 2017.
- [44] A. Eddi, E. Fort, F. Moisy, and Y. Couder. Unpredictable tunneling of a classical wave-particle association. *Physical Review Letters*, 102(24):240401, 2009.
- [45] M. Hubert, M. Labousse, and S. Perrard. Self-propulsion and crossing statistics under random initial conditions. *Physical Review E*, 95:062607, 2017.
- [46] A. Nachbin, P. A. Milewski, and J. W. M. Bush. Tunneling with a hydrodynamic pilot-wave model. *Physical Review Fluids*, 2:034801, 2017.
- [47] Y. Couder and E. Fort. Single-particle diffraction and interference at a macroscopic scale. *Physical Review Letters*, 97(15):154101, 2006.
- [48] A. Andersen, J. Madsen, C. Reichelt, S. Rosenlund Ahl, B. Lautrup, C. Ellegaard, M. T. Levinsen, and T. Bohr. Double-slit experiment with single wave-driven particles and its relation to quantum mechanics. *Physical Review E*, 92:013006, 2015.
- [49] G. Pucci, D. M. Harris, L. M. Faria, and J. W. M. Bush. Walking droplets interacting with single and double slits. *Journal of Fluid Mechanics*, 835:1136–1156, 2018.
- [50] M. T. Ellegaard, C. and Levinsen. Interaction of wave-driven particles with slit structures. *Physical Review E*, 102:023115, Aug 2020.
- [51] J. W. M. Bush. Pilot-wave hydrodynamics. *Annual Review of Fluid Mechanics*, 47:269–292, 2015.
- [52] J. W. M. Bush and A. U. Oza. Hydrodynamic quantum analogs. *Reports on Progress in Physics*, 2020.
- [53] R. N. Valani, A. C. Slim, and T. Simula. Superwalking droplets. *Physical Review Letters*, 123:024503, 2019.
- [54] R. N. Valani, J. Dring, T. P. Simula, and A. C. Slim. Emergence of superwalking droplets. *Journal of Fluid Mechanics*, 906:A3, 2021.
- [55] R. N. Valani and A. C. Slim. Pilot-wave dynamics of two identical, in-phase bouncing droplets. *Chaos: An Interdisciplinary Journal of Nonlinear Science*, 28(9):096114, 2018.
- [56] R. N. Valani, A. C. Slim, and T. Simula. Hong–Ou–Mandel-like two-droplet correlations. *Chaos: An Interdisciplinary Journal of Nonlinear Science*, 28(9):096104, 2018.
- [57] J. Moláček and J. W. M. Bush. Drops bouncing on a vibrating bath. *Journal of Fluid Mechanics*, 727:582–611, 2013.

- [58] T. Gilet and J. W. M. Bush. The fluid trampoline: droplets bouncing on a soap film. *Journal of Fluid Mechanics*, 625:167–203, 2009.
- [59] K Okumura, F Chevy, D Richard, D Quéré, and C Clanet. Water spring: A model for bouncing drops. *Europhysics Letters*, 62(2):237–243, 2003.
- [60] J. Moláček and J. W. M. Bush. A quasi-static model of drop impact. *Physics of Fluids*, 24(12):127103, 2012.
- [61] M. M. P. Couchman, S. E. Turton, and J. W. M. Bush. Bouncing phase variations in pilot-wave hydrodynamics and the stability of droplet pairs. *Journal of Fluid Mechanics*, 871:212–243, 2019.
- [62] P. A. Milewski, C. A. Galeano-Rios, A. Nachbin, and J. W. M. Bush. Faraday pilot-wave dynamics: modelling and computation. *Journal of Fluid Mechanics*, 778:361–388, 2015.
- [63] M. Durey and P. A. Milewski. Faraday wave–droplet dynamics: discrete-time analysis. *Journal of Fluid Mechanics*, 821:296–329, 2017.
- [64] F. Blanchette. Octahedra as models of oscillating and bouncing drops. *Physical Review Fluids*, 2:093603, 2017.
- [65] C. A. Galeano-Rios, P. A. Milewski, and J.-M. Vanden-Broeck. Non-wetting impact of a sphere onto a bath and its application to bouncing droplets. *Journal of Fluid Mechanics*, 826:97–127, 2017.
- [66] P. J. Holmes. The dynamics of repeated impacts with a sinusoidally vibrating table. *Journal of Sound and Vibration*, 84(2):173–189, 1982.
- [67] R. M. Everson. Chaotic dynamics of a bouncing ball. *Physica D: Nonlinear Phenomena*, 19(3):355–383, 1986.
- [68] C. A. Galeano-Rios, P. A. Milewski, and J.-M. Vanden-Broeck. Quasi-normal free-surface impacts, capillary rebounds and application to Faraday walkers. *Journal of Fluid Mechanics*, 873:856–888, 2019.
- [69] Ø. Wind-Willassen, J. Moláček, D. M. Harris, and J. W. M. Bush. Exotic states of bouncing and walking droplets. *Physics of Fluids*, 25(8):082002, 2013.
- [70] J. W. Strutt. VI. on the capillary phenomena of jets. *Proceedings of the Royal Society of London*, 29(196-199):71–97, 1879.
- [71] H. Lamb. *Hydrodynamics*. The University Press, 1895.
- [72] S. Chandrasekhar. *Hydrodynamic and Hydromagnetic Stability*. Clarendon Press, 1961.
- [73] C. A. Miller and L. E. Scriven. The oscillations of a fluid droplet immersed in another fluid. *Journal of Fluid Mechanics*, 32(3):417–435, 1968.
- [74] A. Prosperetti. Free oscillations of drops and bubbles: the initial-value problem. *Journal of Fluid Mechanics*, 100(2):333–347, 1980.

- [75] F. Blanchette. Modeling the vertical motion of drops bouncing on a bounded fluid reservoir. *Physics of Fluids*, 28(3):032104, 2016.
- [76] T. Gilet, D. Terwagne, N. Vandewalle, and S. Dorbolo. Dynamics of a bouncing droplet onto a vertically vibrated interface. *Physical Review Letters*, 100:167802, 2008.
- [77] D. Terwagne, F. Ludewig, N. Vandewalle, and S. Dorbolo. The role of the droplet deformations in the bouncing droplet dynamics. *Physics of Fluids*, 25(12):122101, 2013.
- [78] D. Richard, C. Clanet, and D. Quéré. Contact time of a bouncing drop. *Nature*, 417(6891):811–811, 2002.
- [79] L. Matthiessen. Akustische Versuche, die kleinsten Transversalwellen der Flüssigkeiten betreffend. *Annalen der Physik*, 210(5):107–117, 1868.
- [80] L. Rayleigh F.R.S. XXXIII. On maintained vibrations. *The London, Edinburgh, and Dublin Philosophical Magazine and Journal of Science*, 15(94):229–235, 1883.
- [81] L. Rayleigh D.C.L. F.R.S. VII. On the crispations of fluid resting upon a vibrating support. *The London, Edinburgh, and Dublin Philosophical Magazine and Journal of Science*, 16(97):50–58, 1883.
- [82] K. Kumar and L. S. Tuckerman. Parametric instability of the interface between two fluids. *Journal of Fluid Mechanics*, 279:49–68, 1994.
- [83] H. W. Müller. Periodic triangular patterns in the Faraday experiment. *Physical Review Letters*, 71:3287–3290, 1993.
- [84] A. Eddi, E. Sultan, J. Moukhtar, E. Fort, M. Rossi, and Y. Couder. Information stored in faraday waves: the origin of a path memory. *Journal of Fluid Mechanics*, 674:433–463, 2011.
- [85] J. Moláček and J. W. M. Bush. Drops walking on a vibrating bath: towards a hydrodynamic pilot-wave theory. *Journal of Fluid Mechanics*, 727:612–647, 2013.
- [86] L. Tadríst, J.-B. Shim, T. Gilet, and P. Schlagheck. Faraday instability and subthreshold Faraday waves: surface waves emitted by walkers. *Journal of Fluid Mechanics*, 848:906–945, 2018.
- [87] D. Shirokoff. Bouncing droplets on a billiard table. *Chaos: An Interdisciplinary Journal of Nonlinear Science*, 23(1):013115, 2013.
- [88] A. U. Oza, R. R. Rosales, and J. W. M. Bush. A trajectory equation for walking droplets: hydrodynamic pilot-wave theory. *Journal of Fluid Mechanics*, 737:552–570, 2013.
- [89] A. U. Oza, E. Siéfert, D. M. Harris, J. Moláček, and J. W. M. Bush. Orbiting pairs of walking droplets: Dynamics and stability. *Physical Review Fluids*, 2(5):053601, 2017.

- [90] S. E. Turton, M. M. P. Couchman, and J. W. M. Bush. A review of the theoretical modeling of walking droplets: Toward a generalized pilot-wave framework. *Chaos: An Interdisciplinary Journal of Nonlinear Science*, 28(9):096111, 2018.
- [91] D. M. Harris and J. W. M. Bush. Generating uniaxial vibration with an electrodynamic shaker and external air bearing. *Journal of Sound and Vibration*, 334:255–269, 2015.
- [92] N. Sampara and T. Gilet. Two-frequency forcing of droplet rebounds on a liquid bath. *Physical Review E*, 94:053112, 2016.
- [93] S. I. Lieber, M. C. Hendershott, A. Pattanaporkratana, and J. E. Maclennan. Self-organization of bouncing oil drops: Two-dimensional lattices and spinning clusters. *Physical Review E*, 75(5), 2007.
- [94] T. Besson, W. S. Edwards, and L. S. Tuckerman. Two-frequency parametric excitation of surface waves. *Physical Review E*, 54:507–513, 1996.
- [95] G. B. Thomas and R. L. Finney. *Calculus and analytic geometry*. Addison-Wesley, 9th edition, 1996.
- [96] K. Kumar. Linear theory of Faraday instability in viscous liquids. *Proceedings of the Royal Society of London. Series A, Mathematical and Physical Sciences.*, 452(1948):1113–1126, 1996.
- [97] J. C. Sprott. *Chaos and Time-Series Analysis*. Oxford University Press, Inc., New York, NY, USA, 2003.
- [98] D. L. Kramer and R. L. McLaughlin. The behavioral ecology of intermittent locomotion. *American Zoologist*, 41(2):137–153, 2015.
- [99] T. Y. Wu. Fish swimming and bird/insect flight. *Annual Review of Fluid Mechanics*, 43(1):25–58, 2011.
- [100] A. C. Gleiss, S. J. Jorgensen, N. Liebsch, J. E. Sala, B. Norman, G. C. Hays, F. Quintana, E. Grundy, C. Campagna, A. W. Trites, B. A. Block, and R. P. Wilson. Convergent evolution in locomotory patterns of flying and swimming animals. *Nature Communications*, 2(1):352, 2011.
- [101] B. V. Hokmabad, R. Dey, M. Jalaal, D. Mohanty, M. Almukambetova, K. A. Baldwin, D. Lohse, and C. C. Maass. Stop-and-go droplet swimmers. arXiv:2005.12721, 2020. doi: <https://arxiv.org/abs/2005.12721>.
- [102] S. Perrard, E. Fort, and Y. Couder. Wave-based turing machine: Time reversal and information erasing. *Physical Review Letters*, 117:094502, 2016.
- [103] S. C. Chapra. *Applied Numerical Methods W/MATLAB: for Engineers & Scientists*. McGraw-Hill Education, 2011.
- [104] J. Guckenheimer and P. Holmes. *Nonlinear oscillations, dynamical systems, and bifurcations of vector fields*, volume 42. Springer Science & Business Media, 2013.

- [105] H. Ebata and M. Sano. Swimming droplets driven by a surface wave. *Scientific Reports*, 5:8546, 2015.
- [106] A. Einstein, B. Podolsky, and N. Rosen. Can quantum-mechanical description of physical reality be considered complete? *Physical Review*, 47:777–780, 1935.
- [107] R. Hanbury Brown and R. Q. Twiss. A Test of a new type of Stellar Interferometer on Sirius. *Nature*, 178:1046–1048, 1956.
- [108] C. K. Hong, Z. Y. Ou, and L. Mandel. Measurement of subpicosecond time intervals between two photons by interference. *Physical Review Letters*, 59:2044–2046, 1987.
- [109] H. Fearn and R. Loudon. Theory of two-photon interference. *Journal of the Optical Society of America B*, 6(5):917–927, 1989.
- [110] R. Kaltenbaek, B. Blauensteiner, M. ukowski, M. Aspelmeyer, and A. Zeilinger. Experimental interference of independent photons. *Physical Review Letters*, 96:240502, 2006.
- [111] H. Kim, S. M. Lee, and H. S. Moon. Two-photon interference of temporally separated photons. *Scientific Reports*, 6:34805, 2016.
- [112] R. Lopes, A. Imanaliev, A. Aspect, M. Cheneau, D. Boiron, and C. I. Westbrook. Atomic Hong-Ou-Mandel experiment. *Nature*, 520:66–68, 2015.
- [113] S. Mährlein, S. Oppel, R. Wiegner, and J. von Zanthier. Hong-Ou-Mandel interference without beam splitters. *Journal of Modern Optics*, 64(9):921–929, 2017.
- [114] M. Hubert, S. Perrard, M. Labousse, N. Vandewalle, and Y. Couder. Tunable bimodal explorations of space from memory-driven deterministic dynamics. *Physical Review E*, 100:032201, 2019.
- [115] Howard C. Berg and Douglas A. Brown. Chemotaxis in escherichia coli analysed by three-dimensional tracking. *Nature*, 239(5374):500–504, 1972.
- [116] R. Stocker. Reverse and flick: Hybrid locomotion in bacteria. *Proceedings of the National Academy of Sciences*, 108(7):2635–2636, 2011.
- [117] M. Durey, S. E. Turton, and J. W. M. Bush. Speed oscillations in classical pilot-wave dynamics. *Proceedings of the Royal Society A: Mathematical, Physical and Engineering Sciences*, 476(2239):20190884, 2020.
- [118] M. Durey. *Faraday wave-droplet dynamics: a hydrodynamic quantum analogue*. PhD thesis, University of Bath, 2018.
- [119] J. Moláček. *Bouncing and walking droplets : towards a hydrodynamic pilot-wave theory*. PhD thesis, Massachusetts Institute of Technology, 2013.
- [120] E. N. Lorenz. Deterministic Nonperiodic Flow. *Journal of the Atmospheric Sciences*, 20(2):130–141, 1963.

- [121] Sparrow C. *The Lorenz Equations: Bifurcations, Chaos, and Strange Attractors*. Springer-Verlag, New York, 1982.
- [122] K. Takeyama. Dynamics of the Lorenz model of convective instabilities. *Progress of Theoretical Physics*, 60(2):613–615, 1978.
- [123] R. Festa, A. Mazzino, and D. Vincenzi. Lorenz deterministic diffusion. *Europhysics Letters*, 60(6):820–826, 2002.
- [124] K. Takeyama. Dynamics of the Lorenz model of convective instabilities. II. *Progress of Theoretical Physics*, 63(1):91–105, 1980.
- [125] R. Festa, A. Mazzino, and D. Vincenzi. Lorenz-like systems and classical dynamical equations with memory forcing: An alternate point of view for singling out the origin of chaos. *Physical Review E*, 65:046205, 2002.
- [126] M. Durey. Bifurcations and chaos in a lorenz-like pilot-wave system. *Chaos: An Interdisciplinary Journal of Nonlinear Science*, 30(10):103115, 2020.
- [127] R. M. Corless. Continued fractions and chaos. *The American Mathematical Monthly*, 99(3):203–215, 1992.
- [128] Y. Aizawa. Global aspects of the dissipative dynamical systems. I: Statistical identification and fractal properties of the Lorenz chaos. *Progress of Theoretical Physics*, 68(1):64–84, 1982.
- [129] F. Aicardi and A. Borsellino. Statistical properties of flip-flop processes associated to the chaotic behavior of systems with strange attractors. *Biological Cybernetics*, 55(6):377–385, 1987.
- [130] J. M. Sancho. Stochastic processes driven by dichotomous Markov noise: Some exact dynamical results. *Journal of Mathematical Physics*, 25(2):354–359, 1984.
- [131] C. Beck. Dynamical systems of Langevin type. *Physica A: Statistical Mechanics and its Applications*, 233(1):419 – 440, 1996.
- [132] T. Shimizu. Chaotic force in Brownian motion. *Physica A: Statistical Mechanics and its Applications*, 195(1):113 – 136, 1993.
- [133] L.Y. Chew and C. Ting. Microscopic chaos and gaussian diffusion processes. *Physica A: Statistical Mechanics and its Applications*, 307(3):275 – 296, 2002.
- [134] G. Trefán, P. Grigolini, and B. J. West. Deterministic Brownian motion. *Physical Review A*, 45:1249–1252, 1992.
- [135] G. Huerta-Cuellar, E. Jiménez-López, E. Campos-Cantón, and A.N. Pisarchik. An approach to generate deterministic Brownian motion. *Communications in Nonlinear Science and Numerical Simulation*, 19(8):2740 – 2746, 2014.
- [136] J. Lei and M. C. Mackey. Deterministic Brownian motion generated from differential delay equations. *Physical Review E*, 84:041105, 2011.
- [137] H. Löwen. Inertial effects of self-propelled particles: From active Brownian to active Langevin motion. *The Journal of Chemical Physics*, 152(4):040901, 2020.



# Appendix A

## Effects of horizontal vibrations and air currents in experiments

### Effects of horizontal vibrations

The oscillations of the bath were not completely uniaxial and unavoidably had horizontal components of acceleration,  $\Gamma_{H40}$  and  $\Gamma_{H80}$ , corresponding to the primary  $f = 80$  Hz driving and subharmonic  $f/2 = 40$  Hz driving. We performed additional experiments to quantify their effect on the superwalking behaviour. Over a period of half an hour of continuous use of the experimental setup, these horizontal accelerations approximately doubled in magnitude for constant vertical acceleration. During this time, we recorded the superwalking speed of different sized droplets. A small- to moderate-sized superwalker continued to walk for the entire half an hour duration while jumbo superwalkers typically coalesced a few times presumably due to the impurities present on the liquid surface. Thus, multiple identical jumbo superwalkers were created using a syringe over the half an hour duration. The results are shown for several droplet sizes in figure [A.1\(a\)](#). In addition, we added an off-centre weight to the bath in one case to deliberately amplify the horizontal vibrations further. As shown in figure [A.1\(a\)](#), the horizontal accelerations only have a small effect on the walking speed indicating that the superwalking behaviour is quite robust.

### Effects of air currents

To the naked eye, superwalkers seem more robust than walkers as they do not seem to be affected significantly by the ambient air currents, presumably due to their large

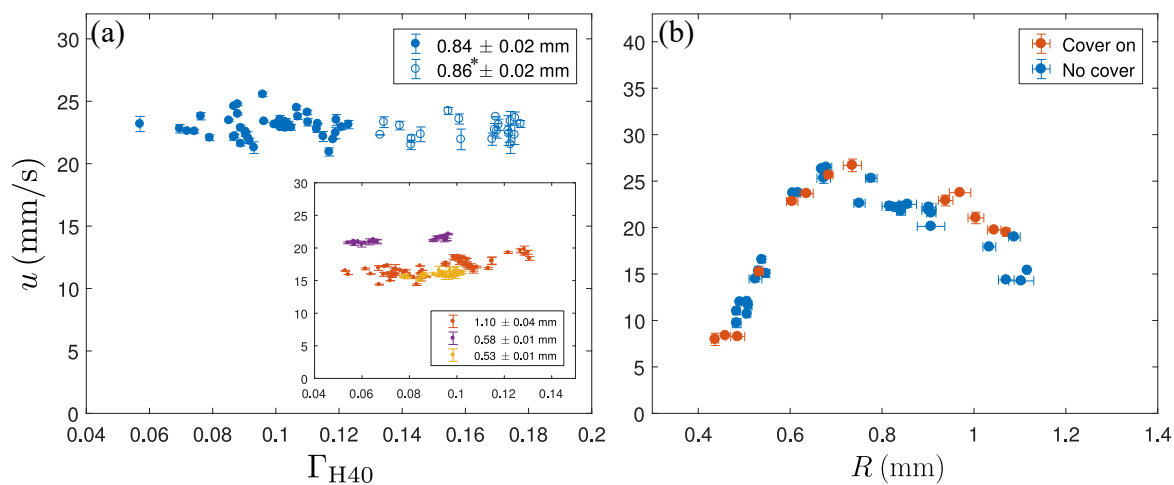


Figure A.1 (a) Speed of a superwalker as a function of the horizontal vibration amplitude  $\Gamma_{H40}$  (the larger of the two horizontal accelerations). Here the vertical vibration amplitudes were  $\Gamma_{80} = 3.8$ ,  $\Gamma_{40} = 0.6$  and the phase difference  $\Delta\phi = 130^\circ$ . To obtain the dataset at higher values of  $\Gamma_{H40}$ , indicated by an asterisk in the legend, an off-centre weight was added to the bath to deliberately increase the horizontal vibration component. (b) Comparison of speeds of droplets of different sizes with and without the lid on top of the bath. Parameters  $\Gamma_{80} = 3.8$ ,  $\Gamma_{40} = 0.6$ , and  $\Delta\phi = 130^\circ$ .

inertia. However, to quantify the effect of ambient air currents on the superwalkers, we performed additional experiments with and without a lid covering the bath. We used a clear acrylic lid with a rubber sheet acting as a sealant between the lid and the bath. The results of these control experiments are shown in figure A.1(b). Based on these results we conclude that the air currents do not have a major effect on the droplet speed.

# Appendix B

## Determination of parameters in simulations with superwalkers

The theoretical model for simulating superwalkers presented Chapter 4 has three free parameters that are currently not known for superwalkers: (i) the dimensionless spring constant  $K$  (ii) the dimensionless damping coefficient  $B$  and (iii) the contact drag coefficient  $C$ . In our study we fixed  $C = 0.17$ , a typical value that is used for walkers [85]. To determine values of  $K$  and  $B$ , we simulated superwalkers in the  $(K, B)$  parameter space and selected values that provide a good fit to our experimental results presented in Chapter 3. We found that using a constant values of  $K = 0.70$  and  $B = 0.60$  provided a reasonably good fit for small- to moderate-sized superwalkers on the ascending branch of the speed-size curves presented in figure 4.6, but failed for the largest superwalkers on the ascending branch for  $\Gamma_{40} = 1$ . By allowing the parameter  $K$  to vary linearly with the droplet radius  $R$  while keeping the parameter  $B$  fixed to 0.60, we were able to obtain a better fit on the ascending branch for the results presented in figure 4.6. To arrive at this linear relationship, we simulated superwalkers for a fixed  $\Gamma_{80} = 3.8$ ,  $\Delta\phi = 130^\circ$  and four different values of  $\Gamma_{40} = 0, 0.3, 0.6$  and 1. Droplet size that line to the ascending branch in figure 4.6 were simulated. Typical graphs that show the droplet's superwalking speed and bouncing modes are shown in figure B.1. For each droplet size and  $\Gamma_{40} = 0.6$  and 1, the region of the  $(K, B)$  parameter space where the relative difference between the speed of a simulated superwalker and the corresponding experimental value  $\Delta u/u_{\text{exp}} = (u - u_{\text{exp}})/u_{\text{exp}}$  is within 20% was determined and then a value of  $K$  was selected from that region that matched with the experimentally observed bouncing mode. A linear best fit through all such  $K$  values for different sized droplets results in one generic linear relationship given in equation (4.27). We note that obtaining a more accurate dependence of  $K$  and

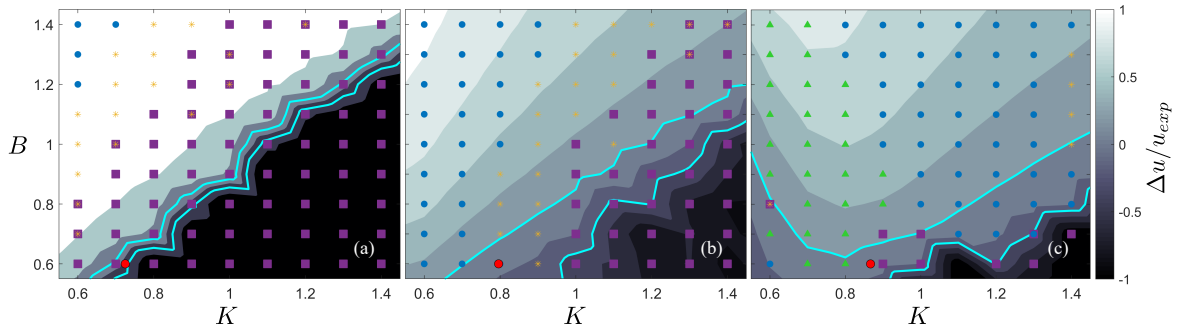


Figure B.1 Determination of the parameter values  $K$  and  $B$ . Bouncing modes (markers) and relative difference between the numerical and the experimental values of the walking speed  $\Delta u/u_{\text{exp}} = (u - u_{\text{exp}})/u_{\text{exp}}$  (contours) in the  $(K, B)$  parameter space for three different droplet radii (a)  $R = 0.5$  mm, (b)  $R = 0.6$  mm and (c)  $R = 0.7$  mm at  $\Gamma_{80} = 3.8$ ,  $\Gamma_{40} = 1$  and  $\Delta\phi = 130^\circ$ . In all the three panels, blue circles are  $(1, 2, 1)^{\text{H}}$ , green triangles are  $(1, 2, 1)^{\text{L}}$ , yellow asterisks  $*$  are  $(2, 4, 2)$  and purple squares represent chaotic or other higher periodicity bouncing modes. The cyan solid lines represent the boundaries of the region inside which  $|\Delta u/u_{\text{exp}}| < 20\%$  and the red circle corresponds to our chosen  $K$  according to (4.27) and a fixed  $B = 0.60$ .

$B$  on  $R$  would require performing experiments of droplets of different radii rebounding on a vibrating bath to obtain the corresponding  $K$  and  $B$  for each droplet radius  $R$ . Since this is beyond the scope of the thesis, we have just used our existing experimental results chosen  $K$  and  $B$  that best fit that experimental data.

# Appendix C

## Numerical Method for simulating droplets in the stroboscopic model

To simulate pair of droplets in Chapter 6 and 7, we numerically integrate equations (6.1) using the Leap-Frog method [97], a modified version of the Euler method where the new horizontal and vertical positions of the droplet are calculated using the old velocities and then the new velocities are calculated using the new positions. In Chapter 6, for  $t < 0$ , the droplets are assumed to be in a parallel walking state with  $\mathbf{x}_{O1} = (x_{O1}, y_{O1}) = (0, \mathcal{U}_1(\beta)t)$  and  $\mathbf{x}_{O2} = (x_{O2}, y_{O2}) = (\mathcal{D}_1(\beta), \mathcal{U}_1(\beta)t)$ . The new position of the droplet is calculated from the old position using a forward Euler step as follows:

$$\mathbf{x}_i(t_{n+1}) = \mathbf{x}_i(t_n) + \mathbf{v}_i(t_n)\Delta t$$

We calculate the new velocity using the updated position as follows,

$$\begin{aligned} \mathbf{v}_i(t_{n+1}) = \mathbf{v}_i(t_n) + \frac{\Delta t}{\kappa} & \left[ \beta \left( \mathbf{f}_{ij}(\mathbf{x}_i) e^{-t_n} \right. \right. \\ & + \int_0^{t_n} \frac{J_1(|\mathbf{x}_i(t_{n+1}) - \mathbf{x}_i(s)|)}{|\mathbf{x}_i(t_{n+1}) - \mathbf{x}_i(s)|} (\mathbf{x}_i(t_{n+1}) - \mathbf{x}_i(s)) e^{-(t_{n+1}-s)} ds \\ & \left. \left. + \int_0^{t_n} \frac{J_1(|\mathbf{x}_i(t_{n+1}) - \mathbf{x}_j(s)|)}{|\mathbf{x}_i(t_{n+1}) - \mathbf{x}_j(s)|} (\mathbf{x}_i(t_{n+1}) - \mathbf{x}_j(s)) e^{-(t_{n+1}-s)} ds \right) - \mathbf{v}_i(t_n) \right] \end{aligned} \quad (\text{C.1})$$

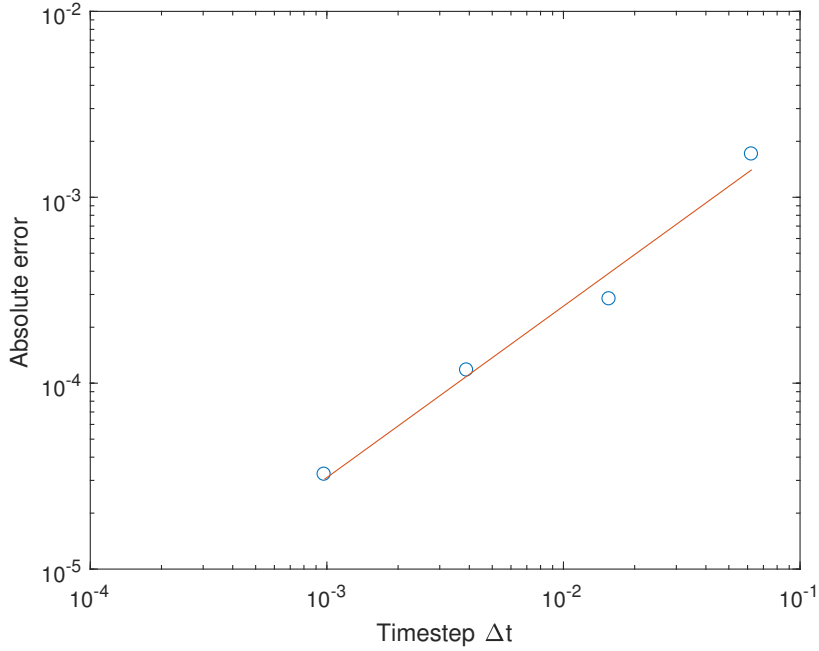


Figure C.1 Comparison of the parallel walking numerical solution using the modified Euler method with the exact solution for timesteps  $\Delta t = 2^{-4}$ ,  $2^{-6}$ ,  $2^{-8}$  and  $2^{-10}$ . The absolute difference in the parallel walking velocity is plotted for different timesteps (blue circles) with a line of best fit (orange line) of gradient  $\approx 0.92$ . Parameter values are  $\kappa = 0.5$  and  $\beta = 3$ .

where,

$$\begin{aligned} \mathbf{f}_{ij}(\mathbf{x}_i) = & \int_{-\infty}^0 \frac{J_1(|\mathbf{x}_i(t_n) - \mathbf{x}_{O_i}(s)|)}{|\mathbf{x}_i(t_n) - \mathbf{x}_{O_i}(s)|} (\mathbf{x}_i(t_n) - \mathbf{x}_{O_i}(s)) e^s ds \\ & + \int_{-\infty}^0 \frac{J_1(|\mathbf{x}_i(t_n) - \mathbf{x}_{O_j}(s)|)}{|\mathbf{x}_i(t_n) - \mathbf{x}_{O_j}(s)|} (\mathbf{x}_i(t_n) - \mathbf{x}_{O_j}(s)) e^s ds. \end{aligned} \quad (\text{C.2})$$

The integration in equation (C.1) was performed using the trapezoidal rule where we consider the contribution from all the previous impacts for the first 1280 timesteps ( $t = 20$  using  $\Delta t = 2^{-6}$ ) and then the contribution from the last 1280 impacts for  $t > 20$ . At 1280 previous impacts, the exponential damping factor has reached  $e^{-20} \approx 10^{-9}$  so we neglect all the contribution from impacts beyond 1280 previous steps. The integrals in equation (C.2) were calculated using an adaptive Gauss-Kronrod quadrature routine built into MATLAB. The convergence of this method for the parallel walking solution is shown in Fig. C.1. Using this method, we have been able to reproduce the exotic trajectories of a single walker in a rotating frame by Tambasco et al. [28] and Oza et al. [37].

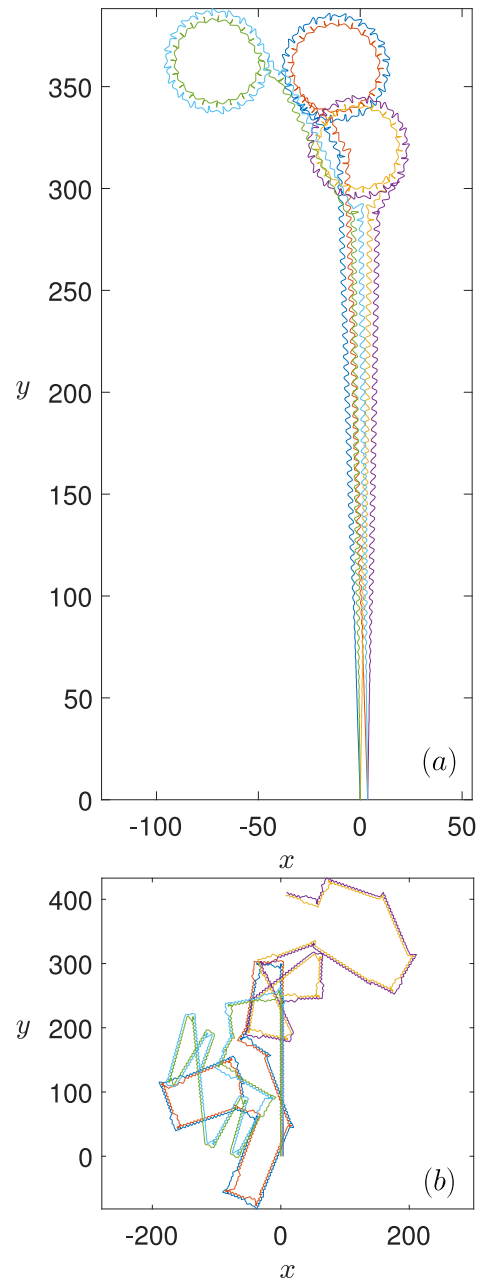


Figure C.2 Comparison of trajectories for (a)  $\kappa = 0.6$  and  $\beta = 4$  and (b)  $\kappa = 0.5$  and  $\beta = 6$  starting as parallel walkers with random noise using timesteps  $\Delta t = 2^{-6}$  (blue and orange),  $2^{-8}$  (yellow and purple) and  $2^{-10}$  (green and cyan). All three timesteps eventually lead to the exotic trajectory of closed circles with lopsided walkers for (a) and right-angled discrete turning walking for (b).

Figure C.2 shows the comparison with different timesteps of the closed circular trajectory at  $\kappa = 0.6$  and  $\beta = 4$  where the pair of walkers are in a lopsided mode and the right-angled discrete turning walkers at  $\kappa = 0.5$  and  $\beta = 6$ . Simulating trajectories

at this parameter value with timesteps  $\Delta t = 2^{-6}$ ,  $2^{-8}$  and  $2^{-10}$  with noise in initial conditions confirm that these exotic behaviours are robust.